Joining Si_3N_4 to FA-129 Iron Aluminide

by

MATHIEU BROCHU

Department of Mining, Metals and Materials Engineering
McGill University
Montreal, Canada

A Thesis submitted to the
Faculty of Graduate Studies and Research
In partial fulfillment of the requirements for the degree of
Doctor of Philosophy

Library and
Archives Canada

Published Heritage
Branch

395 Wellington Street
Ottawa ON K1A 0N4
Canada

Bibliothèque et
Archives Canada

Direction du
Patrimoine de l'édition

395, rue Wellington
Ottawa ON K1A 0N4
Canada

Your file Votre référence
ISBN: 0-612-98215-7
Our file Notre référence
ISBN: 0-612-98215-7

NOTICE:
The author has granted a non-exclusive license allowing Library and Archives Canada to reproduce, publish, archive, preserve, conserve, communicate to the public by telecommunication or on the Internet, loan, distribute and sell theses worldwide, for commercial or non-commercial purposes, in microform, paper, electronic and/or any other formats.

The author retains copyright ownership and moral rights in this thesis. Neither the thesis nor substantial extracts from it may be printed or otherwise reproduced without the author's permission.

AVIS:
L'auteur a accordé une licence non exclusive permettant à la Bibliothèque et Archives Canada de reproduire, publier, archiver, sauvegarder, conserver, transmettre au public par télécommunication ou par l'Internet, prêter, distribuer et vendre des thèses partout dans le monde, à des fins commerciales ou autres, sur support microforme, papier, électronique et/ou autres formats.

L'auteur conserve la propriété du droit d'auteur et des droits moraux qui protège cette thèse. Ni la thèse ni des extraits substantiels de celle-ci ne doivent être imprimés ou autrement reproduits sans son autorisation.

In compliance with the Canadian Privacy Act some supporting forms may have been removed from this thesis.

While these forms may be included in the document page count, their removal does not represent any loss of content from the thesis.

Conformément à la loi canadienne sur la protection de la vie privée, quelques formulaires secondaires ont été enlevés de cette thèse.

Bien que ces formulaires aient inclus dans la pagination, il n'y aura aucun contenu manquant.

Canada

Foreword

This thesis has been constructed in a manuscript-type format and contains six main sections. The introduction gives the reader the basic knowledge as well as justification for its existence. Four different sections, each of them containing chapters with independent result and discussion sections, guides the reader through the scientific and engineering approach undertake by the author. In addition, each sub-chapter contains a specific literature review appropriate to that section. The four main sections are:

1. Analysis of Si_3N_4 Ceramic with a Low Voltage Scanning Electron Microscope,
2. Wetting and Interactions of Cu-Ti Alloys on Iron Aluminide Alloys,
3. Fabrication and Characterization of a High-Ti content Cu Brazing Alloy,
4. Joining Si_3N_4 to itself and to an Iron Aluminide Alloy using a High-Ti content Cu Brazing Alloy.

The thesis ends with a general discussion, conclusions and contribution to original knowledge, which link all the previous chapters.

I would like to acknowledge the contribution of Prof. R.A.L. Drew (McGill University) and M.D. Pugh (Concordia University) as thesis supervisors for their assistance through suggestions/corrections during the elaboration of all manuscripts presented in this thesis, Prof. R. Gauvin and H. Demers for their suggestions during the elaboration of the manuscript presented in Chapter 2 and of Prof. S.F. Corbin (University of Waterloo) for having giving me access to his DSC as well as his suggestions during the writing of the manuscript presented in Chapter 6.

Again, I, the author, would like to advise you that thesis is a manuscript-type of theis, but I think that this format better reflects all the steps I have been through during my research endeavors.

Enjoy reading,

Mathieu

Abstract

Joints between dissimilar materials are characterized particularly by compositional gradients and microstructural changes, which yield large variations in chemical, physical and mechanical properties across the joint. The joining of dissimilar materials is therefore more complex than the joining of similar materials. In this project, the joining procedure, from the interaction between the different components in a joint to the determination of the mechanical properties was applied to the Si_3N_4/FA-129 system. This iron aluminide intermetallic alloy (FA-129), was developed by Oak Ridge National Laboratories (ORNL) to have high temperature properties with good room temperature ductility. This intermetallic is replacing high strength ferritic stainless steel (SS) in moderate strength applications due to cost and property reasons. Joints between SS and Si_3N_4 are already used industrially and this project was to evaluate the potential to replace these Si_3N_4/SS joints by those of Si_3N_4/FA-129.

Characterisation and analysis have been performed using techniques such as: atomic absorption, atomic force microscopy, conventional and field emission scanning electron microscope, microprobe, x-ray diffraction, optical microscopy and image analysis, differential scanning calorimetry, sedimentation, microhardness, and flexural strength testing. In some cases, new analytical procedures have been developed. In all cases, the results were compared to literature data where possible, to reinforce the scientific statements made during the project.

Broadly stated, the results obtained during this project are as follows:

I. The E_2 energy for Si_3N_4 ceramic was calculated to be 3.01 keV.
II. The wetting of iron aluminide alloy by copper has been achieved and the spreading and reaction kinetics are influenced by the presence of Cr as alloying element.
III. The penetration and decohesion of the FA-129 microstructure is significantly reduced by the utilization of a Cu alloy containing a high titanium concentration.
IV. An active brazing alloy containing a high active element content can be fabricated by an electroless deposition technique.

V. The melting behavior of the powder was characterized and complete melting occurs in a multi-step process at different temperatures, which are a function of the heating rate.
VI. The strength of joint produced by brazing Si_3N_4 to itself using the composite powder reached 400 MPa.
VII. Direct brazing of Si_3N_4 to FA-129 was shown to be unsuccessful and therefore a soft Cu interlayer was inserted to absorb residual stresses. The maximum joint strength reached was 160 MPa.
VIII. Partial Transient Liquid Phase Bonding was successfully applied to the Si_3N_4/FA-129 system using a nickel interlayer. The conventional silicide and nitride layers were not observed as the silicide layer dissolved into the nickel core at high temperature. The strength of the assembly was measured and a strength of 80 MPa was obtained, independent of the joining parameters.

Résumé

Les joints entre les matériaux dissimilaires sont caractérisés particulièrement par des gradients de composition et changements de microstructures, entraînant des variations importantes des propriétés chimiques, physiques et mécaniques dans le joint. L'union de matériaux dissimilaires est donc plus complexe que dans le cas des matériaux similaires. Dans ce projet, la procédure d'assemblage, débutant par l'interaction entre les différentes parties du joint jusqu'à l'évaluation des propriétés mécaniques, a été appliquée au système Si_3N_4/FA-129. Cet alliage de ferro-aluminium a été développé par ORNL, visant l'obtention de bonnes propriétés à haute température combinées à une bonne ductilité à la température de la pièce. Cet intemétallique remplace les aciers inoxydables ferritiques à haute résistance pour des applications à contrainte modérée pour des raisons de coûts et de propriétés. Des joints entre des aciers inoxydables et le Si_3N_4 sont déjà utilisés industriellement et ce projet vise à évaluer le potentiel de remplacement de ces joints par des joints Si_3N_4/FA-129.

La caractérisation des résultats expérimentaux ainsi que l'analyse des résultats ont été réalisées en utilisant les techniques suivantes: absorption atomique, microscopie à force atomique, microscopie électronique conventionnelle et à effet de champ, microscopie optique et analyse d'images, DSC, technique de sédimentation, micro-dureté, essai de flexion. Dans quelques cas, de nouvelles procédures d'analyses ont été développées. Dans tous les cas, les résultats ont été comparés aux résultats disponibles dans la littérature (lorsque possible) pour raffermir les énoncés scientifiques faits au cours du projet.

Voici les grandes lignes des résultats obtenus au cours de ce projet:

I. L'énergie E_2 pour la céramique Si_3N_4 a été calculée à 3.01keV.
II. La mouillabilité du Cu sur l'alliage du ferro-aluminium a été obtenu, de même que l'évasement et la cinétique de réaction qui sont influencés par la présence de Cr comme élément d'alliage.
III. La pénétration et la décohésion de la microstructure du FA-129 sont réduites significativement par l'utilisation de Cu contenant une haute concentration en Ti. La fabrication d'un alliage de brasage actif à haute

teneur en élément actif a été réalisée par une technique de déposition autocatalytique.

IV. Le comportement lors de la fusion de la poudre a été caractérisé et la fusion complète fut obtenue par un procédé en plusieurs étapes et s'est terminé à différentes températures, qui sont fonction de la vitesse de chauffage.

V. La résistance de joints produits par brasage de Si_3N_4/Si_3N_4 en utilisant la poudre composite a atteint 400 MPa.

VI. Le brasage direct du Si_3N_4 au FA-129 ne fut pas concluant et une couche intermédiaire a été insérée pour absorber les contraintes résiduelles. Les propriétés maximales obtenues sont de 160 MPa.

VII. PTLPB a été appliqué avec succès au système Si_3N_4/FA-129 en utilisant une couche intermédiaire de Ni. Les couches conventionnelles de siliciure et de nitrure n'ont pas été observées dû à la dissolution de la couche de siliciure à haute température dans la couche de Ni. La résistance des joints a été mesurée et est approximativement de 80 MPa, indépendamment des paramètres utilisés.

Acknowledgements

During my thesis studies, several people contributed in various ways to this final product and I would like to take a few lines to immortalise the main contributors:

Firstly, Robin and Martin, forming the perfect supervisor duo by giving me the chance to express myself from the beginning and for giving me the proper latitude for my personal scientific development. They also supplied me opportunities and challenges to acquire, display and improve my scientific and human skills. You were and I hope you will remain, an important source of inspiration. It was delightful to work with you, thanks.

I have to acknowledge all the organisation who sponsored the project or granted me scholarships. Natural Science and Engineering Council of Canada (NSERC), Fond Québécois de recherche sur la nature et les technologies (FQRNT; formerly FCAR) and McGill University.

I have to thank all the personnel of the department, for your friendship, help and "5 minute social talk" we had over the last 3¾ years. Special thanks to Helen Campbell, Edwin Fernandez, Barbara Hanley, Ray Langlois, Purnima Mudjumdar, Robert Paquette, Florence Paray, Glenn Poirier, Slavek Poplowski, Norma Proscyshin, Monique Riendeau, Carol Rousseau and Genny "Genevieve" Snider.

It would be impossible to complete a Ph.D residency without the help and support of friends. I should remember: Claudia and Juan (sorry homo, I put the lady first!), Mamoun, Mehrdad, Pui Kei, Xin, David, Fabian, Farzad, Ozgur, Ramona, Abdel, Gregg, Faramarz, Pascal, Rocco, Hendrix, Paula, Roberto, David, José, Jerry, Ralph, Dominique, Kevin, Neivi, Zhen, Khaled, Chunyi, Hamad, Will, Lan, Ben, Darryl, Raed, Bae Kyun. To my dear close friends who had to support my temper, humour and ... basically me, thanks. Thanks also to everybody else not listed!

Je me dois aussi de remercier la gang de Québec, ceux avec qui j'ai passé toute ma jeunesse et vécu des expériences par toujours racontables: Rémi, Jean-Michel, Eric, Vincent et tous les autres.

J'aimerais remercier sincèrement ma famille; mon père Yvon, ma mère Ginette, mes sœurs Magalie et Anne-Marie et mon grand-père Aurèle, de leur support et tolérance face à mes sautes d'humeur et commentaires quelque fois critiques. Malgré les apparences, votre contribution fut plus qu'importante. Merci du plus profond de mon cœur.

Finalement, la plus grosse pièce du casse-tête, et quel casse-tête se fut, Amour (Isabelle), qui a sûrement fait les plus gros sacrifices que la terre ait connu dans les dernières 3¾ années. Sans ton support, tes nombreux encouragements, ta présence, ta compréhension et ton amour, je serais parvenu à ce résultat, mais avec beaucoup plus de difficultés. Maintenant que j'ai terminé, sort ta liste des nombreuses activités que nous avons remises pour que je puisse travailler, parce qu'on va les faire!

Table of Contents

Foreword i

Abstract ii

Resume iv

Acknowledgements vi

Table of Content viii

List of Figures xiv

List of Tables xxii

Chapter 1. Introduction

- 1.1 Why Ceramic-Metal Joints? 1
- 1.2 What is Silicon Nitride (Si_3N_4)? 4
- 1.3 What are Iron Aluminides Alloys (Fe_3Al alloys)? 6
- 1.4 Interface Formation in Ceramic/Metal Joints 10
  - 1.4.1 Liquid State Interface Formation 11
    - 1.4.1.1 Non-Reactive Systems 11
    - 1.4.1.2 Reactive Systems 13
  - 1.4.2 Solid/Solid Interface Formation 14
- 1.5 Joining Processes 14
  - 1.5.1 Reactive Brazing 15
  - 1.5.2 Diffusion Bonding 17
  - 1.5.3 Eutectic Melt Joining 18

1.5.4 Partial Transient Liquid Phase Bonding 19
1.6 Difficulties in Joining Dissimilar Materials 20
1.7 Objectives 24
1.8 References 25

Part 1 - Analysis of Si_3N_4 Ceramic with a Low Voltage Scanning Electron Microscope

Chapter 2. Determination of E_2 Energy for Si_3N_4 Ceramic

2.1 Introduction 29
2.2 Experimental Procedure 32
2.3 Results 35
2.4 Discussion 41
2.5 References 41

Part 2 - Wetting and Interactions of Cu-Ti Alloys on an Iron Aluminide Alloy

Chapter 3. Wetting Behaviour of Copper on an Iron Aluminide Alloy

3.1 Introduction 43
3.2 Experimental Procedure 44
3.3 Results 46
3.4 Discussion 51
3.5 References 54

Chapter 4. Interfacial Microstructure Characterisation between Molten Cu-XTi and FA-129 Intermetallic

4.1 Introduction 55

4.2 Experimental Procedure 56
4.3 Results 57
4.3.1 Penetration Results 57
4.3.2 Microstructural Characterisation 59
4.3.2.1 Cu/FA-129 Interactions 59
4.3.2.2 Cu-5wt%Ti/FA-129 Interactions 64
4.3.2.3 Cu-20wt%Ti/FA-129 Interactions 67
4.3.3 Effect of Cu and Ti Penetration on Hardness 70
4.4 Discussion 70
4.5 References 74

Part 3 - Fabrication and Characterization of a High-Ti containing Cu Brazing Alloy

Chapter 5. Fabrication of a Composite Powder and Utilization as Active Brazing Alloy

5.1 Introduction 76
5.2 Experimental Procedure 78
5.3 Results 81
5.3.1 Powder Pre-treatment 81
5.3.2 Effect of pH on Deposition 81
5.3.3 Effect of Starting Powder Morphology 82
5.3.4 Plating Iterations 82
5.3.5 Particle Size Distribution 84
5.3.6 Evaluation of Wetting Behavior on Ceramic Substrate 88
5.4 Discussion 89
5.5 References 92

Chapter 6. Assessment of Melting Behavior of Cu-Coated Ti Powders using Thermal Analysis

6.1 Introduction 94

6.2 Experimental Procedure 95

- 6.2.1 DSC Measurement 95
- 6.2.2 X-Ray Diffraction 96
- 6.2.3 Metallography 96

6.3 Results 96

- 6.3.1 DSC of Pure Cu 96
- 6.3.2 Melting of Cu-rich Powder in Ar 97
- 6.3.3 Melting of Cu-rich Powder in N_2 103
- 6.3.4 Melting of Cu-rich Powder in Presence of Si_3N_4 Ceramic 105

6.4 Discussion 106

6.5 References 111

Part 4 - Joining Si_3N_4 to Itself and to an Iron Aluminide Alloy using a High-Ti containing Cu Brazing Alloy

Chapter 7. Joining Silicon Nitride Ceramic using a Composite Powder as Active Brazing Alloy

7.1 Introduction 113

7.2 Experimental Procedure 113

7.3 Results 115

- 7.3.1 DSC Results 115
- 7.3.2 Joint Microstructure 117
- 7.3.3 Reaction Layer Evolution and Kinetics 120
- 7.3.4 Mechanical Properties of the Joints 124

7.4 Discussion 125

7.5 References 129

Chapter 8. Brazing Silicon Nitride to an Iron-based Intermetallic using a Copper Interlayer

8.1 Introduction 131
8.2 Experimental Procedure 132
  8.2.1 Raw Materials 132
  8.2.2 DSC Experiments 133
  8.2.3 Bonding Procedure 133
  8.2.4 Microscopic Evaluation 133
  8.2.5 Mechanical Properties 134
8.3 Results 134
  8.3.1 Joint Simulation in DSC 134
  8.3.2 Microstructural Analysis 135
    8.3.2.1 Si_3N_4/Cu Interface Characterisation 137
    8.3.2.2 Cu/FA-129 Interface Characterisation 141
  8.3.3 Mechancial Properties 144
8.4 Discussion 145
8.5 References 147

Chapter 9. PTLPB of Si_3N_4 to FA-129 using Nickel as a Core Interlayer

9.1 Introduction 148
9.2 Experimental Procedure 149
  9.2.1 Starting Materials 149
  9.2.2 Bonding Procedure 150
  9.2.3 Microstructural Analysis and Mechanical Testing 150
9.3 Results 151
  9.3.1 Microstructural Characterisation 151
    9.3.1.1 Si3N4/Ni Interface 151
    9.3.1.2 Ni/FA-129 Interface 158
  9.3.2 Mechanical Properties 162
9.4 Discussion 163

9.5 References 165

Chapter 10. General Discussion

10.1 Introduction 167
10.2 Characterisation Tools 168
10.3 Iron aluminide Alloy Intermetallic 170
10.4 Fabrication of High Ti-Content Active Brazing Alloy 172
10.5 Metal-Ceramic Reaction Layer Formation 174
10.5.1 Direct Brazing of Si_3N_4 174
10.5.2 Brazing of Si_3N_4 using a Cu Interlayer 176
10.5.3 Partial Transient Liquid Phase Bonding of Si_3N_4 177
10.6 Mechanical Properties of the Various Interfaces 178
10.7 References 181

Chapter 11. Conclusions 183

Chapter 12. Contributions to Original Knowledge 186

Appendix A. Activation Energy 188

Appendix B. Copyright Wavers 196

List of Figures

Chapter 1. Introduction

Figure 1.1- Structure of ceramic tappet. 4

Figure 1.2 – Picture of brazed Si_3N_4 tappet. 4

Figure 1.3 – Overhead Valve (OHV) diesel engine. 4

Figure 1.4 – Fe-Al phase diagram. 7

Figure 1.5 – Comparison between (a) high temperature tensile strength and (b) elongation of SS 409 and wrought FA-129. 8

Figure 1.6 - Effect of aluminum content and testing atmosphere on room temperature elongation 9

Figure 1.7 – Schematic representation of (a) wetting and (b) non-wetting configurations. 11

Figure 1.8 – Wetting configuration of a ceramic-reactive metal system. 13

Figure 1.9 – Sequence of events occurring during solid-state bond formation between a metal and a ceramic. 15

Figure 1.10 – Sketch of hybrid joining process mechanism. 20

Figure 1.11 - Schematic illustration of the failure mode observed for systems with large CTE mismatch (C=ceramic; M=metal). 21

Figure 1.12 – Finite element analysis of residual stresses created at a Si_3N_4/steel interface. 22

Figure 1.13 – Amplification of shrinkage occurring during cooling of a Si_3N_4/steel joint. 22

Figure 1.14 – Typical concave-convex type of fracture. 23

Figure 1.15 – Finite Element analysis of residual stress magnitudes and plasticity of interlayer as a function of interlayer used. 24

Chapter 2. Determination of E_2 Energy for Si_3N_4 Ceramic

Figure 2.1 - Variation with incident energy of the ratio of the total emitted current to the primary beam current. 32

Figure 2.2 - AFM micrograph of surface topography of Si_3N_4 after polishing. 33

Figure 2.3 Example of linear fit of the last portion of the bremsstrahlung for Si_3N_4 sample ($E_0 = 2.8$ keV, 500 s live time). 34

Figure 2.4 - Example of scattering effect from time normalized spectra acquired for (a) 20 s and (b) 350 s of live time exposure. 35

Figure 2.5 - Effect of live time acquisition on scattering of E_{DHL}. 36

Figure 2.6 - Example of reproducibility of E_{DHL} acquisition. 37

Figure 2.7 - E_{DHL} vs E_0 for Al-Mg alloy. 38

Figure 2.8 - E_{DHL} measurement vs E_0 for Si_3N_4 ceramic. 39

Figure 2.9 - Si_3N_4 grain boundaries imaged at (a) 2.5 keV, (b) 3.0 keV and (c) 4.0 keV. 40

Chapter 3. Wetting Behavior of Copper on an Iron Aluminide Alloy

Figure 3.1 - Optical micrograph of the FA-129 intermetallic microstructure. 44

Figure 3.2 - Schematic representation of the sessile drop apparatus. 45

Figure 3.3 - *In situ* picture of Cu on FA-129 at 1070°C for (a) 45 min and (b) 60 min. 46

Figure 3.4 - Macrograph of the sample tested at 1050°C for 60 minutes. 47

Figure 3.5 - Evolution of spreading and melting of the Cu cube for times of (a) 0 sec, (b) 44 sec, (c) 83 sec and (d) 110 sec. (0 sec corresponding to furnace at 1080°C). 48

Figure 3.6 - Example of grain boundary decohesion after soaking times of (a) 3 minutes and (b) 60 minutes at 1110°C. 48

Figure 3.7 - (a) Optical micrograph of liquid infiltration in the FA-129 grain boundary, (b) back-scattered micrograph of eutectic structure in infiltrated grain boundary and Cu presence in grain structure and (c) optical micrograph of the drop region. 50

Figure 3.8 – Al line scan along the dashed line in Fig. 3.6(a). 51

Chapter 4. Interfacial Microstructure Characterisation between Molten Cu-Xti and FA-129 Intermetallic

Figure 4.1 – Tubuolar furnace used for interaction tests. 57

Figure 4.2 - Penetration of molten alloy in the FA-129 intermetallic as a function of (a) test temperature and (b) superheating temperature, respectively. 58

Figure 4.3 - Interface between FA-129 with (a) Cu, (b) Cu-5wt%Ti and (c) Cu-20wt%Ti, (dotted lines indicates yellow-orange boundary). 60

Figure 4.4 - Optical micrographs of (a) penetration of liquid in grain boundary, (b) dissolution of intermetallic grains and (c) rounding of grain edges. 61

Figure 4.5 - Back-scattered micrograph of (a) eutectic structure and (b) iron-based precipitate. 62

Figure 4.6 - Isothermal section of the Al-Cu-Fe phase diagram at 600°C. 63

Figure 4.7 - (a) Back-scattered micrograph of an intergranular region and the corresponding X-ray elemental mapping (b) Al, (c) Cu, (d) Fe, (e) Ti and (f) Cr. 65

Figure 4.8 - Isothermal section of the Al-Fe-Ti phase diagram at 800°C. 66

Figure 4.9 - (a) Back-scattered micrograph of the upper part of the drop for Cu-5wt%Ti. 67

Figure 4.10 - (a) Back-scattered micrograph of the interface FA-129/Cu-20wt%Ti and the corresponding X-ray maps for (b) Ti, (c) Fe and (d) Cu. 68

Figure 4.11 - Back-scattered micrograph of the middle section of the Cu-20wt% drop. 69

Figure 4.12 - Back-scattered micrograph of the upper part of the Cu-20wt% drop. 69

Figure 4.13 - Microhardness measurment of as-received FA-129 and Cu-affected FA-129 grains as a function of soaking temperature. 70

Figure 4.14 - Optical micrograph of hardness indentation on (a) Cu-affected grains and (b) Cu-Ti-affected grains. 71

Figure 4.15 - Sketch of penetration behavior of low and high Ti-content alloys. 72

Chapter 5. Fabrication of a Composite Powder and Utilisation as Active Brazing Alloy

Figure 5.1 – (a) Particle size distribution of dense and sponge Ti powders and (b) micrograph of dense Ti particles. 79

Figure 5.2 – XRD pattern of the starting Ti powder. 80

Figure 5.3 - Micrograph of Cu deposit performed at (a) pH 12 and (b) pH 12.8. 82

Figure 5.4 - Cu depostion inside pore of sponge Ti particle. 83

Figure 5.5 - Amount of Cu deposited as a function of plating iterations. 84

Figure 5.6 – Particle size distribution of composite powder plated at pH 12. 85

Figure 5.7 - Back-scattered micrograph of agglomerate of particles coated at pH 12. 86

Figure 5.8 - Effect of time (a) and iteration step (b) on particle size distribution. 87

Figure 5.9 – EDS analysis of both composite powder surfaces. 87

Figure 5.10 - In situ photographs of composite powder pill on Si_3N_4 substrate at (a) 910°C and (b) 932°C. 88

Figure 5.11 - Contact angle of molten composite powder on Si_3N_4 ceramic (950°C). 89

Chapter 6. Assessment of Melting Behavior of Cu-Coated Ti Powders using Thermal Analysis

Figure 6.1 - Cu-Ti phase diagram. 95

Figure 6.2 - DSC curve for pure Cu sample in a Nb-lined Al_2O_3 crucible. 97

Figure 6.3 - DSC traces of Cu-Ti powder heated at 10 and 40°C/min, respectively. 98

Figure 6.4 - XRD pattern of (a) starting powder and (b) powder heated to 880°C at 40°C/min and 10°C/min. 100

Figure 6.5 - Back-scattered electron micrograph and corresponding EDS line scan of the composite powder heated to 880°C at (a) 40°C/min and (b) 10°C/min. 102

Figure 6.6 - Back scattered electron micrograph of composite powder heated to 890°C at (a) 40°C/min and (b) 10°C/min. 103

Figure 6.7 - DSC trace of Cu-Ti powder heated in N_2. 104

Figure 6.8 - XRD spectrum of Cu-Ti powder heated in N_2. 104

Figure 6.9 - Back-scattered micrograph of the edge of the powder heated under N_2. 105

Figure 6.10 - DSC trace of ABA powder and ABA/Si_3N_4 powder mix at 40°C/min in Ar. 106

Figure 6.11 – (a) Sketch of the different thermodynamically feasible interlayers in the Cu-Ti diffusion couple according to the equilibrium phase diagram and (b) the equilibrium structure (below 870°C) of the composite particle that would be predicted after a long diffusion time. 107

Figure 6.12. Sketch of melting sequence of a ABA powder heated at 40°C/min. 111

Chapter 7. Joining Silicon Nitride Ceramic using a Composite Powder as Active Brazing Alloy

Figure 7.1 - XRD pattern of Ceralloy 174-31N. 114

Figure 7.2 - DSC traces of powder mixture soaked for 6 minutes at 925, 975 and 1025°C, respectively. 116

Figure 7.3 - General micrograph of a Si_3N_4/ABA/Si_3N_4 joint. 117

Figure 7.4 - XRD pattern of interface fracture surface. 118

Figure 7.5 - Reaction layer formed at Si_3N_4/ABA interface. 119

Figure 7.6 - Low voltage EDS line scan of an interface formed at 1075°C for 12 minutes. 120

Figure 7.7 - Reaction layer microstructural evolution for joints brazed at (a) 975°C for 1 min, (b) 1025°C for 1 min and (c) 1075°C for 1 min. 121

Figure 7.8 - Measurement of the reaction layer thickness as a function of brazing time. 122

Figure 7.9 – Analysis of the reaction layer growth by (a) the parabolic analysis and (b) activation energy measurement with Arrhenius equation. 123

Figure 7.10. Four-point bending strength of brazed samples. 124

Figure 7.11 - Macrographs of fracture surfaces for a strength of (a) 400 MPa and (b) 250 MPa. 125

Chapter 8. Brazing Silicon Nitride to an Iron-based Intermetallic using a Copper Interlayer

Figure 8.1 - Four DSC traces; (a) melting of single ABA powder, (b) melting of ABA in presence of Cu (c) melting and reaction of ABA with Si_3N_4 and (d) melting of ABA in presence of Cund Si_3N_4. 136

Figure 8.2 - Optical micrograph of (a) a complete interface, (b) the FA-129/Cu interface and (c) the Cu/Si_3N_4 interface. 137

Figure 8.3 - (a) Back-scattered micrograph of a Si_3N_4/Cu interface and (b) EDS analysis of the precipitate identified in Fig 3(a). 138

Figure 8.4 - Back-scattered micrographs of the interface between the Si_3N_4 and the Cu interlayer for sample brazed at (a) 975°C for 1 minute, (b) 1025°C for 1 minutes and (c) 1025°C for 12 minutes. 139

Figure 8.5 - Low voltage line scan of the reaction layer observed in Fig 8.4(b). 140

Figure 8.6 - Reaction layer thickness as a function of brazing parameters. 140

Figure 8.7 - Modeling of the reaction layer growth by (a) the parabolic analysis and (b) activation energy measurement with Arrhenius equation. 142

Figure 8.8 - (a) Back-scattered micrograph of the FA-129 very close to the Cu/FA-129 interface, (b) and (c) EDS analysis of two reactions products formed close to the intermetallic. 143

Figure 8.9 - (a) Back-scattered montage of the FA-129/Cu interface interlayer, (b) EDS analysis of Ti precipitates and (c) EDS analysis of Cu-Al matrix, respectively. 144

Figure 8.10 - Four-point bending strength of the joints as a function of reaction layer thickness. 145

Chapter 9. PTLPB of Si_3N_4 to FA-129 using Nickel as a Core Interlayer

Figure 9.1 - Sketch of the multiple interlayer joint. 150

Figure 9.2 – Heat treatment profile. 151

Figure 9.3 – SEI micrograph of the Si_3N_4/Ni interface. 152

Figure 9.4 - Microstructural evolution with respect to heating cycle; (a) heat treatment, (b) back scattered micrograph of the interface at point 1 Fig4(a), (c) line scan of Fig.4(b), (d) line scan of interface at point 2 of Fig4(a), (e) back scattered micrograph of the interface after point 3 of Fig4(a) and (f) line scan of interface Fig4(e). 154

Figure 9.5 – Effect of (a) homogenization temperature and (b) time on total reaction layer thickness. 156

Figure 9.6 - Microprobe line scan across the Si_3N_4/Ni interface of a sample homogenised at 1150°C for 180 minutes. 157

Figure 9.7 – Maximum Cu concentration observed near the interface as a function of reaction time. 158

Figure 9.8 – SEM micrograph of the Ni/FA-129 interface. 159

Figure 9.9 – Microprobe line scan across the interface of Figure 9.8. 159

Figure 9.10 – Projection of chemical composition on Fe, Ni and Al ternary phase diagram at 600°C. 161

Figure 9.11 – X-ray diffraction pattern of intermediate layer. 161

Figure 9.12 – Flexural strength as a function of homogenization time and temperature. 162

Chapter 10. General Discussion

Figure 10.1 – Comparison of probe diameter as a function of different electron sources in SEM. 169

Figure 10.2 Sketch of the 3 different diffusion couples at the Si_3N_4 interface. 174

Appendix A. Activation energy

Figure A.1 – Schematic representation of the reaction layer growth under the reaction diffusion model. 188

Figure A.2 – Reaction layer thickness measured versus time for the systems (a) Si_3N_4/Cu-5Cr, (b) AlN/Cu-22Ti and (c) Si_3N_4/Cu-25Ti. 191

Figure A.3 – Reaction layer thickness measured versus square root of time for the systems (a) Si_3N_4/Cu-5Cr, (b) AlN/Cu-22Ti and (c) Si_3N_4/Cu-25Ti. 192

Figure A.4 – Relation between the thickness of the reaction layer and square root of holding time for the two growth stages model. 193

Figure A.5 – Activation energy measurement with Arrhenius equation for the system AlN/Cu-22Ti and Si_3N_4/Cu-25Ti. 195

List of Tables

Chapter 1. Introduction

Table 1.1 - Applications of Ceramic-Metal joints in engines. 3

Table 1.2 - Mechanical Properties of Silicon Nitride as a Function of Fabrication Process. 6

Table 1.3 - Contact angles of liquid metals on ceramics at their melting points. 12

Chapter 3. Wetting Behavior of Copper on an Iron Aluminide Alloy

Table 3.1 – Chemical composition of iron aluminide alloy. 44

Table 3.2 – EPMA results of different locations. 51

Chapter 4. Interfacial Microstructure Characterisation between Molten Cu-Xti and FA-129 Intermetallic

Table 4.1 – Experimental temperature as a function of copper alloy composition. 57

Table 4.2 - EPMA chemical analysis of different locations affected by Cu. 62

Table 4.3 - EPMA chemical analysis of different locations affected by Cu-5wt%Ti alloy. 66

Chapter 5. Fabrication of a Composite Powder and Utilisation as Active Brazing Alloy

Table 5.1 - Density of elements commonly used in filler metals. 77

Table 5.2 - Chemical composition of electroless Cu bath. 80

Table 5.3 - Amount of Cu plated as a function of time. 83

Chapter 9. PTLPB of Si_3N_4 to FA-129 using Nickel as a Core Interlayer

Table 9.1 - Effect of first soaking temperature on reaction layer thickness. 155

Table 9.2 – Effect of joining parameters on thickness of reaction layer formed. 160

Chapter 10. General discussion

Table 10.1 – E_2 energy of different ceramics. 170

Chapter 1

Introduction

1.1 Why Ceramic-Metal Joints?

In our vast world where more and more engineering components are required to operate in extreme conditions, material performance has to be increased to be reliable in aggressive environments, more specifically when thermal, chemical, dynamic and mechanical environments exceed the capabilities of traditional materials. These conditions are usually found in aerospace applications, advanced engines, energy production plants and, more generally, whenever the environment is highly aggressive and hostile [1.1]. The interest in using ceramics in these fields creates new fabrication challenges for complex monolithic pieces or substrate/substrate joints.

Producing complex shaped ceramic parts at low cost is challenging [1.2]. A solution to this problem is to join ceramics with other materials, usually metals, to fabricate complex designs. Many simple-shaped ceramic pieces can be joined together to form a complex component [1.2]. Moreover, monolithic materials cannot always offer the best performance in very hostile environments. To overcome this engineering problem, joints between two or more materials can be achieved to exploit the advantageous characteristics of both materials. These new ways of processing technical components create a need for reliable and effective ceramic-metal joining processes [1.2].

Many different applications illustrate commercially reliable ceramic/metal joints. In low stress/low temperature applications, adhesives have been used extensively [1.3]. For example, a hip implant is composed of an alumina ball (selected for its high wear resistance and biocompatibility) and a stainless steel (or titanium) stem, glued together and implanted into the femur [1.2]. Another example is the copper/graphite couple used extensively in the nuclear industry. These materials are brazed together with an Ag-Cu-Ti brazing alloy [1.2]. Silicon nitride has not escaped from the joining technology craze because Si_3N_4 represents a candidate possessing outstanding potential for high temperature structural applications. This ceramic exhibits properties such as high wear resistance, high strength at low and high temperatures, low thermal expansion coefficient and high resistance to aggressive chemical environments. Silicon nitride has already found applications in automotive engine components [1.4, 1.5].

The automotive industry is using several parts where ceramic and metal are joined. These technically advanced parts improve efficiency of the various systems which in turn improves the overall vehicule performance. Table 1.1 presents some engine components where ceramic/metal joints are used.

One of these examples is the tappet. Since 1993, silicon nitride discs have been joined to a steel body to form a high wear resistant component. They were brazed with an active filler metal with a flexible interlayer to absorb the thermal mismatch [1.6]. Figure 1.1 presents the design of a ceramic tappet. Figure 1.2 presents a picture of tappets and Figure 1.3 presents the position occupied by the tappet in an overhead valve (OHV) diesel engine.

Table 1.1 - Applications of Ceramic-Metal joints in engines [1.5].

Component	Car Company	Ceramic Company	Commercial	Aim
Glow Plug	Isuzu	Kyocera	1981	Starting properties
	Mitsubishi	Kyocera	1983	
	Mazda	Kyocera	1985	
	Nissan	NGK Spark Plug	1985	
	Toyota	Denso	1992	
Precombustion Chamber	Isuzu	Kyocera	1983	Economy Power Low Emission
	Toyota	Toyota	1984	
	Mazda	NGK Insulators	1986	
	Mitsubishi	Kyocera	1993	
Rocker Arm	Mitsubishi	NGK Insulators	1984	Wear resistance
	Nissan	NGK Insulators	1987	
	Nissan	NGK Spark Plug	1988	
Turbocharger Rotor	Nissan	NGK Spark Plug	1985	Turbo lag
	Nissan	NGK Insulators	1986	
	Isuzu	Kyocera	1988	
	Toyota	Toyota	1989	
	Toyota	Toyota	1990	
	Catapillar	NGK Spark Plug	1992	
Injector Long Ring	Cummins	Toshiba	1989	Wear resistance
Cam Roller	Detroit Diesel	Kyocera	1992	Wear resistance
Tappet	Nissan	NGK Spark Plug	1993	Wear resistance
	Diesel	NGK Spark Plug	1994	
	Isuzu			
Exhaust gas seal	Toyota	Kyocera	1993	Seal

As a general rule, metal-ceramic joints should possess the following characteristics in order to be commercially applied: [1.1]

- High mechanical strength at high temperature and in aggressive environments,
- High oxidation resistance,
- High stability under service conditions,
- Low production price.

As no perfect solution has been obtained, research in the ceramic-metal joining field continues.

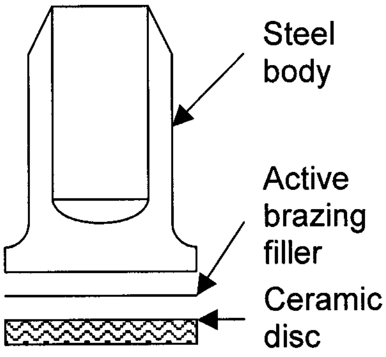

Figure 1.1- Structure of ceramic tappet [1.5].

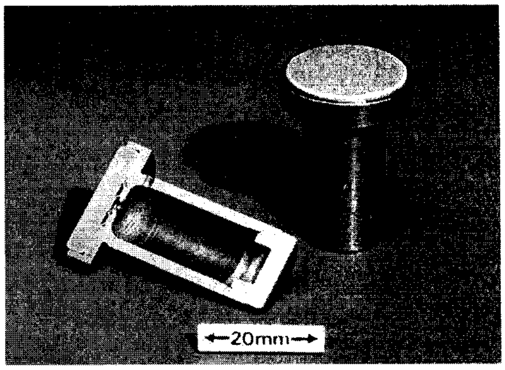

Figure 1.2 – Picture of brazed Si_3N_4 tappet [1.2].

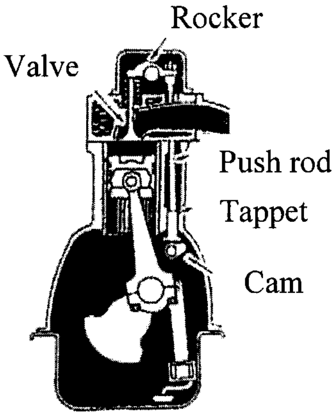

Figure 1.3 – Overhead valve (OHV) diesel engine [1.5].

1.2 What is Silicon Nitride (Si_3N_4)?

Si_3N_4 is a technical ceramic formed of 3 atoms of silicon (Si) and 4 atoms of nitrogen (N). It exists in two phases, α and β. These two phases both possess an hexagonal crystal structure. The α–phase has a unit cell approximately twice as long as the β-phase [1.7]. Good structural parts are obtained by starting with powders having a high α–phase content, a consistent and controllable composition and high purity. Good silicon nitride powder contains at least a 9:1 ratio of α-β phase [1.8]. This is required as the sintering mechanism of silicon nitride involves the α-β phase transformation. Without the high α-phase content, the sintered material will not develop the interlocked grain structure required for high strength [1.9].

Although silicon nitride has high strength and high hardness properties, the high-energy, covalent chemical bonds giving rise to these properties is a disadvantage during fabrication [1.8]. Alternative approaches have been developed using liquid phase densification created by reactions with some additives. The first family of additives included MgO and Y_2O_3. Later on, a mixture of Y_2O_3 and Al_2O_3 was developed and better densification than the first family through modification of the grain boundary phase was achieved [1.7]. Other researchers have shown that new additives, like rare earth oxides, increase the high temperature properties [1.10]. Many processes are used to densify the ceramic powder into bulk components. The most commonly used for Si_3N_4 are: hot-pressing (HPSN), sintering (SSN), sintered reaction-bonding (SRBSN) and hot isostatically pressing (HIPSN) [1.7]. Table 1.2 shows some mechanical properties of bulk silicon nitride as a function of the fabrication route used for densification.

For any particular fabrication process, room temperature mechanical strength and fracture toughness depend on two major points. Firstly, the aspect ratio of the β-silicon nitride grains and secondly, the overall grain size. Variation in these parameters are responsible for large variations in fracture strength and fracture toughness [1.9]. These variations are attributed to the difference in microstructures [1.7]. During sintering, the α / β transformation occurs, and the grain shape changes from equiaxed to elongated giving better toughness properties. However, once the transformation is complete, grain growth begins and a reduction of toughness properties occurs. A high aspect ratio of the Si_3N_4 grains increases the resistance to crack propagation by crack deflection [1.9]. With acicular grains, a higher level of crack deviation is achieved and grain pull-out occurs, resulting in a higher energy required for crack growth.

Table 1.2 - Mechanical Properties of Silicon Nitride as a Function of Fabrication Process [1.7].

Material type	RBSN	HPSN	SSN	SRBSN	HIP-SN
Relative density (% of theoretical)	70-88	99-100	95-99	93-99	99-100
Young`s Modulus E (GPa)	120-250	310-330	260-320	280-300	
Poisson`s ratio	0.20	0.27	0.25	0.23	
Flexural strength (MPa) At 25°C At 1350°C	150-350 140-340	450-1000 250-450	600-1200 340-550	500-800 350-450	600-1050 350-550
Weibull Modulus	19-40	15-30	10-25	10-20	
Fracture toughness K_{1c} (MPa $m^{1/2}$)	1.5-2.8	4.2-7.0	5.0-8.5	5.0-5.5	4.2-7.0

1.3 What are Iron Aluminides (Fe_3Al) Alloys?

Aluminum possesses a high level of solubility in iron. This solubility can be observed from the phase diagram shown in Figure 1.4 [1.11]. The solubility is over 20 at.% at room temperature and increases with temperature. If the atomic percent of aluminum is increased above 20%, a disordered solid solution is formed [1.12]. The crystal structure of this single phase (α) is A_2 (bcc). Between 24 and 36 at.%, Fe_3Al phase is stable below 550°C. This phase possess the DO_3 structure (fcc). For the higher temperatures between the Fe_3Al phase and the solution of iron and aluminum (α), the FeAl phase is present and its structure is B_2. This phase is an ordered phase and the critical temperature of ordered-disordered transformation is 760°C. If the atomic percent of aluminum is increased again, between 36 to 50%, the B_2 structure is stable even at room temperature.

High temperature strength and excellent environmental resistance have revived the interest in iron-aluminide alloys and Oxide Dispersed Strengthening-Fe_3Al as potential cost effective replacements for some high strength ferritic stainless steels [1.13]. For example, Figure 1.5 presents (a) a comparison between the high temperature yield strength of the 409 ferritic stainless steel [1.14] with an iron aluminide alloy (FA-129) [1.13] and (b) the high temperature elongation. Clearly, the iron aluminide alloy possesses a much higher yield strength when the temperature is increased to approximately 600°C. Up to ≈ 650°C, the elongation behavior is similar for both materials but then, the iron aluminide alloy exhibits higher ductility with temperature. However, the use of iron aluminides as structural engineering materials has been inhibited by their low room temperature ductility, poor weldability and moderate creep resistance[1.13]. The addition of some alloying elements and grain size control have been shown to give improvements in room temperature ductility [1.15].

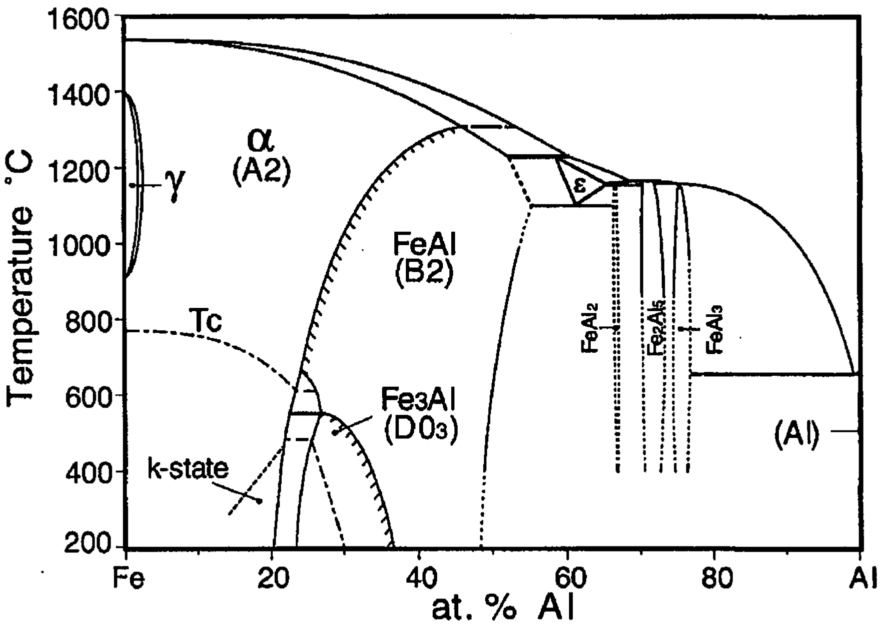

Figure 1.4 – Fe-Al phase diagram [1.11].

The ductility of pure iron aluminide at room temperature is limited and decreases when the aluminum content increases. Many mechanical tests have been performed under different conditions; vacuum, dry argon, dry hydrogen, air, and water vapour saturated gas [1.16]. Figure 1.6 presents the effect of aluminum content as well as testing atmosphere on the elongation at room temperature of pure iron aluminides. The poor ductility has been associated with moisture-induced environmental embrittlement for Fe_3Al [1.17].

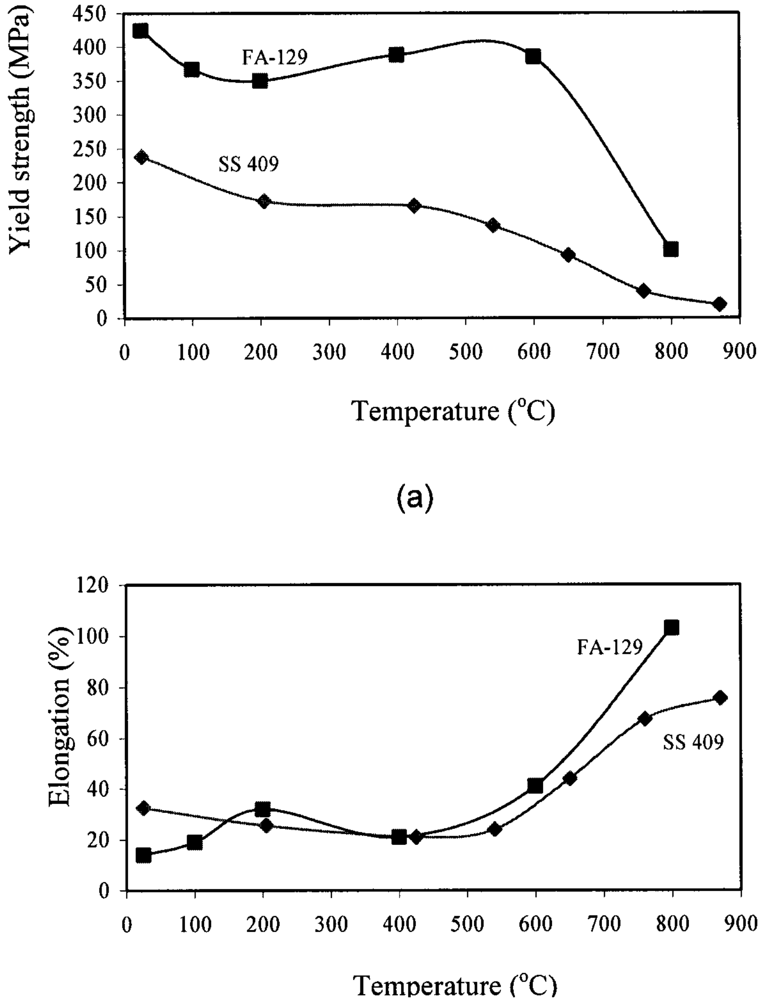

(a)

(b)

Figure 1.5 – Comparison between (a) high temperature tensile strength and (b) elongation of SS 409 and wrought FA-129.

The suggested mechanism for embrittlement is similar to the one proposed in aluminium alloys. Water vapour penetrates into the alloy through small cracks at the surface. A reaction between water vapour and aluminum produces alumina and hydrogen (eq. 1.1) [1.18].

$$2\,Al + 3H_2O = Al_2O_3 + 6\,H \qquad \text{(eq. 1.1)}$$

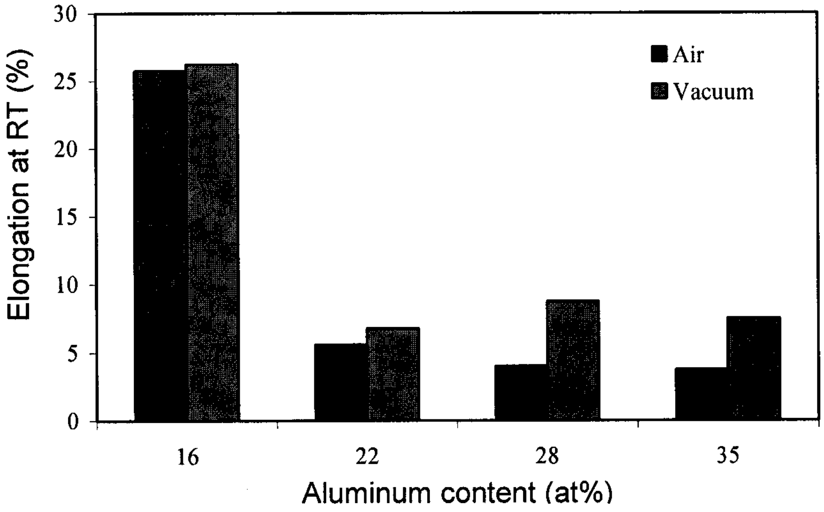

Figure 1.6 - Effect of aluminum content and testing atmosphere on room temperature elongation [1.18].

The adsorbed hydrogen diffuses in the lattice and lowers the atomic bond strength [1.16]. Some alloying elements, such as chromium, have been found to increase the room temperature mechanical properties and reduce hydrogen embrittlement through modification of the surface reaction with water vapour [1.19].

Adding alloying elements has two different objectives. The first is to change the kinetics of the surface reaction with the environment [1.13]. Addition of 2 to 5 wt%

chromium has several benefits. For example, the tensile ductility reaches 20% during room temperature testing [1.13, 1.18]. This is associated with the previously mentioned modification of the surface reaction and reduction of moisture embrittlement. Secondly, the chromium retards the B_2-DO_3 transformation during cooling. The ductility increases if a B_2 structure is retained at room temperature. Chromium has proved to have no significant influence on high temperature mechanical properties [1.13].

The second objective in alloying Fe_3Al is the production of a second phase dispersion. This phase reduces the tendency for localised deformation. A uniform deformation is then promoted and the ductility is improved [1.20]. Generally, strong carbide and boride formers are used, such as niobium and zirconium.

The FA-129 iron aluminide alloy has been developed by Oak Ridge National Laboratories (ORNL). The main alloying elements added are chromium, niobium and carbon, for the reasons mentioned previously. This alloy has been design to give high-temperature tensile strength with good room-temperature ductility [1.13].

1.4 Interface Formation in Ceramic/Metal Joints

The driving force for the formation of an interface between materials is the reduction of the free energy of the system [1.21]. The interfacial energy reaches the lowest achievable value as the bond is formed for the joining conditions used, but further modifications can occur to the joint entity if the service conditions reach a level where a lower free energy state of the system can be obtained. Even if the scientific community uses equilibrium to define joints, an interface is never in total equilibrium. The interface formation in metal-ceramic systems is obtained in two main ways, liquid or solid state reaction. The following sections describe the essential features of these two processes.

1.4.1 Liquid State Interface Formation

The sessile drop test is often used to determine the wettability of a metal (reactive or not) on a ceramic substrate. This involves placing a drop of molten metal on a solid substrate. The critical contact angle is 90 degrees. If the angle is lower than 90°, the sessile drop is said to wet the substrate and if the angle is higher, no wetting is observed. Figure 1.7 presents a schematic representation of (a) wetting and (b) non-wetting behavior of a molten metal on a substrate.

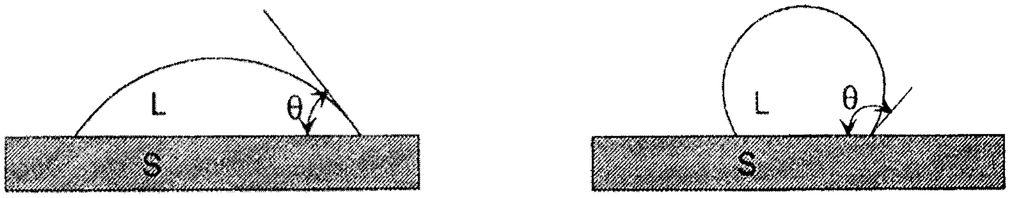

$0 < \theta < 90^{\circ}$

(a)

$\theta > 90$

(b)

Figure 1.7 – Schematic representation of (a) wetting and (b) non-wetting configurations [after 1.22].

1.4.1.1 Non-reactive Systems

The driving force for wetting of a solid substrate by a molten metal is given by:

$$Fd(t) = \sigma_{SV} - \sigma_{SL} - \sigma_{LV} \cos\theta(t) \qquad \text{(eq.1.2)}$$

Where σ^{o}_{SV}, σ^{o}_{SL} and σ^{o}_{LV} are, respectively, the solid-vapour, solid-liquid and liquid-vapour surface energy at instant t. At equilibrium, the driving force (Fd(t)) is zero and eq. 1.2 can be written as the Young equation (eq. 1.3). Young concluded in 1805, that for each combination of a solid and fluid there is an appropriate angle of contact, which means that the contact angle is a unique material characteristic for that environment [1.23]. As the viscosity of molten metals is generally very low, the time to reach equilibrium for a droplet is within 0.1 second in a non-reactive wetting system [1.24].

$$\cos\theta = \frac{\theta_{SV} - \theta_{SL}}{\theta_{LV}} \qquad \text{(eq. 1.3)}$$

The main reason for the poor wetting behavior of molten metals on ceramics is the difference in the nature of their respective bonding forces. A metal lattice can be viewed as an array of positive ions in a 'gas' of delocalized electrons. The electron movement confers the characteristics of generally high electrical and thermal conductivity [1.25]. In contrast, ceramic lattices are held together by the sharing of specific pairs of electrons to form covalent bonds or else by the transfer of electrons from one type of atom to another to create arrays of electrically charged ions that are held in place by electrostatic forces (ionic bonding) [1.25]. Thus there is a lack of delocalized electrons in ceramic lattices and a metal-ceramic interface represents a major electronic discontinuity that requires considerable energy to overcome. In practice, the energies of metal-ceramic interfaces are often so high that they exceed the free surface energy of the solid ceramic, $\gamma_{sl} > \gamma_s$, and hence the contact angle assumed by the liquid metal is larger than 90°. [1.26] For example, Table 1.3 presents some contact angle values of pure molten metals on ceramic substrates. These show that pure metals are generally not suitable for creating interfaces in a metal/ceramic joint.

Table 1.3 - Contact angles of liquid metals on ceramics at their melting points [1.26].

Ceramic	Ag	Al	Au	Cu	Ni	Fe
Al_2O_3	144	128	138	138	128	141
SiC	128	127	138	130	65	
TiC	153	118		128	32	
Si_3N_4	138	157		135	90	
TiN	141		113	112		

1.4.1.2 Reactive Systems

The expression "reactive wetting" implies the formation of a reaction product which is wetted by the molten metal and direct contact between the molten metal and the substrate is avoided. Reactive wetting is the most common process used to obtain wettability of ceramic substrates by molten metals. A sketch of the drop configuration is presented in Figure 1.8. The final contact angle in a reactive system can be evaluated with good accuracy from the Young equation using the surface energies of the molten metal and the reaction product formed [1.24]. The time for spreading of the molten metal is in the range of 10 to 10000 seconds and is controlled by the interfacial reaction and not the viscous resistance of the molten metal as in non-reactive wetting. In a reactive system, two spreading process limitations may occur; reaction-limited spreading or diffusion-limited spreading [1.24].

Reaction-limited spreading occurs when diffusion in the droplet is rapid and the reaction produces no significant changes in the droplet composition. This ensures that the chemical composition at the triple line is constant with time. The spreading initiates with the formation of the reaction layer and steady state spreading begins when the reaction product covers the entire surface between the molten metal and the substrate. From then on, the rate of spreading is a function of the kinetics of the reaction between the metal and the substrate. This type of wetting behavior is observed for aluminum on vitreous carbon for example [1.24].

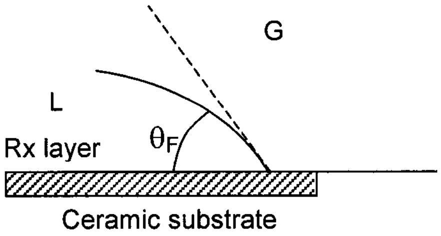

Figure 1.8 – Wetting configuration of a ceramic-reactive metal system [after 1.24].

Diffusion-limited spreading occurs when the reaction rate at the interface is high and a chemical gradient within the droplet is formed. This spreading mechanism is time-dependant. Cu-Ti alloys on alumina substrates exhibit this type of behavior [1.24].

1.4.2 Solid/Solid Interface Formation

The formation of a solid state interface is more difficult than in the liquid state due to the lower mobility of the atoms in the solid. In solid state diffusion, bonding occurs with or without mass transfer across the interface. Physical bonding (no mass transfer), possesses low joint properties, as the interface is formed by the formation of van der Waals bonds between both materials. Mass transfer occurs when atomic diffusion across an interface occurs between the original materials. Chemical bonding occurs and chemical reactions or diffusion layers are formed and are responsible for the adhesion. The solid state mechanism is divided into two different steps [1.27, 1.28]. The first one, influenced by the roughness of the two specimens in contact, is to form an intimate interface to increase the diffusion area. The elimination of the large volume of voids is produced by mass transfer mechanisms, diffusion and/or plastic flow. Simultaneously to this interface accommodation step, an adhesion process takes place to produce interfacial strength. A third step can also occur, but may produce irreversible consequences: chemical reactions may promote the formation of a compound at the interface. This compound can increase or decrease the mechanical strength of the joint [1.26, 1.27]. Figure 1.9 illustrates this mechanism.

1.5 Joining Processes

The choice of the joining technique depends on the materials to be joined, the joint design and the future service conditions. All the joining techniques can be classified into four families: mechanical, indirect, direct and hybrid joining. Each of these family contains multiple types and variations of processes. For the purpose of this thesis, only brazing, diffusion bonding, eutectic melt joining and partial transient liquid phase bonding will be described. The other techniques, such as welding, are described in detail [1.3].

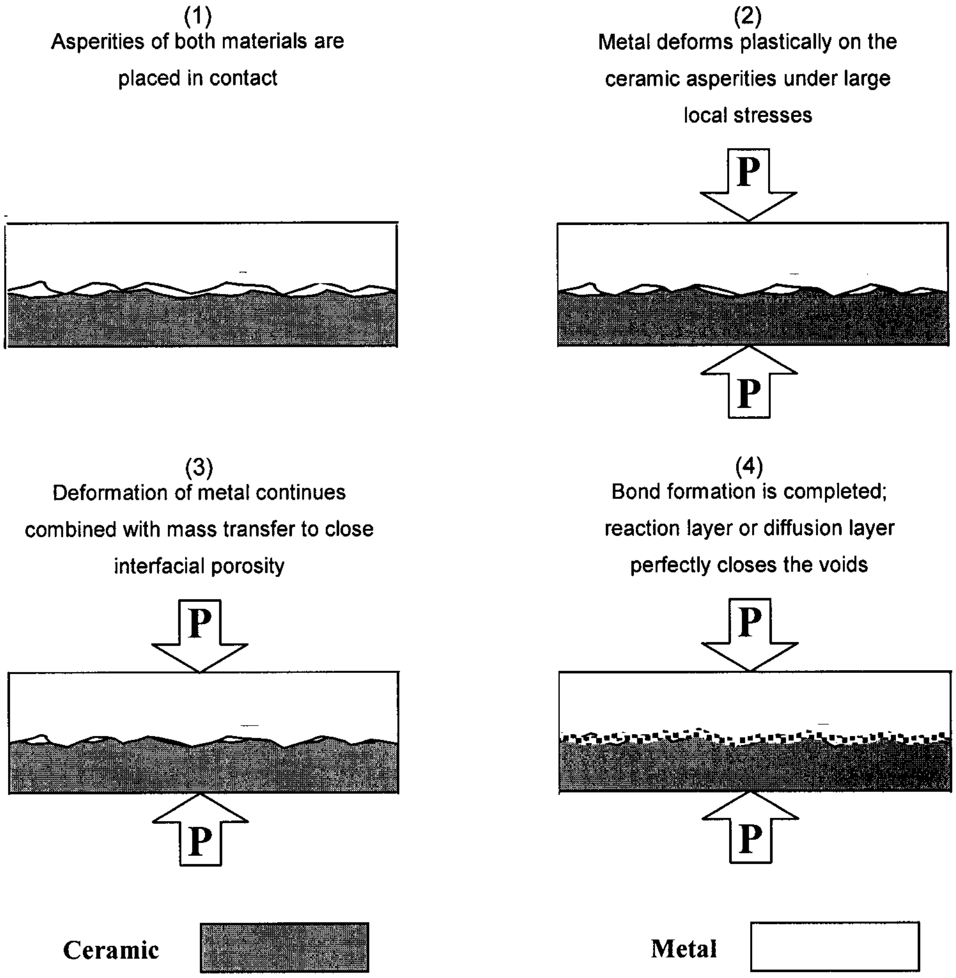

Figure 1.9 – Sequence of events occurring during solid-state bond formation between a metal and a ceramic [1.28].

1.5.1 Indirect Joining: Reactive Brazing

Indirect bonding of ceramics includes the techniques in which the interface is formed from a liquid flow [1.26]. Brazing is a joining process where the joint is heated, in the presence of a filler metal between the parent materials, at a temperature above the melting point of the filler metal and below that of the base materials [1.29]. The molten filler metal spreads between the surfaces to form an interface and solidification of the filler metal occurs during cooling. A joint is then formed. A low melting point layer remains at the interface after the process. Obviously, the wetting behavior of the filler metal has to be characterised for both surfaces.

In conventional brazing, the families of filler metals are mostly copper, silver and nickel-based alloys. Several different compositions exist to respond to particular service applications. The melting temperature of these filler metals varies from 715 to 1090°C [1.30]. The main difference in the chemical composition of the filler metal for ceramic brazing is the presence of an active element, usually a transition metal such as titanium, which has the property of reacting with the ceramic and forming a reaction layer. The thermodynamic activity of the transition metal in the filler as well as its contents dictate the reactive behavior of the active element. The reaction layer formed possesses optimum characteristics, including thickness, composition and morphology, for mechanical behavior. To optimise the properties, knowledge of the previous factors have to be combined with the physical parameters which influence the joint such as the coefficient of thermal expansion mismatch, yield stress and strain hardening coefficient of the metal and the filler metal.

Some advantages of active brazing are as follow:

1. Brazing is a simple and flexible process which can use existing equipment, requires little capital investment and can be readily adapted to mass-production operations,
2. Large or complex assemblies can be joined in a single step operation and in a stress-free condition especially with respect to ceramic-to-metal joining,
3. Joints comprising components of different sizes and/or thicknesses can be brazed to each other.

However, the main disadvantage is the low service temperature of the assembly. Increasing the operating temperature produces a softening of the interlayer and eventually reaches a point where the mechanical properties become too low to be useful [1.4, 1.26, 1.31-1.33].

1.5.2 Direct Joining: Diffusion Bonding (DB)

Diffusion bonding can be described simply as the assembly of two flat surfaces, heated at high temperature under pressure for a certain period of time. The interface is created by the solid state atomic diffusion at the junction between the parts. Joining similar materials with this technique is very simple, but when different materials have to be joined, some difficulties arise [1.34]. Again, diffusion bonding of ceramics requires a metal possessing a certain activity to destabilise the ceramic bond to form an interface [1.4, 1.26].

The four main variables in diffusion bonding are temperature, time, pressure and surface roughness. These factors are not independent. The optimum joining condition is found by simultaneously optimising the interactions of these factors. Raising the temperature increases the interaction between the metal and the ceramic at the contact interface by increasing the mobility of the atoms. It also increases the mobility of the dislocations which accommodate the plastic deformation of the metal [1.26, 1.27, 1.31, 1.32]. Usually, a relatively short bonding time is required to form a strong bond. Unnecessarily increasing the bonding time can produce irreversible reactions which decrease the mechanical properties [1.26, 1.27, 1.31, 1.32]. The main idea of applying pressure is to produce an intimate contact between the ceramic and the metal. Another important role is to destroy the surface oxide film at the surface of the metal (for metals which form surface oxide layers), and thus allow contact of the ceramic with the bulk metal. The applied pressure depends on the metal/ceramic system, thickness of the metal layer and the bonding temperature [1.26, 1.27, 1.31, 1.32]. The asperities of a rough surface prevent large plastic deformation at the surface due to mechanical gripping of the metal. This greatly limits the development of pure metal/ceramic contacts and of course, affects the strength of the interface [1.35].

Solid state diffusion bonding produces no deformation of the metal, except near the interface zone [1.27]. This major advantage, compared to brazing, results in near net shape joining. These parts are more likely to be used for high accuracy applications. Another advantage over brazing arises from the absence of a low melting point braze filler metal. The diffusion-bonded parts can thus be used at much higher service temperatures than the braze assembly [1.27]. However some disadvantages prevent the widespread application of this technique. The ductility of ceramics is very low, so an intimate initial contact between the pieces is more difficult to obtain [1.27]. The temperatures needed to achieve bonding with ceramics are very high (higher than for metallic materials) as the interface is formed from the solid state and not from the liquid state like brazing. Another important factor is the high cost of the equipment, which raises the final cost of the pieces [1.26].

1.5.3. Direct Joining: Eutectic Melt Joining

This joining process is in reality, a sub-category of diffusion bonding. This joining technique involves the flow of molten liquid formed at the interface during diffusion, resulting in a similar microstructure to diffusion bonding. Usually, a metallic layer is used between the two parts to be joined [1.4]. This metallic layer is chosen to achieve a specific reaction (a molten reaction compound) between the structural parts. The main difference from brazing is that the reaction compound melts and not the metallic layer placed between.

Most transition metals such as iron, nickel, cobalt and their alloys (low alloy steel, stainless steel and nickel base superalloys) react with silicon ceramics, for example, to form a eutectic liquid between the ceramic and the metal [1.4]. This reaction is used to form the interface during bonding. These reactions can be predicted from the phase diagrams of the components in question [1.4]. This process has proved to be successful in only some specific systems, limiting its application.

1.5.4 Hybrid Joining: Partial Transient Liquid Phase Bonding

In conventional metal-ceramic joining processes such as brazing or diffusion bonding, the joining temperature is higher than the service temperature. This implies that if the service temperature has to be raised, higher joining temperature must be used. Increasing the joining temperature directly affects the reaction layer growth and an excessively thick layer may be formed which degrades the performance and integrity of the joint [1.36]. The main idea behind the development of a transient liquid phase is to take advantage of conventional joining processes by combining a low joining temperature and the potential for high service temperature application [1.26, 1.36 – 1.38].

Partial transient liquid phase bonding (PTLPB) uses much smaller thickness of filler metal than brazing, thus controlling the amount of interface reaction. The filler metals have similar compositions to the brazing alloys and have a lower melting point than either parent material [1.26, 1.36 – 1.38]. When heated to the joining temperature, the low melting point alloy melts because its liquidus has been exceeded or because interdiffusion between it and the interlayer core produces a liquid eutectic composition which is formed initially at the interface. Ultimately, the surface of the interlayer is covered by a liquid film which fills the capillary gap between the ceramic component and the interlayer. The isothermal resolidification is due to the interdiffusion with the interlayer. Finally, maintaining the heat treatment after the liquid layer has resolidified homogenises the interlayer, which produces a composition a little different from that of the original interlayer [1.26]. This is presented in Figure 1.10. In PTLPB, the initial interlayer consists essentially of a high melting temperature metal (HT) or alloy core with two thinner samples of lower melting temperature alloy (LT) on each side [1.26, 1.36 – 1.38].

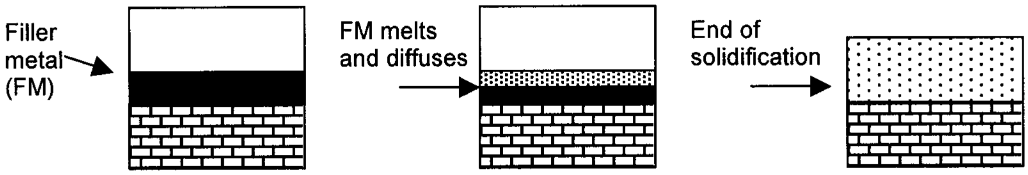

Figure 1.10 – Sketch of hybrid joining process mechanism.

1.6 Difficulties in Joining Dissimilar Materials

The major problem for ceramic-metal joining is related to the residual stresses induced in the bonded assembly upon cooling from the joining temperature as a result of the thermal expansion (CTE) and elastic modulus mismatches between the metal and the ceramic [1.39]. In addition, the strain hardening coefficient, yield stress and interlayer thickness have considerable effects on the residual stress formation and distribution [1.40]. At a certain intensity, these stresses may causes crack initiation through different regions of the joint.

Generally, the stresses created in the material will differ as a function of the respective CTE of the materials joined. Figure 1.11 presents a sketch of the location where the most intense stress peaks will be formed, depending on the orientation of the CTE gradient, suggesting locations for crack initiation and propagation. In both cases, the cracks initiate in the most intense tensile stress zone of the ceramic body. As ceramics are weaker under this loading condition, the configuration of the interface has to take into account the possibility of crack formation during cooling and every way of reducing these tensile residual stresses in the ceramic should be used.

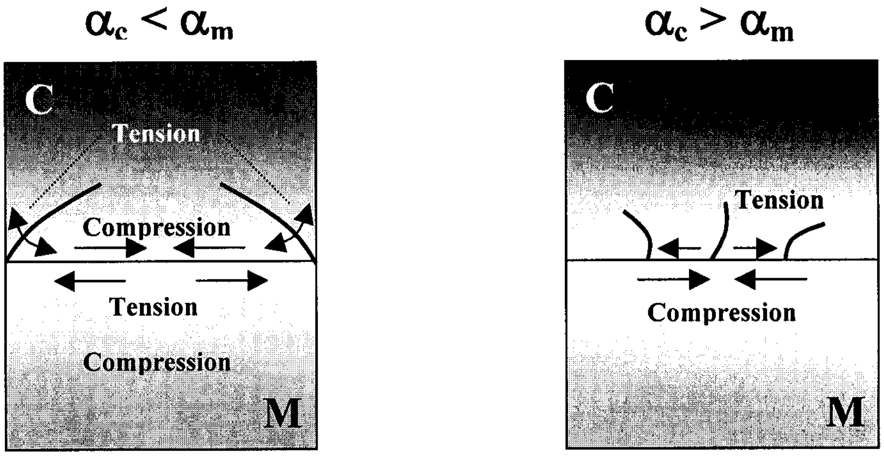

Figure 1.11 - Schematic illustration of the failure mode observed for systems with large CTE mismatch (C = ceramic; M = metal) [1.41].

In the case of silicon nitride, it has been demonstrated that the mechanical behavior of the joint increases with the reduction of the product of the CTE mismatch and the Young modulus [1.31]. These stresses peak at the edges and corners of the joint and constitute the major source of failure for ceramic-metal joints [1.32]. In the case of elastic mismatch, the stresses induced near the edge are singular; very large tensile and shear stresses could exist over small regions next to the edge [1.39]. The thermal expansion mismatch has a similar effect: large residual stresses near the edge scale with the metal thickness and are lower for thinner metals. Figure 1.12 presents a finite element analysis of the location and magnitude of the stresses generated near the interface for the system Si_3N_4/steel (CTE of Si_3N_4 = $3.1X10^{-6}$/K and CTE of steel = $12.6X10^{-6}$/K). In this case, the coefficient of thermal expansion of the ceramic is lower than the CTE of the metal inducing tensile stresses at the edge of the ceramic.

At the joining temperature, both ceramic and metal are essentially in a stress-free state as both components have to expand freely during heating. When the bond between the metal and the ceramic is formed, the expansion and contraction of the parent materials become dependant on each other. Generally, the ceramic will exhibit a smaller contraction than the metal during cooling and the residual stresses created are expected to be absorbed by the metallic portion of the joint when a CTE mismatch exists. An exaggeration of this phenomenon is presented in Figure 1.13.

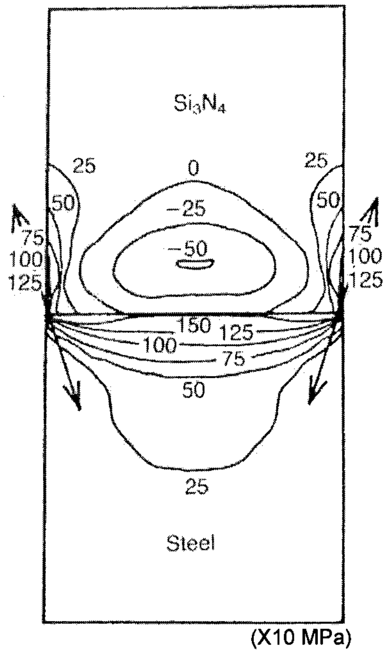

Figure 1.12 – Finite element analysis of residual stresses created at a Si_3N_4/steel interface [1.32].

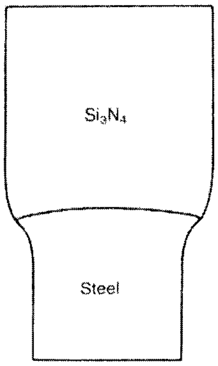

Figure 1.13 – Amplification of shrinkage occurring during cooling of a Si_3N_4/steel joint [1.32].

As mentioned earlier, the most critical of these stresses are the tensile stresses formed in the ceramic component, which act almost normal to the interface and, thus, superimpose on external tensile loads during testing. If the interface is stronger than the affected tensile strength of the ceramic, fracture initiates in the ceramic where the maximum tensile stress acts and proceeds through the sample under a typical concave/convex curvature [1.32]. Figure 1.14 presents a typical micrograph of a concave-convex type of fracture encountered in metal-ceramic systems. Evidently, the joint residual stresses can also produce plastic deformation of the metallic workpiece as well as interfacial decohesion if the affected tensile strength of the ceramic is higher than the interfacial strength.

One way to overcome this problem is to use interlayers possessing CTE's between the CTE of the metal and the ceramic, producing a gradient of thermal expansion mismatch [1.31]. The utilisation of gradient interlayers however is not always practical.

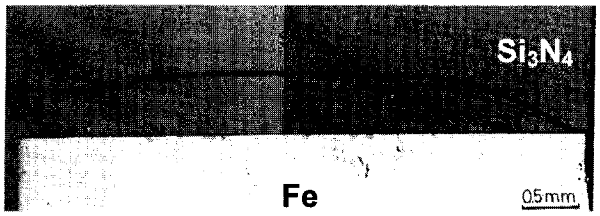

Figure 1.14 – Typical concave-convex type of fracture [1.32].

Another solution is to work with metallic interlayers having a high level of plasticity. A combination of a low yield strength and high thermal expansion matching the material to be joined is desired [1.42]. Finite element analysis has been used to describe the residual stress formation and plastic deformation in Si_3N_4/steel joints as a function of the type of interlayer used (Cu, W, Mo and kovar). The results are presented in Figure 1.15.

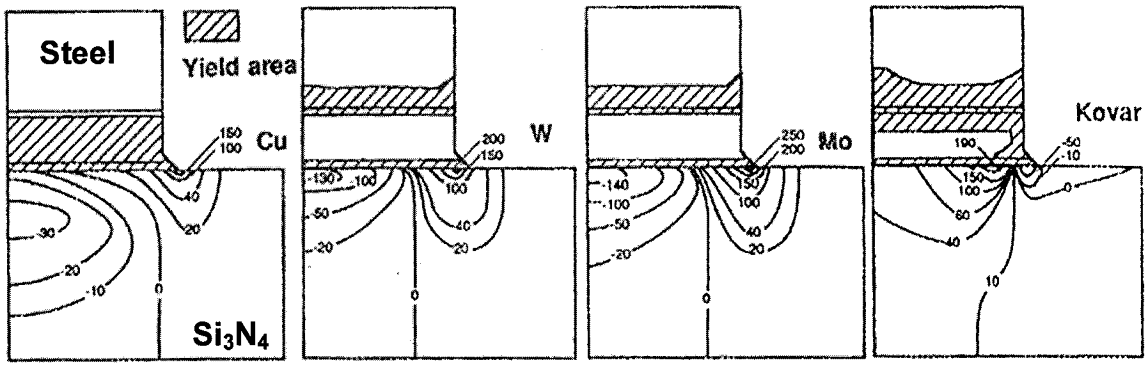

Figure 1.15 – Finite Element analysis of residual stress magnitudes and plasticity of interlayer as a function of interlayer used [1.40].

Obviously, the thickness of the inserted interlayer has been fixed, and optimisation of the joint property might not have been obtained in some of these cases. The results demonstrate that W and Mo did not yield during cooling but that Cu and Kovar did. The results also show that the peak tensile stresses created are lower for Cu and Kovar, both interlayers which exhibit plastic deformation. In all the cases, the fracture has been observed to initiate at the location where the peak tensile stress occurs [1.40]. Copper and nickel interlayers have been found to be more effective than low thermal expansion molybdenum, for the fabrication of strong bonds between Si_3N_4 and steel or nickel-based superalloys [1.31].

1.7 Objectives

This thesis focuses on the application and further development of different processes for joining silicon nitride ceramics to an iron aluminide alloy for potential high temperature applications. Some industrial applications require silicon nitride/stainless steel joints. However, the iron aluminide intermetallic possesses better high temperature properties than the conventional stainless steel and are slowly replacing the 400 series; thus providing impetus for the study of this joining system. This work also focuses on the development and application of a new analysis technique to better understand the joint formation and the residual properties arising from this combination. This thesis describes the history of joining Si_3N_4 to FA-129, from non-conductive material characterisation, wetting and interfacial reaction characterisation on both parent materials, development of a new fabrication route for an active brazing alloy, characterisation of its melting behavior and ceramic joints properties obtained through to brazing and partial transient liquid phase bonding using copper and nickel interlayers.

1.8 References

[1.1] A. Passerone and M.L. Muolo, Joining Technology in Metal-Ceramic Systems, Materials and Manufacturing Processes, Vol 15, No. 5, 2000, p.631-648.

[1.2] J.A. Fernie and W.B. Hanson, Best Practice for Producing Ceramic-Metal Bonds, Industrial Ceramics, Vol. 19, No. 3 1999, p172-175.

[1.3] D. Brandon and W.D. Kaplan, Joining Processes, An Introduction, Wiley, England, 1997, 363 pages.

[1.4] K. Suganuma, Joining Non-Oxide Ceramics, in Ceramics and Glasses, Engineered Materials Handbook, Volume 4, ASM International, 1991, p.523-531.

[1.5] Y. Matsuo, M. Ito and M. Taniguchi, Ceramic-Metal Joining for Automobiles, Industrial Ceramics, Vol. 19, No. 3, 1999, p.203-207.

[1.6] J.A Fernie and A.J. Sturgeon, Joining Ceramic Materials, Metals and Materials, April 1992, p212-217.

[1.7] R.W. Cahn, P. Haase and E.J. Kramer (editors), Structure and Properties of Ceramics, Materials Science and Technology, Volume 11, VCH Publishers, 1994, 841 pages.

[1.8] W.E. Lee and W.M. Rainforth, Ceramics: Microstructure, Properties Control by Processing, Chapman & Hall, London, First edition, 1994, 590 pages.

[1.9] M. Schwartz, Handbook of Structural Ceramics, McGraw-Hill, New York, 1992.

[1.10] Park and H-E Kim, Microstructural Evolution and Mechanical Properties of Si_3N_4 with Yb_2O_3 as a Sintering Additive, Journal of American Ceramic Society, Vol. 80, No. 3, March 1997, pages 750-756.

[1.11] O. Ikeda, I. Ohnuma, R. Kainuma and K. Ishida, Phase Equilibria and Stability of Ordered BCC Phases in the Fe-rich Portion of the Fe-Al system, Intermetallics, Vol. 9, 2001, p755-761.

[1.12] B. Voyzelle, Hot Deformation Behaviour of Alloys for Applications at Elevated Temperatures, Doctoral Thesis, Queen's University, Kingston, Canada, March 1999.

[1.13] V. K.Sikka, in A.K. Koul et al. Development of Nickel and Iron Aluminides and Their Applications, Advances in High Temperature Structural Materials and Protective Coatings, National Research Council of Canada, Ottawa, 1994, p282-295.

[1.14] www.matweb.com

[1.15] E. Batawi, J. Phillips, J.A. Peters and G.Eggeler, Thermomechanical processing and mechanical characteristics of particle-strengthened iron aluminide-based alloys, Journal de Physique IV, Vol. 3, November 1993, p461-464.

[1.16] R.N. Wright, in A.K. Koul et al., Microstructure and Properties of Iron Aluminides, Advances in High Temperature Structural Materials and Protective Coatings, National Research Council of Canada, Ottawa, 1994, p296-308.

[1.17] C.T. Liu, E.P. George, P.J. Maziasz and J.H. Schneibel, Recent advances in B2 iron aluminide alloys: deformation, fracture and alloy design, Materials Science and Engineering, A258, 1998, p84-98.

[1.18] V.K. Sikka and C.T. Lui, Iron Aluminide Alloys for Structural Use, Materials Technology, Vol. 9, 1994, p159-162.

[1.19] R. Balasubramaniam, Hydrogen in Iron Aluminides, Journal or alloys and Compounds, Vol. 330-332, 2002, p506-510.

[1.20] K. Yoshimi and S. Hanada, The Strength Properties of Iron Aluminides, Journal of Metals, August 1997, p46-49.

[1.21] M.W. Finnis, The Theory of Metal-Ceramic Interfaces, Journal of Physics, Vol. 8, 1996, p5811-5836

[1.22] A.P. Tomsia, Ceramic/Metal Joining for Structures and Materials, Journal de Physique IV; supplément au Journal de Physique III, Vol. 3, Nov 1993, p1317-1326.

[1.23] J.T. Klomp, Physicochemical aspect of ceramic-metal joining, Joining of Ceramics, Institute of Ceramics, Chapman and Hall, England, 1990, p113-127.

[1.24] N. Eustathopoulos, Dynamics of Wetting in Reactive Metal/Ceramic Systems, Acta Materialia, Vol. 46, No. 7, 1998, p2319-2327.

[1.25] K.G. Budinski, Engineering Materials; Properties and Selection, fifth edition, Prentice-Hall, USA, 1992, 653 pages.

[1.26] M.G. Nicholas, Joining Processes ; Introduction to brazing and diffusion bonding, Kluwer Academic Publishers, The Netherlands, 1998, 333 pages.

[1.27] B. Derby, Diffusion Bonding, Joining of Ceramics, Institute of Ceramics, Chapman and Hall, England, 1990, p94-111.

[1.28] A.E. Martinelli, A.M. Hadian and R.A.L. Drew, A Review on Joining Non-Oxide Ceramics to Metals, Journal of the Canadian Ceramic Society, Vol 66, No. 4, November 1997, p276-283.

[1.29] ASM Handbook, Volume 6 ; Welding, Brazing and Soldering, ASM International, Ohio, 1993, 1299 pages.

[1.30] www.wesgometals.com

[1.31] S.D. Peteves, G. Ceccone, M. Paulasto, V. Stamos and P. Yvon, Joining Silicon nitride to Itself and to Metals, Journal of Materials, January 1996, p48-52 and 74-77.

[1.32] K. Suganuma, Joining Silicon Nitride to Metals and to Itself, Joining of Ceramics, Institute of Ceramics, Chapman and Hall, England, 1990, p173-193.

[1.33] M.G. Nicholas, Active Metal Brazing, Joining of Ceramics, Institute of Ceramics, Chapman and Hall, England, 1990, p73-93.

[1.34] H. Guo, E. Steinhauer and J.-J. Chêne, Solid State Diffusion Bonding for Structural Joining with Similar and Dissimilar Materials, Welding in the World, Vol. 37, No. 3, p107-113.

[1.35] B. Derby, The Influence of Surface Roughness on Interface Formation in Metal/Ceramic Diffusion Bonds, Ceramic Microstructures'86, Edited by J.A. Pask and A.G. Evans, Materials Science Research Volume 21, p.

[1.36] M.R. Locatelli, B.J. Dalgleish, K. Nakashima, A.P. Tomsia and A.M. Glaeser, New Approaches to Joining Ceramics for High-Temperature Applications, Ceramics International, Vol.23, 1997, p313-322.

[1.37] M. Paulasto, G. Ceccone and S.D. Peteves, Joining of Silicon Nitride via a Transient Liquid, Scripta Materialia, Vol. 36, No. 10, 1997, p1167-1173.

[1.38] C. Zheng, H. Lou, Z. Fei and Z. Li, Partial transient liquid-phase bonding of Si_3N_4 with Ti/Cu/Ni multi-interlayers, Journal of Materials Science Letters, Vol.16, 1997, p2026-2028.

[1.39] S.D. Peteves and M.G. Nicholas, Materials Factors Affecting Joining of Silicon Nitride Ceramics, Metal-Ceramic Joining, Edited by P. Kumar and V.A. Greenhut The Minerals, Metals & Materials Society, Warrendale, 1991, p43-65.

[1.40] M. Gao and F. Bao, Brazing of Silicon Nitride and Steel with Cu-based filler metals: Mechanism and Residual Stress in its joints, Materials Science Forum, Vol. 189-190 (1995) p399-404.

[1.41] J.D. Cawley, Introduction to Ceramic-Metal Joining, Metal-Ceramic Joining, Edited by P. Kumar and V.A. Greenhut, The Minerals, Metals & Materials Society, 1991, p3-11.

[1.42] B.T.J. Stoop and G.D. Ouden, Diffusion Bonding of Silicon Nitride to Austenitic Stainless Steel with Metallic Interlayers, Metallurgical and Materials Transactions A, Vol.26A, January 1995, p203-208.

Part 1 – Analysis of Si_3N_4 Ceramic with a Low Voltage Scanning Electron Microscope

Chapter 2

Determination of E_2 for Si_3N_4 Ceramics using FE-SEM and the DHL Procedure

2.1 Introduction

The main problem in performing SEM or FE-SEM analysis on most ceramics is the electrical insulation of the material, causing a build-up of sub-surface and surface charge. Under electron irradiation, a charge density is trapped inside the specimen and an electric field is produced, which affects the secondary electron signal and the primary electron beam. This leads to visual artefacts and hides information emanating from the specimen. X-ray analysis is also influenced by this charge build-up. The energy of the electrons from the beam are modified by the electric field (reduced or increased). A common technique to reduce this phenomenon is to coat the surface of the specimen with a grounded conductive layer. This solution does not completely eliminate the problem, because the trapped charge inside the specimen may change the parameters of the electron-specimen interaction [2.1]. This solution also hides surface information, especially for high resolution imaging.

In an SEM, four currents are defined at the specimen level and are very important at low beam energy. First, there is the I_B current produced by the primary electron beam (incident on the specimen). These electrons produce back-scattered electrons (I_{BSE}) and secondary electrons (I_{SE}), which are also emitted from the specimen. Finally we have the specimen current, I_S, flowing between the sample and the ground. For a conductive specimen these currents are related by equation 1.

$$I_B = I_{SE} + I_{BSE} + I_S. \qquad \text{(eq. 2.1)}$$

However, for a perfect insulator (eg. ceramics), the specimen current is zero ($I_S = 0$) and equation 2.1 is no longer satisfied. A space charge density builds up inside the specimen and the rate of change of this build up ($\Delta Q/\Delta t$) is given in eq. 2.2. This equation is similar to eq. 2.1 but describes a non conductive sample [2.2].

$$\Delta Q/\Delta t = I_B - I_{SE} - I_{BSE} \qquad \text{(eq. 2.2)}$$

Three states relating to this charge density build-up are observed in the SEM. Firstly, when the beam current is lower than the emitted electron current ($I_B < I_{SE} + I_{BSE}$) a positive charge density is created. The electric field attracts the electrons towards the specimen, accelerating the primary electron beam and the real primary energy, E_R, becomes higher than E_o. Under these conditions, less secondary electrons (SE) are detected. Under a positive charge, the secondary image appears darker as the secondary electrons are attracted by the surface electrical fields and return to the sample. Secondly, when the beam current is higher than the emitted electron current ($I_B > I_{SE} + I_{BSE}$), a negative charge density is observed. The electric field repels the primary electron beam (real primary energy E_R is lower than E_o) increasing the SE yield. The emitted secondary electrons are also accelerated towards the detector by the negative surface electrical field. Both phenomena combined explain why more secondary electrons can be detected. Under these conditions, the secondary image appears brighter. Thirdly, for operating conditions where the beam current and the emitted electron current are equal, no apparent electric field or space charge affect the primary electron beam energy or the secondary electron trajectory (detection and emission). The problem of charging will be avoided and imaging or characterization can be performed satisfactorily. The physical properties of the sample and the energy of the primary electron beam determine in which of these three states the SEM operates.

Figure 2.1 shows the relation between the ratio of total emitted current ($I_{SE} + I_{BSE}$) to the primary beam current (I_B) and the primary energy for a conductive specimen. Two neutral states are possible (E_1 and E_2), but in practice the first one is hardly obtainable in a SEM because energy E_1 is so low (in the eV domain). For an insulating material, the same behavior is found, but the real primary energy is expressed as $E_R = E_o + \Delta E$, where ΔE is the energy lost or gained by the electric field. Two procedures can be used to determine the E_2 energy. The first procedure uses the secondary electron detector combined with scanning at various magnifications to find under which charging conditions the SEM is operating (observation of darker or brighter fields). This procedure is explained in detail by Joy et al. [2.2]. The E_2 (neutral state) is reached when no brightness change occurs when the magnification is reduced. Some difficulties exist regarding this technique for determining the E_2 energy such as subjectivity (operator judgement) and contamination present in the microscope chamber. Contamination leaves black prints on the surface scanned by the beam, creating an artefact on the color definition of the scanned area.

In this chapter, a new procedure to determine E_2 is presented. This technique is based on the measurement of the high energy cut-off, the Duane-Hunt limit (E_{DHL}), of the bremsstrahlung x-ray emitted from the sample. Physically, it is impossible to produce x-rays possessing an energy exceeding the landing energy of an electron [2.3]. The spectrum gives the real primary energy ($E_R = E_{DHL}$), and the neutral state is obtained when this energy is equal to the incident energy, E_o ($\Delta E = 0$). To find this energy, theoretical relations between E_{DHL} and E_0 for a conductive material ($E_{DHL} = E_R = E_0$ for all E_0) is plotted with the experimental curve of the relation between E_{DHL} and E_0 for an insulator. The intersection of the two curves gives the neutral state (E_2). This technique was applied to Si_3N_4 ceramic.

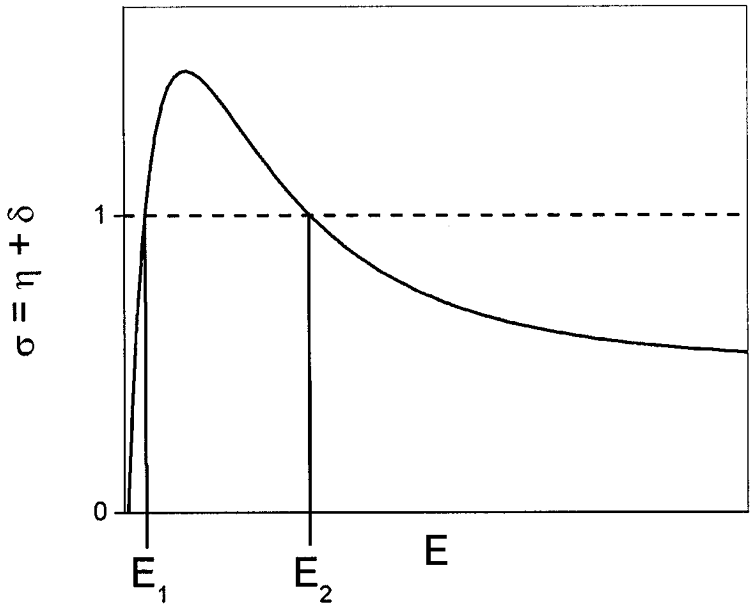

Figure 2.1 - Variation with incident energy of the ratio of the total emitted current to the primary beam current.

2.2 Experimental procedures

Silicon nitride bars (Ceradyne) containing between 7 to 8 wt% of Y_2O_3-Al_2O_3 as sintering additive were cut into discs of 1 mm thickness. All pieces were polished to 0.05 microns using Al_2O_3 and diamond as polishing media. Figure 2.2 presents a representative atomic force (AFM) micrograph (DI 3100 Scanning Probe Microscope) of the surface after polishing showing a relatively flat surface (RMS = 10.2 nm and Ra = 3.1 nm). The spikes present are noise produced during analysis.

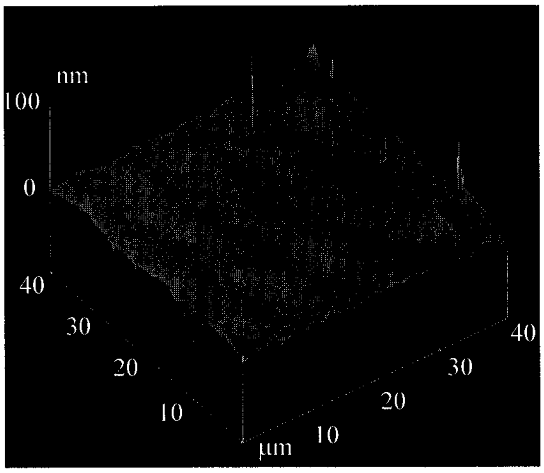

Figure 2.2 - AFM micrograph of surface topography of Si_3N_4 after polishing.

The analyses were performed using a Field Emission Scanning Electron Microscope (FE-SEM Hitachi S-4700 coupled with an Oxford EDS detector with a Ultra Thin Polymeric Window (UTPW) allowing the detection of light elements). The incident beam energy was varied on the microscope by increments of 100eV. Each analysis was performed as follows:

1. The energy of the incident beam was selected. The emission current was fixed at 20μA.
2. The surface of the ceramic was focused using a working distance of 12 mm, the optimum distance for x-ray collection for this microscope.
3. The magnification was changed to 100X and the beam was moved slightly from the focus point.
4. The magnification was increased to 1000X and the EDS spectrum acquisition was performed for a defined live time. The live time was varied between 20 and 1000 seconds.

Myklebust et al [2.4] have demonstrated that a linear fit of the last portion of the bremsstrahlung gives a better fit than an approach using a second degree polynomial equation. The quadratic fit is more sensitive to the convolution introduced by the x-ray detector, however this type of fit gives poor results for E_{DHL} determination. For this reason, the last portion of all spectra were modelled using a linear approach where Kramers equation for x-ray intensity is linear on 1/E [2.5]. Figure 2.3 illustrates an example of the linear fit performed on the spectrum intensity for a Si_3N_4 sample tested at 2.8 keV for 500 s live time. The data used for the fit were the 100 points (channels) before the value of E_0; when values of E_0 were below E_2, the data points used were between 2keV and E_0, as the presence of the x-ray peaks interferes with the linear fit. For example, the linear fit was performed between 2.0 and 2.8 keV.

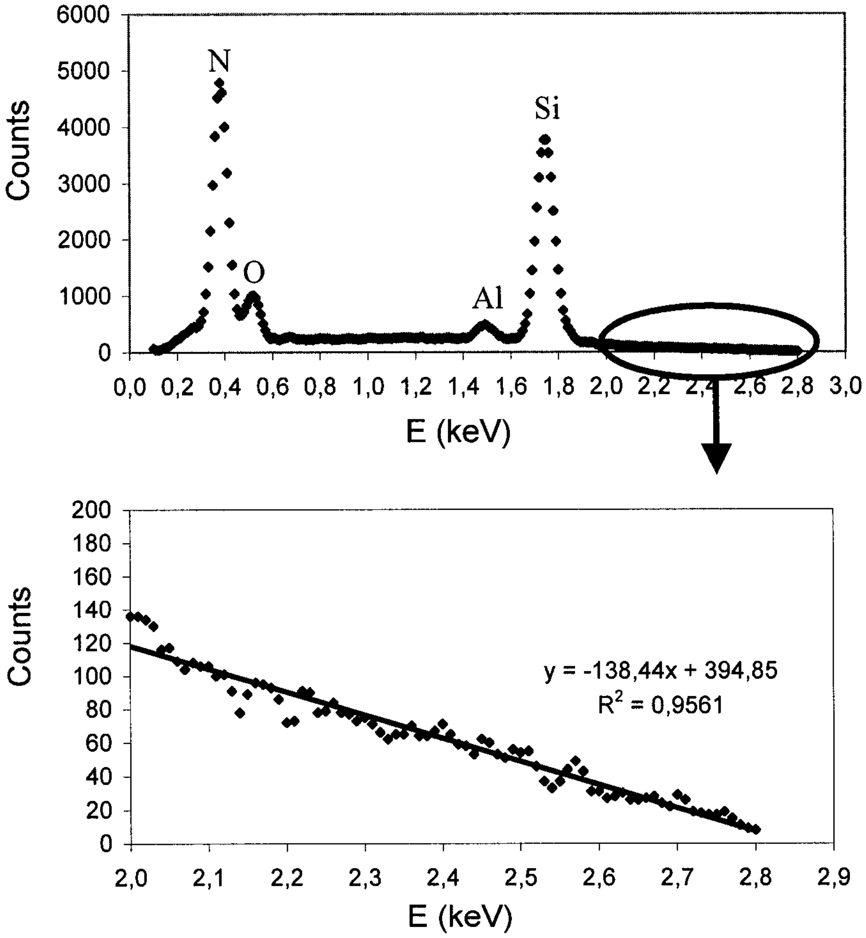

Figure 2.3 Example of linear fit of the last portion of the bremsstrahlung for an Si_3N_4 sample (E_0 = 2.8 keV, 500 s live time).

2.3 Results

Figures 2.4(a) and (b) illustrates the scattering phenomenon of E_{DHL} normalized as a function of time for a sample exposed for 20 and 350 seconds, respectively. The large deviation from the average value (around 400 eV for 20 seconds of exposure) illustrates the statistical importance of the live time exposure. E_{DHL} scattering becomes negligible after 500 seconds and therefore, this time was chosen for the analysis.

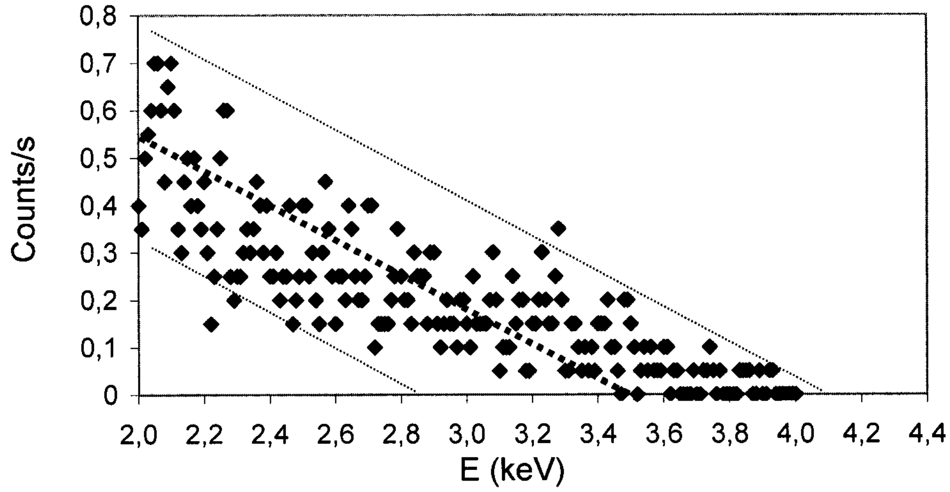

(a)

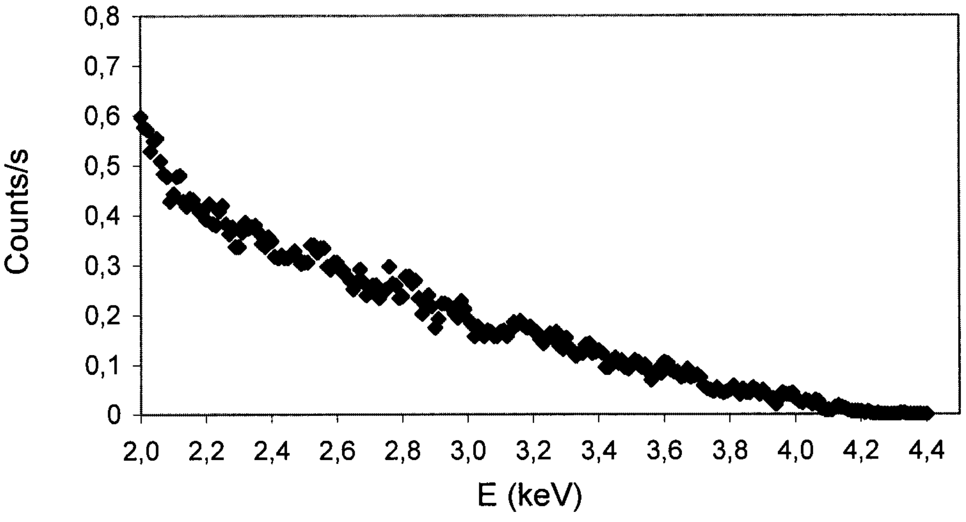

(b)

Figure 2.4 - Example of scattering effect from time normalized spectra acquired for (a) 20 s and (b) 350 s of live time exposure.

Figure 2.5 presents the variation of E_{DHL} of a Si_3N_4 sample as a function of the exposure time under the electron beam. Three different curves are observed. The two dashed lines represents the upper and lower values of E_{DHL} (see Fig 2.4(a)). The series of points in between represents the average value of E_{DHL}. All three curves regroup after a certain exposure time to a saturation value.

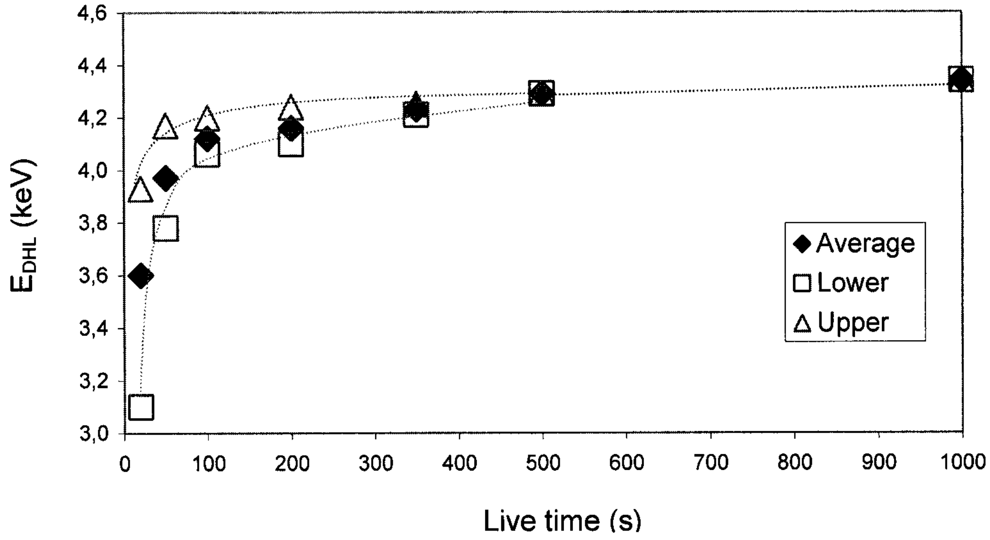

Figure 2.5 - Effect of live time acquisition on scattering of E_{DHL}.

Figure 2.6 presents the E_{DHL} determination of three Si_3N_4 samples analysed at 2.8 keV for 500 s of live time exposure. The average E_{DHL} in all three cases was determined and is 2.88, 2.86 and 2.90 keV, respectively. The reproducibility of the E_{DHL} from the EDS spectrum shows a small scattering in results, ranging between 20 eV (0.7%).

E_{DHL} was determined for an Al-Mg alloy sample and compared to the theoretical curve where E_R should be equal to E_0 for a conductive material. As no charging should occur for a conductive material ($I_B = I_{SE} + I_{BSE} + I_S$), the electron energy from the electron beam will have the same kinetic energy as when they were extracted from the filament as no electric field is present on the surface of the material. The results of E_{DHL} as a function of E_0 are presented in Figure 2.7.

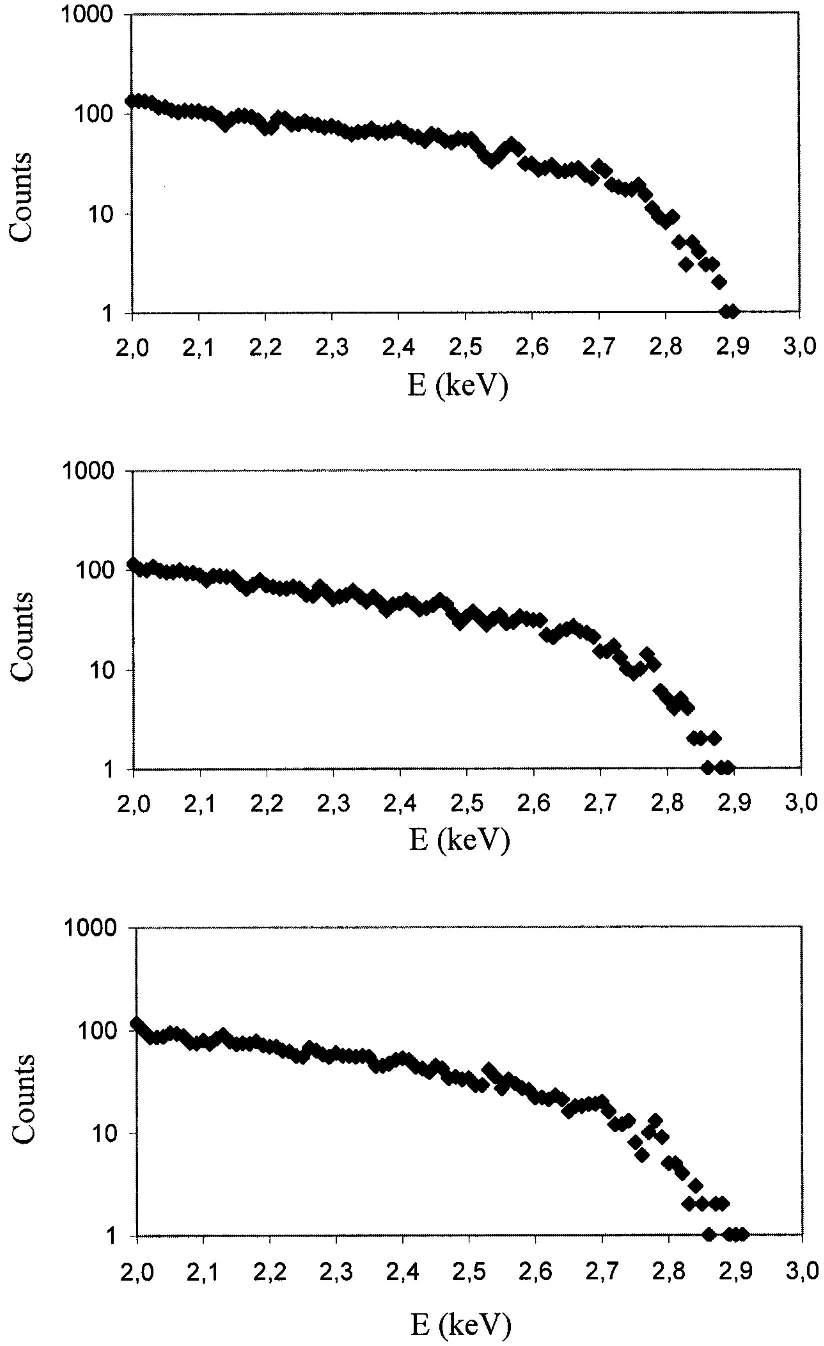

Figure 2.6 - Example of reproducibility of E_{DHL} acquisition.

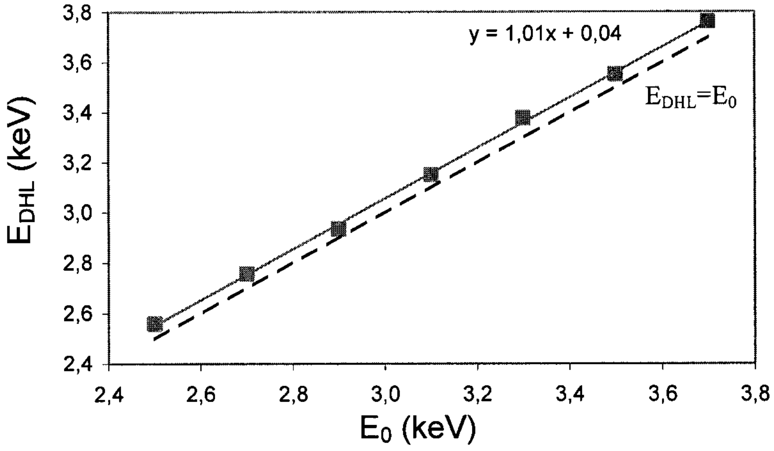

Figure 2.7 - E_{DHL} vs E_0 for Al-Mg alloy.

This graph shows that both curves, the theoretical (dashed line) and the linear fit of the experimental data, possess similar slopes. This confirms that the determination of E_{DHL} for a conductive material reproduces the theoretical behavior. However, a small deviation of 40 eV is observed. This variation between E_{DHL} and E_0 remains constant with increasing values of E_0 and might be associated with the calibration of the gun of the microscope.

The surface charge of the ceramic substrate will affect the kinetic energy of the incoming electrons. A positive charge will accelerate the electrons due to electrical attraction. Therefore, the electron kinetic energy will increase, which should lead to E_{DHL} values higher than E_0. The opposite phenomenon should be observed for negative charging. Figure 2.8 presents a graph where the best-fit curve for E_{DHL} is superimposed on the unity curve (theoretical curve of E_R=E_0). The expected difference in kinetic energy, measured by the displacement of E_{DHL}, is observed. The E_{DHL} for the lower values of E_0 tested, was found to be higher than the E_0, illustrating positive charging. The opposite behavior is found for higher values of E_0. Both curves intercept at the E_2 value for the material analysed, which is 3.01 keV for Si_3N_4. The standard deviation of the repeatability on the measurement of E_{DHL} is smaller than the thickness of the point on the graph.

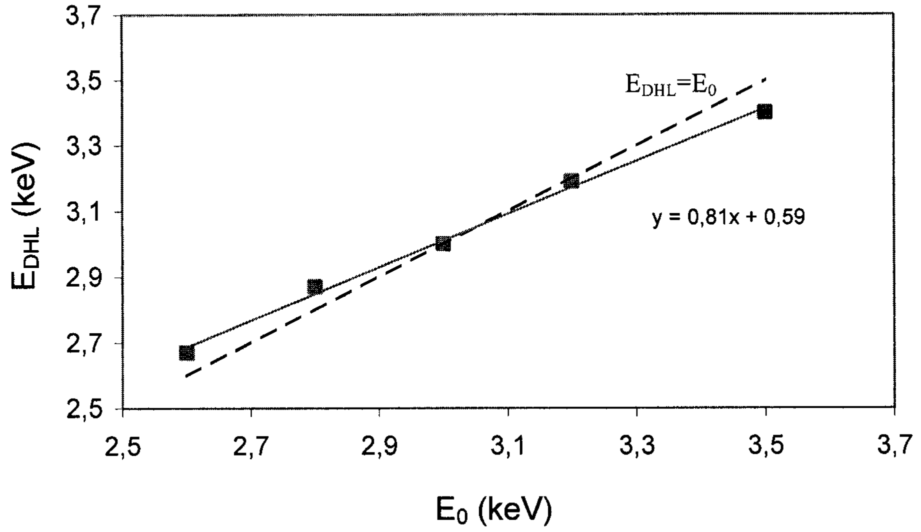

Figure 2.8 - E_{DHL} measurement vs E_0 for Si_3N_4 ceramic.

Figure 2.9 presents micrographs taken at the same magnification of the Si_3N_4 grain structure under different incident beam energies at a scan acquisition time of 20 seconds. Figure 2.9(a) and 2.9(c) demonstrate the effect of the formation of an electrical field at the surface of the specimen (positive and negative charging, respectively) on the resolution. No clear structure or grain boundary is observed in the case of positive charging as the grain boundaries act as charge trapping locations. In the case of negative charging, more contrast is observed at the grain boundaries but charging effects are more pronounced from the voids presents at the triple point of the grains. This case also illustrates the effect of cavities on charging. The above E_0 energy values were chosen to demonstrate the effect of the choice of beam energy value away from the E_2 value of the material, on artefact formation. However, for an incident beam energy closer to the E_2 value of the insulator, higher resolution and proper imaging become possible. Figure 2.9(b) presents an example of application of the E_2 energy value determined through the E_{DHL} method for high resolution imaging.

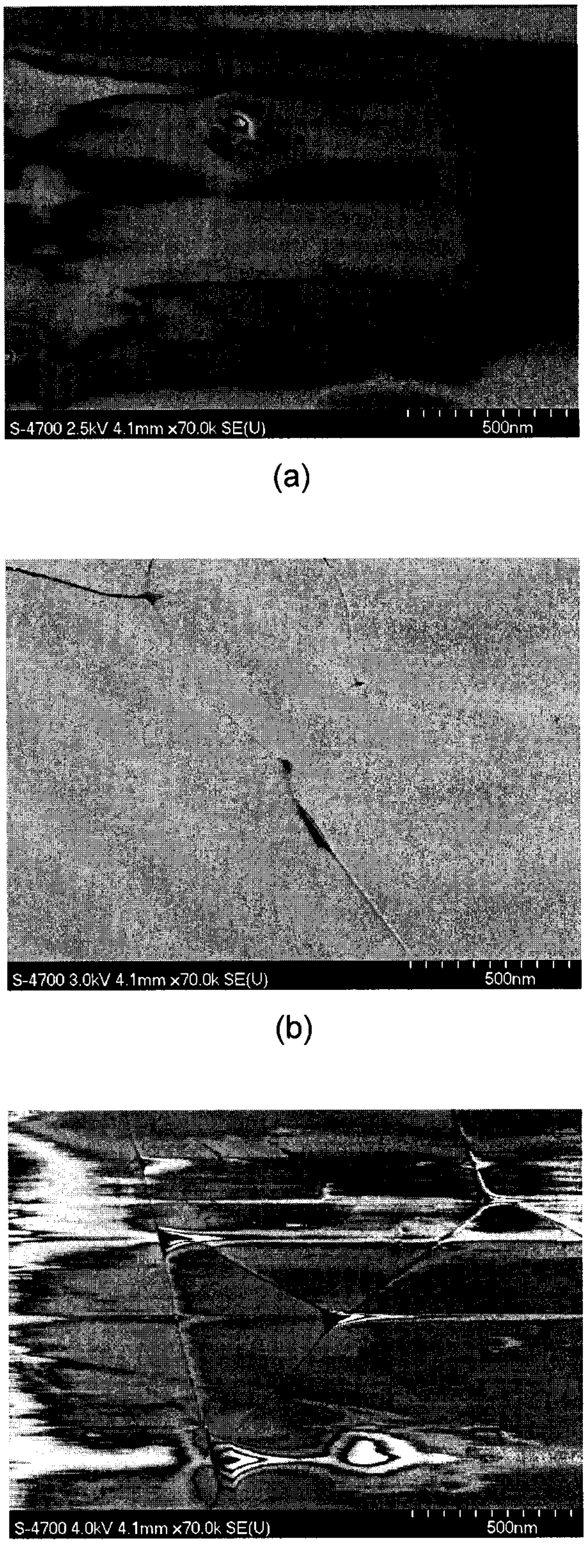

(a)

(b)

(c)

Figure 2.9 - Si_3N_4 grain boundaries imaged at (a) 2.5 keV, (b) 3.0 keV and (c) 4.0 keV, respectively.

2.4 Discussion

This technique has shown the potential for characterising the charging behavior of nitride ceramics. However, two major limitations of this technique should to be known by the user. (1) Flat and polished surfaces are preferred to powder samples as charge trapping occurs preferentially at the edge of the structure (interaction volume near the edge and more atomic defects), limiting its use to mostly bulk and polished materials. (2) The other limitation comes from the acquisition rate of x-rays from the EDS detector. This work has shown the effect of short acquisition times on the scattering of the E_{DHL} values as well as on the low number of counts. This statistical problem enables this technique to give information regarding the dynamics of charging but only for the determination of the E_2 value of steady state charging.

This procedure for the determination of the E_2 was compared to the procedure developed by Joy et al. [2.2] on Si_3N_4. Even with the subjectivity of their procedure, the results obtained were within the same range (3.01 keV with E_{DHL} technique compared to 2.9-3.0 keV for Joy's technique). The main advantage of using the E_{DHL}, other than accuracy, is the independence of the x-ray emission from the sample from the level of contamination or operator judgement. However, the technique developed by Joy et al. [2.2] is faster and simpler as the E_2 energy is determined from direct observations.

2.5 References

[2.1] J. Cazaux, Electron probe microanalysis of insulating materials: Quantification problems and some possible solutions, X-Ray Spectrometry, Vol. 25, 1996, p1-16.

[2.2] D.C. Joy and C.S. Joy, Low voltage scanning electron microscopy, Micron, Vol. 27, No. 3-4, 1996, p247-263.

[2.3] L. Reimer, Scanning Electron Microscopy: Physics of Image Formation and Microanalysis, *Springer*, second edition, Country, 1998.

[2.4] R.L. Myklebust, C.E. Fiori and D.E. Newbury, A Robust Method for Determining the Duane-Hunt Limit from Energy-Dispersive Spectra, Microbeam Analysis - 1990, p147-149.

[2.5] H.A. Kramers, Phil. Mag. 46 (6th ser), 1923, p836.

Part 2 – Wetting and Interactions of Cu-Ti Alloys on an Iron Aluminide Alloy

Chapter 3

Wetting Behaviour of Copper on an Iron Aluminide Alloy

3.1 Introduction

Santella and Patterson have studied the wetting of pure iron aluminide by silver, gold and copper [3.1]. The chemical composition of Fe_3Al used in their study was Fe-14.0Al-0.05Si-0.006C-0.002S-0.006O wt%. Pure copper showed a non-wetting behaviour, where the wetting angle decreased from 134° to 124° in 10 minutes at 1092°C. Santella et al. explained this non-wetting behaviour of copper on pure iron aluminide by the formation of an alumina film at the surface of the sample (a common phenomenon in aluminides) where the contact angle observed is similar to the wetting angle of copper on alumina [3.1]. With such results, copper becomes unattractive as the principal filler metal used in brazing operations.

Chromium is one of the most popular alloying elements in iron aluminide metallurgy as it changes the surface state. It has been shown that the presence of Cr accelerates the nucleation of the α-Al_2O_3 protective oxide layer [3.2, 3.3]. Chromium and iron atoms were detected in the protective layer for aluminide alloys, which is not the case for pure aluminides (without Cr) [3.2].

The objective of this work was to study the wetting behaviour of copper on an alloyed iron aluminide in order to evaluate the modification of the surface composition due to chromium additions.

3.2 Experimental Procedures

The chemical composition of the Fe_3Al alloy used (FA-129) is shown in Table 3.1. An optical micrograph of the FA-129 intermetallic is presented in Figure 3.1.

Table 3.1 –Chemical composition of iron aluminide alloy.

(wt%)	Al	Cr	Nb	C	Fe
Chemical Composition	16.6	4.67	1.14	0.027	Bal.

Figure 3.1 – Optical micrograph of the FA-129 intermetallic microstructure.

The sessile drop test was used to evaluate wettability. A schematic representation of the sessile drop apparatus is presented in Figure 3.2. Square samples of FA-129 (20X20X6 mm^3) were cut from a large plate and polished down to a 0.05 micron finish. Each side of a copper cube (99.89% pure) of 1 gram ± 2% was polished down to a 5 micron finish and then washed in HNO_3 (15vol%), washed for 15 minutes in acetone and finally rinsed in 2-propyl alcohol to reduce the quantity of residue left on the surface. All the cleaning procedures were performed in an ultrasonic bath. The copper cube was centred on the FA-129 substrate and placed in a tube furnace. The sample was then inserted at room temperature in the middle of the hot zone to simulate brazing conditions, as components for brazing are normally heated and cooled inside the furnace. A window was placed at one end of the tube furnace in order to observe the wetting behaviour. A binary mixture of argon (99.8% purity) / hydrogen with a ratio of 98 / 2vol% respectively was used as the wetting atmosphere. A heating rate of 20°C/min and furnace cooling were used. Different temperatures were tested, varying from 1070 to 1190°C and the soaking time was varied from 2 to 60 minutes, depending on the spreading kinetics. *In situ* pictures of the contact angle between the liquid drop and the Fe_3Al substrate were taken at different times. Cross sections of the final drop were prepared for metallographic examination. Optical microscopy and image analysis (CLEMEX system), scanning electron microscopy (JEOL-840/EDAX), FE-SEM (Hitachi S4700/Oxford) and electron probe microanalysis (JEOL-8900/WDS; ZAF correction model; E_0=20keV) were used to characterise the microstructures.

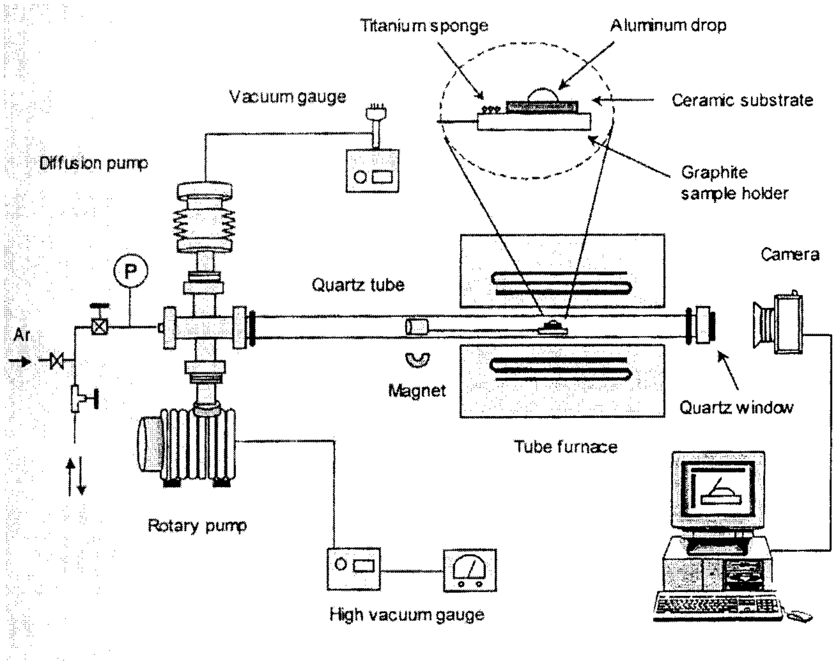

Figure 3.2 – Schematic representation of the sessile drop apparatus.

3.3 Results

In situ pictures of the experiments carried out at 1070°C for soaking times of 45 and 60 minutes are presented in Figure 3.3. This temperature is approximately 15°C lower than the nominal melting temperature of pure copper (1084.9°C). No major changes were observed in the early part of the test as the cube geometry remains after 45 minutes. However, after 60 minutes, the two bottom corners possess a wetting configuration as opposed to one upper corner which retains a square angle. This observation suggests partial melting of the copper cube at a lower temperature than the reference melting temperature.

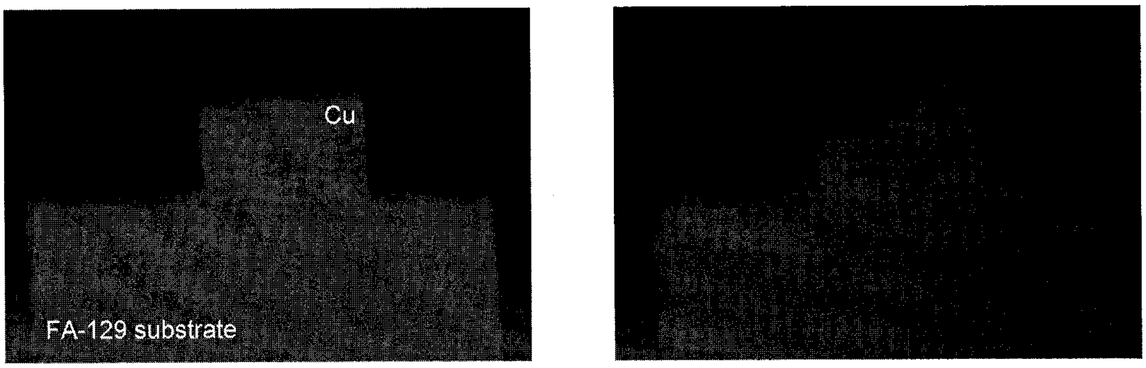

a) 45 min

b) 60 min

Figure 3.3 - *In situ* picture of Cu on FA-129 at 1070°C for (a) 45 min and (b) 60 min.

Figure 3.4 presents a macrograph of the sample after cross-sectioning and polishing. The main feature observed is the presence of two distinct regions within the substrate. One possesses the characteristic copper color whereas the remainder of the substrate exhibits a yellow color. EDS analysis has shown that the yellow region is associated with the presence of aluminum and EPMA analysis has quantified this to be of the order of 8 wt%. The analysis has also detected between 4 to 4.5 wt% Fe, depending on the region analysed, suggesting dissolution of the intermetallic.

Figure 3.5 presents the evolution of spreading of copper, as a function of time on the Fe_3Al substrate as the temperature in the hot zone of the furnace increases. The pictures were taken during the heating stage up to the set-point temperature of 1110°C. Timing began (zero time) the instant the furnace temperature reaches 1080°C, 5°C below the nominal melting point of copper. Complete spreading of the copper was obtained in less than 2 minutes. The change in shape of the Cu cube with time suggests that melting started from the bottom where liquid spreading is observed: however when the furnace reached the temperature where copper melts, complete spreading was achieved.

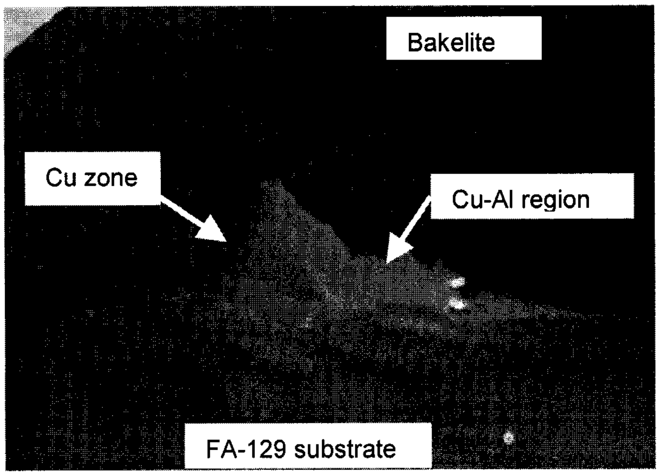

Figure 3.4 - Macrograph of the sample tested at 1070°C for 60 minutes

Figure 3.6 presents a comparative SEM micrograph of substrates soaked at 1110°C for 3 and 60 minutes. Both cases show similar features but to a lesser degree for the shorter soaking time. After 60 minutes, the grain structure near to the interface was completely infiltrated and the Fe_3Al grains are no longer contiguous, whereas for three minutes, the infiltration depth is lower.

The copper-aluminum liquid has infiltrated the structure along the grain boundaries (Figure 3.7(a)) and has also diffused into the grains. The copper has precipitated within the Fe_3Al alloy structure as well. An island of Cu-rich Al eutectic structure is shown in Figure 3.7(b), which possesses a composition of 10.3wt%Al. EPMA results show that an affected grain contains an average of 10.4 wt%Cu. After 60 minutes, the

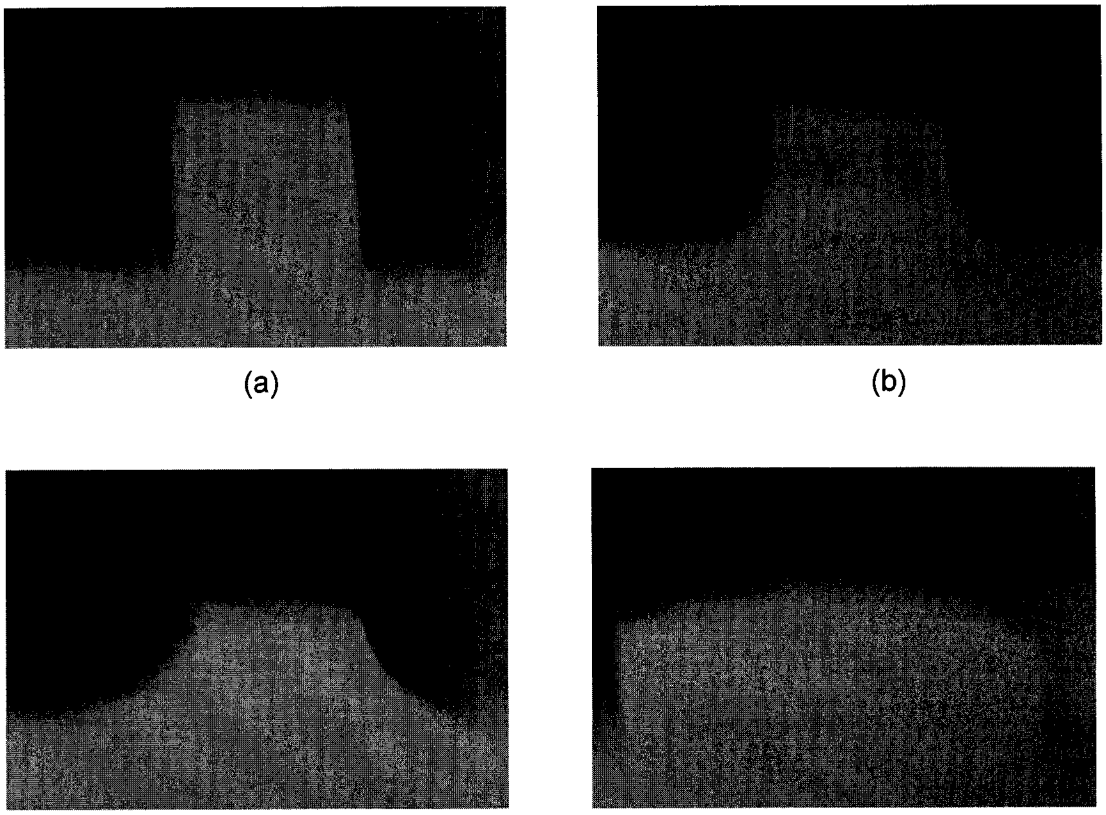
(a) (b)

(c) (d)

Figure 3.5 - Evolution of spreading and melting of the Cu cube for times of (a) 0 sec, (b) 44 sec, (c) 83 sec and (d) 110 sec. (0 sec corresponding to furnace at 1080°C).

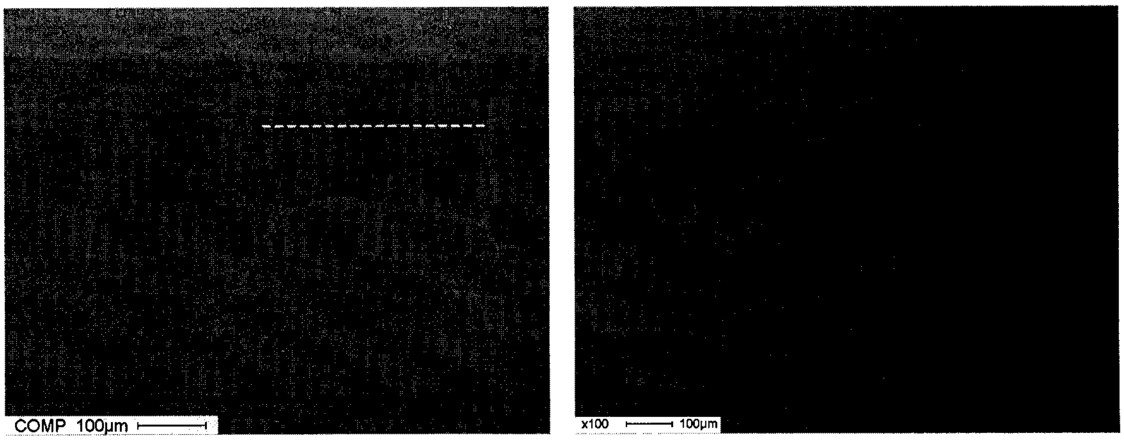

(a) (b)

Figure 3.6 - Example of grain boundaries decohesion after soaking times of (a) 3 minutes and (b) 60 minutes at 1110°C, respectively.

intergranular content of Al in the grains and in the Cu-Al alloy suggests that concentration has reached equilibrium. EPMA results of grains affected by copper are presented in Table 3.2. The chemical composition of the as-received FA-129 is also included for comparison. The measurements demonstrate that the Al content of the aluminide decreases by ≈40%. The Fe content decreases slightly but Cr and Nb remain in the same composition range. Reporting the chemical composition the aluminide to the Fe-Al phase diagram [3.4], shows that the Al content is now too low to form the DO3 structure during cooling and that the grains affected by a reduction in Al-content should have the α-Fe b.c.c. structure. Dissolution of the FA-129 grains was demonstrated through the presence of precipitates possessing a dendritic shape (Figure 3.7(c)) found in the drop for the samples soaked for 60 minutes. EPMA analysis of the precipitates is presented in Table 3.2. The dissolution is clearly observed for the sample soaked for 60 minutes by the presence of wavy grain boundaries (Figure 3.7(c)). However, after 3 minutes, the dissolution of the intermetallic in the molten metal has not started yet, as the original shape of the grain boundary is maintained (Figure 3.6(a)). This suggests that grain boundary penetration occurs first and is followed by grain dissolution.

Figure 3.8 presents a low voltage (5 keV) line scan of Al content following the dashed line illustrated in Figure 3.6(a). The results demonstrate an Al gradient across the width of the grain. Maximum Al concentration is observed in the centre, whereas a lower concentration is detected near the grain boundary. Monte Carlo simulations, using *Win X-Ray* [3.5], predicted an interaction volume of 150 nm in α-Fe and 175 nm in Fe_3Al when an accelerating voltage of 5 keV is used. The small interaction volume validates the concentration gradient and clearly demonstrates the diffusion of Al from the intermetallic grain to the molten Cu. This Al gradient is observed after only three minutes, suggesting rapid diffusion process. This reinforces the observation of the equilibrium concentration of Al between the grain and the Cu-Al phase during longer soaking time experiments.

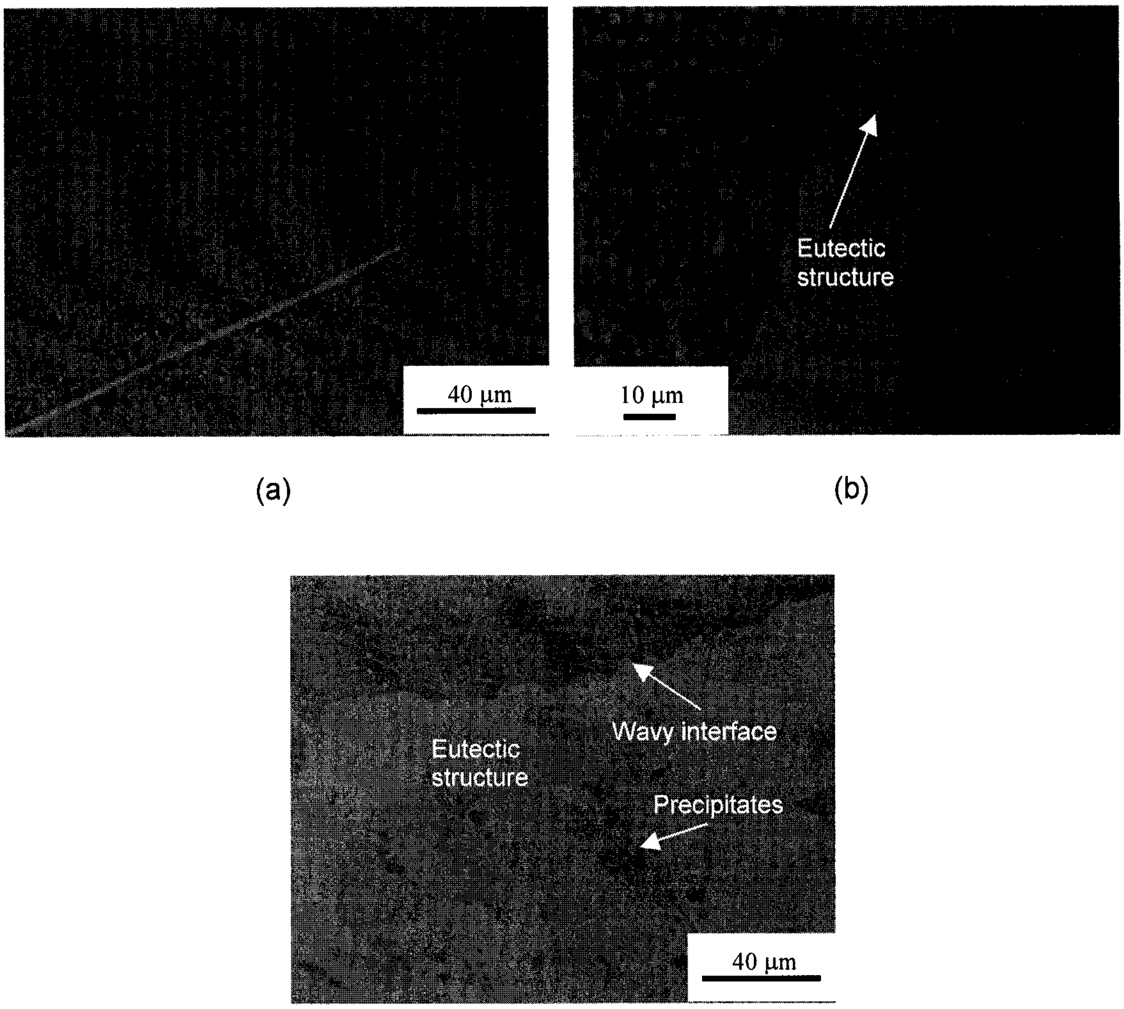

(a) (b)

(c)

Figure 3.7 - (a) Optical micrograph of liquid infiltration in the FA-129 grain boundary, (b) back-scattered micrograph of eutectic structure in infiltrated grain boundary and Cu presence in grain structure and (c) optical micrograph of the drop region.

Table 3.2 – EPMA results of different locations.

Location of analysis	Chemical Analysis (wt%)				
	Fe	Al	Cr	Nb	Cu
Reference FA-129	76.45	18.04	4.98	1.06	0
Grain after 60 min	73.18	10.4	4.82	0.99	10.76
Dendritic precipitate	78.05	11.25	3.4	0.78	7.2

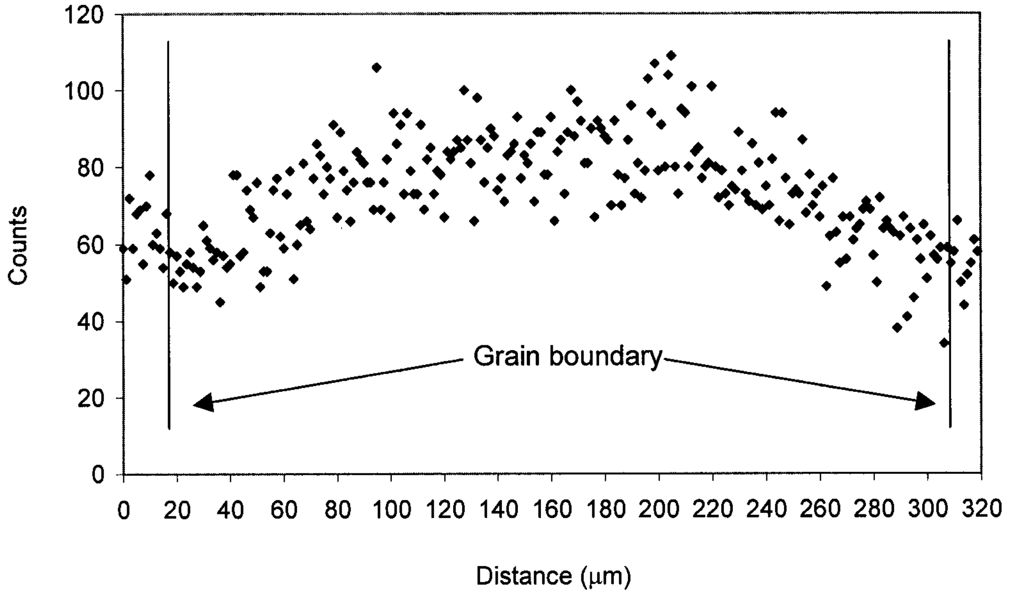

Figure 3.8 - Aluminum line scan along the dashed line in Fig.3.6(a).

3.4 Discussion

The corrosion resistance of iron aluminide is obtained by the formation of a passive alumina layer due to surface oxidation. In air or in low oxygen pressure, the oxide layer formation and growth will occur but with different kinetics as the oxygen potential changes. The addition of chromium has the effect of accelerating the initial growth of the oxide film [3.2]. Lee et al. have shown that Cr diffuses from the substrate into the oxide scale and forms a solid solution of Cr_2O_3-Al_2O_3 [3.2]. The presence of Fe or Cr in the alumina layer may increase the internal energy level and increase the defect mobility, which has a direct influence on diffusion [3.2].

García-Méndez et al. [3.6] have shown that in a thin-film diffusion couple, Al diffuses rapidly in Al_2O_3 and intermixed phases are observed for heat treatments at temperatures as low as 600°C. Chen et al. [3.7] have studied the Cu/Al_2O_3/bulk Al diffusion couple and have observed the presence of copper in the bulk Al substrate. As aluminum diffuses and mixes with Al_2O_3, the thermodynamic driving force for copper diffusion becomes the formation of a Cu-Al alloy [3.7]. These observations correlate with the results obtained in this work. Aluminum diffuses from the FA-129 through the oxide film into the copper cube forming a Cu-Al alloy and a clear example is observed in Figure 3.4, where distinct Cu and Cu-Al zones are present. Experiments performed below the melting temperature of pure copper have shown partial wetting as complete melting was not achieved.

The contact angle between a liquid and a solid is controlled by the equilibrium of the various surface tensions. The wetting equation can be written as follows:

$$\cos \theta = (\gamma_{sv} - \gamma_{sl})/ \gamma_{lv} \qquad \text{(eq. 1)}$$

where γ_{sv}, γ_{sl} and γ_{lv} are respectively the solid-vapour, solid-liquid and liquid-vapour surface tensions. Wetting is improved by decreasing θ, which is achieved by increasing γ_{sv}, decreasing γ_{sl} or decreasing γ_{lv}. The solid-liquid surface tension (γ_{sl}) can be reduced by changing the material system [3.8]. The in situ alloying of the copper substrate by aluminum changes the value of this surface tension. Naka et al. [3.9] have demonstrated that the equilibrium contact angle decreases with increasing content of Al in Cu and that the work of adhesion increases simultaneously. The modification of the surface composition through Cr diffusion will also affect this value. This term of the equation is also highly dependant on temperature and decreases rapidly with increase in temperature (super-heated melt). The effect of alloying copper with aluminum depresses the melting temperature as the concentration of aluminum increases, the highest melting point component in the system being pure copper [3.10]. As the reference melting temperature for such an alloy decreases, the drop gradually becomes super-heated, which reduces the value of γ_{sl}.

The microstructural degradation occurs through grain boundary penetration by molten metal. However, the penetration of molten metal is associated with the diffusion of Al from the intermetallic to the Cu substrate. At room temperature, the lattice parameters of the pure α-Fe and Fe_3Al are 2.98 and 5.78Å, respectively [3.11]. Initially, the diffusion of Al will reduce the volume of the unit cell which will reduce the volume of each grain and allow sufficient room for molten metal infiltration. Increasing the area of contact increases the diffusion rate of Al. The results at low interaction time have shown that only infiltration at grain boundaries occurred and no copper penetration was yet observed. In addition to the Al diffusion phenomenon, liquid infiltration favours grain separation and increases the contact area for copper diffusion into the grains. Grain dissolution also occurs because copper has a higher Fe solubility at high temperature, as do Cu-Al alloys [3.12].

The results of Santella and Patterson have shown a 10° decrease in the contact angle (from 134 to 124°) after 10 minutes at 1092°C for the Cu-pure Fe_3Al system, and contact angle data exhibited an equilibrium contact angle of 138° for the system with the pure copper/alumina ceramic [1.26]. Moreover, they have observed diffusion of Al from the Fe_3Al substrate to the sessile drops of Ag and Au [3.1]. Gold wets the Fe_3Al substrate at approximately 900°C, which is 160°C below the nominal melting temperature and wetting was explained by the formation of a lower melting point eutectic in the Au/Al system [3.1]. The same explanation was used for the Ag system. However, in all three systems (Au, Ag, Cu), Al can diffuses though the Al_2O_3 film and the decrease in wetting angle from 134 to 124° should be associated with the initiation of alloying in the copper-containing system. Unfortunately, microstructural analysis was not performed by Santella and Patterson. as wetting conditions were never achieved.

Wettability of Cu on iron aluminide alloy is directly influenced by aluminum diffusion from the substrate. The diffusion kinetics of Al through the oxide film is faster when chromium is present in the alloy due to the oxide composition and the presence of points defects. In the current study, wetting of copper was observed in less than 2 minutes. Pure copper should therefore wet any substrate of iron aluminide but the spreading kinetics are controlled by the diffusion of aluminum, which is influenced by the contact area (solid-solid or solid-liquid).

3.5 References

[3.1] M.L. Santella and A.B. Patterson, Wetting of Iron Aluminide Alloys by Ag, Au and Cu, Materials Science and Engineering, A258, 1998, p270-275.

[3.2] D.B. Lee, G.Y. Kim and J.G. Kim, The Oxidation of Fe_3Al-(0, 2, 4, 6%)Cr alloys at 1000°C, Material Science and Engineering, A339, 2003, p109-114.

[3.3] J.H. DeVan and P.F. Tortorelli, The Oxidation-Sulfidation Behavior of Iron Alloys Containing 16-40at% Aluminum, Corrosion Science, Vol. 35, No.5-8, 1993; p1065-1071.

[3.4] ASM Handbook Vol 3, Phases Diagrams (ASM International, USA) p 2·73.

[3.5] H. Demers, P. Horny, R. Gauvin and E. Lifshin, Win X-Ray V1.0.0.4, ©2002-2003 McGill University.

[3.6] M. García-Méndez, N. Valles-Villarreal, G.A. Hirata-Flores and M.H. Farías,Study of Thermal Diffusion between Al_2O_3 and Al thin Films, Applied Surface Science, Vol. 151, 1999, p139-147.

[3.7] J.G. Chen, M.L. Colainni, W.H. Weinberg and J.T. Yates Jr., The $Cu/Al_2O_3/Al(111)$ Interface: Initial Film Growth and Thermally Induced Diffusion of Copper into the Bulk, Surface Science, Vol. 279, 1992, p223-232.

[3.8] G. Humpton and D.M. Jacobson, Principles of Soldering and Brazing, ASM International, USA, 1993, 281 p.

[3.9] M. Naka, Y. Hirono and I. Okamoto, Joining of Alumina/Alumina using Al-Cu Filler Metal and its Application to Joining of Alumina/Aluminum, Quaterly Journal Japanese Welding Society, Vol. 5, No. 3, 1987, p93-98.

[3.10] ASM Handbook Vol 3, Phase Diagrams (ASM International, USA) p 2·44.

[3.11] X-ray pattern database, JCPDS index, 1998.

[3.12] ASM Handbook Vol 3, Phase Diagrams (ASM International, USA) p 3·10.

Chapter 4

Interfacial Microstructure Characterisation of Molten Cu-Ti and an Iron-based Aluminide

4.1 Introduction

The previous chapter has demonstrated the complementary diffusion of Cu and Al, modifying the chemical composition and thus, affecting the phases present. Cu additions in pure iron aluminide have been shown to produce a major increase in the yield strength but a considerable reduction in room temperature ductility [4.1]. The DO_3 structure remains stable with Cu addition up to 15at% [4.1]. Ti additions have been shown to raise the transition temperature $DO_3 \rightarrow A_2$ [4.2, 4.3]. Ti also increases the tensile properties at the expense of a reduction in room-temperature ductility [4.4, 4.5].

The objective of this study was to evaluate the possibility of reducing the penetration and reaction between alloyed Cu (copper-5wt% titanium and copper-20wt% titanium) with the FA-129 alloy and compare the results with pure copper. The different compositions of active brazing alloy were chosen in order to obtain a zero, low and high Ti-content. The addition of Ti in Cu-based filler metal is commonly used when brazing ceramics, including Al_2O_3. It also allows lower temperature testing as a higher titanium content decreases the melting temperature of the alloy.

4.2 Experimental Procedure

Square blocks of (20X20X5 mm^3) of FA-129 were cut with a diamond blade. Each substrate was ground with silicon carbide paper and polished down to a 0.05 microns finish with colloidal silica. The substrates were washed in water and then cleaned in acetone in an ultrasonic bath.

Cubes of 1 g were cut from an electrolytic copper block. Copper-titanium alloys (5 and 20 wt% Ti) were produced by a powder metallurgy process. Copper powder (99%; -100 mesh) and titanium powder (99.4%, -100 mesh) were mixed in a mixing device, cold pressed into pellets at 390 MPa and sintered at 800°C for 3 hours. For both compositions, cubes of 1g ± 2% were cut. Immediately before the experiment, each sample was washed in 15 vol% HNO_3 for 1 min and rinsed in an ultrasonic bath in acetone for 5 minutes.

For each experiment, the iron aluminide alloy substrate with a centred piece of copper alloy was inserted in the middle of an alumina tube furnace prior to heating (see Figure 4.1). The following procedure was used to simulate a brazing cycle, including a heating ramp. Each end of the tube was water-cooled and one end was equipped with a window to allow photography of the specimen. The chamber was purged with a 95% argon- 5% hydrogen mixture for 20 minutes before heating. The heating also took place in this atmosphere. The temperature was measured with an N-type thermocouple. Each sample was heated to the test temperature with a heating rate of 18°C/min and held for 1 hour. The experimental temperatures used as a function of alloy composition as well as their theoretical melting temperature are listed in Table 4.1.

Transverse sections of selected specimens were ground and polished for metallography. Optical microscopy and image analysis were performed on a Clemex system. Scanning electron microscopy (SEM) was performed on a JEOL-840 equipped with an electron dispersive spectrometer (EDAX). EPMA was performed with a JEOL-8900 microprobe equipped with a WDS system (ZAF correction model; E_0=20keV). XRD was performed with a Philips PW1710 diffractometer ($CuK\alpha$ =

1.54098Å). A Leco M-400-G2 microhardness tester with a Vickers indentor was used to characterize different phases with a load of 300g.

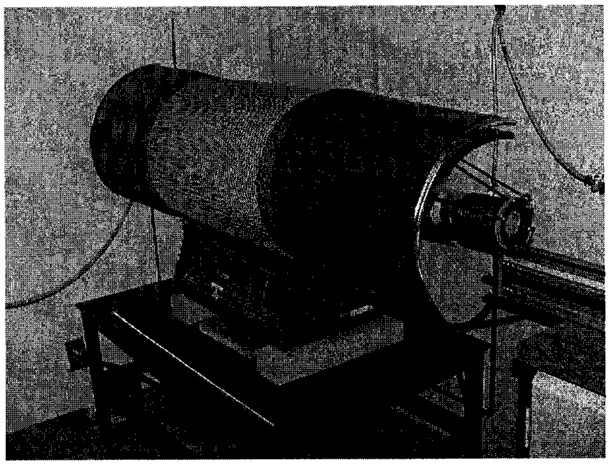

Figure 4.1 - Tubular furnace used for interaction tests.

Table 4.1 – Experimental temperature used as a function of copper alloy composition.

Temp. (°C)	Theor. Melt. T	990	1030	1070	1110	1150	1190
Cu	1085			X	X	X	X
Cu-5Ti	1040			X	X	X	X
Cu-20Ti	910	X	X	X			

4.3 Results

4.3.1 Penetration Results

Figure 4.2 presents plots of the penetration by the different copper alloys into the FA-129 substrate as a function of (a) the test temperature and (b) the superheat temperature, respectively. Both graphs present the percentage of penetration (measured as the ratio of the penetration distance to the total thickness of the FA-129 substrate): each value reported is the average of the worst case for each optical mosaic of the entire thickness (six per sample). The results shows that independently of the alloy composition, the molten metal penetration reaches a plateau with increasing temperature. The highest penetration was observed for the sample containing 5wt%Ti, whilst the lowest penetration was obtained for 20wt%Ti, even if the samples were submitted to a high level of superheating. The penetration of pure copper is slightly lower than for Cu-5wt%Ti.

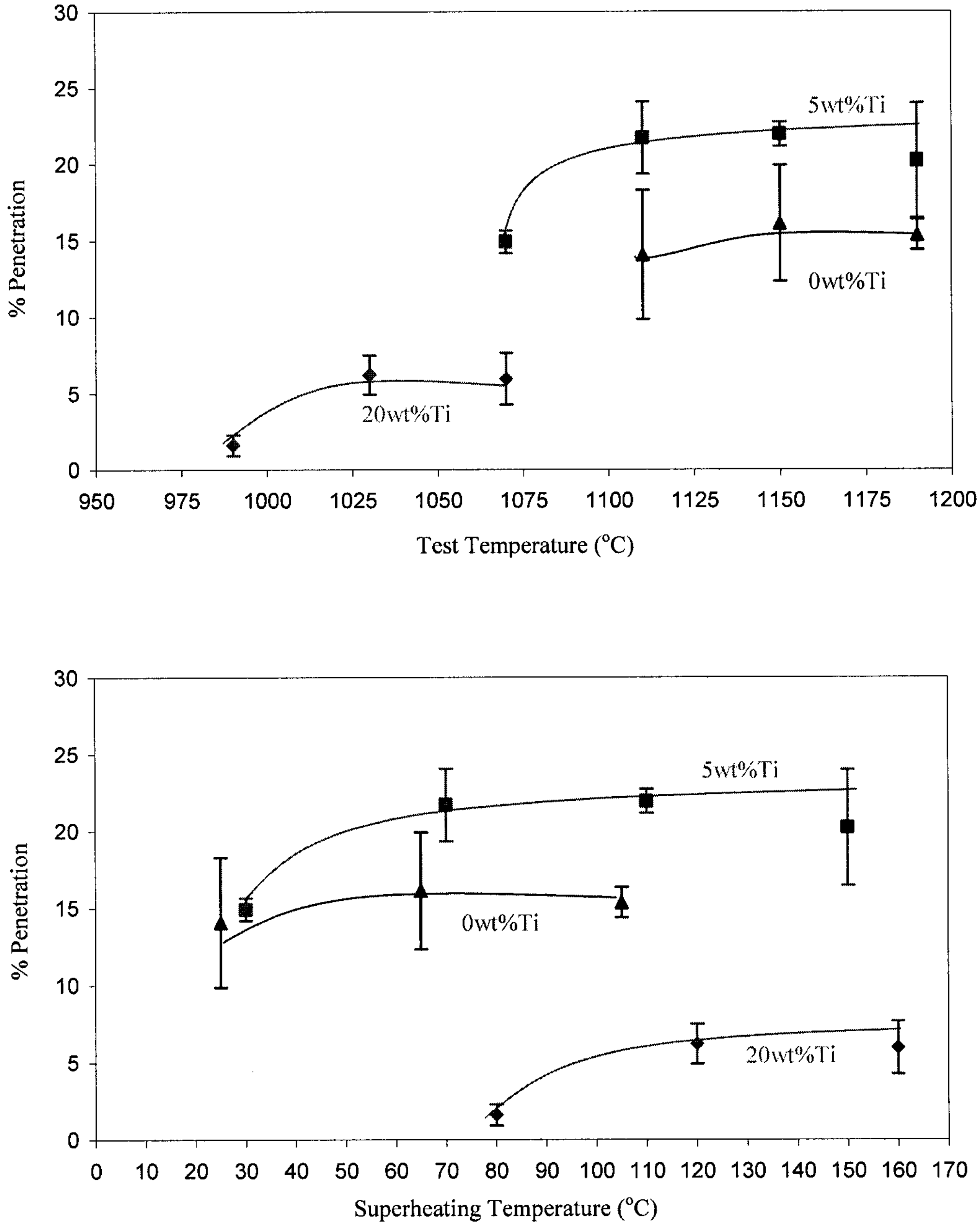

Figure 4.2 - Penetration of molten alloy in the FA-129 intermetallic as a function of (a) test temperature and (b) superheating temperature.

Figure 4.3 presents optical micrographs of the interface between the metal drop and the intermetallic substrate for (a) pure Cu, (b) Cu-5wt%Ti and (c) Cu-20wt%Ti. The main difference between the penetration mode is observed between the alloys containing little or no Ti and the highest Ti content. In the former cases (Fig 4.3(a) (0wt%Ti) and Fig 4.3(b) (5wt%Ti)), the penetration of the molten alloy occurs at the grain boundaries and subsequently, decohesion of the grain structure occurs. In both cases, the original position of the intermetallic grains is easily observed due to the complementary shape of the grains. In the case of high Ti content, the penetration of the molten alloy does not occur as above. Instead the entire intermetallic surface reacts with the molten alloy and a general penetration front is observed. In the case of pure Cu, the intergranular phase and remaining of the molten drop possess a yellow color under the optical microscope. However, for both Ti alloys, a boundary exists between the intergranular phase (yellow color) and the remaining of the drop (characteristic Cu color), suggesting reaction implying Ti. The boundaries are illustrated by the dashed lines on Fig 4.3(b) and (c).

4.3.2 Microstructural Characterization

4.3.2.1 Cu/FA-129 Interactions

Figure 4.4 presents various optical micrographs of unetched interfaces after a soaking time of 1 hour at 1110°C. Figure 4.4(a) illustrates the mechanism of grain boundary decohesion through penetration of molten liquid at grain boundaries. The penetration of liquid into a single grain through diffusion is also observed. The boundary between the affected and unaffected region is represented by the dashed line. Precipitates are observed near the grain/molten metal interface and an unaffected structure is observed at a further distance from the interface (lower left hand side). Figure 4.4(b) shows the interface between a grain which was initially in contact with the molten copper drop. The flat surface is now wavy, suggesting dissolution of the iron aluminide alloy into the copper melt. A fibrous eutectic is also present as well as smaller precipitates in the molten metal substrate. Figure 4.4(c) shows that the same features observed in Figure 4.4(b) are also present in between the grain structure. A rounding effect is observed as the regular sharp grain corners are not observed any longer. This reinforces the hypothesis of grain dissolution in the melt. The second phase precipitates are also clearly observed in each grain.

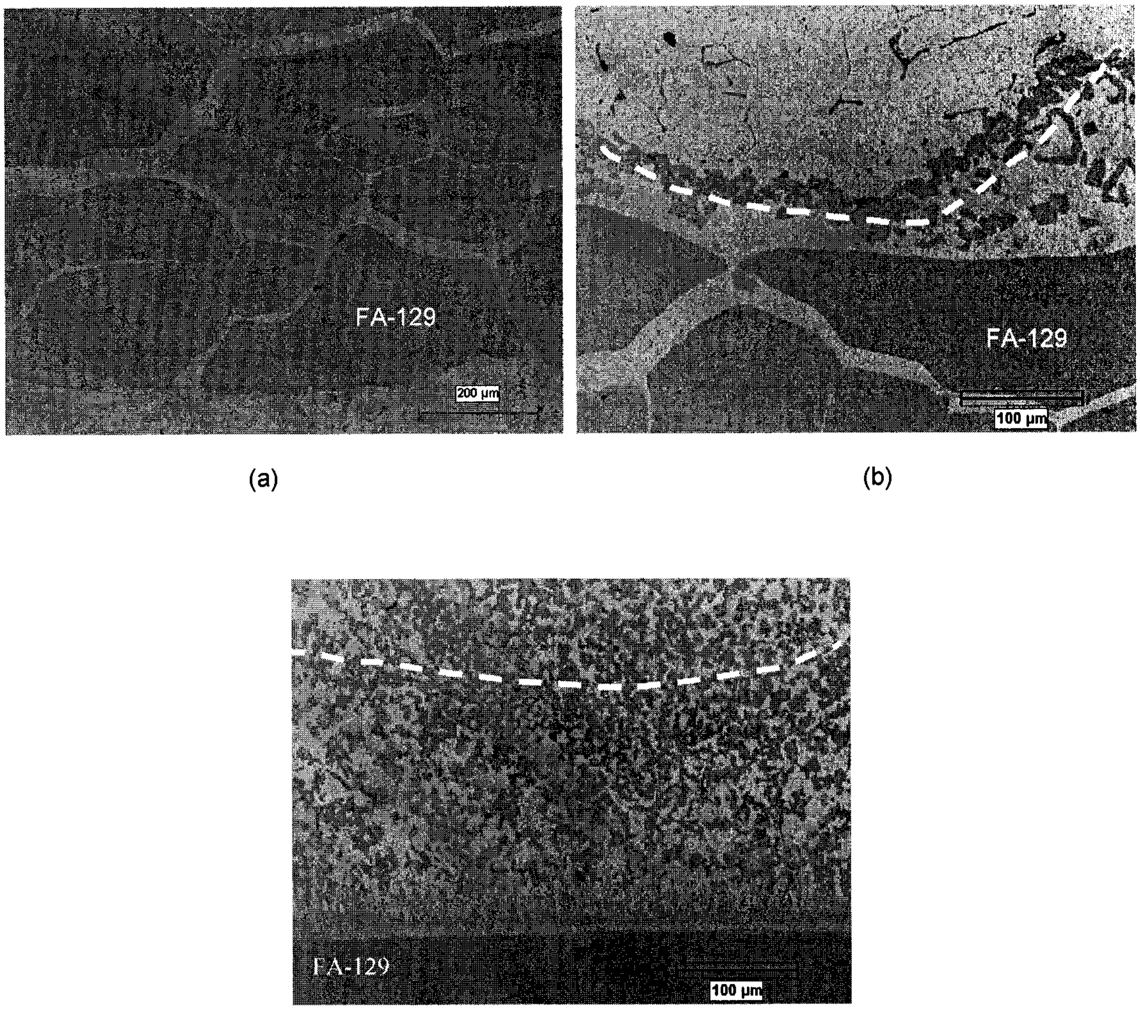

(a) (b)

(c)

Figure 4.3 - Interface between FA-129 with (a) Cu, (b) Cu-5wt%Ti and (c) Cu-20wt%Ti (dotted lines indicates yellow/orange boundary).

Figure 4.5 presents back scattered SEM micrographs of (a) the eutectic structure between grains and (b) the dendrite-like precipitates in the molten drop. The eutectic structure is observed in the Cu-rich zone, in various locations in the drop as well as between grains. Independently of the location, EDS analysis has detected the presence of Al in Cu, with a higher concentration in the eutectic structure. The x-ray analysis also reveals that the penetration observed in the grains is associated with a copper-rich phase with a complementary absence of Fe. The presence of Cu-rich zones was not observed in the vicinity of the grain/liquid interface but only further inside the grains. This was observed for all the grains affected by Cu, independent of the test conditions.

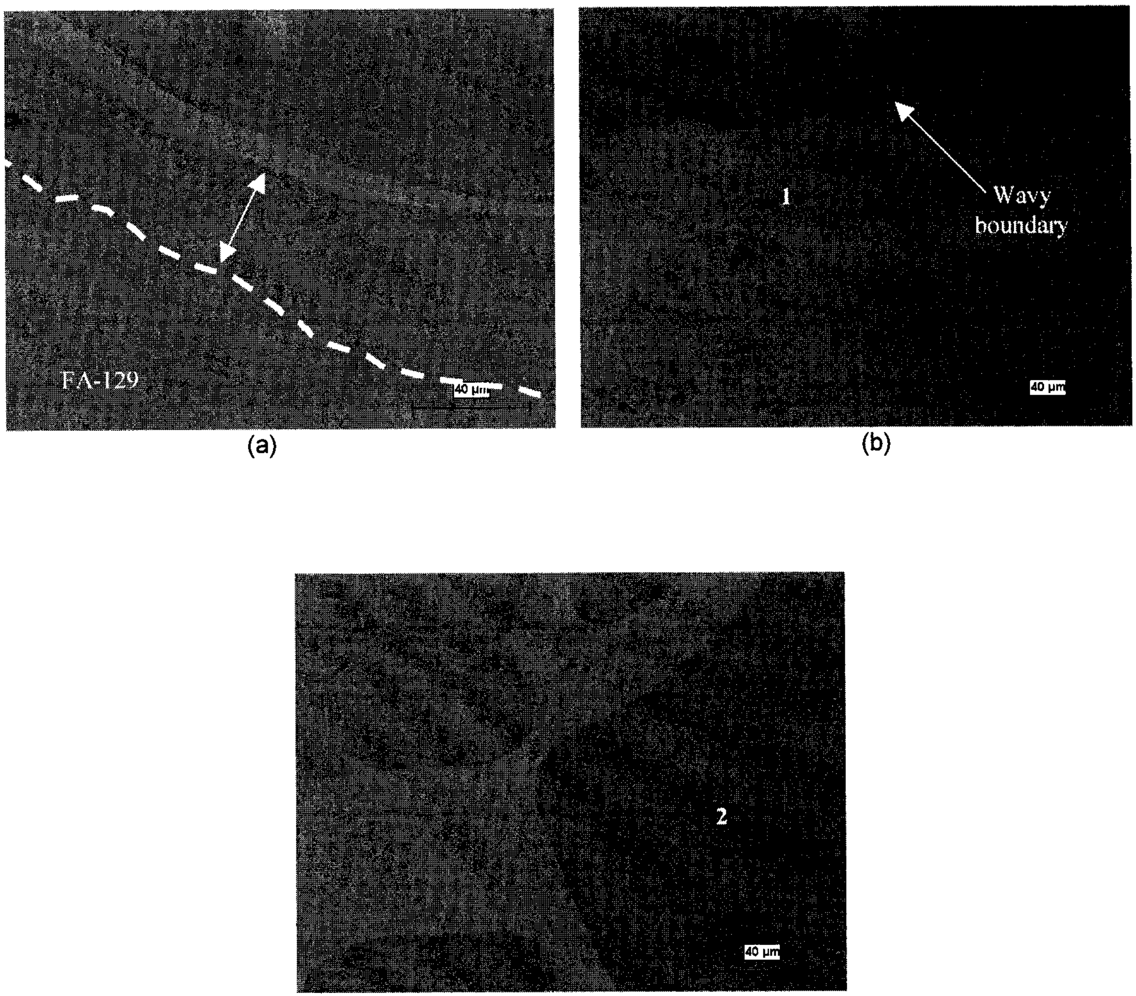

(a)

(b)

(c)

Figure 4.4 - Optical micrographs of (a) penetration of liquid in grain boundary, (b) dissolution of intermetallic grain and (c) rounding of grain edges.

Precipitates with a dendritic shape are also observed in the drop within the penetrated region (Fig. 4.5). This morphology (solidification structure) suggests formation during cooling as the solubility limit of Fe in Cu is reduced during freezing of the liquid. EDS analysis showed that the dendrites are mostly iron-rich containing lower amounts of Al, Cr and Cu.

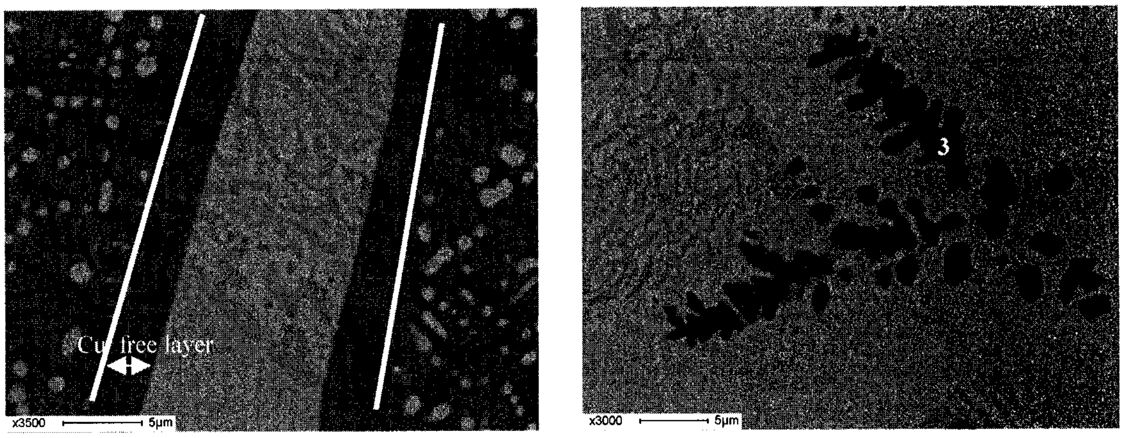

(a) (b)

Figure 4.5 - Back-scattered micrograph of (a) eutectic structure and (b) iron-based precipitate.

Table 4.2 gives the EPMA chemical composition of different features observed in Fig 4.4 and 4.5 as well as the locations of the analyses. The chemical analysis of the as-received FA-129 was included to illustrate the variation in elemental composition from reaction and diffusion. The chemical analysis demonstrates that Al diffuses from the intermetallic to the copper to form an alloy as the initial Al concentration in the copper is nil and that approximately 10wt% is detected in the drop after testing (Table 4.2, spot 1). Figure 4.6 presents the isothermal section of the Al-Cu-Fe ternary phase diagram at 600°C [4.6]. The chemical composition of the Cu-Al alloy analysed falls into the Cu + β two-phase region, explaining the observation of the Cu-rich eutectic structure embedded in a Cu-Al solid solution.

Table 4.2 - EPMA chemical analyses of different locations affected by copper.

Spot	Location in Figure	Chemical Analysis (wt%)				
		Fe	Al	Cr	Nb	Cu
Reference FA-129		76.45	18.04	4.98	1.06	0
1	4.4c	2.23	10.35	0.11	0.09	89.4
2	4.4d	73.18	10.4	4.82	0.99	10.76
3	4.5b	78.05	11.25	3.4	0.78	7.2

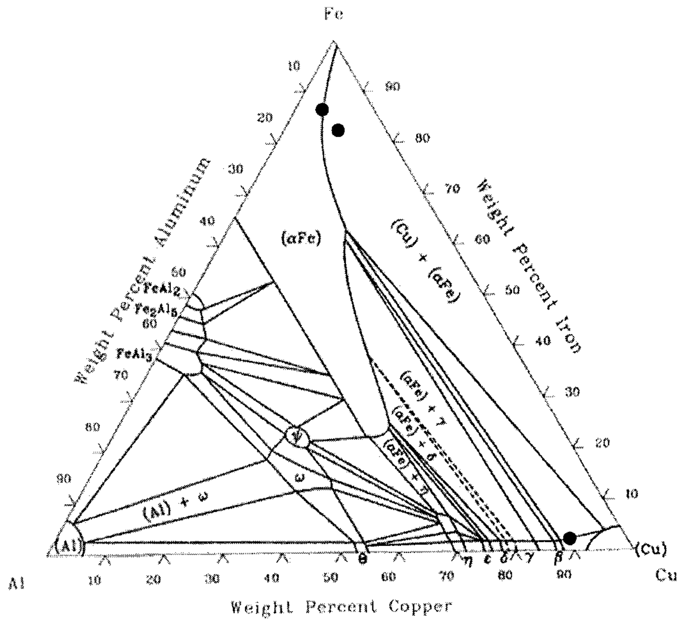

Figure 4.6 - Isothermal section of the Al-Cu-Fe phase diagram at 600°C [4.6].

The chemical composition of the grains affected by copper reached a level of nearly 11wt% in Cu and a reduction of Al content to ≈10wt% in the intermetallic structure (Table 4.2, spot 2). In addition, the Cu concentration measured in the grains levels out at this value, suggesting that the solubility limit has been reached. This reduction demonstrates that the diffusion of Al is complementary to the diffusion of Cu in the FA-129. With the exception of Al and Cu, the remaining elemental composition of an affected grain is similar to its initial value. Reference to the phase diagram indicates the presence of α-Fe + Cu. The Cu phase has a slight solubility for Fe and vice-versa. The α-Fe will retain its b.c.c. structure after cooling as the Al concentration is now too low to form the DO_3 structure of the FA-129.

Comparing the chemical composition of the dendrite-like precipitates to the phase diagram (Table 4.2, spot 3), again indicates α-Fe and Cu phases. The back-scattered micrograph shows clearly that the precipitates are composed of a single phase. This suggests that during cooling from high temperature, a rejection of Cu occurs, explaining the formation of the dendritic microstructure as elemental segregation takes place. In addition, the interaction volume of the electron beam of the EPMA could have generated X-rays from the Cu surrounding the precipitates leading to phase analysis errors. According to the phase diagram, this phase should be α-Fe with little or no Cr, Cu or Al in solid solution.

4.3.2.2 Cu-5wt%Ti/FA-129 Interactions

Similar results to those for Cu were observed for the Cu-5Ti alloy regarding the decohesion of the intermetallic microstructure and the formation of the Cu-rich/Al eutectic. However, the presence of Ti as alloying element modifies the behavior of the molten metal with respect to diffusion and reaction product formation. The Cu-rich/Al eutectic structure was observed only in some locations between the grains. Figure 4.7 presents a back-scattered micrograph of the intergranular space as well as X-ray mapping of the elements for a sample tested at 1070°C for one hour. The addition of Ti as alloying element did not inhibit the penetration of copper into the grains. As in the case of pure Cu, Cu-based islands are found inside the grains and the Cu-free boundary is also present at the edge of the grains. Ti was also found to penetrate into the grains but the zones rich in Ti are depleted in Cu. However, Cu is locally observed at the boundary between the Ti-rich precipitates and the original intermetallic. Another type of precipitate was found in the intergranular region and contains mostly Ti and Fe. These precipitates possess a regular shape, which differentiates them from the non-Ti-containing precipitates observed in the case of pure Cu.

The chemical compositions of the two regions shown in Figure 4.7(a) are presented in Table 4.3. The location corresponding to the analysis is also indicated. The presence of Ti in the grains is associated with a reduction in Al- and Cu-content (Table 4.3, spot 4) compared to the case when no Ti was present. Transferring the composition to the isothermal section of the ternary phase diagram Al-Fe-Ti at 800°C [4.7] (see Figure 4.8), the composition falls into the A2 structure but close to the A2/Fe_2Ti boundary. Obviously, in this case, the effect of copper was not considered as it was previously demonstrated that Cu segregates from the Fe-based grains and rather forms isolated islands. This suggests that the remaining chemical composition of the grain structure is a function of the interaction volume of the probe and that the microstructure can be deduced to be composed of three phases: α-Fe matrix (as the Al level is too low to maintain the intermetallic structure), Fe_2Ti precipitates and Cu islands.

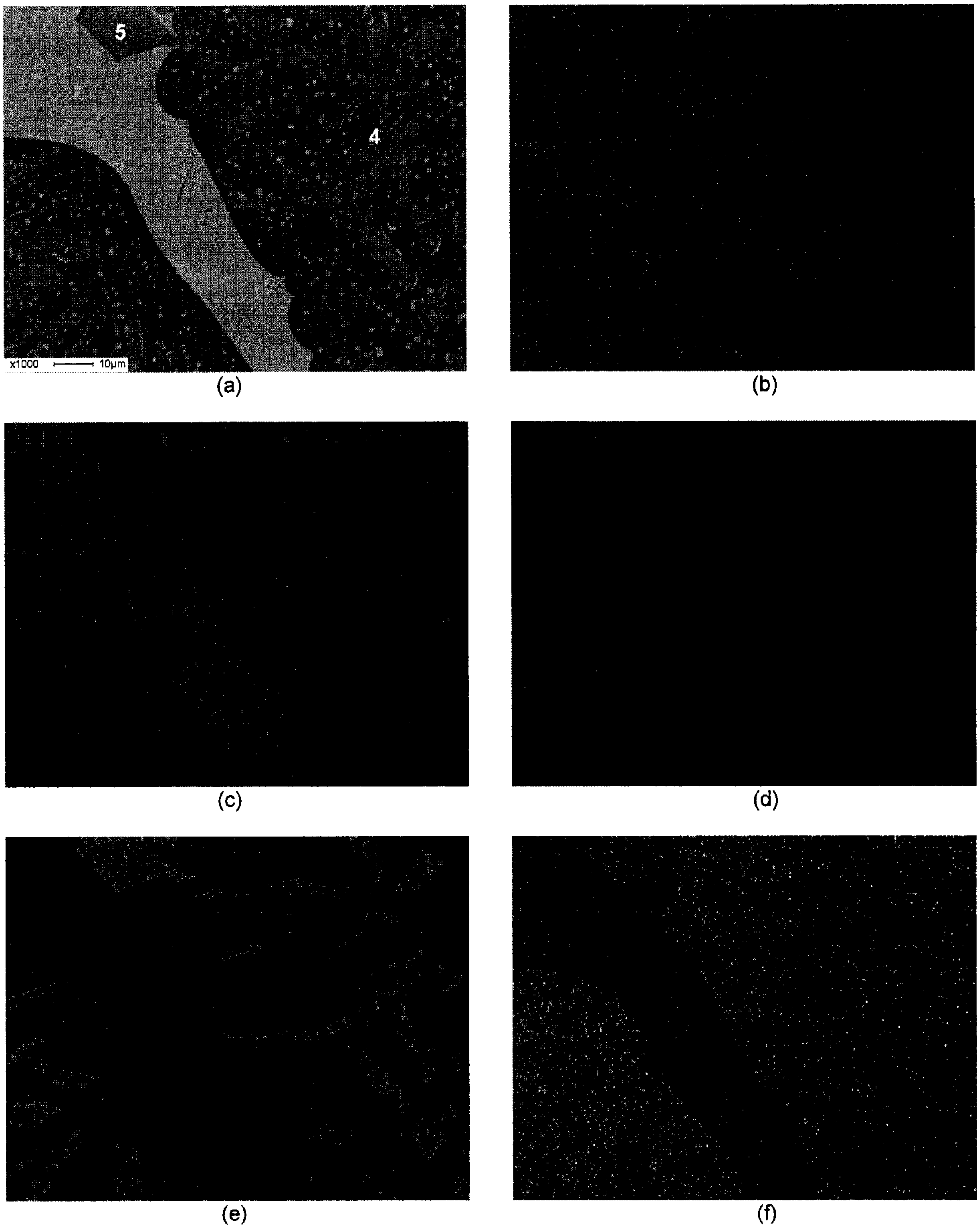

Figure 4.7 - (a) Back-scattered micrograph of an intergranular region and the corresponding X-ray elemental mapping (b) Al, (c) Cu, (d) Fe, (e) Ti and (f) Cr.

Table 4.3 - EPMA chemical analysis of different locations affected by Cu-5wt%Ti alloy.

Spot	Location in Figure	Chemical Analysis (wt%)					
		Fe	Al	Cr	Nb	Cu	Ti
4	4.7a	76.27	7.24	5.33	0.94	7.61	3.44
5	4.7b	62.13	3.28	3.12	11.24	2.30	16.83

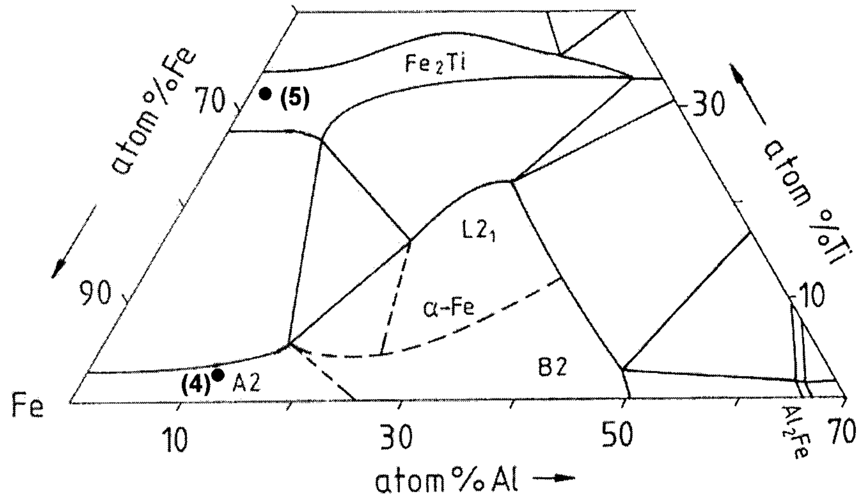

Figure 4.8 - Isothermal section of the Al-Fe-Ti phase diagram at 800°C [4.7].

The chemical composition of the regular shaped-precipitates was also plotted on the phase diagram (Table 4.3, spot 5). However, as a phase diagram containing all the elements is not available in the literature, the effect of niobium was assumed to be similar to Ti for the following reasons: (i) at high temperature, both elements possess the same crystal structure and a perfect solid solution is observed [4.8] and (ii) Schneider et al. [4.9] have found that Nb forms NbC and Laves phases when the chemical composition is rich in C. However, if the C-content is reduced, the presence of NbC should be minimised and only the Laves phase should be observed, possessing a similar composition to our precipitates if Ti and Nb are combined,. The composition falls into the Fe_2Ti phase, which should contain a certain level of Nb and would then be written as $Fe_2(Ti,Nb)$.

Figure 4.9 presents a back-scattered micrograph of the upper part of the drop containing 5wt%Ti. The results show that Al reaches the upper part of the drop but in this case forms a lower Al-content Cu-Al alloy and intermetallic precipitates with Ti, leaving an Al-depleted matrix compared to the case of pure Cu. The consumption of Al by the formation of the intermetallic is responsible for the smaller amount of Cu-Al eutectic phase. The chemical analysis of the precipitates is similar to that obtained for the precipitates observed between the grains (Table 4.3, spot 5) but with lower Nb- and higher Ti-contents, suggesting the formation of $Fe_2(Ti,Nb)$.

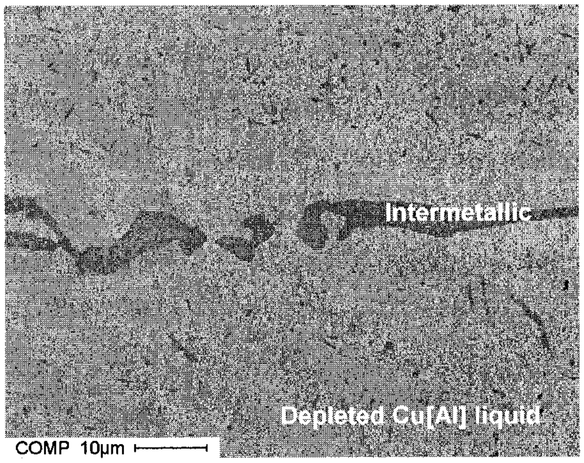

Figure 4.9 - Back-scattered micrograph of the upper part of the drop for Cu-5wt%Ti.

4.3.2.3 Cu-20wt%Ti/FA-129 Interactions

Figure 4.10(a) presents a micrograph close to the interface where dissolution occurs as well as the corresponding elemental x-ray mapping for (b) Ti, (c) Fe and (d) Cu. The x-ray mapping demonstrates that Ti and Fe are the complementary elements to Cu. The dissolution of the intermetallic structure occurs along a general front more than along grain boundaries as in the low Ti-content alloys. The reaction forming the lamellae suggests a dissolution-precipitation process. The chemical composition determined by EPMA of the overall lamellae structure is 37.6wt%Cu, 17.0 wt%Ti, 39.3 wt%Fe, 3.7 wt%Al and 2.3 wt% Cr. With the assumption that copper segregates from the Fe-Ti compound, the Fe and Ti-rich phase observed corresponds to the Fe_2Ti intermetallic, but instead of precipitating in the grains, is formed at the dissolution front due to a higher Ti concentration. The precipitate forms in a lamellar structure near the

Fe_3Al interface but changes to a more spheroidal morphology away from the interface.

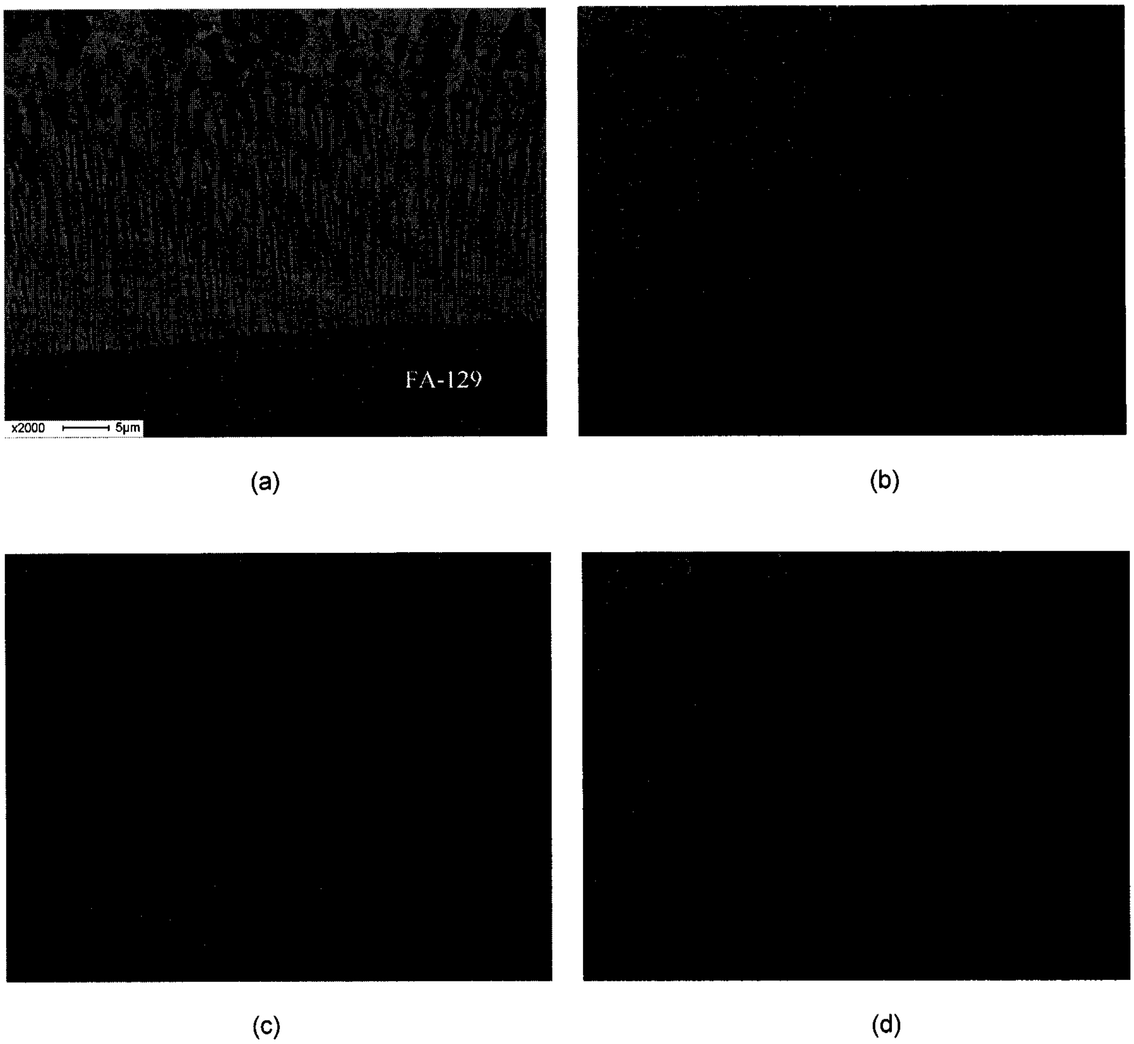

Figure 4.10 (a) Back-scattered micrograph of the interface FA-129/Cu-20wt%Ti and the corresponding X-ray maps for (b) Ti, (c) Fe and (d) Cu.

Figure 4.11 presents a back-scattered micrograph of the structure observed in the section adjacent to the dissolution zone. The lighter precipitates are identified as Fe_2Ti. However, the darker precipitates, smaller in amount, contain a higher concentration of Fe and Cr. No phase diagram is available for this system as many components are present and therefore, no phase identification has been performed. However, the precipitates were only observed in this part of the sample.

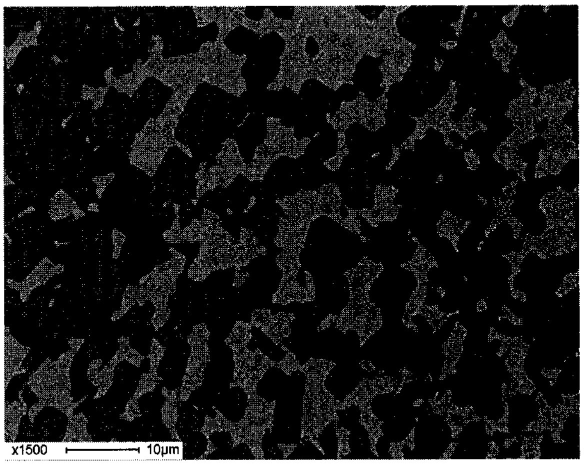

Figure 4.11 - Back-scattered micrograph of the middle section of the Cu-20wt% drop.

Figure 4.12 presents a back-scattered micrograph of the upper part of the drop. EDS analysis shows that Al is no longer present as an alloy with Cu but forms intermetallics with Ti as in the case of the Cu-5wt%Ti alloy. Two different phases are observed, where one is richer in Ti than in Al and the opposite stoichiometry is observed for the other precipitate. As Al is forming compounds with Ti, the alloy surrounding the precipitates is mainly composed of Cu. The X-ray diffraction results have demonstrated the presence of Cu with Cu_4Ti, which should contain a certain Al level. However, several low intensity peaks were observed but no indisputable phase identification could be performed.

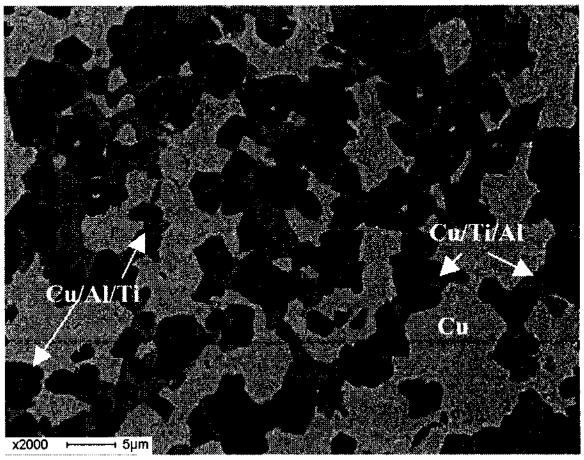

Figure 4.12 - Back-scattered micrograph of the upper part of the Cu-20wt% drop.

4.3.3 Effect of Cu and Ti Penetration on Hardness

The change in the plastic behavior of the Fe_3Al intermetallic with the presence of Cu, evaluated through hardness measurements, is presented in Figure 4.13. The presence of Cu in the grains increases the hardness by 33%, from ≈290HV to ≈400 HV. The different interaction temperatures show similar hardness measurements as the Cu-concentration observed is in the same range for all samples.

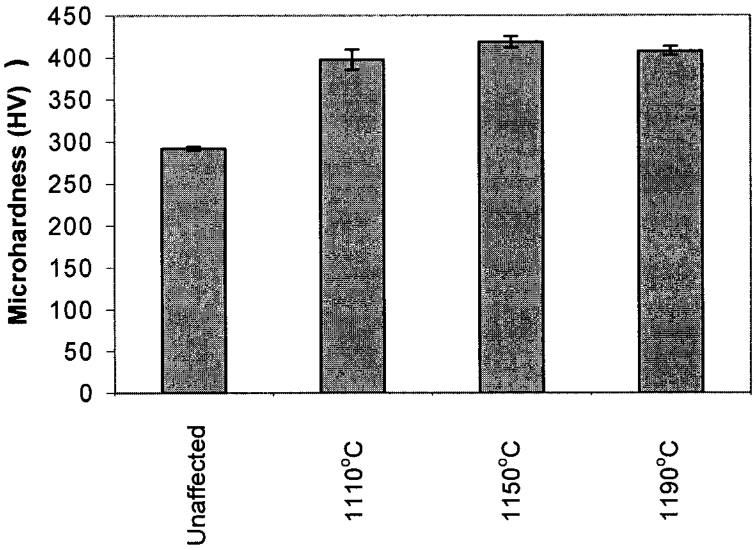

Figure 4.13. Microhardness measurment of as-received FA-129 and Cu-affected FA-129 grains as a function of soaking temperature.

Similar measurements were performed on the grains affected by Cu and Ti but cracks formed from the corners of the Vickers pyramid after indentation. Figure 4.14 shows an optical micrograph of an indentation and the corner-crack from each apex. This result shows that the presence of a small Ti concentration in the intermetallic grain structure leads to a major reduction in plasticity. Due to the formation of these cracks, no reliable hardness measurements were obtained.

4.4 Discussion

Figure 4.15 presents a schematic of the penetration behavior of the molten metal observed on the Fe_3Al substrate. The penetration is influenced by the fluidity, viscosity and surface tension of the melt, its composition and level of super-heating, which increases the driving force for reaction and penetration. In this case, the degree of penetration along the grain boundaries in the intermetallic structure by Cu and Cu-5wt%Ti is relatively similar with respect to the superheat temperature. In both cases, Al was found to diffuse from the intermetallic to the molten Cu, reducing the volume of the unit cell and opening up gaps for molten metal infiltration at grain boundaries. The presence of titanium has been found to increase the penetration and can be related to the fact that the density of the alloy containing Ti is lower than for the pure Cu sample. For the same sample weight, the volume of Cu-5wt%Ti is higher than for pure Cu, leading to a potentially higher volume of metal which can penetrate before a steady state is achieved. In the case of higher Ti-content, a dissolution phenomenon of the intermetallic grains occurs at the molten metal/substrate interface rather than infiltration at the grain boundaries. The dissolution of the interface occurs through the formation of lamellae in the normal direction to the interface. The intermetallic is now dissolving as the interaction is no longer driven by Al diffusion but by Fe_2Ti intermetallic formation.

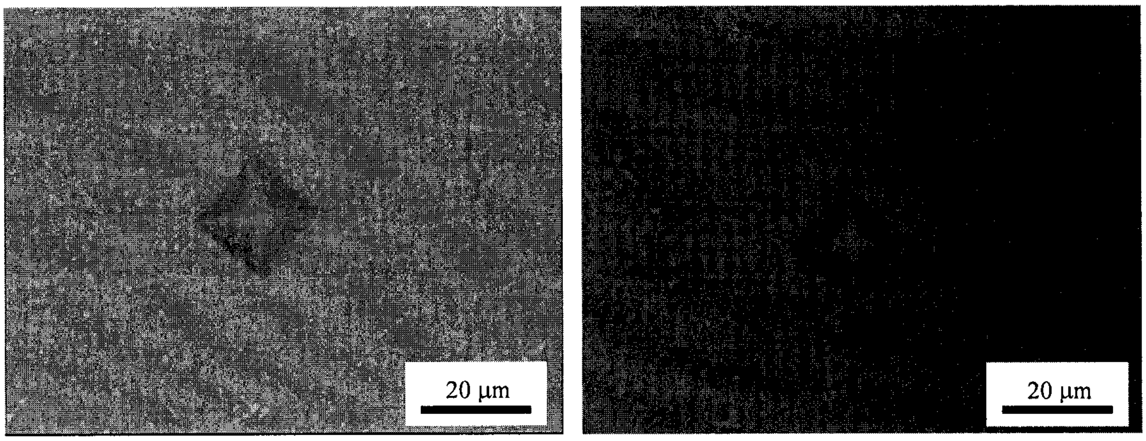

(a) (b)

Figure 4.14 Optical micrograph of hardness indentation on (a) Cu-affected grains and (b) Cu-Ti-affected grains.

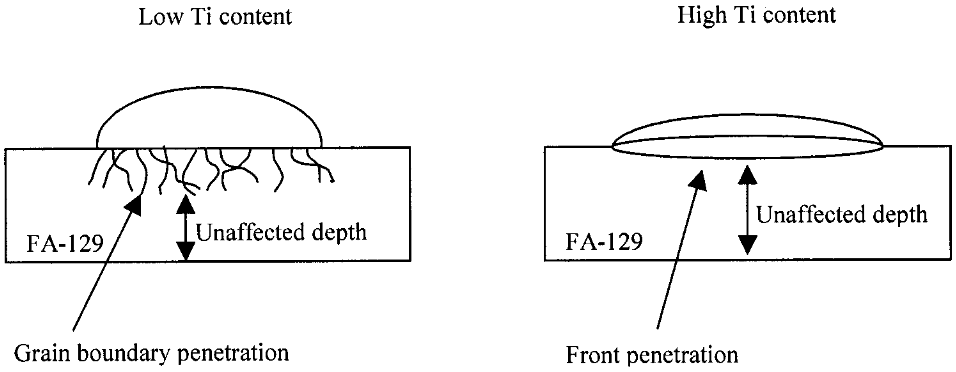

Figure 4.15 - Sketch of penetration behavior of low and high Ti-content alloys.

The dissolution of the FA-129 intermetallic in the melt is a function of the amount of Ti, and different mechanisms are observed. In the case of pure Cu, diffusion of Al from the intermetallic to the melt, forming a Cu-Al alloy, is observed. A simple dissolution of the intermetallic in the liquid melt occurs and is a function of the solubility limit of Fe in the Cu-Al alloy. The morphology of Fe-based precipitates observed in the drop suggests solidification by segregation - reduction of solubility with temperature - of Fe in the Cu-Al alloy. The presence of Al increases the solubility limit of Fe in Cu, leading to a higher degree of dissolution of Fe than for the Fe-Cu system alone [4.6]. The Cu diffusion gradient leads to the penetration of Cu into the intermetallic grains, as at high temperature, the Fe-based grains possess a certain solubility. The presence of 5wt%Ti changes the simple diffusion behavior to a diffusion-reaction phenomenon, as the formation of Fe_2Ti occurs simultaneously in the grains and $Fe_2(Ti,Nb)$ in the region in between the grains. As the thermal stability of the $Fe_2(Ti,Nb)$ intermetallic is higher than the Fe-based precipitates observed in the case of pure Cu, these precipitates should be solid in the molten liquid and remain stable at room temperature. These precipitates also absorb the Nb (dissolved in the Cu melts) as the Nb and Cu are practically insoluble in each other [4.10]. The Fe_2Ti in the Fe_3Al grains is believed to be formed by diffusion of Ti into the grains but as the Ti concentration in the drop is low, no reaction front occurs. The presence of Al in Cu is not observed as clearly as in the case of pure Cu. Al and Ti possess a high affinity for each other and other types of intermetallic are observed. The presence of a high Ti-containing melt initiates the formation of a Fe_2Ti intermetallic rather than Al diffusion itself. The formation of this intermetallic is observed only in the centre of the drop, illustrating its stability at high temperature as no traces of Fe were observed in the upper part of the drop (dissolved atomic Fe diffusion in molten Cu). As the quantity of Ti available in the drop is higher, this reaction becomes more favourable than straight diffusion.

During the heating stage, Al was found to diffuse from the aluminide to the Cu substrate and three different cases are again observed. For pure Cu the diffusion of aluminum reaches equilibrium as the Al content in the grains and in the molten alloy become similar and the diffusion gradient is then reduced. The equilibrium composition is close to the Cu-rich eutectic, explaining the formation of the eutectic structure in the drop or in the grain boundaries. In the presence of small amounts of Ti, an Fe-Ti intermetallic is the predominant compound to form and a slight absorption of Al by these intermetallics occurs. However, the matrix surrounding the precipitates formed in the drop still possesses a small quantity of aluminum. The residual concentration observed in the grains is lower than the concentration observed in the case of pure Cu as the absorption of Al by the Fe-Ti intermetallic maintains a diffusion gradient towards the molten metal/FA-129 interface. In the presence of an excess of Ti, the behavior of the melt changes as two distinct zones are now created. The upper part of the drop remains unaffected by Fe. The aluminum diffusion does not form the Cu-Al solution, such as found in the tests without Ti or low Ti-content but rather forms Cu-Ti-Al and Cu-Al-Ti compounds. The high availability of Ti and high affinity between Cu-Ti and Cu-Al, forming intermetallics with lower free energies of reaction, suggests a de-alloying of the melt and formation of two distinct phases. The respective chemical composition is a function of the solubility limits of the compounds.

The microhardness results demonstrate that the Cu addition associated with a reduction in Al produces a higher UTS as hardness increases but a certain level of plasticity remains as no cracks were created during measurement. This result was expected as disordered alloys with chemical compositions similar to that of the affected grains possess a higher level of plasticity than ordered structures such as Fe_3Al. The brittle behavior of the grains affected by Ti and Cu is believed to be associated with the plastic behaviour of both intermetallic components. All fractures were observed to occur at the interface between the residual α-Fe and the Fe_2Ti.

Boundary adhesion in intermetallic alloys is a major problem and fracture usually follows the easiest path, which in this case is the interface between these phases. Zhu et al. [12] have observed that the addition of Ti decreases the ductility of the intermetallic, which is related to the reduction in grain boundary strength (interface). This correlates with the results obtained as the crack propagation occurred at the boundary with the $Fe_2(Ti,Nb)$ phase.

Overall, the utilisation of nil or low Ti-contents in molten Cu produces major grain decohesion associated with dilution of Al in the melt. In both cases, the FA-129 structure is not retained in the interaction zone as the Al concentration is too low to maintain the DO_3 structure at room temperature. However, the utilisation of a high Ti-content alloy changes the interaction behavior and a limited penetration is observed combined with retention of the ordered DO_3 structure at room temperature. The high Ti content alloy possesses potential for brazing iron aluminide alloys if low temperatures and low brazing times are used.

4.5 References

[4.1] J.A. Horton, C.T. Liu and C.C. Koch, Alloying Effects and microstructure of Iron aluminides,The Metallurgical Society/AIME, 1984, p309-321.

[4.2] S-M Zhu and K. Iwasaki, Materials Science and Engineering, A270, 1999, p170-177.

[4.3] C.H. Sellers, T.A. Hyde, T.K. O'Brien and R.N. Wright, Phase Transformations in Fe_3Al+Ti Alloys, Journal of Physic and Chemistry of Solids, Vol.55, No.6, 1994, p505-515.

[4.4] C. Testani, A.Di Gianfrancesco, O. Tassa and D. Pocci, in S.C. Deevi, P.J. Maziasz, V.K. Sikka, R.W. Cahn (Eds), Proc. Int. Symp. On Nickel and Iron Aluminides: Processing, Properties and Applications, The Materials Information Society, 1997, p213-222.

[4.5] S-M. Zhu, K. Sakamoto, M. Tamura and K. Iwasaki, Effects of Titanium Addition on the Microstructure and Mechanical Behavior of Iron Aluminide Fe_3Al, Materials Transactions, Vol. 42, No. 3, 2001, p484-490.

[4.6] ASM Handbook Vol 3, Phase Diagrams (ASM International, USA) p 3·10.

[4.7] U. Prakash and G. Sauthoff, Structure and Properties of Fe-Al-Ti Intermetallics Alloys, Intermetallics, Vol.9, 2001, p107-112.

[4.8] ASM Handbook Vol 3, Phase Diagrams (ASM International, USA) p 2·307.

[4.9] A. Schneider, L. Falat, G. Sauthoff and G. Frommeyer, Constitution and Microstructures of Fe-Al-M-C (M=Ti, V, Nb, Ta) Alloys with Carbides and Laves Phase, Intermetallics, Vol.11, 2003, p443-450.

[4.10] ASM Handbook Vol 3, Phase Diagrams (ASM International, USA) p 2·172.

Part 3 – Fabrication and Characterization of a High-Ti containing Cu Brazing Alloy

Chapter 5

Fabrication of a Composite Powder and Utilisation as an Active Brazing Alloy

5.1 Introduction

It is well known that ceramic materials are generally poorly or even non-wetted by molten metals. One way to overcome this problem is by using an active liquid metal which will destabilize the covalent, or ionic bonds of the ceramic, producing at the same time, an intermediate reaction layer. This intermediate reaction layer is now wetted by molten metal [5.1, 5.2]. The most popular element added to low melting point metals to produce an active alloy is titanium [1.33]. Ceramic brazing requires such an active brazing alloy (ABA) to overcome the wettability problem. It is possible to find commercially available ABA, like TiCuSil® for example, produced by Wesgo Metals. However as the need for brazing alloys with improved properties is always increasing, new processing techniques and new chemistries are being studied. For the development of new compositions, one easy way of producing synthetic, laboratory scale quantities of ABA is by powder mixing (for the fabrication of paste for example). However with the combination of various elemental powders, homogeneity could become an issue if there is a significant density difference between the different powders used [5.3]. Table 5.1 summarizes the density of different alloying elements commonly used in an active brazing alloy composition. Using fine powders with similar densities usually minimizes this segregation during powder mixing [5.3].

Table 5.1 - Density of elements commonly used in filler metals.

Element	Density (g/cm^3)	Element	Density (g/cm^3)
Copper	8.96	Tin	7.3
Silver	10.5	Indium	7.31
Gold	19.3	Titanium	4.5
Nickel	8.9	Zirconium	6.49

Due to this limitation, powder coating becomes an attractive method for producing alloyed particles. The density and composition of the coated powder can be adjusted by controlling the thickness of the coating deposited at the surface (as a function of the density of the element deposited). Powder mixing is the simplest, most effective technique for different powders having similar properties in terms of density and size to form an exotic chemical composition. In other situations, one of the two main powder-coating techniques, electro- and electroless plating, may prove more suitable [5.4].

The electroplating technique implies the application of an electric current through a chemical bath, in which the powder to be coated is used as the anode and the metallic anions are discharged to form a film. This technique produces coatings on electrically conductive substrates only [5.4, 5.5]. The coating is often non-adherent and must be processed with care. Electroless plating (also referred to as autocatalytic plating) is very different, as no external electrical current source is needed. Also, the final deposit is less porous and re-entrant surfaces can also be coated using this technique. The metallic coating is produced by chemical reduction of a metallic salt by a reducing agent in the plating bath [5.5]. A major advantage over electrolytic plating is that any surface can be plated after an activation treatment (if the surface is not conductive) [5.5]. The most common pre-treatment known is the stannous chloride/palladium reaction. This treatment leaves a conductive metallic deposit on the surface, which is then used as the precipitation site for the metallic reduction [5.6].

In addition to the metallic salt ($CuSO_4$ in the case of electroless Cu), the chemistry of the plating bath is composed of formaldehyde as a reducing agent, EDTA as a metallic salt complexing agent and other additives for bath stabilization [5.5]. The Cu reduction reaction (eq. 5.1) is performed in a basic bath where the pH is adjusted with NaOH.

$$Cu^{2+} + 2HCHO + 4OH^- \rightarrow Cu^0 + H_2 + 2H_2O + 2HCO_2^- \qquad \text{(eq. 5.1)}$$

Due to the nature of the reaction, plating is self-sustaining as long as the chemical bath is not exhausted or decomposed. The chemical compounds present in the plating solution have various effects on the plating deposit morphology, the rate of metallic deposition, and the amount of Cu available for deposition.

5.2 Experimental Procedures

Two different titanium powders were used: one is a dense powder and the other is a more porous powder known as titanium sponge. Both of the Ti powders used were 99% pure with a particle size of –325 mesh. For the purpose of this work, 100 g of powder were cleaned and activated prior to coating because of the surface film of oxide. Figure 5.1(a) presents the particle size distribution of the dense and porous as-received Ti powders. Both powders have similar distributions except that the porous powder size is slightly finer. The d_{50} for the dense and porous powders are 26 and 22μm, respectively. Figure 5.1(b) shows a micrograph of the dense powder prior to the plating process. Many facets are present. The numerous edges play an important role during the plating process as they are more favorable for deposition. The surface area of the powder was measured with the BET technique to compare the possible effect of surface area on the plating rate. The surface areas obtained for the dense and the porous powders were 0.37g/m^2 and 0.42g/m^2, respectively. For a similar difference in surface area, it has been shown that the plating rate is not really influenced by this parameter [5.7]. Figure 5.2 presents the XRD pattern of the Ti powder used.

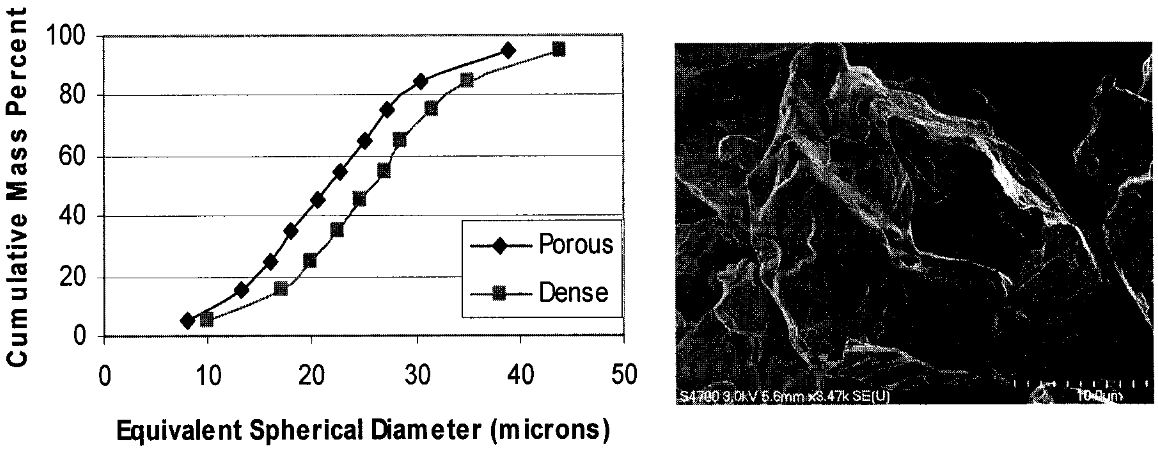

(a)

(b)

Figure 5.1 – (a) Particle size distribution of dense and sponge Ti powders and (b) micrograph of dense Ti particles.

The activation steps are identified as follows: (1) the powder was immersed in acetone in an ultrasonic bath for 15 minutes, (2) sensitization was done in a slightly acidic solution (HCl) containing tin chloride and (3) activation was performed by immersion of the powder in a solution of palladium chloride [5.7].

In order to build up a sufficient Cu coating thickness, iterative depositions were carried out and a new bath solution was used each time. The composition of the electroless chemical bath is presented in Table 5.2. The Cu plating was performed in a 1L bath for 15 g of powder. Tests were carried out at various pH between 12 and 12.8 using NaOH in order to optimize the quality of Cu deposit. Initial times of 5, 10, 20, 40 and 60 minutes were used to study plating kinetics.

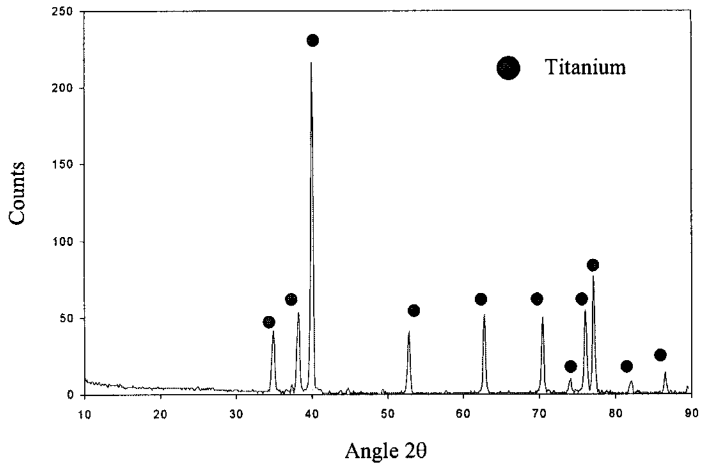

Figure 5.2 – XRD pattern of the starting Ti powder.

Table 5.2 - Chemical composition of electroless copper bath.

Copper (II) sulfate, pentahydrate	$CuSO_4 \bullet 5H_2O$	8g/L
EDTA, disodium salt	$C_{10}H_{14}O_8N_2Na_2 \bullet 2H_2O$	32g/L
2,2'-Dypyridyl	$C_{10}H_8N_2$	20mg/L
Potassium hexacyanoferrate	$K_4Fe(CN)_6 \bullet 3H_2O$	60mg/L
Formaldehyde, 37% solution	HCHO	7ml/L

Between each plating stage, the Cu coating from 5 samples was dissolved in high purity hydrochloric acid. The Cu content was analyzed by atomic absorption spectroscopy (Perkin Elmer 3110) to determine the total weight deposited as a function of the number of coatings. The powder morphology as well as the precipitate quality was evaluated with SEM (Hitachi S-4700 and JEOL-840). The particle size distribution of the coated powder was studied as a function of coating build-up using sedimentation (Sedigraph 5000). The melting behavior of the powder was determined by Differential Scanning Calorimetry (Netzsch DSC 404C) using ultra high purity Ar gas as a protective atmosphere. Niobium sheet was inserted in the Al_2O_3 crucible to avoid contact between the molten active brazing alloy and the ceramic.

The wetting behavior of this binary ABA was evaluated on silicon nitride ceramic substrate using the sessile drop technique in a horizontal tube furnace (see section 3.2). The wetting behavior on silicon nitride was tested at 950°C. The sample was inserted in the center of the hot zone prior to heating in order to simulate the heating stage in a brazing process. Photographs were taken at different intervals to evaluate the change of wetting angle with time. Prior to heating, a vacuum of $5X10^{-5}$ Torr was applied followed by back filling with ultra high purity argon which was used as a static atmosphere during the experiment.

5.3 Results

5.3.1 Powder Pre-treatment

Before describing the results obtained during the fabrication of this composite powder, it is important to emphasize the significance of the pretreatment. Due to the high affinity of Ti for oxygen, Ti powder possesses a non-conductive natural oxide surface film. As the electroless plating technique requires a conductive surface to allow exchange of surface electrons, the process was not successful in the case of powders without pre-treatment. To obtain a conductive surface, a stannous chloride/palladium chloride treatment was applied on the powder. Due to small quantity of deposit, XRD analysis did not show any trace of palladium residing on the powder after the pre-treatment.

5.3.2 Effect of pH on Deposition

The electroless deposition of Cu is usually performed in basic solutions when using a sulfate bath. The pH of the chemical bath was varied from 12 to 12.8. This small pH difference produces a major change in the deposit morphology. The electroless process is a technique in which atomic Cu is precipitated from a salt bath solution. Figure 5.3 presents high magnification micrographs of nanocrystalline Cu deposits produced at pH 12 and 12.8. At the lower pH (pH=12), the Cu initially precipitates on the highest Pd concentration regions, which are usually found at the grain boundaries. Furthermore, the deposit forms rounded clusters, like cauliflower which grow in the three dimensions to finally produce a completely covered surface. This growth is illustrated in Figure 5.3(a). At higher pH (pH=12.8), the growth of the Cu precipitates does not occur in the form of spherical precipitates but are more flake-like, which grow in 2 dimensions, by elongation of the facets.

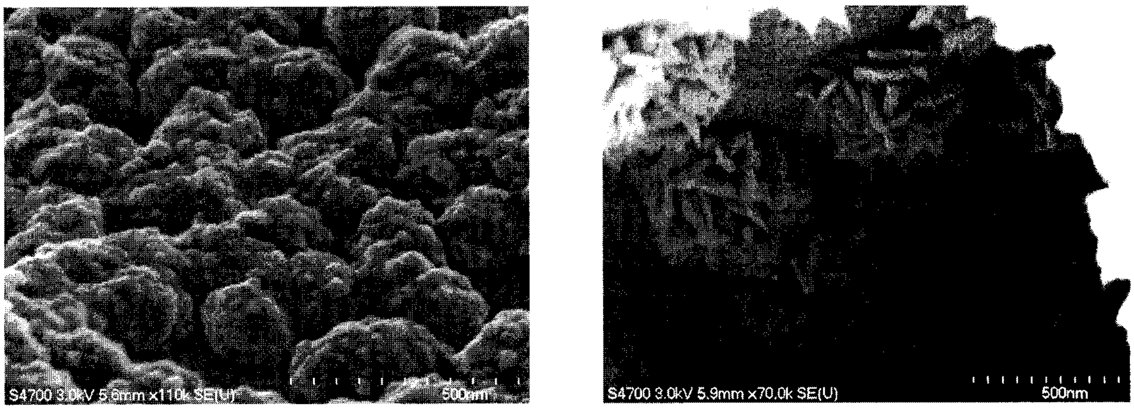

(a) (b)

Figure 5.3 - Micrograph of Cu deposit formed at pH 12 (a) and pH 12.8 (b).

5.3.3 Effect of Starting Powder Morphology

Interesting results concerning the initial powder morphology were also found. The possibility of plating into cavities is a characteristic of the electroless plating process. Figures 5.4 (a and b) shows, respectively, a low magnification micrograph of a porous Ti particle, and a micrograph taken looking into a pore. Cu deposition is observed in the pores of the sponge Ti.

5.3.4 Plating Iterations

The total Cu content in the chemical bath used is 2.08g/L for a concentration of 8g/L of $CuSO_4 \bullet H_2O$. In the first instance, the effect of copper plating as a function of time was evaluated to determine the optimum plating time. Table 5.3 shows the wt% Cu deposited after 5, 10, 20, 40 and 60 minutes. In the case of deposition performed at pH 12, the bath was never exhausted as the final color was slightly blue. However, at pH 12.8, the bath was mostly exhausted after 40 minutes, as the solution turned clear. From these results, a plating time of 60 minutes for the deposition at pH 12 and 40 minutes for pH 12.8 were chosen. Both plating times were kept constant for each iteration of the process.

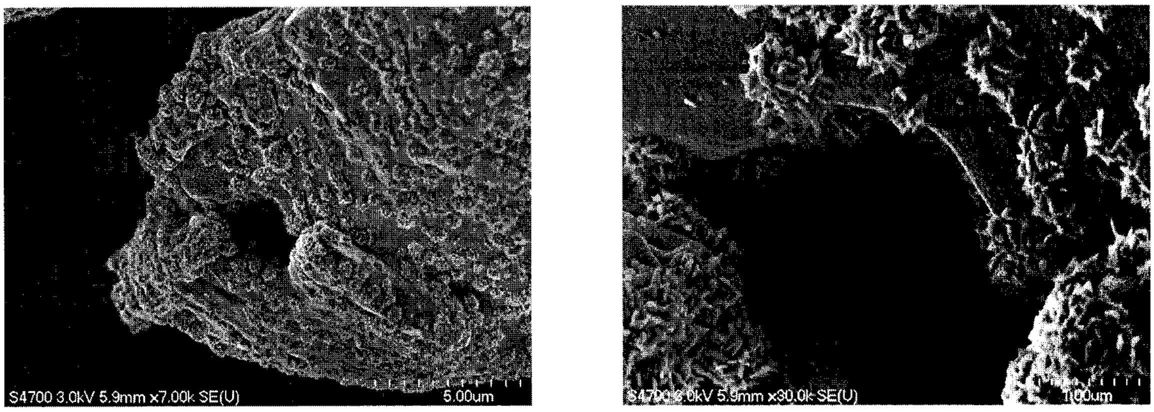

(a) (b)

Figure 5.4 - Copper deposition inside a pore of sponge Ti particle.

Table 5.3 - Amount of Cu plated as a function of time.

	Conventional Ti Powder (wt%)		Sponge Ti Powder (wt%)	
Deposition time (min)	Average	Std Dev	Average	Std Dev
5	5.66	0.25	9.64	1.19
10	6.16	0.17	10.36	1.51
20	6.83	0.25	10.91	0.97
40	-	-	11.36	0.85
60	8.90	0.59	11.48	0.53

Figure 5.5 presents the curves of the net concentration of copper on both types of powder as a function of the number of deposition steps. To obtain the target composition of 75wt%Cu, 19 iterations were necessary when a bath solution of pH 12 was used. The higher bath pH required 15 iterations, which is one

advantage of increasing the pH. In both cases, the curves follow a parabolic trend: the curves exhibit this shape as the wt% is calculated as the ratio of the weight of Cu deposited to the total weight of the powder. In both cases, the curves are tending to a plateau with increasing iterations. This result shows the difficulty and limitation of producing filler alloy containing a low quantity of active element (starting powder) using this process alone (i.e. not using a Ti and Cu powder mixture for example).

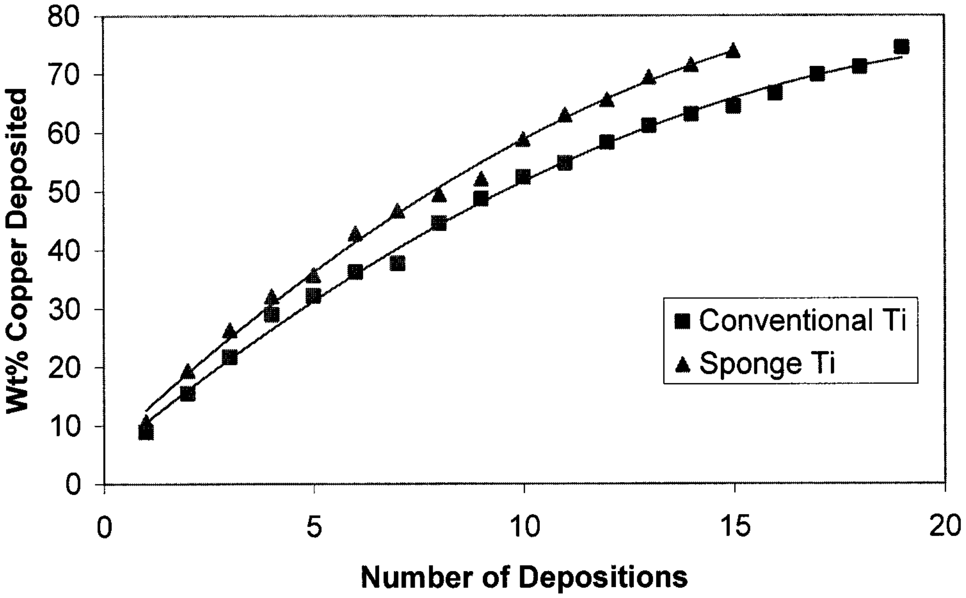

Figure 5.5 - Amount of Cu deposited as a function of plating iterations.

5.3.5 Particle size distribution

The particle size was evaluated in order to observe if the Cu coating build-up is uniform and to observe the possibility of agglomeration. The particle size distributions of the initial powder and the final composite powder coated at pH 12 are presented in Figure 5.6. The starting Ti powder is representative of a Gaussian-type of distribution. The mode of the distribution is between 20-30 microns. The particle size distribution of the final ABA is shifted to the right, indicating that the particle size has increased. As opposed to the starting powder, the distribution no longer follows a Gaussian-type of distribution. The mode of the distribution cannot be as easily determined, as the difference in quantity of powder having a final size between 40 and 65 microns is not very significant. The right hand side of the particle size distribution curve of the final ABA powder, which does not decline as sharply as for a typical distribution, indicates the presence of a higher percentage of larger particles, compared to a Gaussian distribution. The larger particles are created by powder agglomeration. Figure 5.7 presents a back-scattered electron image of a cross-section of such an agglomerate. The outside, lighter layer, is the Cu coating and the darker core is the original Ti particle. The diameter of the agglomerate at its maximum is approx. 90 microns, which corresponds to the larger values indicated in the particle size distribution.

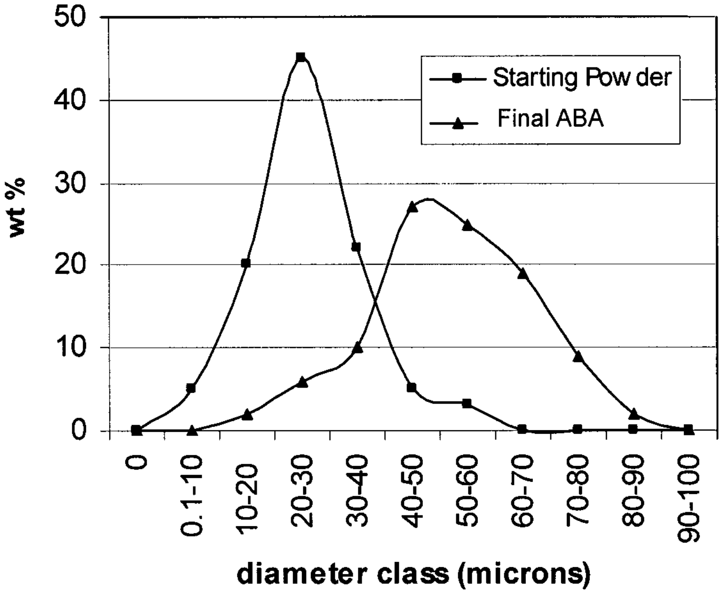

Figure 5.6 – Particle size distribution of composite powder plated at pH 12.

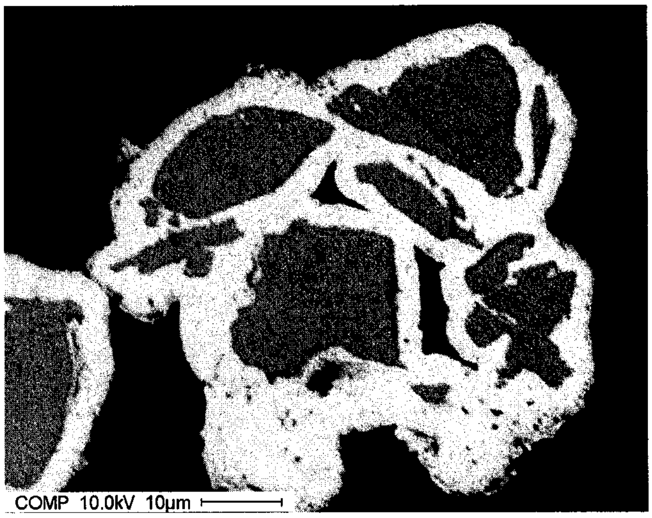

Figure 5.7 - Back-scattered micrograph of agglomerate of particles coated at pH 12.

Figure 5.8 presents the variation in particle size distribution of the porous powder plated at pH 12.8 as a function of time during the initial plating (a) and as a function of iteration step (b). After 5 minutes of plating, the composite powder contains 9.6wt%Cu whilst after 60 minutes it contains 11.5wt%. In Figure 8(a), the distribution curve moves to the right due to the growth of the powder diameter with quantity of Cu deposited but the shape remains similar. This illustrates that no agglomeration occurs. Figure 5.8(b) presents the initial distribution of the powder as well as its evolution after 4 and 15 platings. After 4 platings, considerable agglomeration of the particles can be observed, as the slope on the right side of the curve is not as sharp compared to the initial powder. The final particle size has been affected by severe agglomeration, where the mode of the distribution is 210 microns, as opposed to ≈ 45 microns for the powder plated at pH 12.

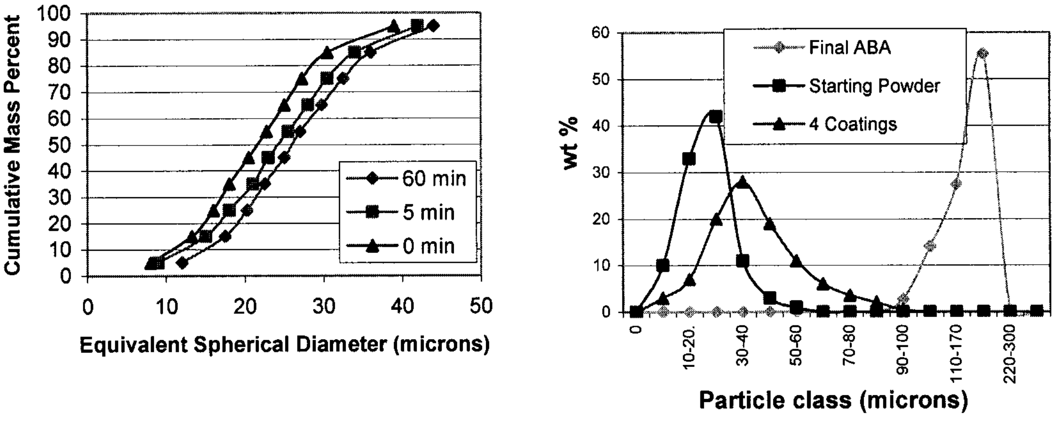

(a) (b)

Figure 5.8 - Effect of time (a) and iteration step (b) on particle size distribution.

Low voltage FE-SEM coupled with EDS was used to characterize the surface of the copper deposit. FE-SEM possesses the advantage over conventional scanning electron microscope of the possibility of having sufficient beam current for EDS analysis at low voltage, which reduces substantially the interaction volume. Figure 5.9 presents the EDS analysis of both powder surfaces. The surface concentration of oxygen is higher for deposits formed at higher pH, which is related to a secondary-reaction during the deposition.

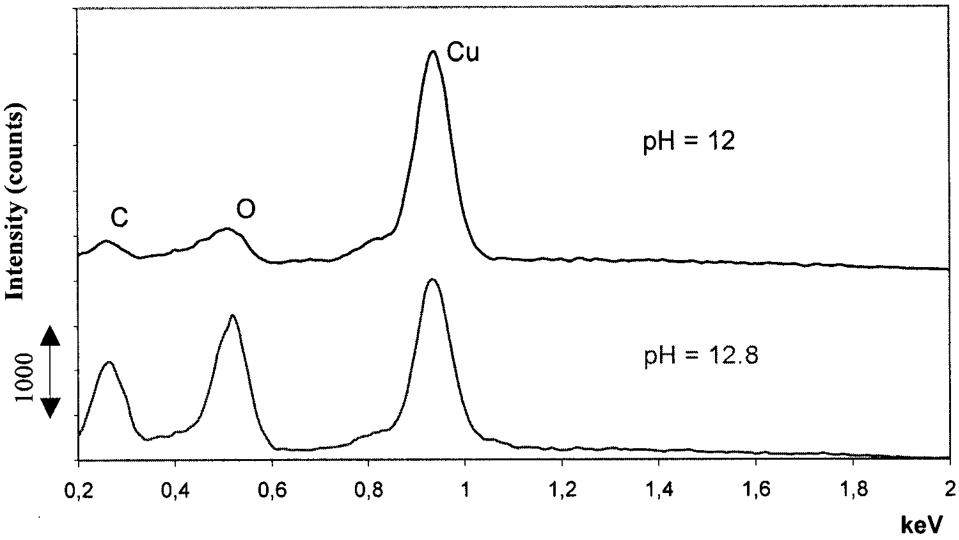

Figure 5.9 – EDS analysis of both composite powder surfaces.

5.3.6 Evaluation of Wetting Behavior on Ceramic Substrates

Ceramic brazing is achieved by furnace brazing in which the pre-applied filler metal follows the same heating cycle as the parts to be joined. A pill of coated powder was inserted in a wetting furnace at room temperature and was heated at 10°C/min. Pictures were taken at different time intervals to correlate the behavior of a macro sample of powder to the results obtained with the DSC (see Chapter 6). Figure 5.10(a) is a picture of the pill at 910°C. The initial geometric form of the pill is still constant, which mean that complete melting has not yet occurred. However, Figure 5.10(b) shows a picture of the same pill two minutes later, at 932°C. A complete drop has formed on the surface of the ceramic substrate. It can also be observed that the alloy instantaneously wets the ceramic substrate. Sufficient diffusion between the Cu and Ti combined with the furnace temperature gradient has produced total melting of the pill by 932°C.

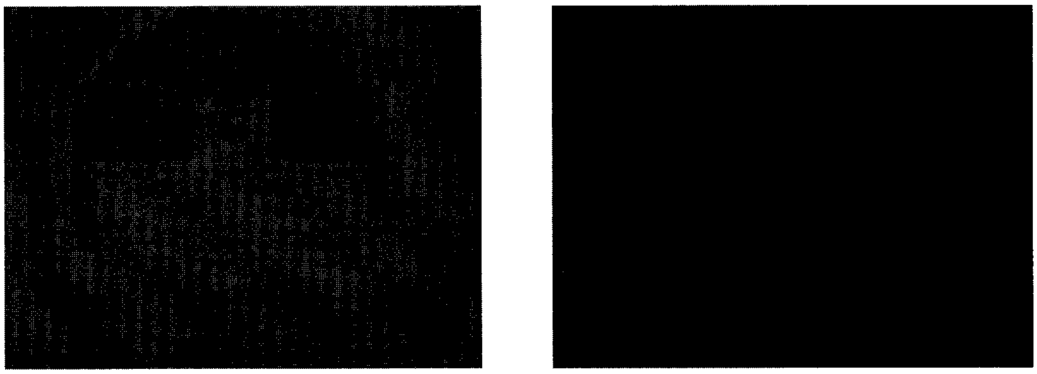

(a) (b)

Figure 5.10 - In situ photographs of composite powder pill on Si_3N_4 substrate at (a) 910°C and (b) 932°C.

The wetting behavior of the composite powder was tested on Si_3N_4 ceramic substrate in order to compare the contact angle values obtained with values published in the literature. The temperatures used were only slightly higher than the melting point of the composite powder in order to see the rate of decrease of contact angle as it is well known that a molten metal with high active element content, typically possesses a very low contact angle and the equilibrium contact angle is reached rapidly [1.26]. The wetting curve is presented in Figure 5.11. The equilibrium contact angle for this system is around 18° for samples tested at 950°C. For higher temperatures, the contact angle decreases rapidly and becomes nearly zero, at which point it becomes very hard to measure. This behavior was expected, as the titanium concentration is very high. Filler metal with a lower active element concentration has also been found to have a very low equilibrium contact angle. The wetting angle also decreases rapidly with the concentration of active element. The results obtained for the Si_3N_4/75Cu-25Ti system are also similar to those in the literature [5.8].

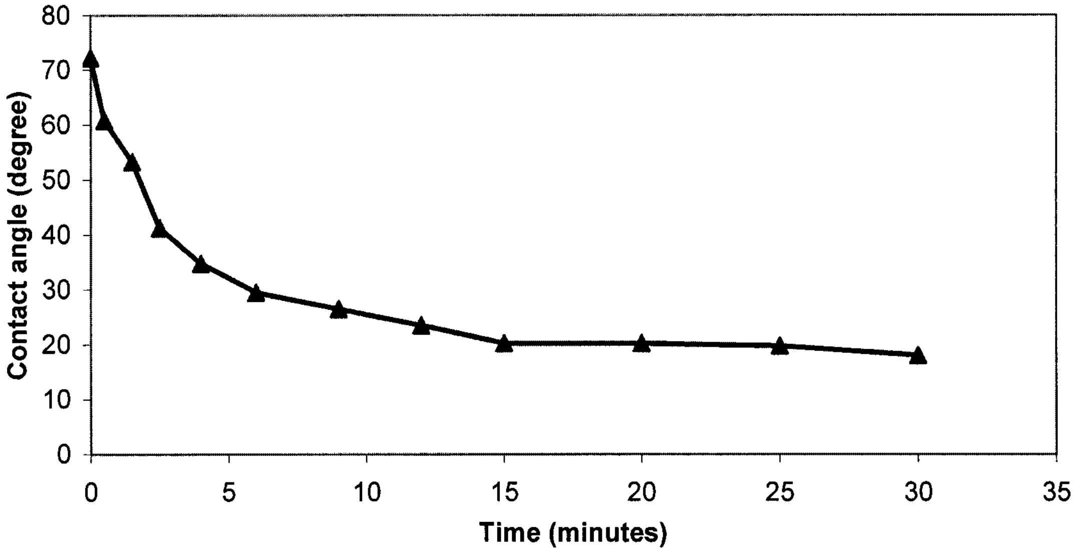

Figure 5.11 - Contact angle of molten composite powder on Si_3N_4 ceramic (950°C).

5.4 Discussion

In order to produce a composite powder, the electroless plating process has certain advantages compared to powder mixing and the electrolytic process. The metal is deposited uniformly on all surfaces exposed to the solution, not only on the outer surface. Hence an advantage is that the amount of Cu plated may be increased when the powder contains open porosity. The mass of a Ti sponge particle is lower than that of a conventional Ti particle of similar particle size due to the presence of pores. Thus the final density of the plated powder will be higher for the sponge powder for a similar particle size. This can produce a powder with a similar target composition but smaller in size compared to using conventional Ti powder as the core.

The morphology of the Cu deposit has been shown to be greatly influenced by the chemical composition of the plating bath; from rounded nucleation sites (three-dimensional growth) to faceted (two-dimensional growth). Previous researchers have reported that the composition of the chemical bath may change the growth mode. Weber et al [5.9] mentioned that a cyanide-containing bath produces a strong decrease in the nucleation rate, which changes the growth mode from 3D (for the additive-free bath) to 2D growth mode. Clearly developed crystals with sharp edges and flat crystal faces were observed during plating at pH 13. They also observed that additive-free baths produce rounded Cu precipitates under pH 13. The presence of precipitates possessing flat crystal faces has to be associated with the additive which is used to avoid self-decomposition, enhance the deposition rate and improve the deposit properties. In the present work, the deposit morphology obtained for plating performed at pH of 12.8 is similar to that produced by Weber, since faceted crystals were formed. However, by lowering the pH of the bath, the Cu deposit grows in three dimensions, in a similar fashion to that reportedly obtained under additive-free or accelerator-containing baths. Cu deposition under this lower pH shows a lower deposition rate, as formaldehyde oxidation occurs only at pH values above 12 and this oxidation rate is a function of pH. When the pH reaches lower values, the plating process stops altogether.

Lowering the bath pH mainly diminished the plating process efficiency. The amount of Cu plated during each deposition is around 70% of the total available Cu when plating at low pH for a plating time of 60 minutes. The efficiency increases up to almost 100% in the case of pH 12.8 for a duration of only 40 minutes. Because the autocatalytic process decreases the pH of the bath during plating, and the formaldehyde oxidation occurs only at or above pH 12 (formaldehyde is required for deposition), the overall reaction is strongly governed by the pH of the initial bath. At lower pH, the plating reaction is stopped earlier as the reducing agent becomes inactive.

The agglomeration of the composite powder at higher pH becomes a real problem because the larger agglomerate size will create a thicker layer of filler in between the pieces to be joined. Normally, agglomeration is associated with a zeta potential of zero. This observation is valid for non-conductive materials, which exhibits a double layer formation in polar solutions. In the present case, the surface is composed of metal (electrical conductors) and no agglomeration should occur, as observed at lower pH. Agglomeration was observed during plating at higher pH, suggesting that the agglomeration problem is strongly correlated to the bath composition. Shukla et al. [5.6] have shown that CuO can be formed at the surface of the metallic Cu deposit during electroless deposition. The Cu color was not observed on the powder when plated at pH of 12.8 but a color more characteristic of copper oxide was obtained. Low voltage EDS analysis demonstrated a large variation in surface oxygen, suggesting higher oxidation of the deposit for higher processing pH. In addition to the non-metallic surface, complexes can be created which promote the formation of Van der Waals bonding, which can be strong enough to attract and link particles together by precipitation at the junctions. This precipitation is observed by the presence of voids formed at the triple junction between particles.

The wetting behavior, as well as the interfacial reaction products, are similar to results obtained by previous researchers. Meier et al. have shown that the alloying method, for the case of a copper-titanium binary active alloy, does not influence the final contact angle but changes the spreading kinetics to obtain equilibrium [5.10]. In the present work, the complete melting point of the brazing metal has been raised from around 890°C in the case of pre-alloyed powder to around 930°C in the case of our composite powder. The alloy formation involves the formation of several intermetallic layers, which possess different melting characteristics. In the case of coated powder, melting of intermediate layers occurs before the complete melting of individual particulates.

Ceramic brazing with an active brazing alloy possessing a high active element content has shown that the thickness of the reaction layer increases much more rapidly than for brazing alloys with lower active element content [1.26]. Brazing operations are conventionally performed at temperatures only slightly higher than the melting point of the filler metal, to avoid superheating of the filler metal. Raising the "melting" temperature, compared to pre-alloyed powder, reduces the extent of the reaction between the ceramic and the filler metal during the heating stage, which in turn reduces the growth of the reaction layer and better interfacial control can be achieved. The fabrication of a mixture of the composite powder and pure metal powder can also increase the melting temperature of the filler metal and change the composition. Furthermore, isothermal solidification may occur, depending on the system resulting in an improvement of the control of the reaction rate between the liquid and the ceramic substrate.

5.5 References

[5.1] W. Tillmann, E. Lugscheider, R. Xu and J.E. Indacochea, Kinetic and Microstructural Aspects of the Reaction Layer at Ceramic/Metal Braze Joints, Journal of Materials Science, Vol. 31, 1996, p445-452.

[5.2] W.B. Hanson, K.I. Ironside and J.A. Fernie, Active Metal Brazing of Zirconia, Acta Materialia, Vol.48, 2000, p4673-4676.

[5.3] F. Thümmler and R. Oberacker, An Introduction to Powder Metallurgy, The Institute of Materials, 1993, 332p.

[5.4] G.S. Upadhyaya, Powder Metallurgy Technology, Cambridge International Science Publishing, 1997, 158p.

[5.5] C.A. Deckert, ASM Handbook Vol. 5; Surface Engineering, ASM International, Ohio, USA, 1994, p311-322.

[5.6] S. Shukla, S. Seal, J. Akesson, R. Oder, R. Carter and Z. Rahman, Study of Mechanism of Electroless Copper Coating of Fly-ash Cenosphere Particles, Applied Surface Science, Vol.181, 2001, p35-50.

[5.7] C.A. Leon, Infiltration Processing of Metal Matrix Composites using Coated Ceramic Particulate, Ph.D. Thesis, McGill University, 2001.

[5.8] C.J. Weber, H.W. Pickering and K.G. Weil, Scanning Tunneling Microscopy Investigations during Electroless Copper Deposition, Microstructural Science Volume 25, 1997, p373-377.

[5.9] M. Naka and I. Okamoto, Wetting of Silicon Nitride by Copper-Titanium or Copper-zirconium alloys, Trans. JWRI, Vol.14, No.1, 1985, p29-34.

[5.10] A. Meier, P.R. Chidambaram and G.R. Edwards, Generation of Isothermal Spreading Data and Interfacial Energy Data for Liquid Reactive Metals on Ceramic Substrates: the Copper-Titanium/Alumina system, Journal of Materials Science, Vol. 30, 1995, p3791-3798.

Chapter 6

Assessment of Melting Behavior of Cu-Coated Ti Powders using Thermal Analysis

6.1 Introduction

The mixture of pure Cu and Ti is an important example of a reactive braze used to join ceramics. The previous chapter has demonstrated a new route for producing a Ti-rich-Cu active brazing alloy. The Cu-Ti phase diagram is presented in Figure 6.1 [6.1]. This system exhibits major insolubility between Cu and Ti and the formation of many intermetallics. It also shows several melting temperatures depending on the composition. For a composite powder containing such a diffusion couple, every intermediate compound should be formed through diffusion at the core-coating interface.

In addition, nitrogen strongly reacts with active elements such as Ti ($2Ti+N_2=2TiN$ $\Delta G^\circ = -160500 + 44.4T$ cal [6.2]). This reaction is strongly exothermic in the solid state but is even more exothermic in the presence of a Ti-containing liquid [6.2]. The coefficient of activity of Ti in Cu is approximated to 1 [1.33]. This high activity makes titanium attractive as the active element in copper-based filler metals for joining ceramics.

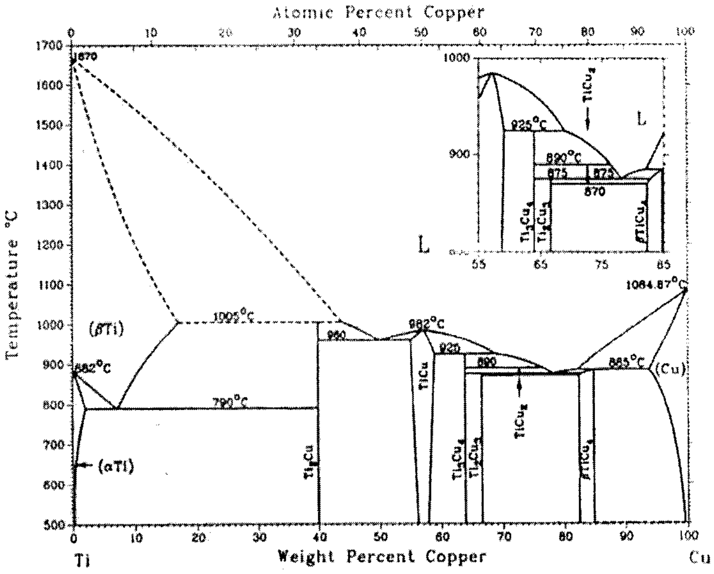

Figure 6.1 - Cu-Ti phase diagram [6.1].

The objective of this chapter was to establish the melting sequence of a Cu-coated Ti active metal braze powder (ABA). The level of interdiffusion between Cu and Ti, which influences the melting behavior, is proportional to the heat treatment performed on the powder. The diffusion couple should exhibit large amounts of diffusion as there is a significant quantity of the two initial elements and diffusion equilibrium should not be reached until liquid is formed. The results obtained in argon were compared to results obtained in nitrogen to identify the appearance of the first liquid. A mixture of ABA and Si_3N_4 powders was used to characterise the appearance of the liquid at the surface of the composite powder.

6.2 Experimental Procedure

6.2.1 DSC measurements

Recent work has established techniques for quantifying the melting behavior of mixed powders during transient liquid phase sintering using Differential Scanning

Calorimetry (DSC) [6.3, 6.4]. These techniques were adapted in the current study to investigate the ABA material. The thermal analysis of the various samples was performed in a DSC (Netzsch, DSC 404C). The powders were heated up to 1090°C at heating rates of 10 and 40°C/min under either ultra high-purity argon or ultra high-purity nitrogen atmospheres. Some interrupted tests were also performed to study the microstructures of the samples at various steps of the cycle. The interrupted tests were cooled at a rate of 40°C/min (maximum cooling rate) to preserve, as much as possible the high temperature structure. All tests were carried out in an alumina crucible, however as copper-titanium alloys are commonly used as brazing alloys for ceramics, the powders were first placed inside a folded Nb foil inserted in the crucible, to prevent contact between the molten alloy and the ceramic crucible.

6.2.2 X-Ray Diffraction

The phase analysis was conducted in a Phillips PW1710 CuKα diffractometer (wavelength of 1.54Å). The scans were performed between 25 and 80° (for 2θ) as the most intense peaks for each composition are present in this interval.

6.2.3 Metallography

The solid and semi-melted powders were hot-mounted in conductive phenolic powder and then polished down to a 0.05 microns finish. The microstructural evaluation and the EDS analysis were conducted on an SEM (JEOL-840) coupled with an EDAX detector and a FE-SEM (Hitachi S-4700) coupled with an X-ray detector (Oxford).

6.3 Results

6.3.1 DSC of Pure Cu

Since the Cu-Ti powder required a Nb foil liner in the DSC crucible, it was important to determine the foil's influence on the DSC signal. This was done by running a high purity Cu standard in the DSC using the Nb foil. Figure 6.2

illustrates the results of this experiment. The first peak is the melting endotherm of pure Cu which had a recorded onset temperature of 1087°C (i.e. very close to the theoretical value of 1085°C). Therefore, the presence of the Nb foil does not prevent accurate measurement of the temperature at which thermal events occur. The enthalpy of this melting peak was recorded as 104.4J/g, which is lower than the 180 to 195 J/g normally recorded for the Cu standard in the absence of the Nb foil. This lower enthalpy reading is likely due to additional thermal resistance created by the Nb foil. The final Cu droplet obtained in the Nb sheeting possesses the typical non-wetting geometry indicating no reaction.

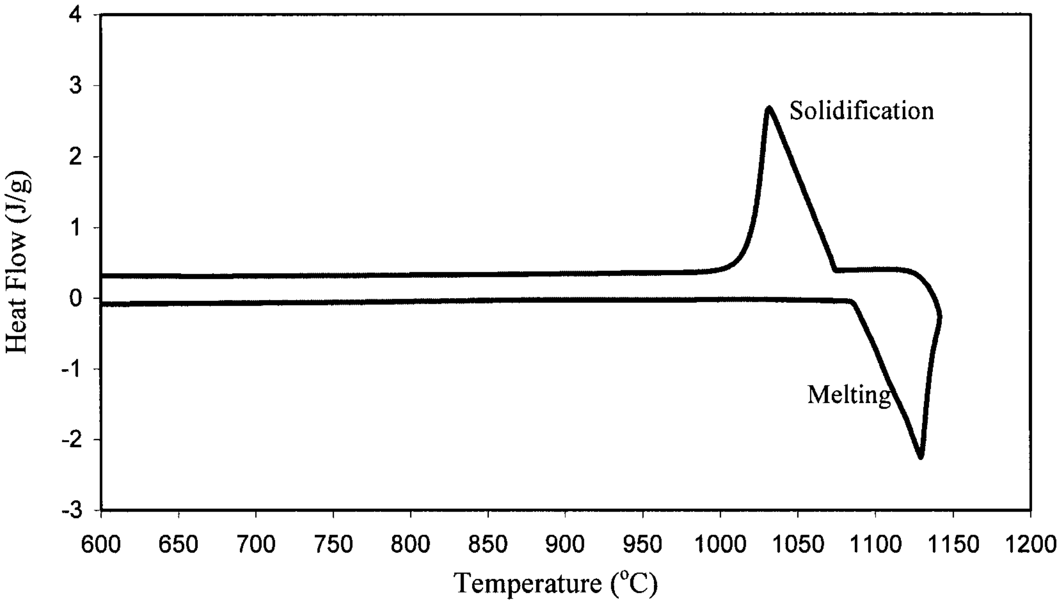

Figure 6.2 - DSC curve for pure copper sample in a Nb-lined Al_2O_3 crucible.

6.3.2 Melting of Cu-rich Powder in Ar

Interdiffusion is critical in the determination of the melting behavior of such a coated powder as the various intermetallics, formed through diffusion, possess different melting characteristics. The extent of diffusion in turn should depend on heating rate. The effect of the heating rate on the heat flow is presented in Figure 6.3 for powders heated at 10 and 40°C/min, respectively. A small exothermic peak with an onset temperature of 870°C appears in the 40°C/min sample. A somewhat broader peak also occurs in the 10°C/min sample at lower temperature (ie ≈ 855°C). Following the exotherm, it can be observed that the onset of a large melting peak occurs in both samples at 886°C and 885°C, respectively. However, the end point of melting is different. For the powder heated at 10°C/min, complete melting has occurred at 900°C as opposed to 915°C for the powder heated at 40°C/min. The experiments performed at 40°C/min show a single melting event as opposed to the powder heated at 10°C/min where melting in two stages is observed. The onset temperature for this second melting event has been determined as 890°C, which looks like a reaction involving $TiCu_2 \rightarrow Ti_3Cu_4$ and initiation of melting of Ti_3Cu_4. The latent heats of fusion determined for the powder heated at 40°C/min and 10°C/min are 113 and 103 J/g, respectively, and are similar to that obtained for pure Cu.

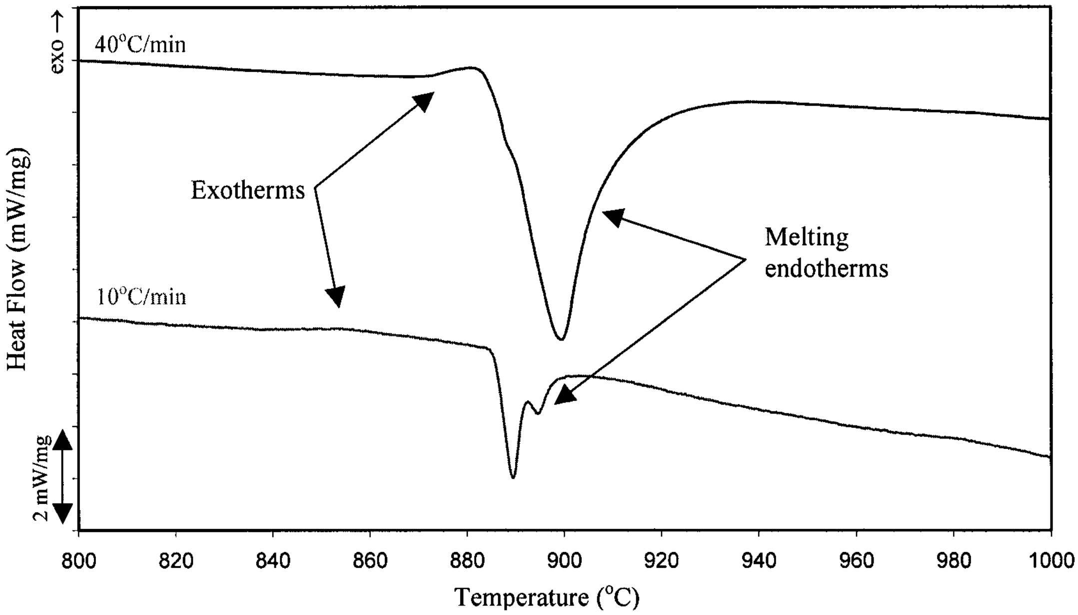

Figure 6.3 - DSC traces of powder heated at 10 and 40°C/min respectively.

In order to clarify the extent of diffusion and its role in multi-step melting, microstructural evaluation of the powder after heating within the DSC to just before and after melting was performed (ie 880°C and 889°C respectively). Figure 6.4 presents the XRD pattern of (a) the initial powder and (b) the powder heated to 880°C for a heating rate of 40 and 10°C/min. The spectrum of the initial powder shows the two initial components; Cu and Ti. After the heat treatment, Cu, $TiCu_4$, Ti_3Cu_4, Ti_2Cu_3 phases were detected but their relative intensity changes as a function of heat treatment. With respect to the X-ray diffraction patterns, a smaller quantity of Cu was observed for a sample heated slowly, whereas the quantity of Cu_4Ti phase has increased.

Figure 6.5 presents a BSE micrograph of a cross-section of a powder heated at (a) 40°C/min and (b) 10°C/min, respectively, to 880°C and the corresponding compositional line scan. Five different layers are clearly observed for the sample heated at 40°C/min (labelled). The boundaries of the different layers are not as clear for the sample heated at 10°C/min.

Figure 6.6(a) presents a BSE micrograph of a cross-section of a powder heated to 890°C with a heating rate of 40°C/min. The heat treatment performed on this powder corresponds to obtaining a partially molten state (Figure 6.3). Two intermetallic layers remain at the interface between the Ti powder and the partially molten Cu-Ti alloy. The morphology of the microstructure adjacent to the Ti-rich core shows a very well defined dissolution zone (wave region) suggesting contact with molten liquid. A Cu layer still surrounds the composite powder and remains solid at this temperature: complete melting will occur either by reaching the melting point of this outer layer of the shell or through dissolution by the core. Figure 6.6(b) presents a similar Ti particulate being partially dissolved into the molten liquid. The 10°C/min heating ramp was stopped at 890°C. The rounding effect of the Ti particle is also observed. The absence of the previous intermetallics with graded Ti-content is now detected. The melting of the low temperature intermetallics contributed to a partial homogenisation of the middle of the Cu-core powder. A similar observation was obtained for the powders heated at 40°C/min.

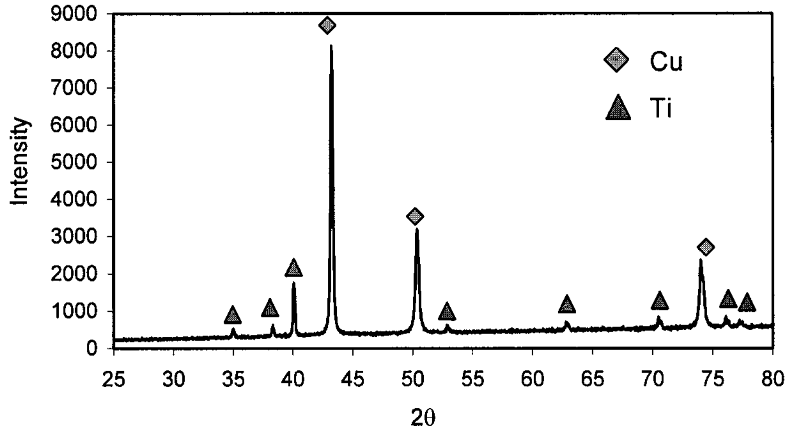

(a)

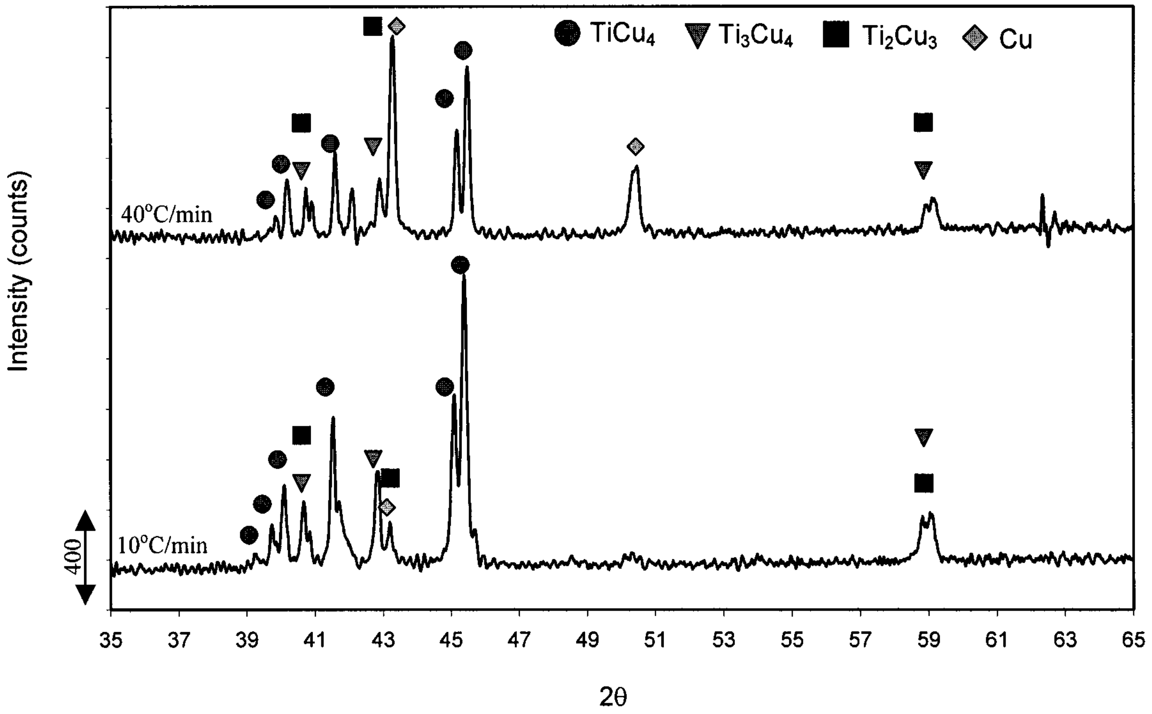

(b)

Figure 6.4 - XRD pattern of (a) starting powder and (b) powder heated to 880°C at 40°C/min and 10°C/min.

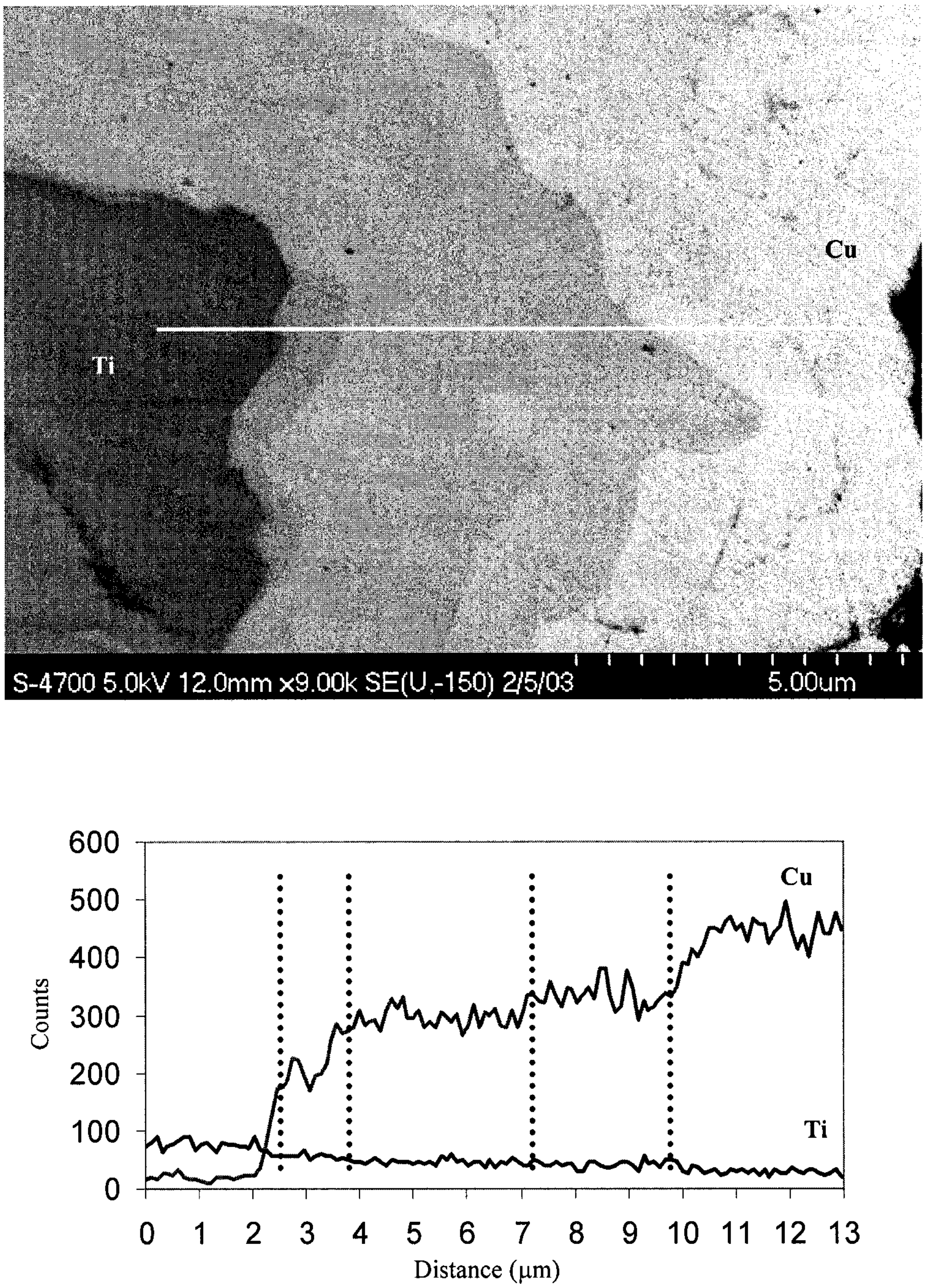
Cu
Ti
S-4700 5.0kV 12.0mm x9.00k SE(U,-150) 2/5/03
5.00um
Counts
600
500
400
300
200
100
0
0 1 2 3 4 5 6 7 8 9 10 11 12 13
Distance (μm)
Cu
Ti

(a)

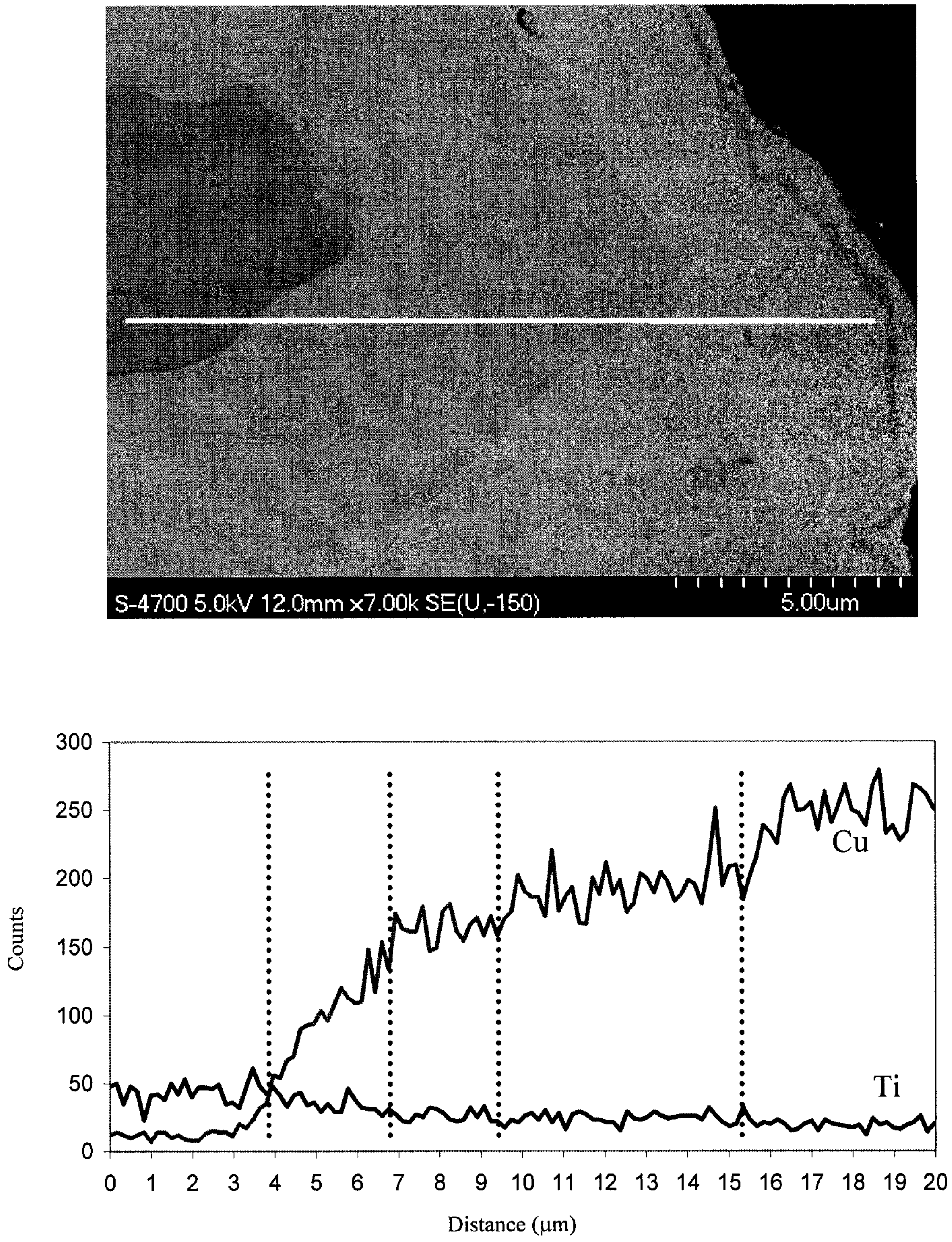

(b)

Figure 6.5 - Back-scattered electron micrograph and corresponding EDS line scan of the composite powder heated to 880°C at (a) 40°C/min and (b) 10°C/min.

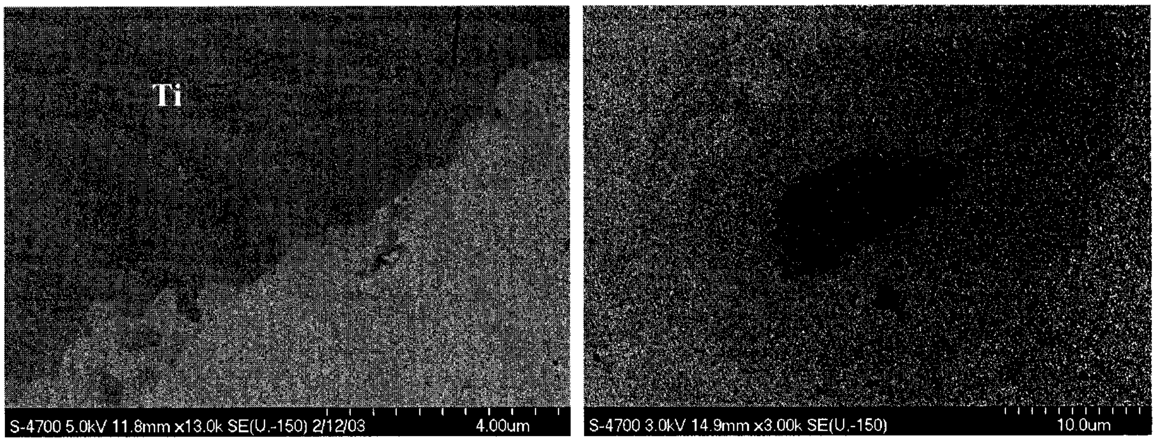

(a) (b)

Figure 6.6 - Back scattered electron micrograph of composite powder heated to 890°C at (a) 40°C/min and (b) 10°C/min.

6.3.3 Melting of Cu-rich Powder in N_2

Figure 6.7 presents the DSC trace of the powder heated in nitrogen. The heating curve shows a major exothermic peak starting at 885°C and no endothermic peaks corresponding to the powder melting. Another exothermic peak is present at 956°C. The cooling curve presents an exothermic peak at 1023°C, corresponding to the solidification of a Cu-Ti alloy. The intense exothermic peak overlaps the melting peak that was observed for the powder heated in Ar. The peak occurs simultaneously with the formation of the first liquid. As melting starts inside the core of the composite powder, the exothermic peak suggests that nitrogen is diffusing through the Cu shell and reacting with the molten active alloy. Such alloys are known to have intense reactions with oxygen or nitrogen. The exothermic peak also suggests that no reaction between the core of the powder and the protective gas occurs until a liquid is formed.

Figure 6.8 presents the XRD spectrum of the powder melted in N_2. The main peaks observed are TiN and Cu. Three other peaks corresponding to the niobium foil are observed as the diffraction of the powder was performed on the bottom part of the protective envelope.

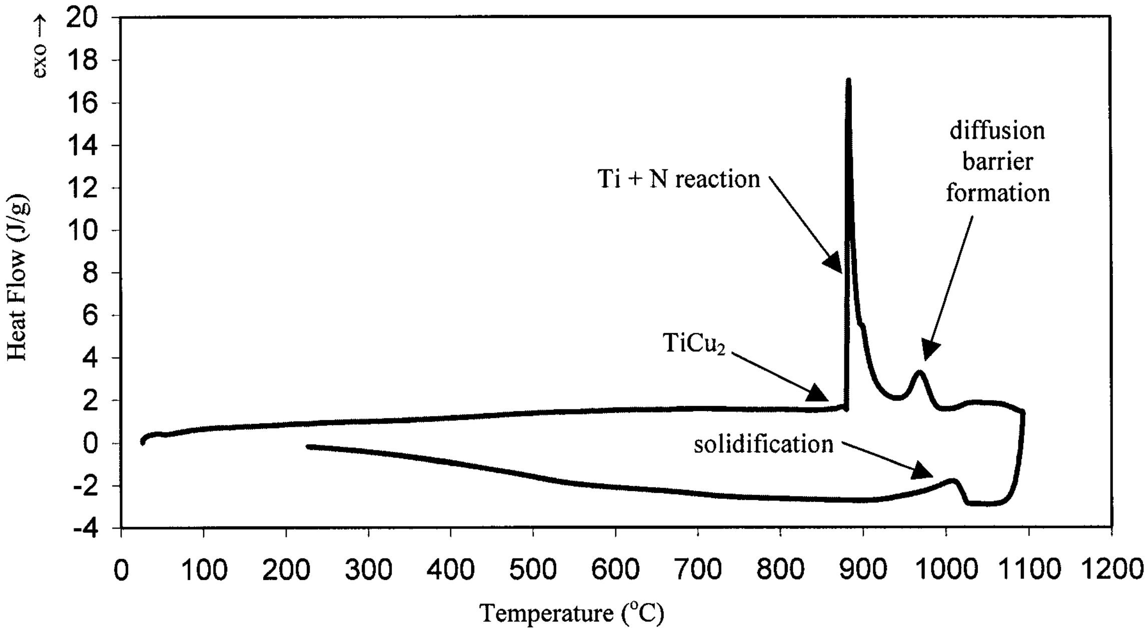

Figure 6.7 - DSC trace of powder heated in N_2.

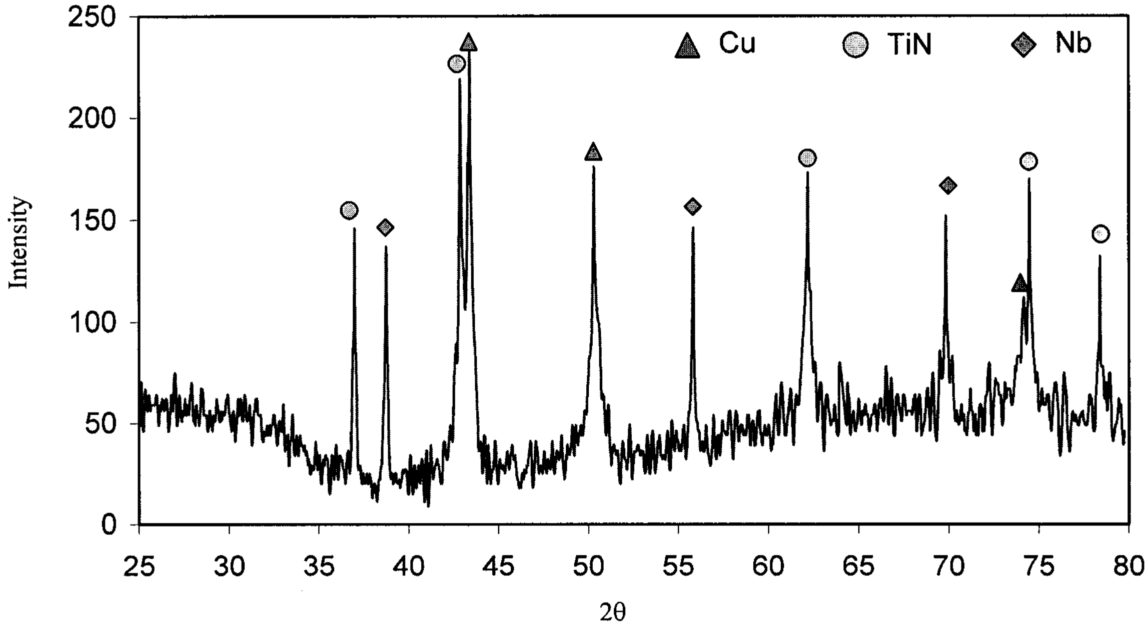

Figure 6.8 - XRD spectrum of powder heated in N_2.

Figure 6.9 presents a low voltage back-scattered micrograph of the cross section of the edge of the sample heated in N_2. Two main phases are observed, Cu-Ti alloy as matrix (lighter phase) and TiN as precipitates (darker phase). The EDS analysis confirmed the presence of residual Ti in the copper matrix, which is also observed by the lower undercooled solidification temperature (see Figure 6.7), detected on the DSC trace. Figure 6.7 also shows a continuous layer of TiN surrounding the solidified melt. The presence of titanium remaining in the drop illustrates the diffusion barrier role played by the TiN reaction layer.

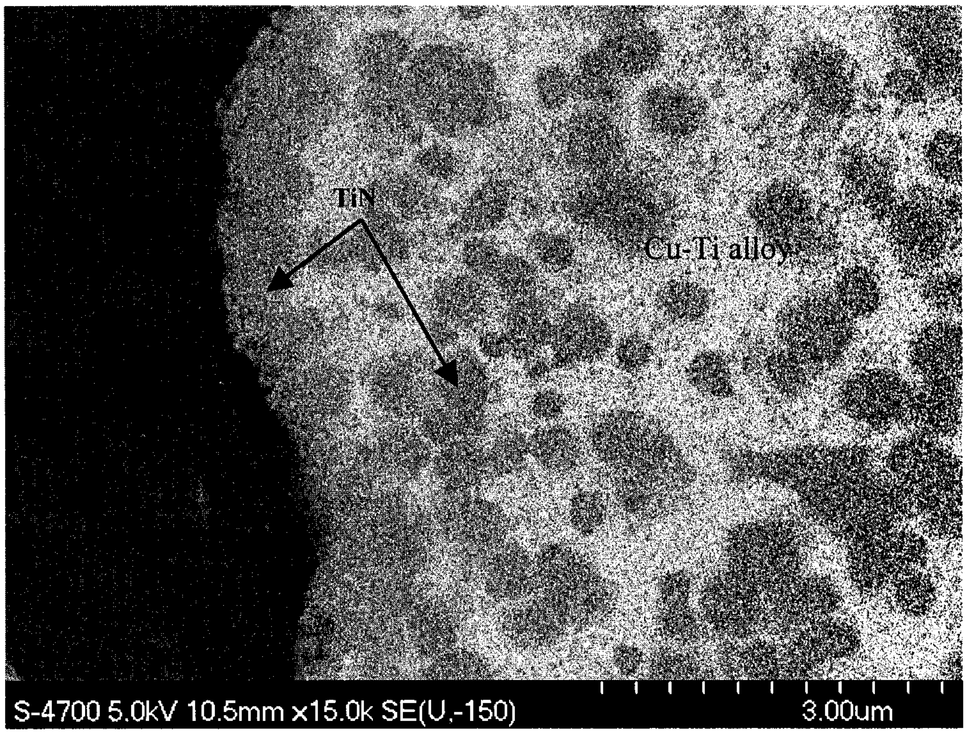

Figure 6.9 - Back-scattered micrograph of the edge of the powder heated under N_2.

6.3.4 Melting of Cu-rich Powder in the Presence of Si_3N_4 Ceramic

The previous results have shown that the active brazing alloy starts melting at 886°C and that the first liquid to be formed is inside the Cu shell. Similar experiments were carried out in which the composite powder was mixed with silicon nitride powder and the DSC trace performed in Ar is presented in Figure 6.10. The trace for the ABA powder alone is included for comparison. Melting in the powder mixture is observed by an endothermic peak but a major exothermic peak is also observed immediately following melting. This peak corresponds to the formation of silicides and nitrides, as the decomposition of Si_3N_4 produces TiN and Ti_5Si_3. This exotherm begins at 894°C. This indicates the temperature at which the first liquid appears on the surface of the ABA powder and is available for reaction with the ceramic powder.

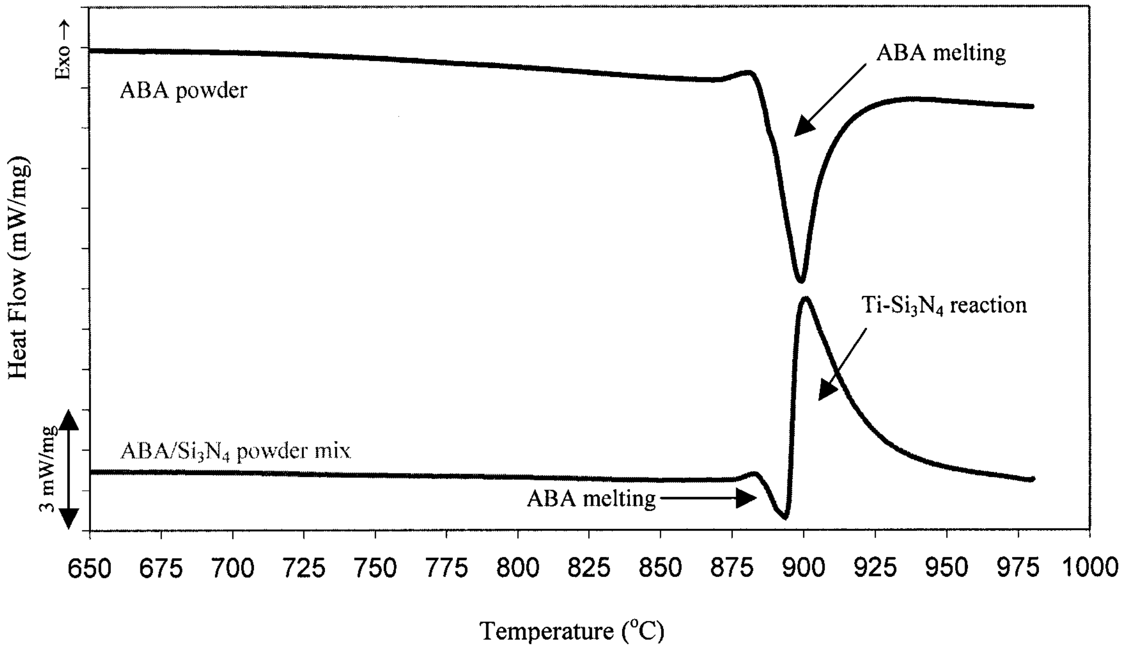

Figure 6.10 - DSC trace of ABA powder and ABA/Si_3N_4 powder mix at 40°C/min in argon.

6.4 DISCUSSION

The melting characteristics of the composite powder is a function of the inter-diffusion between both components, Cu and Ti. As predicted by the phase diagram (Fig 6.1), many intermetallic layers are formed during heating. Figure 6.11(a) presents a sketch of the theoretically expected diffusion couple initially formed based on the equilibrium phase diagram. Figure 6.11(b) indicates the microstructure that would form in a Ti-75wt%Cu composite particle just below 870°C assuming equilibrium was attained during heating. If this structure developed during heating then a significant thermal event at 870°C, corresponding to Ti_2Cu_3 transforming to $TiCu_2$, should be evident in the DSC trace of the ABA powder. This transformation would then produce a powder with a microstructure close to that of the $TiCu_2$–$TiCu_4$ eutectic. With continued heating above 870°C the majority of the particle would then melt at 875°C, resulting in a large endothermic peak present in the DSC trace corresponding to the eutectic reaction. Since the bulk composition of the powder is slightly hypoeutectic, the remaining $TiCu_2$ would continue to melt during heating to 890°C where the peritectic reaction of $TiCu_2 \rightarrow Ti_3Cu_4 + L$ would occur. This reaction would then be followed by more melting up to the liquidus temperature of 895°C.

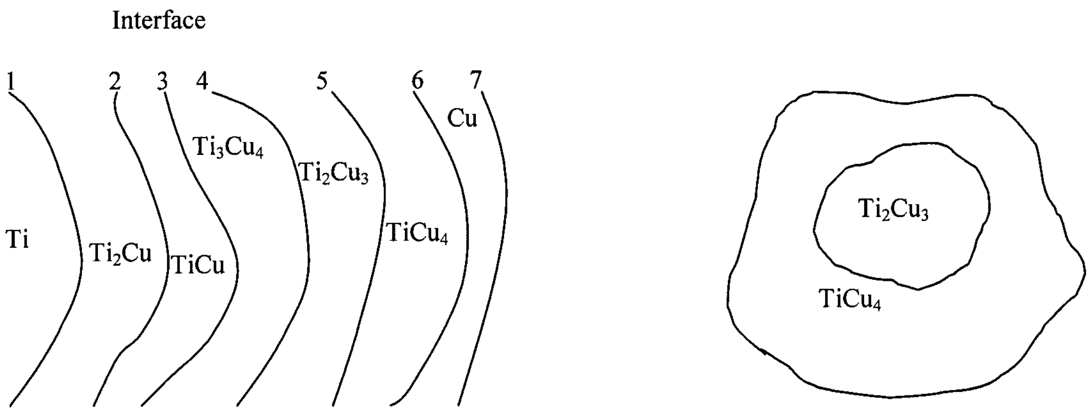

(a) (b)

Figure 6.11 - (a) Sketch of the different thermodynamically feasible interlayers in the Cu-Ti diffusion couple according to the equilibrium phase diagram and (b) the equilibrium structure (below 870°C) of the composite particle predicted after a long diffusion time.

The XRD results of the samples heated to 880°C and cooled indicate the presence of phases other than Ti_2Cu_3 and $TiCu_4$ (i.e. (Cu) and (Ti)) indicating that equilibrium due to interdiffusion was not achieved during heating. This fact is also supported by the measured DSC traces.

The presence of a very small exothermic peak at about 870°C indicates that only a small amount of Ti_2Cu_3 must have developed in the diffusion couple during heating to transform to $TiCu_2$. The lack of a strong melting endotherm with an onset at the eutectic temperature of 875°C also indicates that very little equilibrium eutectic structure was developed during heating. However, the XRD results suggest that a significant amount of $TiCu_4$ is present in the powders at 880°C. Therefore the lack of eutectic melting can be attributed to very little $TiCu_2$ developed in the diffusion couple. A large melting endotherm with an onset at 885°C indicates (in comparison with the phase diagram) a strong peritectic reaction (i.e. $TiCu_4 \rightarrow (Cu) + L$) followed by progressive melting of the remaining (Cu) solid solution. This in turn would indicate that a large portion of the powder remains as a (Cu) solid solution phase but includes a measurable amount of $TiCu_4$. The presence of these phases is also confirmed by the XRD results.

The general melting behaviour observed above for the ABA powder indicates that, despite some interdiffusion and the formation of a multi-layered diffusion couple as indicated in Figure 6.5, the powders still possess a structure far from equilibrium. More specifically, interdiffusion favours the rapid growth of the Cu-rich $TiCu_4$ intermetallic and the formation of a (Cu) solid solution. The fact that the formation of a liquid layer adjacent to the Ti core in Figure 6.6 further supports the lack of development of more Ti-rich intermetallic layers.

Differences in melting behaviour at a heating rate of 10 and 40°C/min indicate that longer heating times result in a more fully developed diffusion couple. However the lack of melting at 875°C and the major endotherm at 885°C indicates that the growth of the $TiCu_4$ is favoured over more Ti-rich phases including Ti_2Cu_3 at heating rates of 10°C as well as 40°C/min. The XRD results support this extensive growth of the $TiCu_4$ at the expense of the (Cu) phase. In addition, a distinct phase transformation at 890°C is observed in the DSC trace of the 10°C/min sample which, as stated above, corresponds to $TiCu_2 \rightarrow Ti_3Cu_4 + L$ pertitectic reaction. Since this reaction is expected based on equilibrium arguments, its presence indicates a more homogeneous structure than that achieved at 40°C/minute.

It is assumed that all the interlayers depicted in Figure 6.11 are present at around 870°C. However, their relative thicknesses are a function of the diffusion kinetics in the couples. More specifically, some layers may be too thin to lead to thermal events measurable by the DSC. Certainly Figure 6.5(a) indicates, under relative high magnification, the presence of only 3 of a possible 5 intermetallic interlayers.

The same diffusion behavior and interlayer formation should occur, independent of the purging gas used in the heating ramp before 885°C as only solid-solid interactions occur. The DSC trace performed in Ar shows that liquid starts to form at 885°C, the temperature corresponding to the most Cu-rich peritectic reaction. This first liquid layer is formed inside the copper shell at the $TiCu_4$-(Cu) interface. Therefore, the molten liquid metal is not exposed to the furnace atmosphere immediately upon melting. In the case of the powder heated in N_2, melting is not observed but the presence of a highly exothermic reaction is. The presence of Ti in a molten filler metal favors reaction with O or N. This ability is used for brazing ceramics. In the case of nitrides, the Ti will preferentially form TiN: this mechanism is responsible for interface formation as the free energy of reaction is lower than the bond stability of the ceramic itself [6.5]. The reaction between nitrogen and molten titanium occurred before complete melting was reached, suggesting diffusion of nitrogen through the copper shell.

The formation of this TiN ceramic is exothermic which totally overshadows the endothermic melting peak. The solidification peak suggests that residual titanium is present in the core of the powder, due to the fact that TiN acts as a diffusion barrier to nitrogen, preventing further reaction. A gradient in titanium was observed between the inner core and the surface of the reacted ABA powder, suggesting migration of Ti for reaction with the furnace atmosphere. Adams et al. have observed migration of Ti to a Ti-free surface from a bi-layer Cu-Ti [6.6]. In this case, the formation of the complete diffusion barrier will occur mainly when the outer shell melts, exposing molten active metal to nitrogen. In the solid state, titanium will diffuse from the inside of the shell towards the outside due to the concentration gradient to react with the nitrogen atmosphere. This migration of titanium was used to produce an effective diffusion barrier where a Cu-Ti alloy was nitrided leaving a relatively pure copper region surrounded by a TiN(O) shell [6.7]. The formation of this diffusion barrier occurs at 956°C, as demonstrated by the second exothermic peak. The observation of distributed TiN precipitates in the matrix is believed to come from the multiple breakage of the TiN layer formed at the interface of the solid copper/molten active metal as internal pressure is developed during the melting process. The strong interface between the reinforcement and the matrix is associated with the presence of residual Ti, forming a chemical interface with TiN. In the case of complete exhaustion of the active element, pure Cu would have been exposed to TiN. The contact angle between these materials has been determined to be 112° [1.26], which would create de-wetting of the particle and expulsion from the molten Cu.

By comparing the results obtained from the composite powder alone, the composite powder heated in nitrogen and the Si_3N_4-ABA powder mixture, the following melting sequence has been determined for the powder heated at 40°C/min. A sketch is presented in Figure 6.12. Independently of the heating rate, intermetallic formation occurs during the heating ramp. Melting initiates in the two phase region ($TiCu_4$ and Ti_2Cu_3), which is inside the Cu shell. The complete dissolution of the Cu-rich portion of the shell ends at 894°C. From this point, only the dissolution of the Ti-rich intermetallic and the remaining Ti core occurs and complete melting occurs at 915°C. The same sequence occurs for the powder heated at 10°C/min but the transition temperatures are slightly lower.

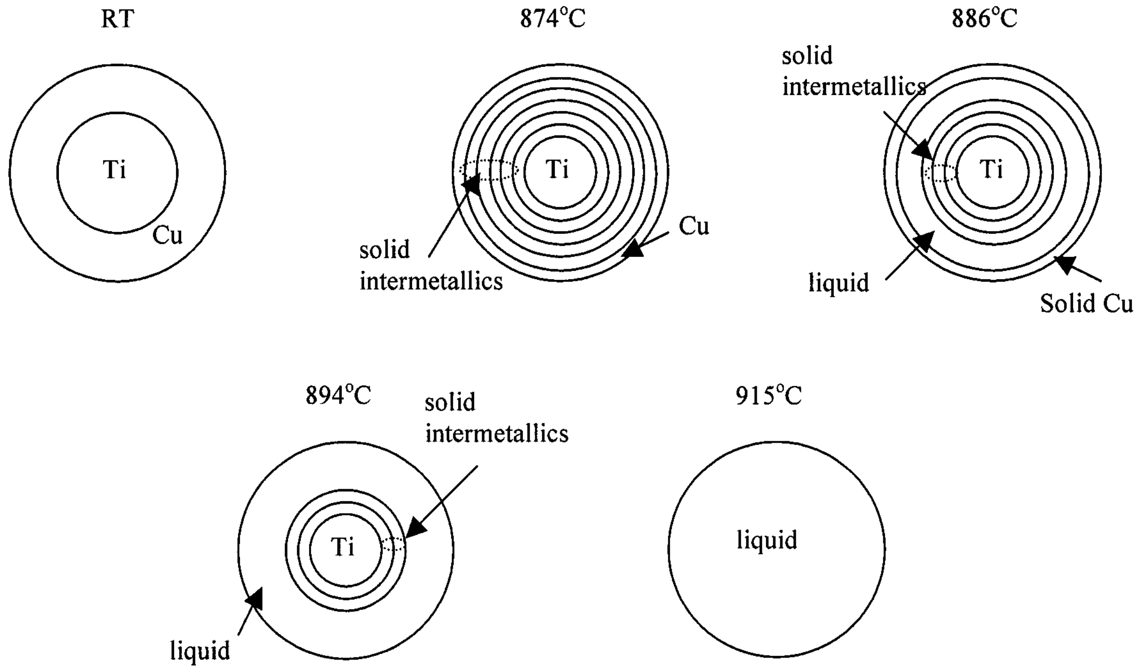

Figure 6.12 - Sketch of melting sequence of a ABA powder heated at 40°C/min.

6.5 REFERENCES

[6.1] *ASM Handbook Volume 3*, Phase Diagrams, ASM International, 1994, 2•180.

[6.2] O. Kubaschewski and C.B. Alcock, *Metallurgical Thermochemistry*, 5th edition, Pergamon Press, Oxford, 1979.

[6.3] S.F. Corbin and P. Lucier, Thermal Analysis of Isothermal Solidification Kinetics during Transient Liquid-Phase Sintering, Metallurgical and Materials Transactions A, Vol.32A, 2001, p971-978.

[6.4] S.F. Corbin, Diffusion-based Model for Isothermal Solidification Kinetics during Transient Liquid-Phase Sintering, Metallurgical and Materials Transactions A, Vol.33A, 2002, p117-124.

[6.5] R.E. Loehman, A.P. Tomsia, J.A. Pask and S.M. Johnson, Bonding Mechanisms in Silicon Nitride Brazing, Journal of American Ceramic Society, Vol. 73, No.3, 1990, p552-558.

[6.6] D. Adams, T.L. Alford, S.A. Rafalski, M.J. Rack, S.W. Russell, M.J. Kim and J.W. Mayer, Formation of Passivation and Adhesion Layers for Cu via Nitridation of Cu-Ti in an Ammonia Ambient, Materials Chemistry and Physics, 43, (1996), p 145-152.

[6.7] D. Adams, T.L. Alford, N.D. Theodore and S.W. Russell, Segregation of cu in Cu(Ti) Alloys during Nitridation in NH_3, Thin Solid Films, Vol.270, 1995, p346-350.

Part 4 - Joining Si_3N_4 to Itself and to an Iron Aluminide Alloy using a High-Ti containing Cu Brazing Alloy

Chapter 7

Joining Silicon Nitride Ceramic using a Composite Powder as Active Brazing Alloy

7.1 Introduction

The objective of this chapter was to evaluate the properties of ceramic-to-ceramic brazed joints made with the composite active brazing alloy powder, produced by the route presented in Chapter 5. In addition, low voltage electron microscopy was used to better understand the reaction layer formation and kinetics. Joining Si_3N_4 to itself isolates the residual stress invariably created by the CTE mismatch problem of metal-ceramic joints, thus providing a better idea of the properties and potential of the composite powder.

7.2 Experimental Procedures

Additive-free alpha-silicon nitride powder (Toshiba) with an average particle size of 2 microns was used for DSC experiments. Bars of 8 mm diameter of commercial sintered silicon nitride (Ceralloy 147-31N®, Ceradyne, California) containing 7-8wt% of yttria/alumina as sintering additive were used for joints.

Figure 7.1 presents the XRD pattern of the Si_3N_4 used. The silicon nitride bars were cut into 3 mm thick discs, which were then polished down to 1 micron. Si_3N_4 ceramic sandwich samples where used. The Si_3N_4 disks were cleaned in acetone and ethanol for 15 minutes in an ultrasonic bath prior to bonding. The brazing paste was applied on both clean surfaces. The total thickness of the paste deposited was evaluated to be ≈100 microns.

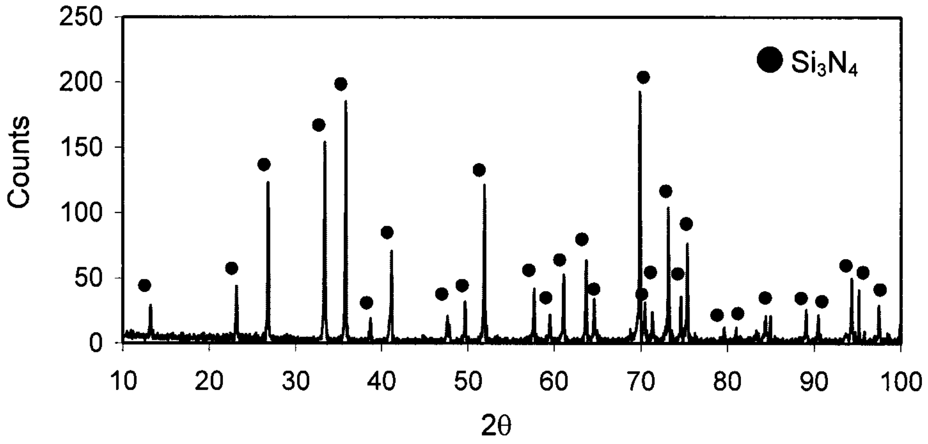

Figure 7.1 XRD pattern of Ceralloy 174-31N.

The reaction between Si_3N_4 powder and Cu-Ti brazing alloy was studied with DSC (Netzsch, DSC 404C). The powder mixture had a weight ratio of 85%ABA-15%Si_3N_4 (70-30 vol%). The mixture was heated between 925 and 1025°C in ultra high purity argon and soaked for 6 minutes in each case. This soaking time was used to ensure temperature equilibrium of the sample between the heating and cooling stages.

The joining cycle was carried out in a graphite furnace. The sample was embedded in a powder bed of boron nitride inside a graphite die. A pressure of 35 kPa was applied to the top of the jig to keep the samples aligned. The bonding temperature was varied between 975 and 1075°C for different joining times ranging between 1 and 12 minutes. Short soaking times were used to limit the reaction layer growth. The heating cycle was as follows: heating at 10°C/minute up to the brazing temperature and cooled down at a rate of 5°C/minute to 300°C. Flowing argon was maintained during the cycle.

The samples were cut, mounted and polished for microscopic evaluation. X-ray diffraction (Philips PW1710, CuKα = 1.54098Å), optical microscope, with an image analysis system (CLEMEX System), SEM coupled with an EDS system (JEOL-840/ EDAX), and low voltage SEM coupled with an EDS detector (Hitachi S-4700/Oxford) were used to characterize the joints.

Four-point bending tests were performed using longer sandwich samples where each ceramic bar was 2.5 cm in length instead of the 3 mm tested for microstructural evaluation of samples. Testing was performed at room temperature on a universal testing machine (Tinius Olsen H25K-5) using a crosshead speed of 0.5mm/min. The inner and outer span distances were 20mm and 40mm, respectively. Each value reported is the average of three tests.

7.3 Results

7.3.1 DSC Results

Figure 7.2 presents the DSC traces for Si_3N_4/ABA powder mixture held for 6 minutes at 925, 975 and 1025°C, respectively. The captions H and C represent, respectively, the heating and cooling part of the curves. The melting events are similar for all three cases. The composite powder begins to melt at 886°C, corresponding to the melting of the two phase region-Cu_4Ti and Cu_3Ti_2-under non-equilibrium conditions. Complete melting of the composite powder was previously determined to have occurred at 915°C when heated at 40°C/min. The reaction between the molten ABA and the Si_3N_4 powder has started at 894°C (transition peak between melting and reaction). This observation illustrates that molten active metal has reached the surface of the composite powder at this moment. The very intense exothermic peak shows the high reactivity between Si_3N_4 and the molten alloy to form TiN. The traces performed at 975 and 1025°C show that the reaction went to completion as the trace returned to the base line.

In both cases, the residual change in melting and reaction energy is the same (-140 J/g), suggesting similar melting and reaction behavior regardless of the test temperature. However at 925°C, the base line was not reached implying that the reaction was not complete at this temperature. No solidification peaks are observed on the cooling traces of the 975 and 1025°C samples, suggesting isothermal solidification due to consumption of the active element through reaction. However the cooling stage for the sample heated at 925°C shows a solidification peak at 867.8°C (-2.23 J/g) indicating that liquid was still present during cooling.

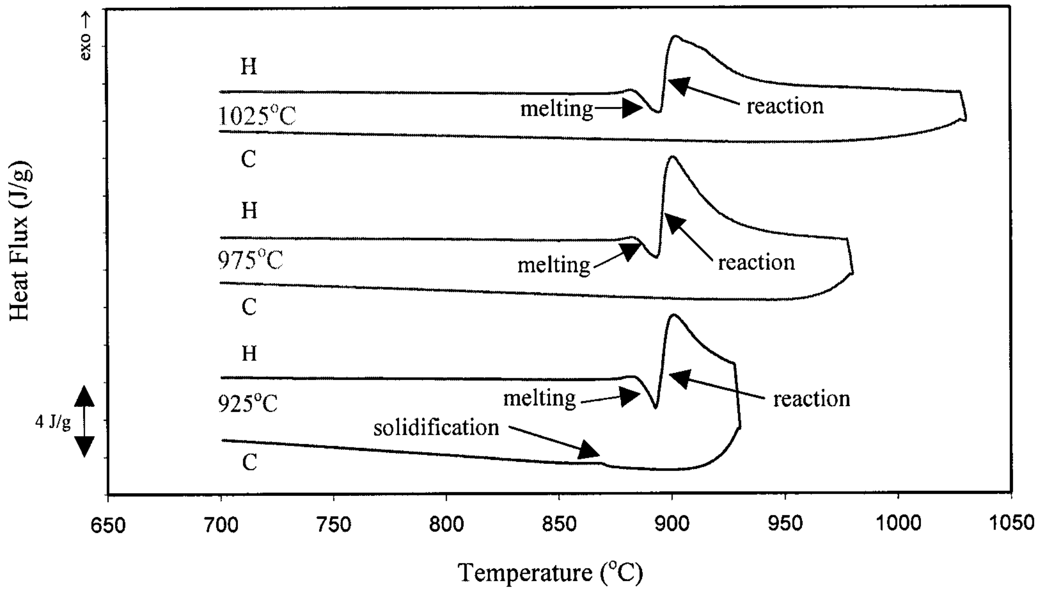

Figure 7.2 - DSC trace of powder mixture soaked for 6 minutes at 925, 975 and 1025°C, respectively.

XRD analysis performed on the samples after the tests have shown the presence of TiN and residual Cu. No silicides were detected due to the detection limit of the diffractometer. However, silicide should be present as a decomposition product of Si_3N_4.

7.3.2 Joint Microstructure

Figure 7.3 illustrates a representative SEI micrograph of a sound joint of Si_3N_4/ABA/Si_3N_4. This joint was produced at 1075°C for a soaking time of 6 minutes. During the heating process, the morphology of the ABA layer undergoes significant changes. The final thickness of the inserted filler metal layer is around 150 microns and is relatively constant for the different tested conditions. The variations in the reaction layer thickness are believed to be due to the non-perfect homogenization of the molten titanium into the molten filler metal (agglomerated particles) where higher localized Ti concentration may be present. The reaction layer possesses some transverse cracks, which are formed during the cooling stage of the heating cycle. Such cracks are common in metal-ceramic joints as in most cases the CTE of the reaction layer is higher than the CTE of the ceramic substrate [1.41].

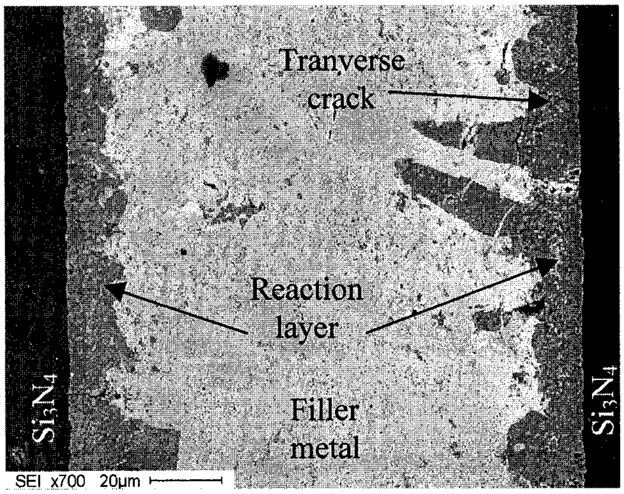

Figure 7.3 - General micrograph of a Si_3N_4/ABA/Si_3N_4 joint.

XRD was performed on a fractured interface and the results presented in Figure 7.4. The main peaks obtained are coming from the base material and reaction products. Mainly, silicon nitride ceramic peaks are present. Various reaction products are also present such as TiN, Ti_5Si_3, CuSiTi, Cu_4Ti and Cu.

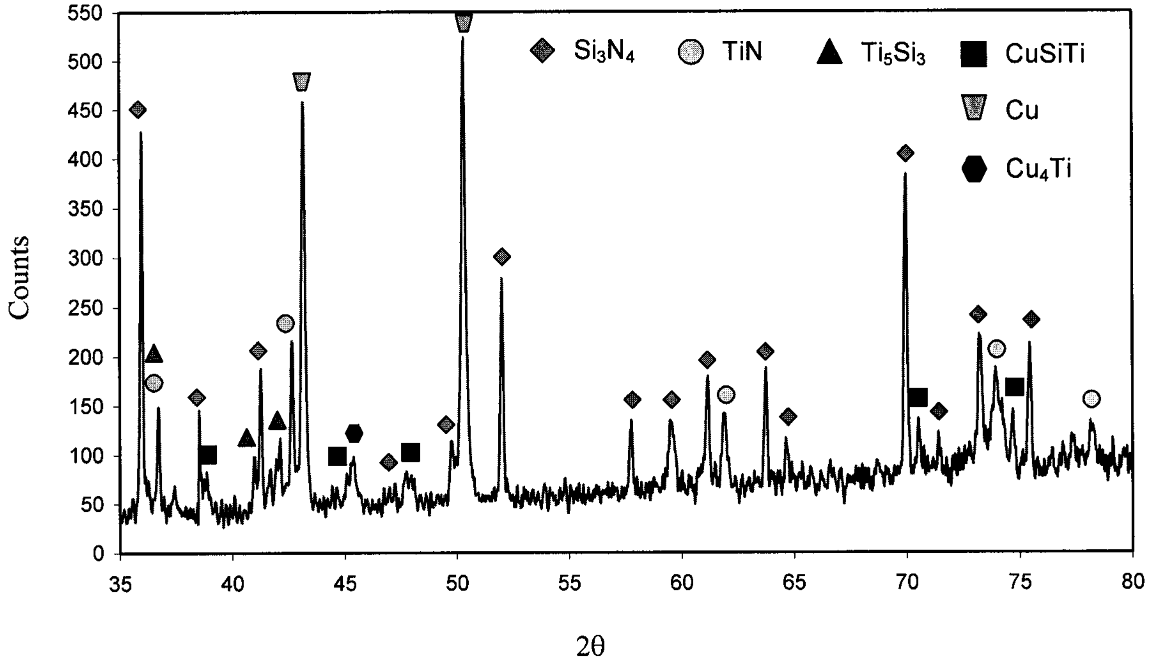

Figure 7.4 - XRD pattern of interface fracture surface.

Figure 7.5 presents a back-scattered electron micrograph of the reaction layer formed at 1025°C for 6 minutes. The silicon nitride is present on the left hand side. The reaction layer is adjacent to the ceramic. The reaction layer is in contact with the residual active brazing alloy (Cu-Cu_4Ti). The Cu_4Ti microstructure is clearly observed. Large particles are also observed and EDS analysis showed the presence of Cu, Si and Ti associated with the CuSiTi phase. Fracture or separation of the reaction layer is observed as a separate particle with the same composition (same color) as the adjacent layer possess complementary shapes (e.g. A-A).

Figure 7.6 presents a low voltage EDS line scan of an interface formed at 1075°C for 12 minutes. This sample was chosen as it has the largest reaction layer which will facilitate observation. Similar analysis of smaller reaction layers is possible. The reaction layer is composed of TiN and Ti_3Si_5. The TiN layer is inferred by the absence of Si (no detection of Si between the Si_3N_4 and Ti_5Si_3 layers). The end of the reaction layer is easily observed by the presence of copper. The Ti and N scans are very similar as both X-ray line energies are close and convolution exists. The presence of localized copper in the silicide layer was also detected. Despite the low number of counts, low voltage EDS has the advantage of having a low interaction volume as opposed to conventional SEM or EPMA, and more accurate distributions and thicknesses can be detected.

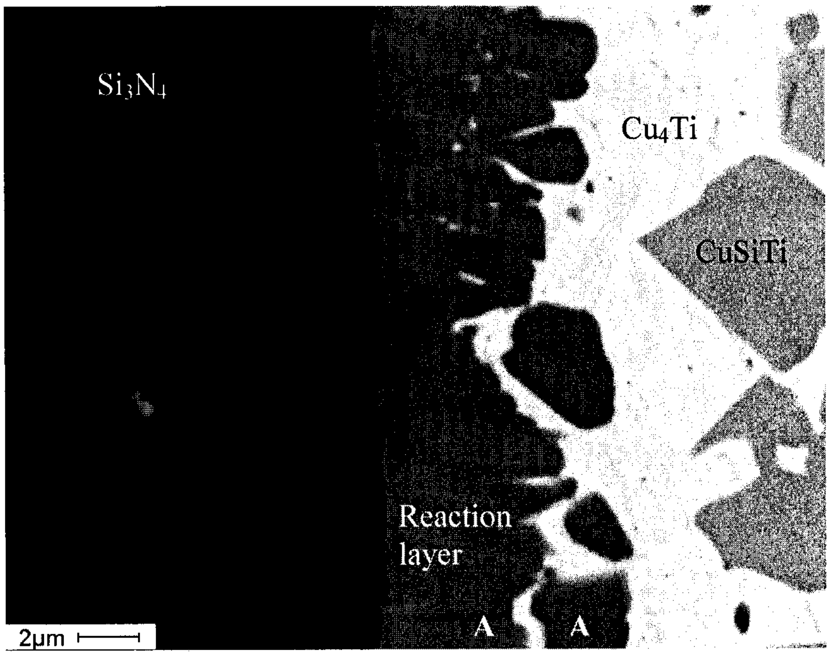

Figure 7.5 - Reaction layer formed at Si_3N_4/ABA interface.

Figure 7.7 presents the back-scattered micrograph showing the microstructural evolution of the reaction layer for the samples joined at 975°C for 1 min, 1025°C for 1 min and 1075°C for 3 min, respectively. These samples were chosen as they are representative of the mechanical test results obtained (see section 7.3.5: *Mechanical Properties of the Joints*). At 975°C, a composite reaction layer is observed, where the darker phase corresponds to a Ti and N-rich phase and the lighter phase is composed of Ti and Si. An increment of 50°C in brazing temperature (1025°C) produces a substantial thickening of the total reaction layer, with two distinct layers being formed. The darker layer, adjacent to the

Si_3N_4 ceramic, is composed of Ti and N. The main layer observed is composed of Ti and Si. Some Ti/N rich precipitates were observed in the Ti/Si-rich layer and into the Cu/Ti brazing alloy. Cu was also observed in some isolated locations. The reaction layer formed at 1075°C had less thickening than for the previous temperature increment. The two main components are still Ti/N-rich and Ti/Si-rich phases. However, the Ti/N layer has grown but more Ti/N rich precipitates are observed in the Ti/Si-rich layer. Copper is also observed in some locations.

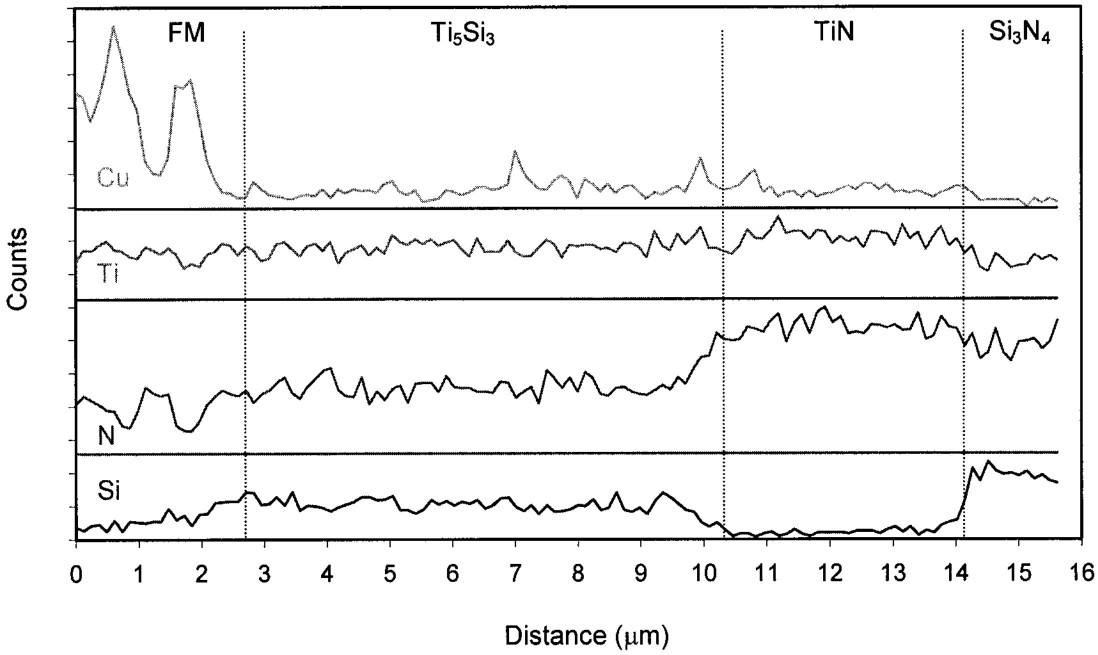

Figure 7.6 - Low voltage EDS line scan of an interface formed at 1075°C for 12 minutes.

7.3.3 Reaction Layer Evolution and Kinetics

Bonding of ceramics implies the formation of a reaction layer. Different researchers agree on the fact that the formation of the interface during brazing is a two step process where the reaction layer is initially formed by reaction of an active element with the ceramic. The initial stage of the interface formation is very fast and is controlled by a liquid/solid reaction. Once the reaction layer possesses a certain thickness and covers the entire initial ceramic surface, the growth rate decreases as growth is now controlled by diffusion through the initial reaction layer.

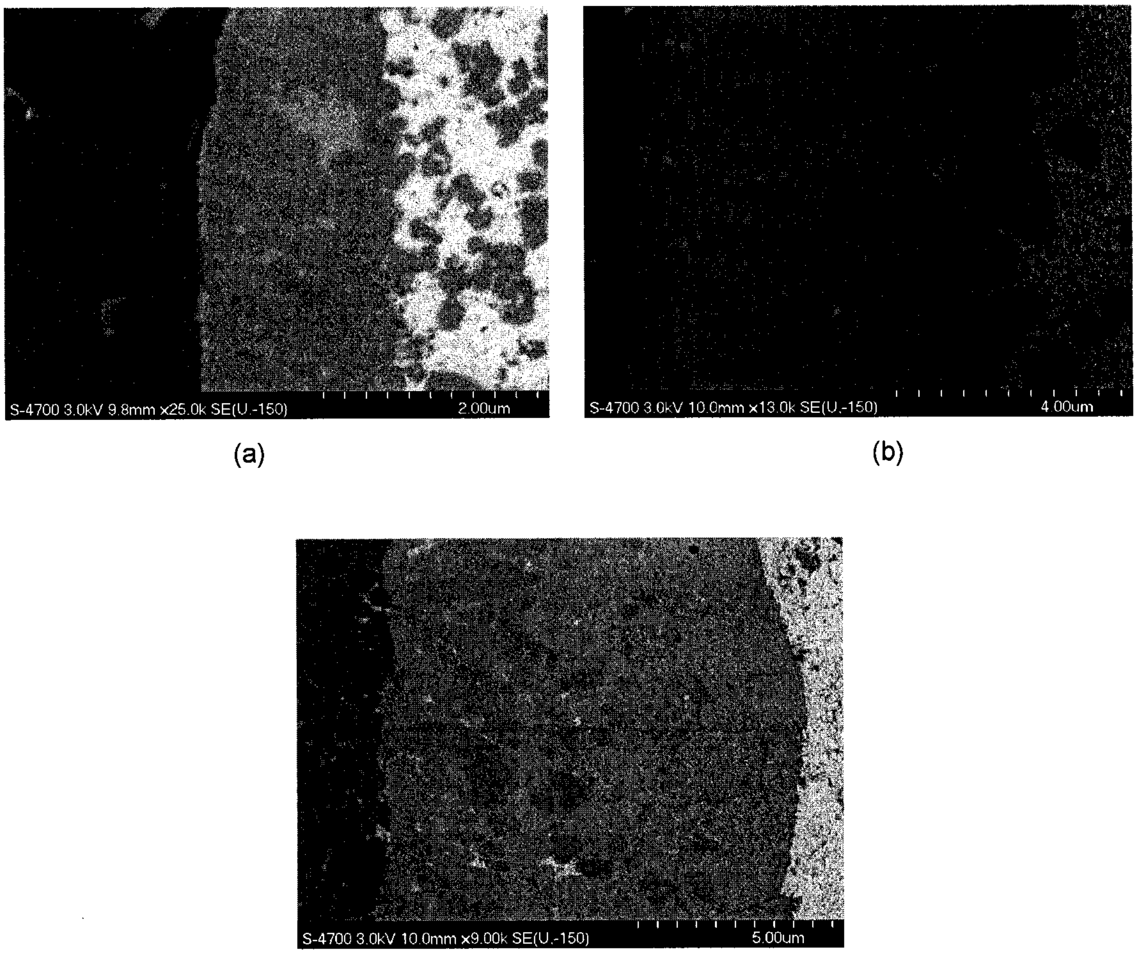

(a) (b)

(c)

Figure 7.7 - Reaction layer microstructural evolution for joints brazed at (a) 975°C for 1 min, (b) 1025°C for 1 min and (c) 1075°C for 1 min.

The total reaction layer thickness (nitride and silicide) of the samples was measured by image analysis and the results are presented in Figure 7.8. The total reaction layer thickness increases with temperature and time and ranges from 4 to 12 microns, depending on the brazing time and temperature. With time, the growth rate of the reaction layer slows down. The trend observed is similar to the final part of a parabolic curve, suggesting that the critical point has been exceeded and that the reaction layer growth mechanism has changed to diffusion control.

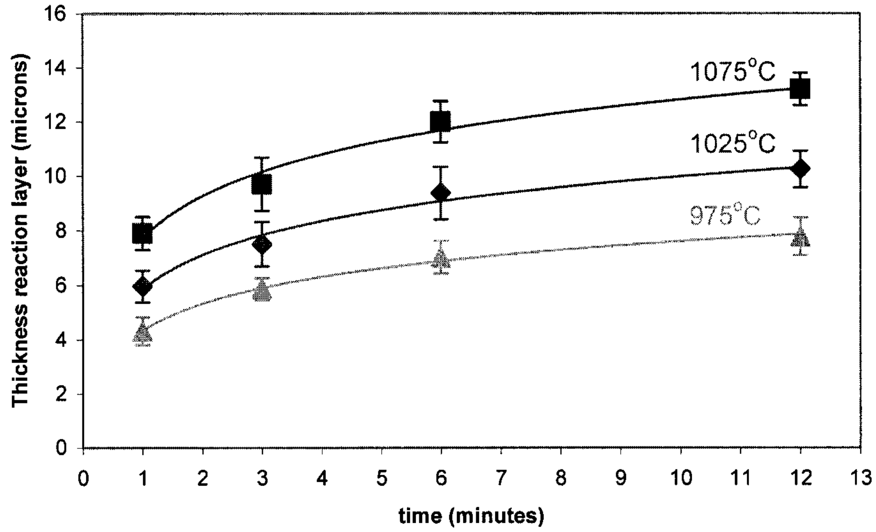

Figure 7.8 - Measurement of the reaction layer thickness as a function of brazing time.

As the growth of the reaction layer is a function of elemental diffusion through itself, the reaction diffusion concept can be used to evaluate the change of reaction layer thickness. Figure 7.9(a) is a replot of the data of Figure 7.8 but as a function of the square root of time. The growth is observed to fit a linear tendency within the error bars implying a parabolic relationship. For all temperatures, the fit suggests that the liquid/solid reaction is complete and growth follows a diffusion controlled mechanism as, upon extrapolation, the lines do not intersect (0,0). The effective activation energy using the Arrhenius equation calculated form Figure 7.9(b) is 64 kJ/mol.

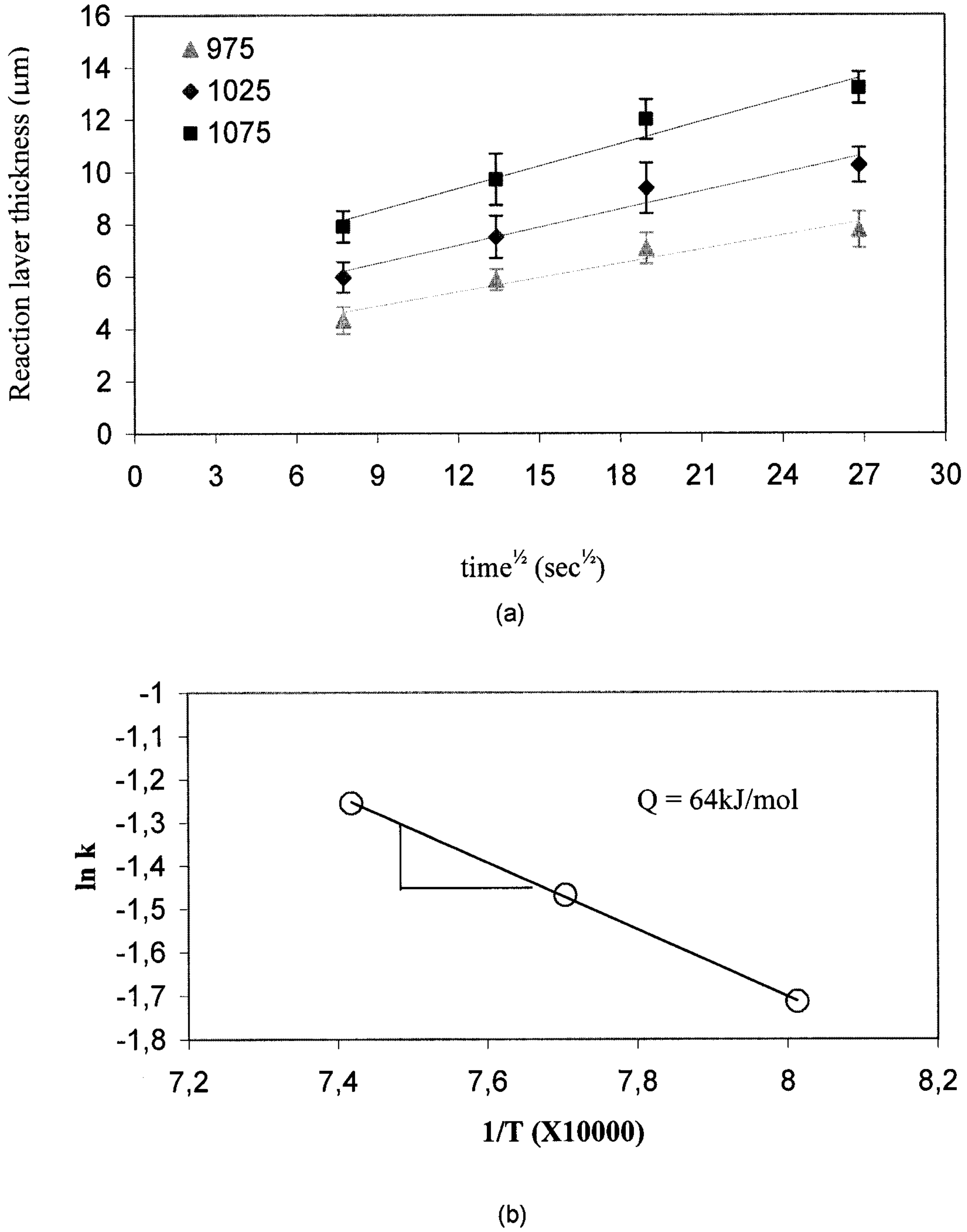

Figure 7.9 - Analysis of the reaction layer growth by (a) the parabolic analysis and (b) activation energy measurement with Arrhenius equation.

7.3.4 Mechanical Properties of the Joints

The effect of time on the mechanical behavior of joints brazed at 975 and 1025°C, as well as the standard deviation is presented in Figure 7.10. The average bending strength ranges from 250 to 400 MPa. The mechanical behavior is directly associated with the reaction layer thickness developed at the ceramic interface. For both brazing temperatures, the peak strength occurs for a similar reaction layer thickness (around 6 microns). In all other cases (thinner or thicker reaction layers), the strength decreases to around 250 MPa. The optimized strength of joints obtained are similar to the strength values published by Tamai and Noka [7.1].

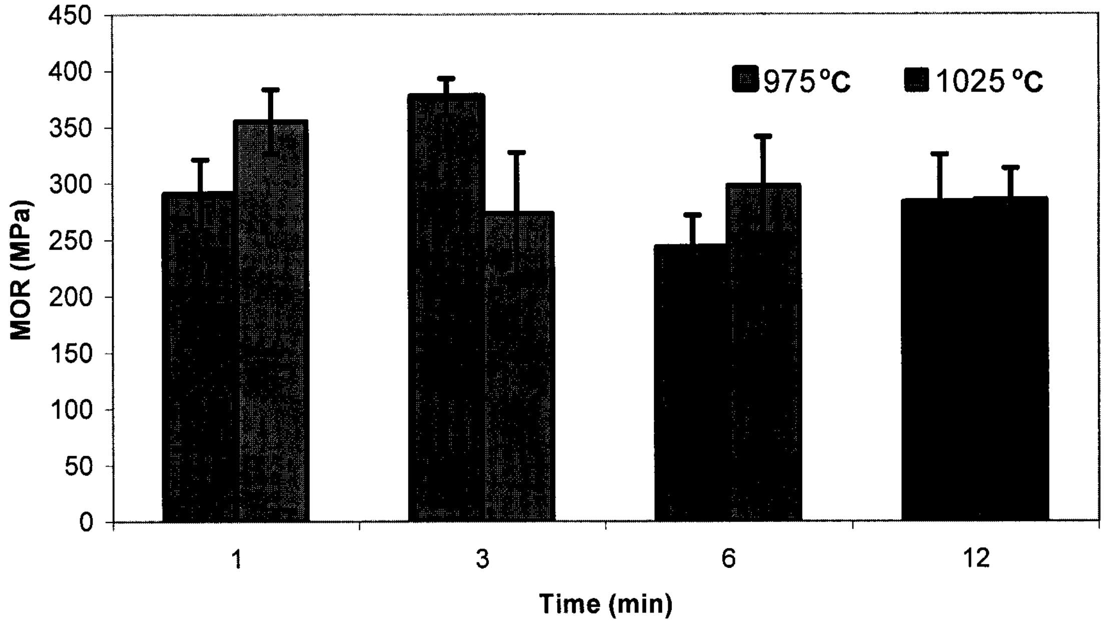

Figure 7.10. Four-point bending strength of brazed samples.

Two different types of fracture surface were obtained and are directly related to the bending strength. Figure 7.11 (a and b) presents two macrographs of fracture surfaces for samples possessing a strength of 400 MPa and 250 MPa, respectively. In the case of the samples possessing the higher strength, all failures occurred in the ceramic substrates with a typical concave/convex fracture. The fracture surfaces demonstrate the existence of an optimum reaction layer thickness. In this case, the interfacial strength was higher than the residual tensile stresses created in the ceramic during cooling. For thinner or thicker reaction layers, fracture occurred directly through the interface.

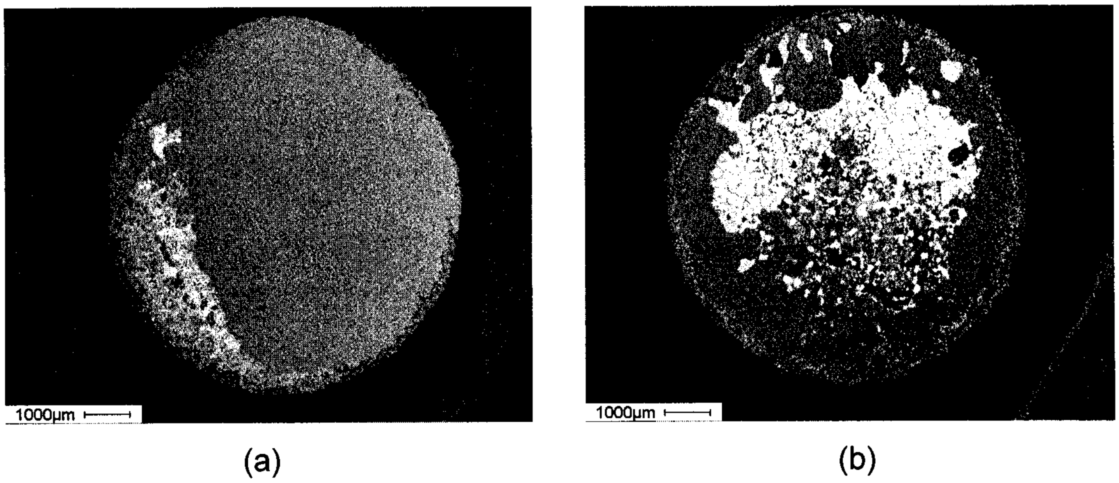

(a) (b)

Figure 7.11 - Macrograph of fracture surface for a strength of (a) 400 MPa and (b) 250 MPa.

7.4 DISCUSSION

The addition of an active element in a filler metal base, like titanium in copper, changes the wetting angle from 138° for pure copper to an angle of 60° and lower, depending on the content of active element [7.2]. The reaction between the Ti-filler metal and the Si_3N_4 ceramic forms TiN and Ti_5Si_3, which corresponds to the lowest free energy reaction products [1.4, 6.5]. The composite powder is shown to begin reacting at 894°C, when the active liquid reaches the surface of the particles. The filler form influences the melting and reaction kinetics but the respective products remain similar.

Titanium is a nitride as well as a silicide former [1.4, 1.26, 1.31, 6.5]. Thus during reaction bewteen Ti and Si_3N_4, Ti-nitrides and Ti-silicides are expected to be formed. Both compounds have been observed in the reaction layer by line scan using low voltage SEM. At low temperature (975°C), the reaction layer contains both intermixed components in the same layer. On raising the brazing temperature to 1025°C, the formation of two distinct layers, as opposed to an intermixed one, occurs. Thermodynamic computations have shown that Ti_5Si_3 is more stable than TiN in a low N_2 partial pressure environment. The combined interactions - reaction between the filler metal and the ceramic (Ti-Si_3N_4) and the dissociation of TiN - allows the formation of a distinct Ti-silicide layer. In the presence of an excess of Ti (from the filler metal), Ti_5Si_3 is the more stable silicide. This decomposition of TiN releases nitrogen which in turn, goes into solution in the Ti_5Si_3 and diffuses towards the filler metal. This N diffusion, indicates a certain level of solubility in Ti_5Si_3, which is observed by the presence of TiN precipitates formed in the reaction layer during cooling. In addition, nitrogen will continue to react with free Ti from the filler metal and form the TiN precipitates observed outside of the reaction layer. This implies that a lower Ti-silicide stoichiometry should be observed around the TiN precipitates present in the Ti_5Si_3 layer: TEM could be used to characterize this Ti depletion further.

On further increase in temperature, elemental diffusion through the reaction layer and TiN dissociation increase but thickening of the TiN layer occurs because the quantity of N in solution increases which decreases the driving force for TiN dissociation. The thickening of the Ti_5Si_3 layer remains in competition with the TiN dissociation and the reaction with the ceramic. However, as the layer increases in thickness, the reactions becomes more dependant on the solubility of nitrogen in the Ti_5Si_3 and diffusion of Ti through the complete reaction layer than at the lower temperature (a reduction in the thickening rate of Ti_5Si_3 is observed). The nitrogen solubility limit decreases during cooling and formation of TiN precipitates in the Ti_5Si_3 layer was again observed. The same low silicon content surrounding the TiN precipitates should be observed. The microstructural evolution demonstrates a complex series of transformations influenced by the competition between the different phenomenon occurring. This demonstrates the impossibility of modeling the reaction layer growth for filler metals with high active element content with conventional models unless modeling is performed for the complete reaction layer growth and effective values are derived.

The formation of the reaction layer is the weak zone in a metal/ceramic interface. However, its formation is mandatory as it is a requirement in overcoming the electronic discontinuity between metal and ceramic. Previous researchers have shown that brazing alloys possessing a high active element content, have a high reaction layer growth rate [1.26] reflected in a more rapid deterioration of properties. The availability and thermodynamic activity of the active element is a major factor in reaction layer growth as it is the driving force for the reaction to occur. Varying the brazing time and temperature for example, are ways to control the reaction layer growth. Moreover, these parameters have to be very accurately controlled when using high active element content in the filler metal.

The model used to describe the total reaction layer growth is rudimentary. However, the application of other models such as the Johnson-Mehl or Austin-Rickett equations requires a deviation from the parabolic law with respect to time [7.3]. In the present case, no deviation from the linear fit was observed, justifying the application of the parabolic law model to analyse the reaction layer growth (see appendix A for more details). Similar observations were made by Nakao et al. [7.3] on the AlN/Cu-Ti system. Their study demonstrated that for an alloy containing 22%Ti, the system follows the parabolic growth law. This was associated with the active element concentration, which remains sufficiently high in the filler metal, and that the consumption effect of the diffusing element was not observed by any deviation from a linear fit. The Si_3N_4/Cu-Ti system with a high titanium concentration follows the same behavior, with the exception of there being two reaction products growing in various configurations instead of only one.

The thickening of the TiN reaction layer depends on the diffusion of N or Ti through the TiN layer but also on the diffusion of Ti through the Ti_5Si_3 and the dissociation of TiN. A similar approach is applied to the thickening of the Ti_5Si_3

layer. In addition, the thickening of a reaction layer depends on the solubility limit of each element (N in Ti_5Si_3) in the filler metal (or other reaction layer), where saturation in one or both elements has to be obtained (if dissolution is thermodynamically favorable) in order to observe growth. These solubility limits of the elements in the reaction layer also influence the thickening as the consumption of the ceramic may occur simultaneously with the dissolution of the reaction layer in the filler metal and no change in thickness would be observed (no interface velocity). To perform accurate modeling of the reaction layer growth and accurately determine the activation energy, several diffusion coefficients as well as the solubility limits of the various phases involved (as previously explained) have to be known: these data are not available in the literature at the moment.

The activation energy for the formation of the reaction layer obtained in this project (64 kJ/mol) is relatively low when compared to work performed by other researchers with copper–titanium systems (ranging between 200-300kJ/mol [7.2 – 7.4]). However, this discrepancy is related to the measurement and interpretation of the reaction layer itself. The formation of the reaction layer in the system Ti-Si_3N_4 implies the formation of two different reaction products, TiN and Ti_5Si_3. As opposed to the AlN-Ti system for example, where only one reaction product is formed and the reaction layer growth is only associated with the diffusion of one species [7.3, 7.5], any reactive metal-Si_3N_4 system which forms both nitrides and silicides, implies a growth competition between both layers, which in turn is influenced by the diffusion and solubility of the reaction products between each other and also into the filler metal.

In this work, the effective activation energy, which is the activation energy for the total reaction layer thickness growth, was measured as the reaction layer goes through several transformations and modeling of the growth behavior becomes very complex. The reaction layer thickness and composition are the dominant factors dictating the subsequent joint properties. The presence of a multi-layer interface inevitably induces complex residual stresses during cooling due to the difference in CTE mismatch (for example: CTE of Si_3N_4 = 3.2X10^{-6} /°C [7.6], CTE of TiN = 9.35X10^{-6}/°C [7.6], CTE of Ti_5Si_3 = 11X10^{-6}/°C [7.6], CTE of Cu = 17X10^{-6}/°C [1.31]). The low value of effective activation energy indicates that for this system, the total thickening is fast, which suggests that rapid degradation of the joint properties will occur if the energy (temperature) involved during brazing or further service application is too high.

Flexural strength testing gives the lowest strength value (tensile or compression) of the interface. The reaction layer thickness and composition, the distribution of the reaction products formed, their coefficient of thermal expansion as well as their respective ability to absorb stress through plastic deformation are important factors which influence the mechanical strength of a joint. In this case, in addition to control of the brazing parameters, the coefficient of thermal expansion of the various components shows a CTE gradient through the interface, which may help reduce the effects of residual stresses created during cooling due to the conventional CTE mismatch. The optimum mechanical strengths were obtained when a thin TiN layer and thick Ti_5Si_3 layers were present. Other reaction layer configurations show a decrease in strength as the interfacial strength becomes lower than the ceramic tensile strength affected by residual stresses created during cooling. As mechanical properties of joints are known to deteriorate with increased layer thickness, no mechanical tests were performed for samples joined at 1075°C as the reaction layers would be thicker than for the sample brazed at 1025°C, and equal or lower strengths should be observed.

7.5 References

[7.1] T. Tamai and M. Naka, Reaction Phases in SiC/SiC or Si_3N_4/Si_3N_4 Joint Brazed with Cu-Ti alloys, Journal of Materials Science Letters, Vol. 15, 1996, p 1025-1027.

[7.2] D.H. Kim, S.H. Hwang and S.S. Chun, The Wetting, Reaction and Bonding of Silicon nitride by Cu-Ti alloys, Journal of Materials Science, Vol.26, 1991, p3223-3234.

[7.3] Y. Nakao, K. Nishimot and K. Saida, Reaction Layer Formation in Nitrides Ceramics (Si_3N_4 and AlN) to Metal Joints Bonded with Active Filler Metals, ISIJ International, Vol. 30, No.12, 1991, p1142-1150.

[7.4] W. Tillmann, E. Lugscheider, R. Xu and J.E. Indacochea, Kinetic and microstructural Aspects of the Reaction Layer at Ceramic/Metal Braze Joints, Journal of Materials Science, Vol. 31, 1996, p445-452.

[7.5] D. Palit and A.M. Meier, Reaction Kinetics and Microstructural Development in Reactive Brazing of Copper to Aluminum Nitride, Proceeding of the IBSC 2003, San Diego, February 17-19, 2003, AWS, CR-ROM.

[7.6] H.O. Pierson, Handbook of Refractory Carbides and Nitrides- Properties, Characteristic, Processing and Applications, Noyes Publication, Westwood, NJ, USA, 1996.

Chapter 8

Brazing Silicon Nitride to an Iron-based Intermetallic using Copper Interlayer

8.1 Introduction

The major factor determining the strength of a metal/ceramic joint is the maximum tensile stress developed in the ceramic during cooling. Soft interlayers, such as Cu or Ni, have been proved to be successful in absorbing the detrimental stresses by plastic deformation [1.31]. Kim et Park [8.1] have studied the effect of residual stress absorption by a copper interlayer in the Si_3N_4/S.S.316 system as a function of the interlayer thickness. The optimum Cu thickness to reduce the effects of residual stress in their system was 200 microns. Thinner interlayers showed less plastic deformation, resulting in higher residual stresses in the ceramic and lower strength joints. Thicker interlayers have shown a slight reduction in mechanical strength, but remain higher than in the case of thinner interlayers (< 200μm).

Previous research work performed by the present author to directly braze Si_3N_4 to FA-129 was not successful as typical concave/convex fracture occurred at the edge of the ceramic body, independently of the brazing conditions used [8.2]. These results were explained by the high stress required to plastically deform the intermetallic alloy, as the yield stress ranges from 425 and 385 MPa between room temperature and 600°C [1.13]. In another set of experiments, the effect of temperature on the microstructure of brazed joints using Cu interlayers was investigated to determine the maximum possible brazing temperature for this system [8.3]. The results obtained showed that for a brazing temperature higher than 1025°C, major damage of the structure occurred. Significant diffusion of Al from the intermetallic into the Cu interlayer occurred, melting the copper interlayer and actually pushing the molten Cu-Al outside of the joint. In addition, the Cu-Al liquid penetrated the FA-129 alloy producing a decohesion of the grain structure.

The objective of this research work was to study the effectiveness of a Cu interlayer in accommodating the residual stresses produced during cooling between the Si_3N_4 and the FA-129. Reaction layer development, microstructural evolution and mechanical properties were used to characterise the joints.

8.2 Experimental Procedures

8.2.1 Raw materials

Si_3N_4 discs of 3 mm thickness (Ceralloy 147-3N, Ceradyne) were cut from the initial rods (100mmX8mm diameter) using a diamond cut-off wheel. All discs were polished down to a 1 micron finish using diamond paste. The active brazing alloy (ABA) used was produced following the procedure described in Chapter 5. FA-129 discs of 8 mm in diameter by 3 mm in thickness were machined and polished to a 1 microns finish. Cu interlayers were punched from a 300 micron thick foil. The thickness was adjusted through grinding and polishing to a thickness of 200 microns. Both surfaces were polished to a 1 micron finish using Al_2O_3 powder.

The sample configuration for microscopic evaluation was Si_3N_4/ABA/Cu/ABA/FA-129. The applied thickness of the filler metal in paste form was approximately 50 microns. The same configuration was used for the mechanical tests except that another Si_3N_4/FA-129 interface was used on the other end of the test specimen producing a sandwich sample Si_3N_4/Cu/FA-129/Cu/Si_3N_4. In both cases, all the components were cleaned in acetone in an ultrasonic bath prior to assembly.

8.2.2 DSC experiments

The independant and combined reactions involved at the interface of the Si_3N_4/Cu interlayer were characterised using differential scanning calorimetry (Netczht DSC 404-C). Comparison of the melting of; ABA, a mixture of ABA and Cu powder (50-50 vol%), a mixture of ABA and Si_3N_4 powders (30-70 vol%) and a mixtures of ABA, Cu and Si_3N_4 powders (39-31-30 vol%) was conducted under a heating rate of 40°C/min. The alumina crucible was lined with Nb foil to avoid contact between ABA and the crucible (a major exothermic peak would otherwise occur when Ti from the molten ABA will reacts with Al_2O_3). All experiments were carried out in flowing high purity argon.

8.2.3 Bonding procedure

The sample was inserted in a graphite die surronded by BN powder and placed in a controlled atmosphere graphite furnace. A static pressure of 300 kPa was placed on the top of the sample and was maintained during all tests. The furnace was heated to the soaking temperature at a heating rate of 10°C/min and then cooled at 5°C/min. The soaking temperatures studied were 925, 975 and 1025°C for holding times of 1, 3, 6 and 12 minutes, respectively. Flowing argon was used during all the joining cycles.

8.2.4 Microscopic evaluation

Selected samples were cut, mounted and polished for microscopic evaluation. An optical microscope with an image analysis system (CLEMEX System), an SEM coupled with an EDS system (JEOL-840/EDAX), and a low voltage SEM coupled with an EDS detector (Hitachi S-4700/Oxford) were used to characterize the joints.

8.2.5 Mechanical properties

Four-point bending tests were performed using the longer sandwich samples where each ceramic bar was 2.5 cm in length instead of 3 mm as for the microstructural evaluation samples. Testing was performed at room temperature on a universal testing machine (Tinius Olsen H25K-5) using a cross-head speed of 0.5mm/min. The inner and outer spans were respectively 20mm and 40mm. Each value reported is the average of three tests.

8.3 RESULTS

8.3.1 Joint simulation in DSC

Differential scanning calorimetry was used to identify the melting and reaction sequences of the active brazing powder with the various components in the joint. Figure 8.1 presents four DSC traces; melting of ABA powder, melting of ABA in the presence of Cu, melting and reaction of ABA with Si_3N_4 and melting of ABA in presence of Cu and Si_3N_4, respectively. Each of these tests was performed under the same conditions.

Trace 1- The melting of the filler metal occurs in one single event, between 886 and 915°C. As the powder is composed of the Cu-Ti diffusion couple, melting initiates in the core of the powder, more specifically in the Cu_4Ti-Cu_3Ti_2 two-phase region (See Chapter 6). The energy absorbed for the complete melting of the powder is –114J/g.

Trace 2- In the presence of copper powder, a dilution effect should occur. In this case, the melting occurs in two stages. Melting also starts at 886°C but an exotherm starting at 894°C is also observed. The mixture starts to absorb energy again and the second endotherm is observed at 898°C. This suggests solidification by dissolution of Cu from the pure powder to the reactive liquid up to its maximum solubility and re-melting of the powder as the temperature of the furnace reaches the liquidus of the powder. The overall energy for the melting event in the presence of copper decreases to -54 J/g.

Trace 3- The third curve presents the reaction behavior between the active brazing alloy and Si_3N_4 powder. Melting of the filler metal begins and initiation of the reaction between Ti and Si_3N_4 starts before complete melting of the ABA powder occurs. This suggests that molten active liquid has reached the surface of the powder and come in contact with the ceramic powder. The temperature where the exotherm starts is 894°C. This temperature is identical to the temperature where the first exotherm begins in the case of ABA-Cu mixtures. The total melting and reaction energy in this case is +141 J/g. The annihilation of the melting peak is due to the high energy released during the reaction between Ti and Si_3N_4 to form TiN and Ti_5Si_3.

Trace 4- The last trace describes the simulation of a joint comprising Si_3N_4/ABA/Cu. A similar behavior to that for the sample Si_3N_4/ABA was observed; initiation of melting and reaction with the ceramic when the active liquid reaches the surface. However, the presence of copper has an effect on the energy released by the reaction as competition between dilution (solidification) and reaction occurs. The simulation of a joint formation shows a complete melting and reaction energy of +100J/g, indicating the effect of ABA dilution by Cu.

8.3.2 Microstructural analysis

Figure 8.2 presents representative optical micrographs of (a) the complete joint, (b) the interface between the FA-129 and the Cu interlayer and (c) the interface between the Cu interlayer and the silicon nitride ceramic. The sample was brazed at 975°C for 6 minutes. Two different types of reaction are occuring simultaneouslty on both sides of the Cu interlayer. At the FA-129/Cu interface, the characteristic Cu color was not found but a yellow layer is present (under optical microscope). This layer is a solution of Cu and Al formed from diffusion of Al from the iron aluminide alloy into the active brazing alloy. In addition, the presence of molten ABA in contact with the iron aluminide produces a reaction zone (100 microns in this case), where the thickness is a function of brazing temperature and time. However, the morphology of the reaction layer is similar and only the thickness changes. The Cu/Si_3N_4 interface shows the formation of a reaction layer at the surface of the ceramic and diffusion of the excess ABA into the Cu interlayer. A zone possessing the characteristic copper color between both diffusion zones is observed, suggesting that the complete interlayer has not yet been affected by diffusion.

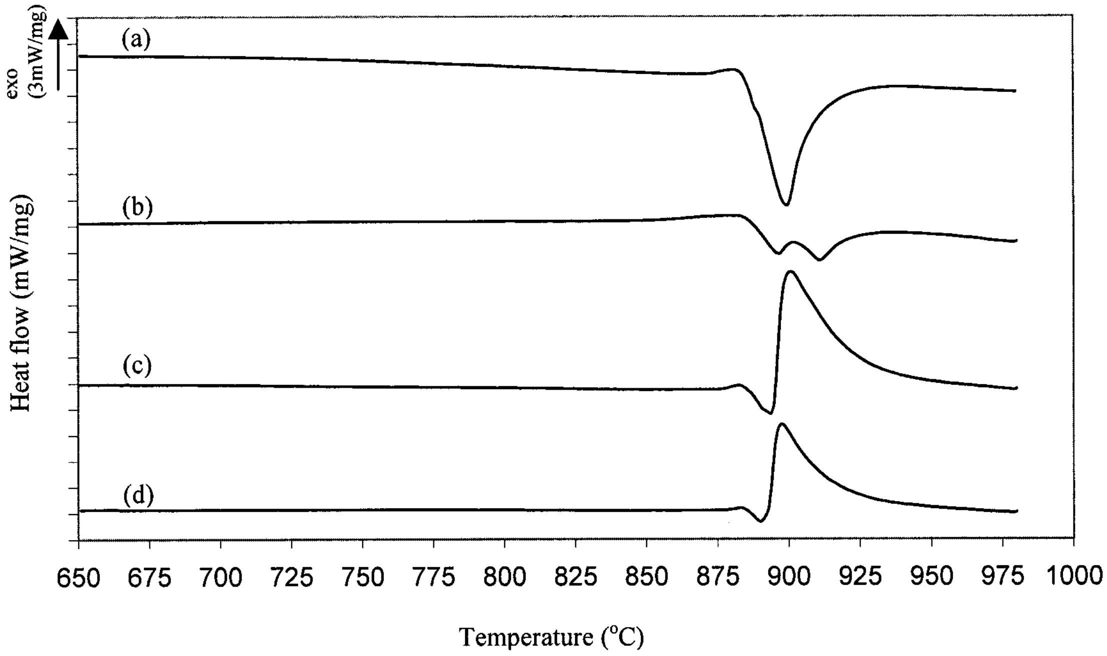

Figure 8.1 - Four DSC traces; (a) melting of single ABA powder, (b) melting of ABA in presence of Cu, (c) melting and reaction of ABA with Si_3N_4 and (d) melting of ABA in presence of Cu and Si_3N_4.

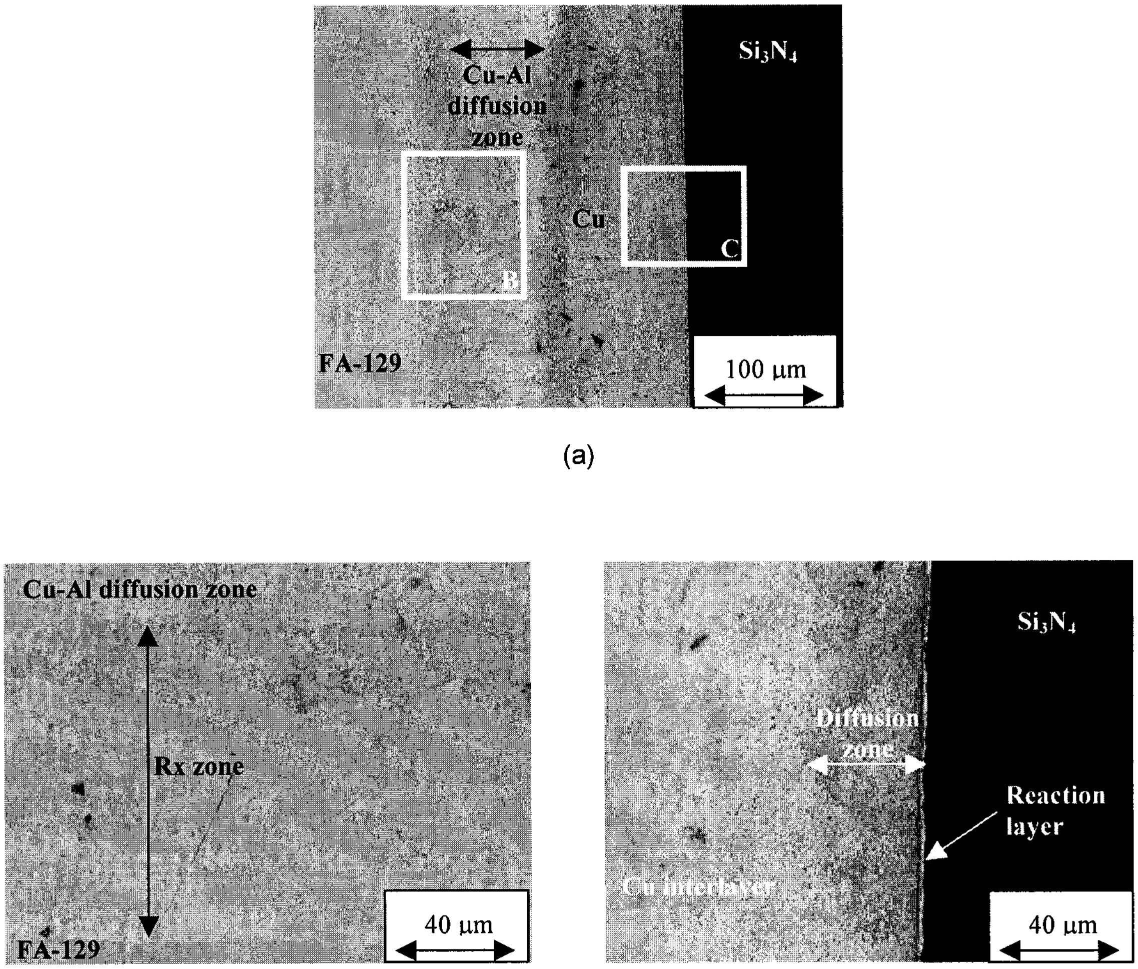

(a)

(b)

(c)

Figure 8.2 - Optical micrograph of (a) a complete interface, (b) the FA-129/Cu interface and (c) the Cu/Si_3N_4 interface.

8.3.2.1 Si_3N_4/Cu interface characterisation

Figure 8.3(a) presents a general back-scattered micrograph of the Cu/Si_3N_4 interface of a sample brazed at 925°C for 12 minutes. In addition to the reaction layer, another type of precipitate is observed close to the reaction layer. The EDS spectrum of this phase is presented in Figure 8.3(b). The main peaks detected are Cu, Si and Ti. The Cu-Ti-Si phase is in contact with the reaction layer in some locations. These precipitates are observed up to a distance of 70 microns from the interface.

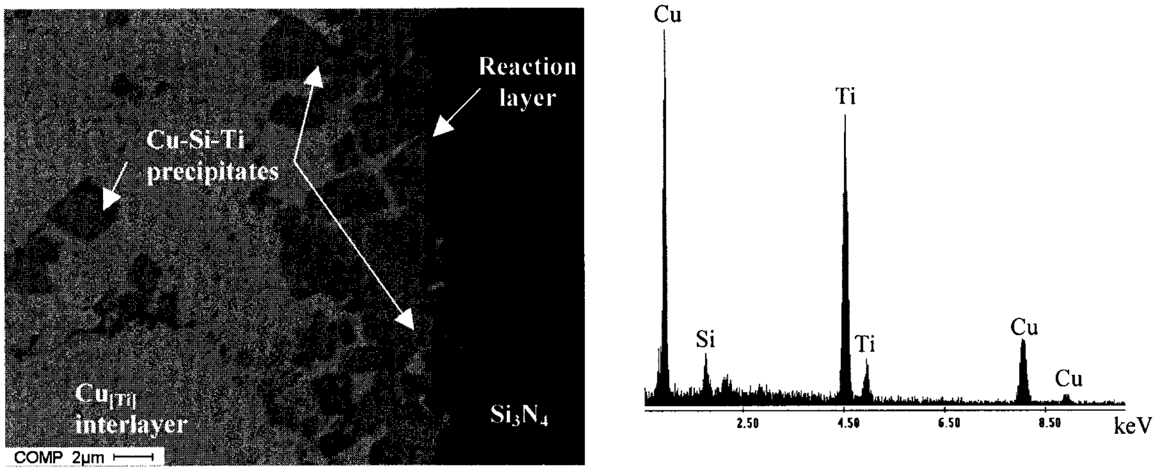

(a) (b)

Figure 8.3 - (a) Back-scattered micrograph of a Si_3N_4/Cu interface and (b) EDS analysis of the precipitate identified in Fig 3(a).

Figure 8.4 presents back-scattered micrographs of the interface between the Si_3N_4 and the Cu interlayer for samples brazed at (a) 975°C for 1 minute, (b) 1025°C for 1 minutes and (c) 1025°C for 12 minutes. Figure 8.5 presents the low voltage line scan of the interface shown in Figure 8.4(b) (dashed line). In all three cases, the interface is composed of two layers possessing similar atomic number composition, independent of the joining conditions. The joining conditions do however, effect the relative thickness of both components of the reaction layer. The low voltage line scan indicates a layer rich in Ti and N adjacent to the interface of the ceramic and a layer rich in Ti and Si and containing Cu next to this layer. The Ti and N-rich layer is believed to be TiN and the Ti-Si is believed to be a Ti_5Si_3 compound containing a certain level of Cu in solution. The effect of temperature on the morphology of the layer shows that both layers grow and the thickness ratio between the TiN layer and the total reaction layer thickness slightly increases with increasing temperature. However, the effect of time at high temperature definitely shows a significant increase in the TiN layer with respect to the total reaction layer. Si has been detected in the filler metal and its concentration decreases further from the reaction layer. The similarity between the Ti and N line scan is produced by the convolution of the X-rays peaks (Ti Lα and NKα).

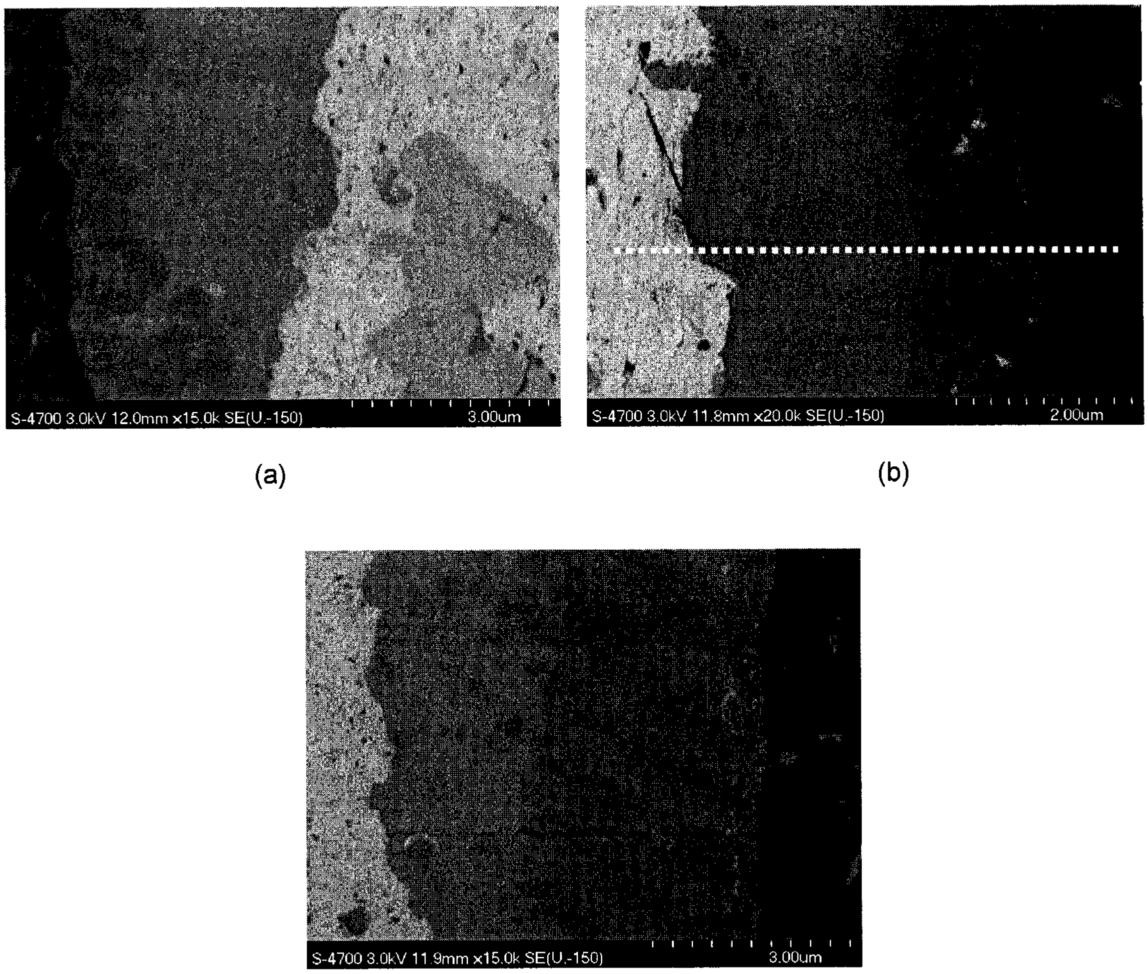

(a) (b)

(c)

Figure 8.4 - Back-scattered micrographs of the interface between the Si_3N_4 and the Cu interlayer for sample brazed at (a) 975°C for 1 minute, (b) 1025°C for 1 minutes and (c) 1025°C for 12 minutes.

As the reaction layer growth is a more complex phenomenon than a single reaction system - due to evidence of growth competition between the different reactions - the total reaction layer thickness was measured as a function of brazing parameters and the results are presented in Figure 8.6. The reaction layer thickness ranges between 0.85 to 5.1 microns. In all three cases, the data fits the final part of a parabolic trend, suggesting that the growth follows a diffusion controlled type of reaction. In addition, the fit suggests that in all cases, the growth rate is diminishing to zero, indicating that the growth is near the end point.

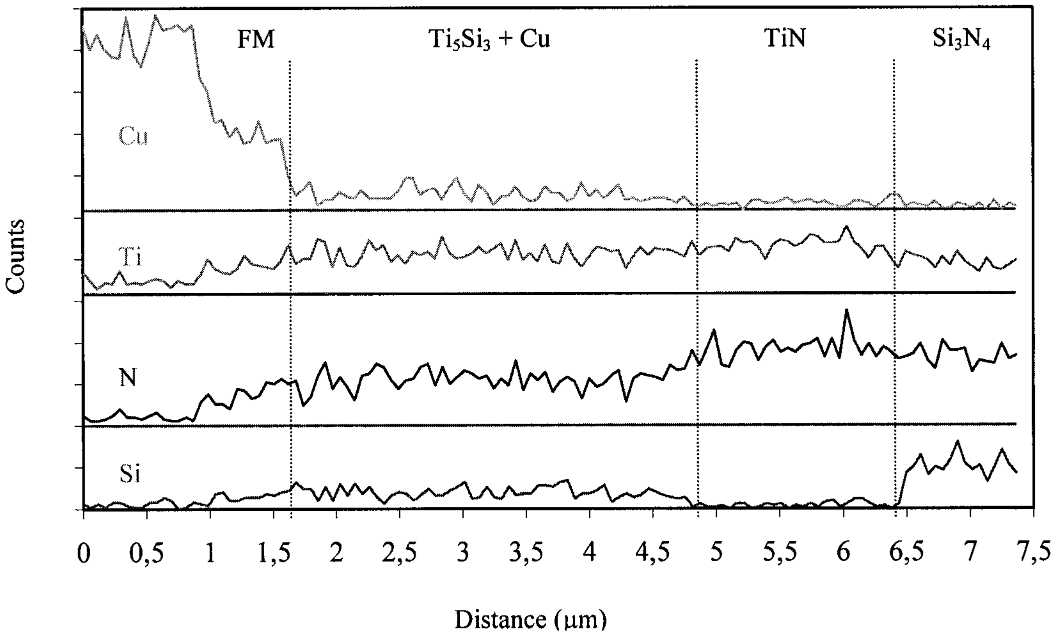

Figure 8.5 - Low voltage line scan of the reaction layer observed in Fig 8.4(b).

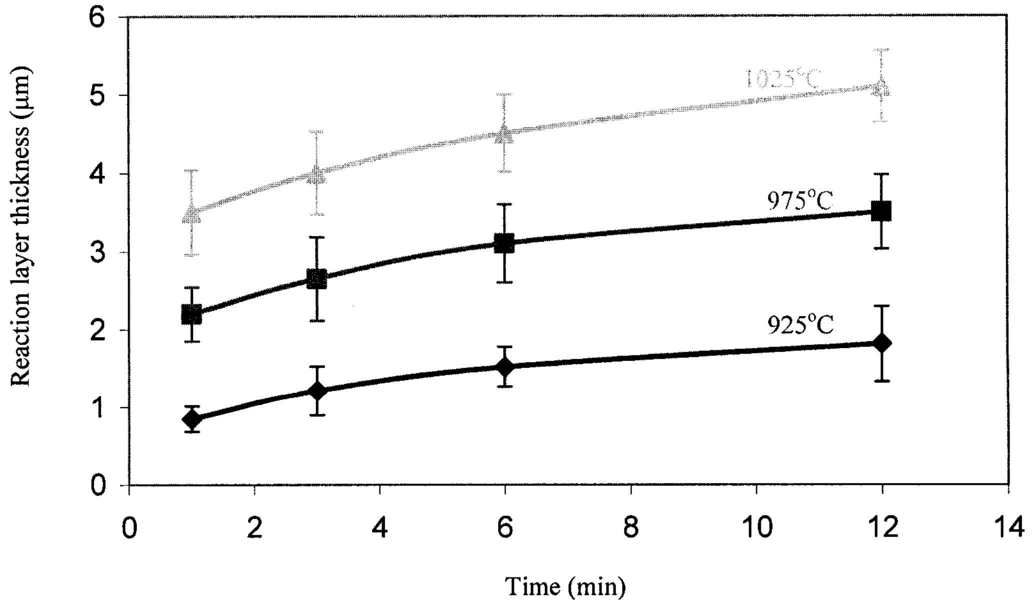

Figure 8.6 - Reaction layer thickness as a function of brazing parameters.

The parabolic growth law was firstly applied to the reaction layer growth data obtained and the results are presented in Figure 8.7(a). In all three cases, the diffusion controlled growth (linear fit) is in agreement with the experimental measurements. None of the trend lines in Figure 8.7(a) pass through the origin, implying that even for very short joining conditions, the solid-liquid reaction is completed (the reaction layer completely covers the Si_3N_4 ceramic surface) and a diffusion process is now controling the further growth of the layer. The good fit of the linear behavior suggests that the parabolic equation is valid for this case and that other analyse such as the Jonhson-Mehl equation are not necessary [7.3] (see appendix A for more details). The effective activation energy calculated for the layer growth is 137 kJ/mol and the plot is presented in Figure 8.7(b).

8.3.2.2 Cu/FA-129 interface characterisation

Figure 8.8(a) presents a back-scattered micrograph of the iron aluminide alloy very close to the Cu/FA-129 interface for a joint brazed at 975°C for 3 minutes. The remainder of the FA-129 bulk material is observed on the left hand side. Cu diffusion in the iron alumide structure is observed as small bright dots. The iron aluminide alloy presents a wavy interface, suggesting dissolution into the molten active metal. Some precipitates are formed close to the iron aluminide dissolution zone. Two distinct compositions are observed and their respective EDS analyses are presented in Fig 8.8b and Fig 8.8c, respectively. The darker precipitates are Ti-based and the brighter ones are Fe-based. All the precipitates formed are surrounded by a Cu-Al alloy.

Figure 8.9(a) presents a back-scattered montage of the complete interface between the FA-129 alloy and the Cu interlayer brazed at 975°C for 3 minutes. The EDS analysis of the larger precipitates is presented in Figure 8.9(b). The chemical analysis of the Ti-based precipitates is similar, independently of the distance from the FA-129 bulk material. The micrograph shows that the Fe-based precipitates are only observed near the interface and that the Ti-based precipitates are present much further from the interface. The Ti-based precipitates are believed to be formed from a combination of the Ti from the active brazing alloy and slight dissolution of the Fe_3Al intermetallic in the Cu-Al molten liquid. Figure 8.9(c) presents the EDS analysis of the Cu-Al matrix and shows that at distances over 100 microns, Al is still present.

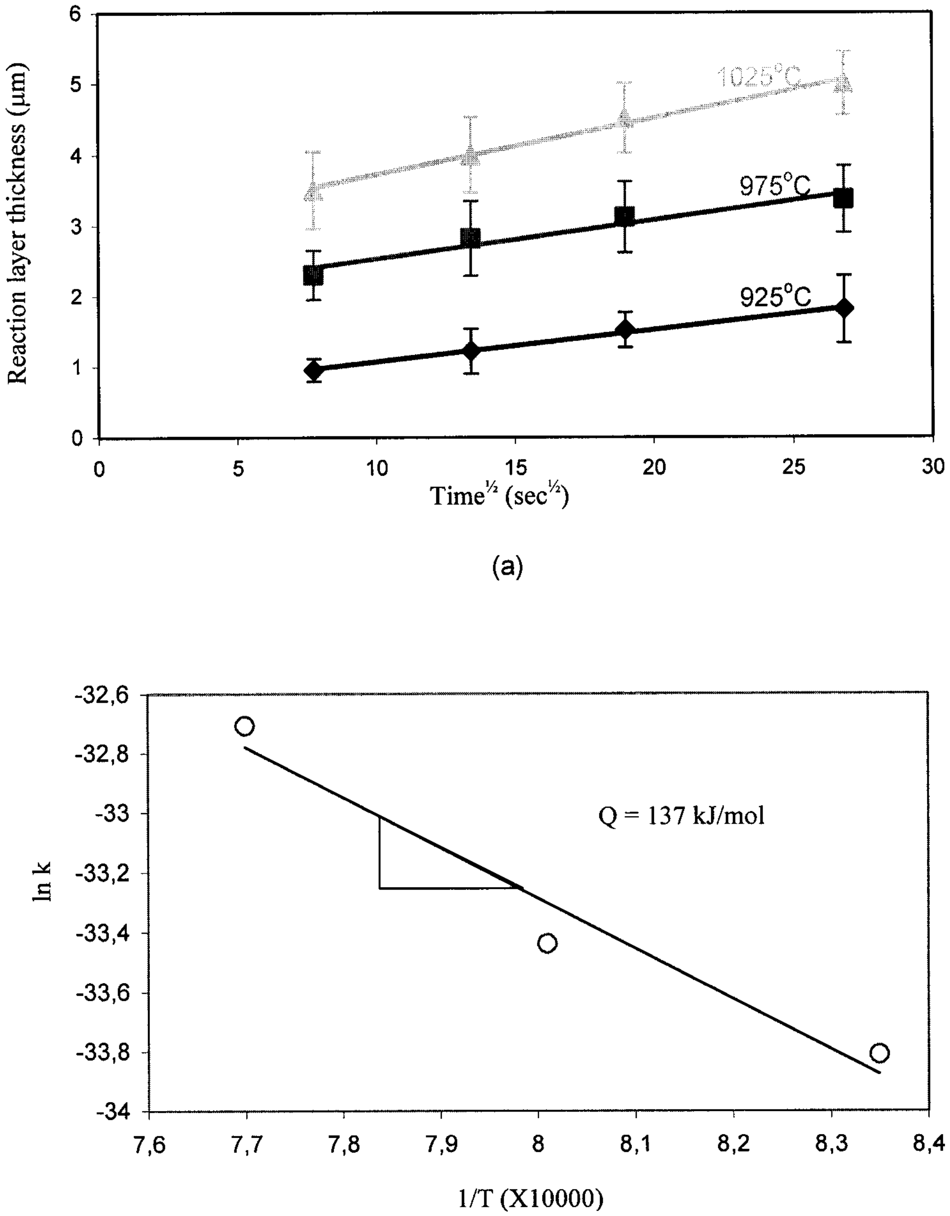

(a)

(b)

Figure 8.7 - Modeling of the reaction layer growth by (a) parabolic analysis and (b) activation energy measurement with Arrhenius equation.

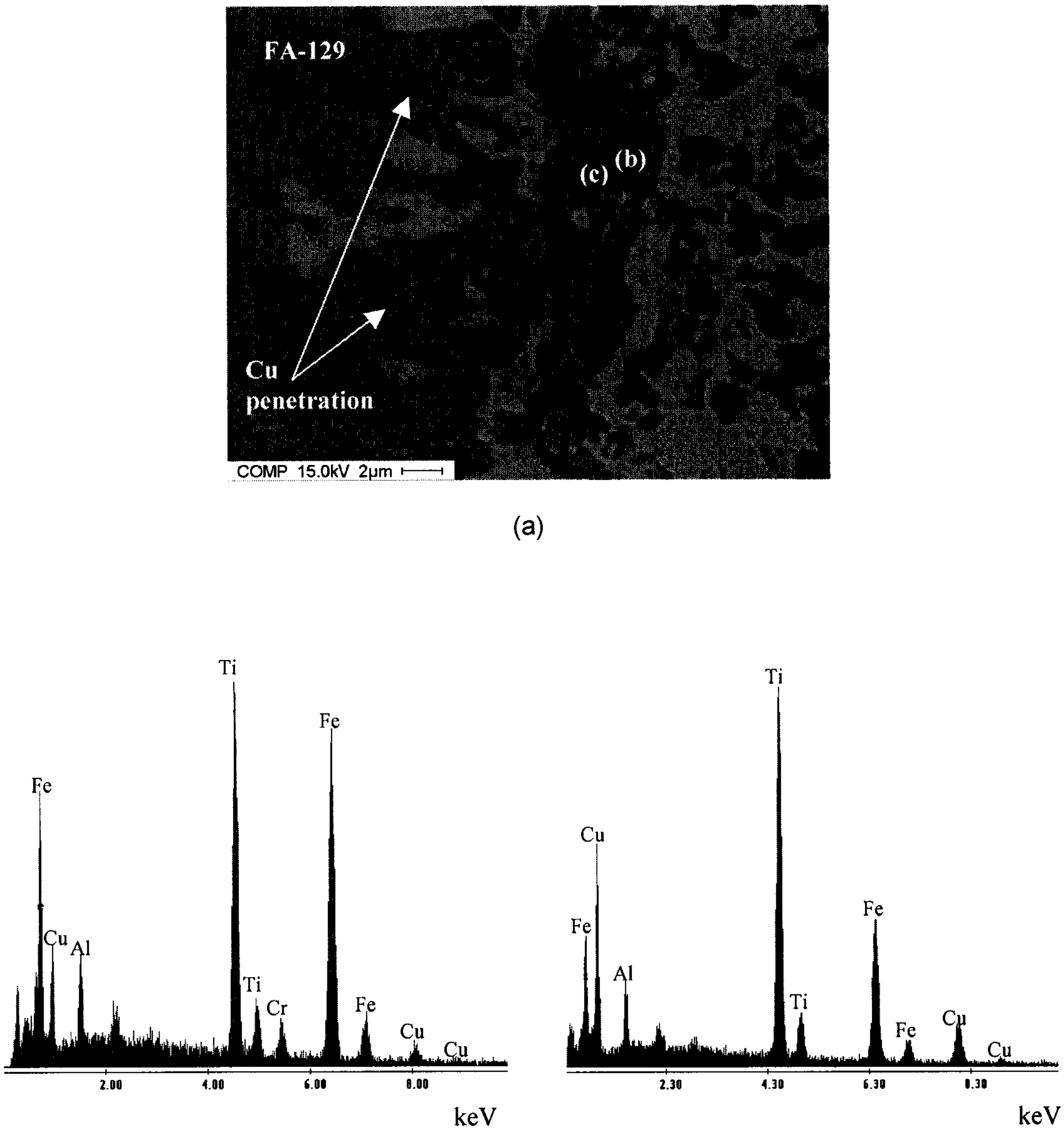

(a)

(b)

(c)

Figure 8.8 - (a) Back-scattered micrograph of the FA-129 very close to the Cu/FA-129 interface, (b) and (c) EDS analyses of two reactions products formed close to the intermetallic.

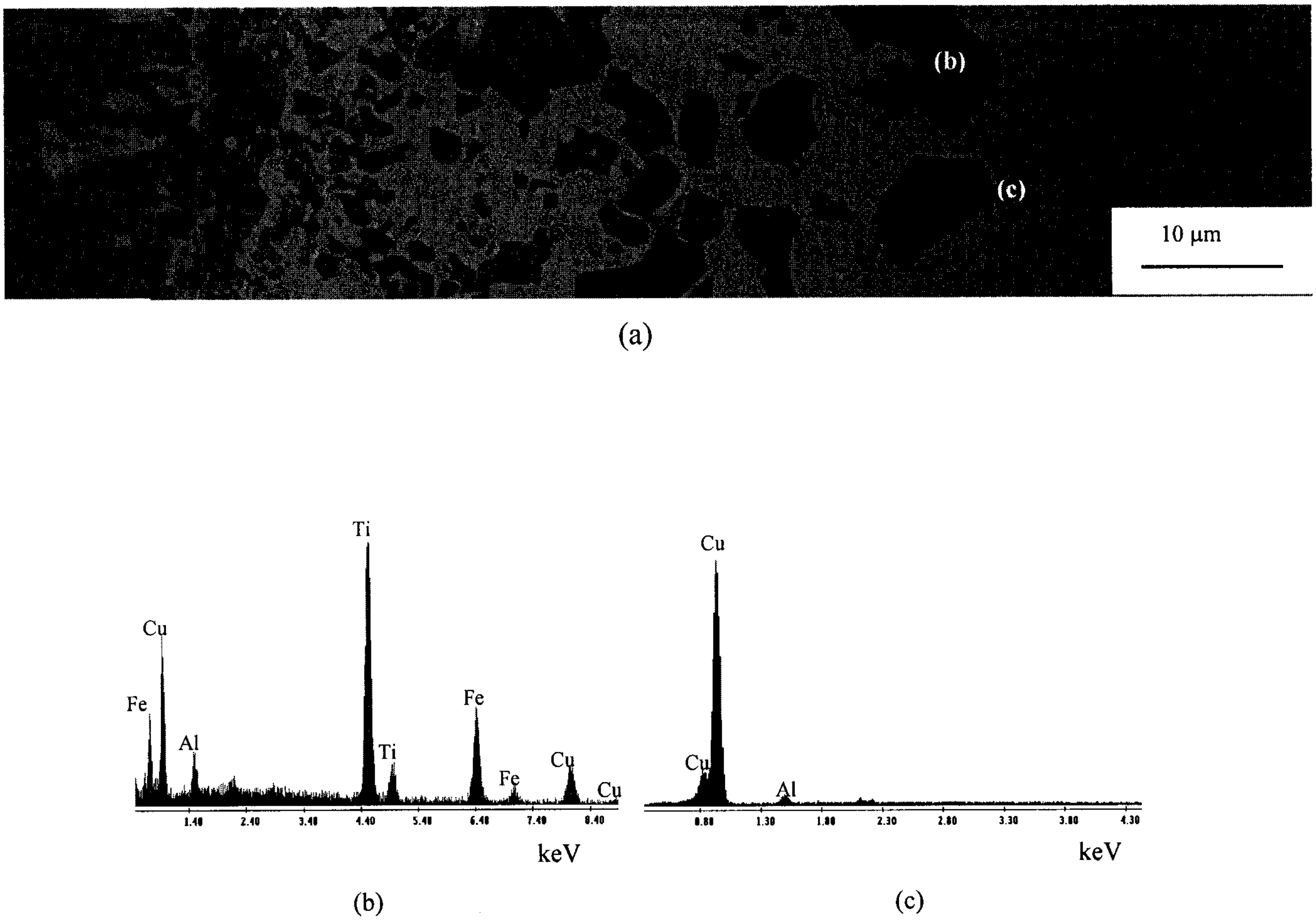

(a)

(b)

(c)

Figure 8.9 - (a) Back-scattered montage of the FA-129/Cu interlayer interface, (b) EDS analysis of Ti precipitates and (c) EDS analysis of Cu-Al matrix, respectively.

8.3.3 Mechanical properties

Figure 8.10 presents the results of the four-point bending tests performed on the joint as a function of the reaction layer thickness. These samples were selected as, within the error bars, they represent a range of reaction layer thicknesses. Their respective joining conditions can be derived from Figure 8.6. The strength increases with the reaction layer thickness. The peak value obtained is 160 MPa. In all cases, the fracture occurs through the ceramic interlayer interface, suggesting that the reaction between the iron aluminide alloy and the Cu interlayer possesses a strength higher than 160 MPa.

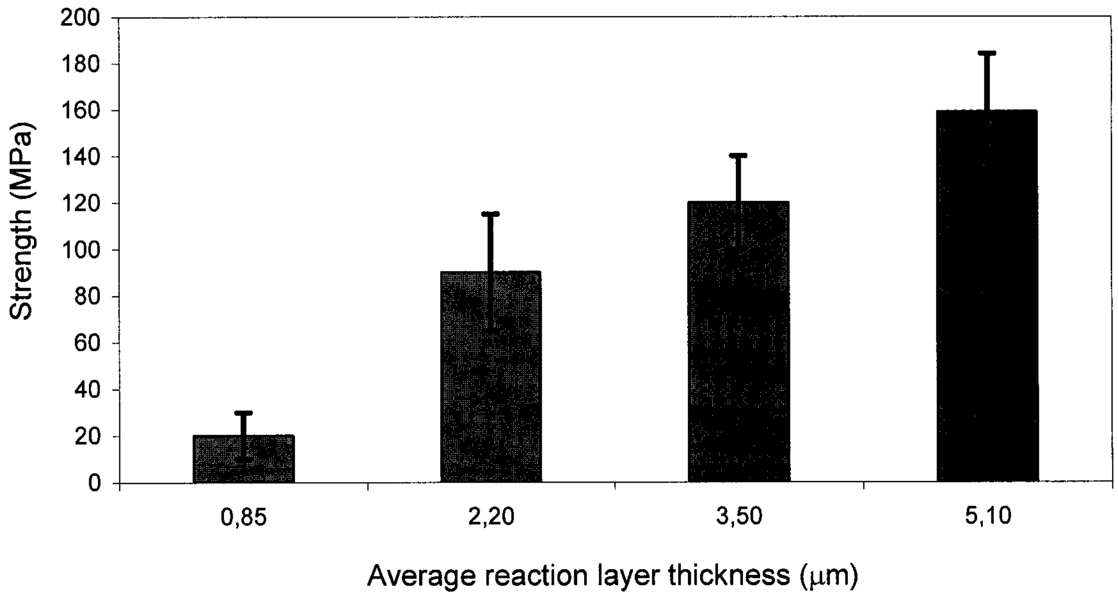

Figure 8.10 - Four-point bending strength of the joints as a function of reaction layer thickness.

8.4 Discussion

The copper interlayer has two main functions: (1) to reduce the residual stresses produced during cooling and (2) to dilute the active brazing alloy by Ti diffusion to obtain a better control on the reaction layer growth. At first, the insertion of the copper seems to have beneficial effects on the joint reliability as sound joints have been produced, as opposed to results obtained previously with direct brazing.

The microstructure formed at the ceramic/interlayer interface is mainly composed of a reaction layer, evolving with time and temperature. This reaction layer is composed of a bi-layer system of TiN and Ti_5Si_3 containing Cu. During reaction between the Ti and the Si_3N_4, TiN and Ti_5Si_3 are the most thermodynamically favorable compounds to be formed [6.5]. However, their respective growth is a function of the adjacent solute composition and the chemical interaction with the reaction layer. The dissolution of the Ti_5Si_3 layer in the filler metal also reduces the thickening. This is observed by the presence of precipitates containing Cu, Ti and Si close to the reaction layer. The silicon content of these precipitates is obviously coming from the Si_3N_4, as its the only source of Si in the system. These precipitates are also present in higher quantity when the brazing conditions are increased.

The reaction competition is also influenced by the dilution of Ti in the Cu interlayer as observed by DSC and modelling of the reaction layer growth. The DSC results show that Cu powder reduces the fusion energy of the active brazing alloy by solidification. Moreover, the joint simulation shows clearly the effect of Cu by reducing the fusion energy by 33%, compared with similar powder mixtures of Si_3N_4 powder and active brazing alloy. Modelling the reaction layer growth through the parabolic law has given an activation energy of 137 kJ/mol. This activation energy is slightly more than double the energy calculated for the system Si_3N_4/ABA/Si_3N_4 using the same starting materials (see Chapter 7). The diffusion of titanium towards the Cu interlayer reduces the availability near the reaction layer front and then slows the growth rate. The presence of Ti has been detected at more than 70μm from the interface.

The interface between the FA-129 and the Cu interlayer is more complicated to explain as a series of reactions occur simultaneously. The formation of a Cu-Al alloy from diffusion occurs in parallel to the penetration of Cu into the iron aluminide alloy. Fe possesses a low solubility in pure Cu but increases slowly in the molten stage. The presence of Ti is believed to increase the solubility of Fe in the filler metal but no phase diagrams are available to confirm this hypothesis. The variation in the composition of both precipitates should be related to the distance from the dissolution point as the precipitates rich in Fe are closer to the FA-129 and the Ti-rich precipitates, away from the interface, are formed from the solidification of the filler metal in the presence of a slight concentration of Fe. Again, no phase diagrams are available to confirm this statement.

The mechancial properties were tested as a function of their total interlayer thickness. From a reaction layer point of view, the maximum strength of the joints will be hardly increased above 160 MPa as the reaction layer growth rate slows down after 12 minutes for all conditions and the effect of time becomes a minor factor. To increase the reaction layer, an increment in the brazing temperature has to be used, but previous results have demonstrated that 1025°C is nearly the maximum operating temperature for this system. Increasing the brazing time at 1025°C has shown strong growth of the TiN layer compared to the total reaction layer.

8.5 References

[8.1] T.W. Kim and S.W. Park, Effects of Interface and Residual Stress on Mechanical Properties of Ceramic/Metal System, Key Engineering Materials, Vols. 183-187, 2000, p1279-1284.

[8.2] M. Brochu, M.D. Pugh and R.A.L. Drew, Microstructure Evolution during Partial Transient Liquid Phase Bonding of Silicon Nitride to an Iron Aluminide Alloy, Proceeding of the Metal/Ceramic Interactions Symposium, COM 2002, CIM, Montreal, Canada, p45-56.

[8.3] M. Brochu, M.D. Pugh and R.A.L. Drew, Active Brazing of Silicon Nitride to Iron Aluminide Alloy, Proceeding of the 10th International Ceramic Congress & 3rd Forum on New Materials, Florence, Italy, July 14-18, 2002, p757-765.

Chapter 9

PTLPB of Si_3N_4 to FA-129 using Nickel as a Core Interlayer

9.1 Introduction

Partial transient liquid phase bonding (PTLPB) is another process which has received considerable attention over the past five years [1.26, 1.36-1.38, 9.1]. It combines the advantage of brazing - as the interface is created from a liquid phase - and diffusion bonding, as the excess liquid diffuses into a complementary core interlayer to completely remove the existence of a low melting point layer at the interface. This process has great potential for high temperature applications due to the isothermal solidification (with service at higher than the joining temperature). In most cases, the PTLPB systems are composed of two types of interlayers. A very thin layer of metal is deposited at the surface of the ceramic and put in contact with the core layer, which possesses a much higher melting temperature. The liquid formation is achieved through two different routes: the liquidus of the low melting point interlayer is exceeded or, interdiffusion between the core and the low melting point layer will form a eutectic liquid [1.26]. In both cases, the solidification of the joint must be performed by isothermal solidification. The utilization of such thin interlayers involves deposition techniques, such as sputtering. However, research into systems using thicker components, to ease processing, have been performed. Zheng et al. [1.38] have found that using thicker interlayers may lead to interesting results: joint strengths of 250 MPa were achieved for the Si_3N_4/Ti/Cu/Ni system.

The objective of this chapter was to evaluate the possibility of bonding silicon nitride ceramic to an iron aluminide alloy through a PTLPB process. Thicker interlayers were used to evaluate the properties of the joints and to compare them to literature results. The joint is composed of two independent systems. PTLPB of Si_3N_4 to Ni, (the core interlayer in this study) and TLPB of Ni to Fe_3Al alloy.

9.2 Experimental Procedure

9.2.1 Starting materials

The silicon nitride was cut into 3 mm thick discs, which were then polished to a 5 micron finish. Round samples of FA-129 of 8mm diameter by 6mm thick were machined from the raw material and similarly polished. The active brazing alloy was produced following the procedure described in Chapter 5. A thin film of this paste was deposited on the surface of the ceramic. Ni interlayers of 8mm diameter were punched from a plate of 0.787 mm initial thickness. The thickness was reduced to 0.7mm when both sides where polished to a 5 micron finish. Al discs of 8 mm diameter were punched from commercially available Al foil of 30 microns thickness. The Cu buffer layer was also punched from foil 60 microns thick giving 8 mm diameter discs. Each of these materials was cleaned prior to bonding in acetone and ethanol for 15 minutes in an ultrasonic bath. Figure 9.1 shows a sketch of the assembly of the multiple interlayer joint.

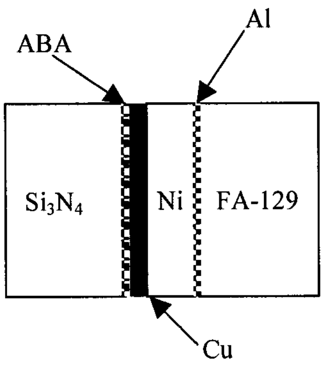

Figure 9.1 - Sketch of the multiple interlayer joint.

9.2.2 Bonding procedure

The joining cycle was carried out in a controlled atmosphere graphite furnace. The sample was embedded in a powder bed of boron nitride inside a graphite die. A pressure of 300 kPa was applied to the top of the jig to keep the sample aligned. Different homogenization temperatures were tested (between 1100 and 1200°C) for each holding time ranging between 1.5 and 6 hours. The process cycle began by heating at 10°C/minute up to the first soaking temperature (reaction stage). This initial soaking temperature was varied between 950°C to 1100°C to allow the formation of a reaction layer at the ceramic interface. In all cases, the initial soaking time was 30 minutes. This was followed by a second heating ramp at 5°C/minute up to the homogenization temperature, soaking, and finally, cooling from the diffusion plateau at a rate of 5°C/minute to 300°C. Flowing argon was maintained during the cycle. The heating profile is presented in Figure 9.2.

9.2.3 Microstructural Analysis and Mechanical Testing

Samples were cut, mounted and polished for microstructural evaluation. X-ray diffraction (Philips PW1710, CuKα), SEM coupled with an EDS system (JEOL-840/ EDAX), FESEM coupled with an EDS system (Hitachi S-4700/ Oxford), EPMA coupled with a WDS system (JEOL-8900) and 25g microhardness (LECO-M-400-2) were used to characterize the joints. Samples with a similar interlayer thicknesses to the microstructure evaluation samples were fabricated but longer pieces (2.5 cm) of Si_3N_4 were bonded on each side of the iron aluminide alloy. Four-point bending tests were performed at room temperature on a universal testing machine (Tinius Olsen H25K-5) using a crosshead speed of 0.5mm/min. The inner and outer span distances were respectively 20mm and 40mm. Each value reported is the average of three tests.

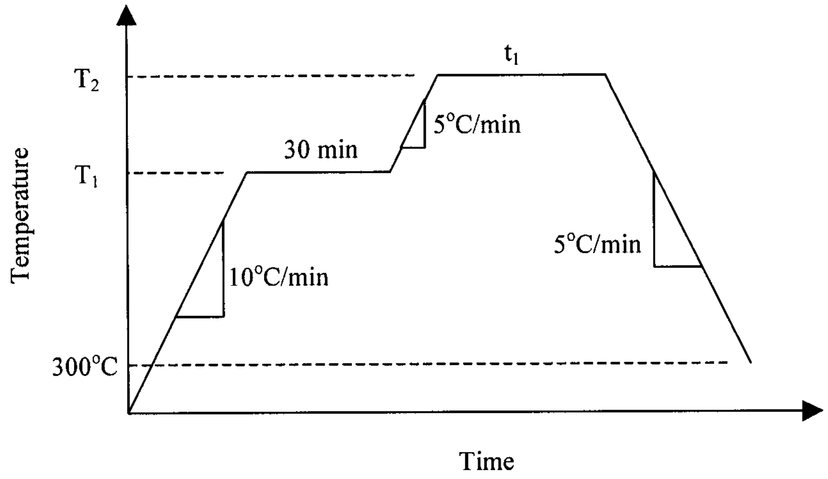

Figure 9.2 – Heat treatment profile.

9.3 Results

9.3.1 Microstructural characterisation

9.3.1.1 Si_3N_4/Ni interface

Figure 9.3 presents a typical secondary image (SEI) micrograph of the interface created between the silicon nitride ceramic and the nickel interlayer. This particular microstructure is derived from a sample bonded at 1150°C for a homogenization time of 180 minutes. On the micrograph, features such as the reaction layer and precipitates within the Ni interlayer are observed. The reaction layer also possesses transverse cracks.

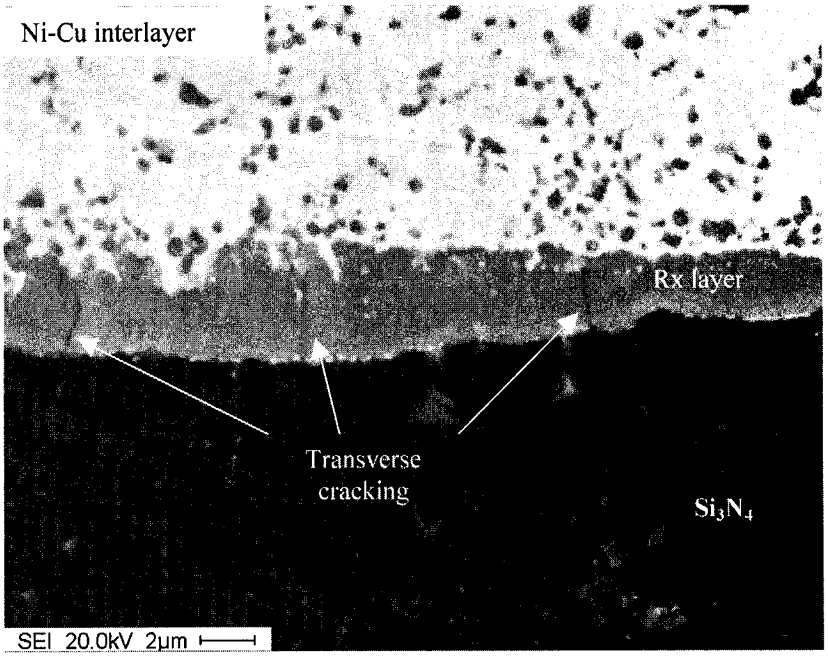

Figure 9.3 – SEI micrograph of the Si_3N_4/Ni interface.

Figure 9.4 shows the heating cycle applied to the joint as well as back-scattered micrographs of the interface and the corresponding line scan for interrupted tests and completed samples. The line scan shows that for a test interrupted at the end of the reaction soaking time (Fig 9.4(b) and 9.4(c)), the total reaction layer is composed of two layers, a Ti and N-rich layer corresponding to TiN, and a Ti and Si-rich layer corresponding to Ti_5Si_3. Cu is also observed, suggesting a certain level of solubility in the silicide. At this point, no adhesion between the copper and the nickel interlayer was observed. Convolution exists between the Ti-Lα and N-Kα x-ray lines, explaining the behavior of the Ti scan but the Ti and N-rich layer is also confirmed by the absence of Si in the reaction layer, suggesting a TiN layer. For a sample interrupted after 15 minutes of homogenization, the reaction layer is now composed only of Ti and N (Fig 9.4(d)). The same reaction layer composition was observed for samples which had completed the joining cycle (Fig 9.4(e) and 9.4(f)). These results suggests that most of the TiN layer growth occurs between the soaking time and the homogenization time.

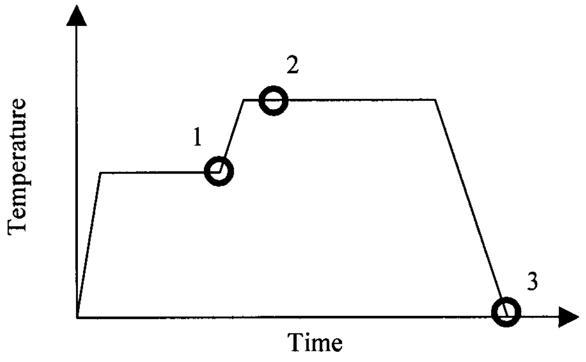
Temperature
Time
1
2
3

(a)

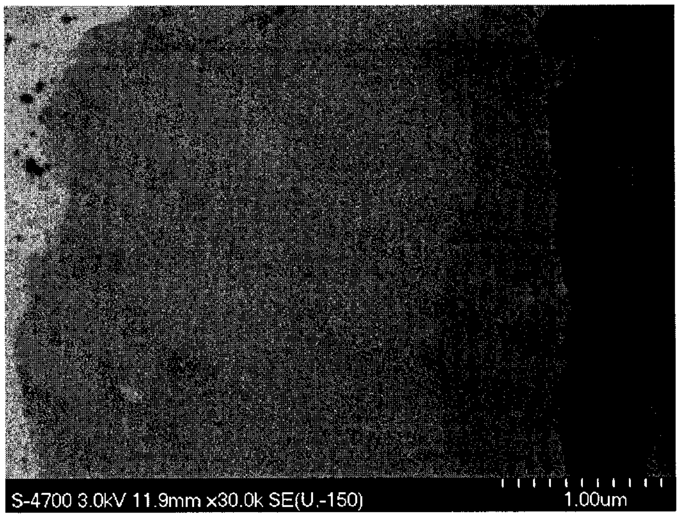
S-4700 3.0kV 11.9mm x30.0k SE(U,-150)
1.00um

(b)

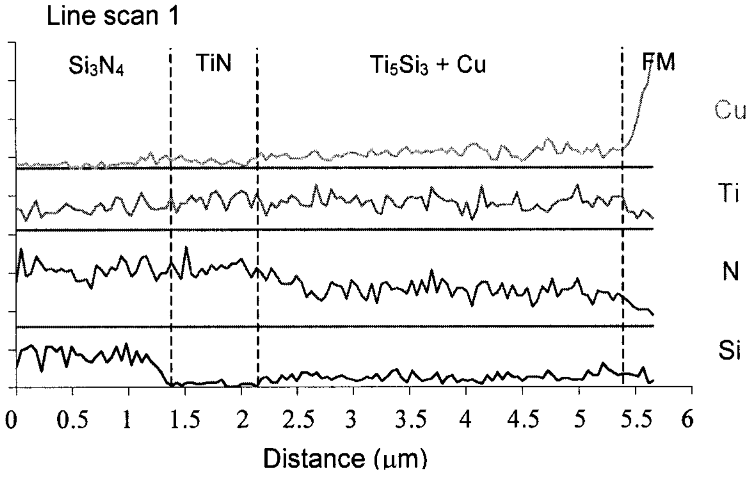
Line scan 1
Si3N4
TiN
Ti5Si3 + Cu
FM
Cu
Ti
N
Si
0
0.5
1
1.5
2
2.5
3
3.5
4
4.5
5
5.5
6
Distance (µm)

(c)

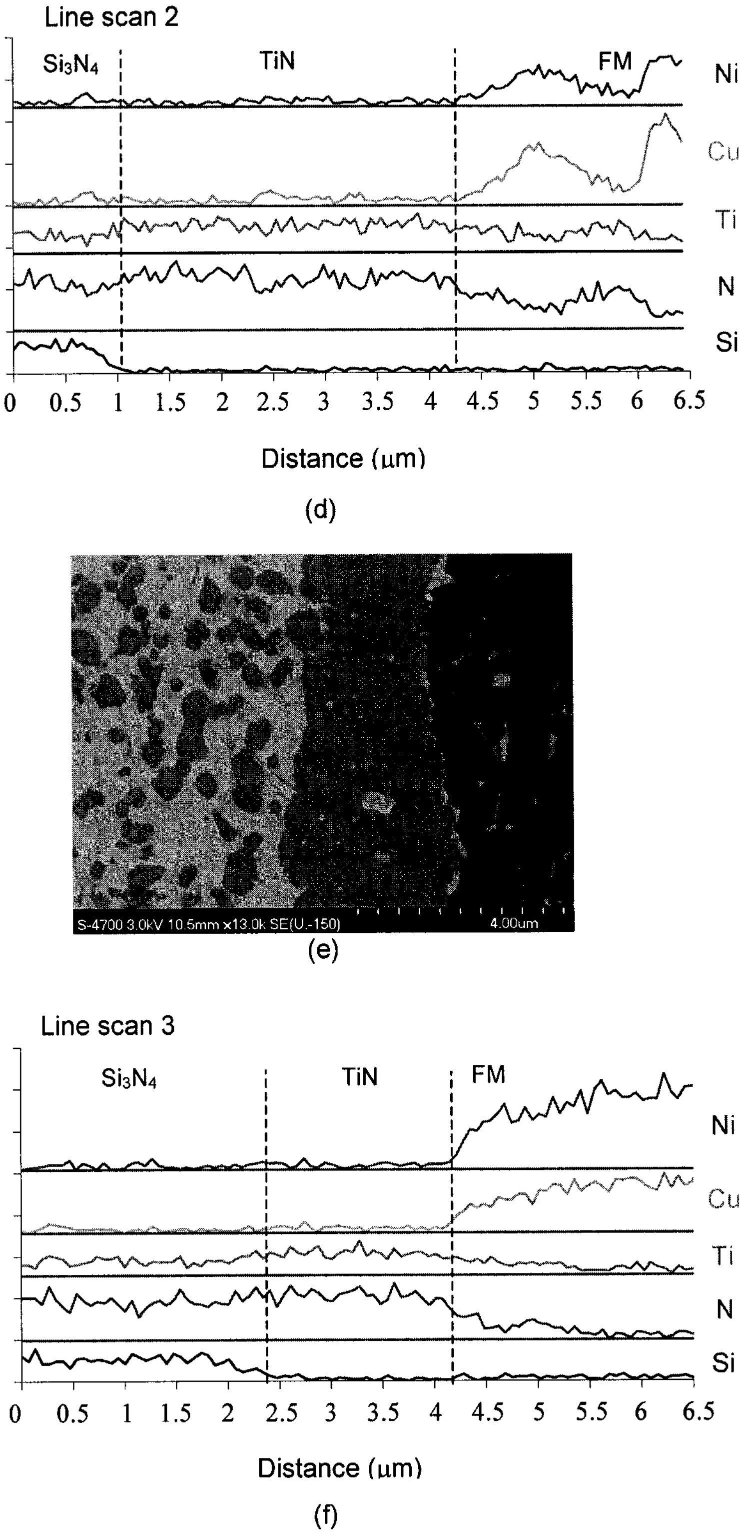

Figure 9.4 - Microstructural evolution with respect to heating cycle; (a) heat treatment, (b) back scattered micrograph of the interface at point 1 of Fig 4a, (c) line scan of Fig. 4b, (d) line scan of interface at point 2 of Fig 4a, (e) back scattered micrograph of the interface after point 3 of Fig 4a and (f) line scan of Fig. 4e.

The heat treatment performed on the sample contains two soaking periods: the first one is to achieve reaction between the brazing alloy and the ceramic and the second one is to homogenize the remaining layers inserted at the interface. Variation of the first soaking temperature was performed in order to investigate the possibility of growth of the final reaction layer (TiN). The soaking time was 30 minutes to ensure that equilibrium is reached. The thicknesses of the total reaction layer are presented in Table 9.1. All the samples were heated up to the homogenization temperature before being cooled down and analysed. Taking into consideration the standard deviation of the measurements, the temperature of the first soaking period seems to have no effect on the final reaction layer thickness. In each case, the reaction layer measured was 2.60 microns in thickness.

Table 9.1 - Effect of first soaking temperature on reaction layer thickness.

Soaking temperature (^oC)	Reaction Layer Thickness (μm)
950	2.56 ± 0.60
1000	2.72 ± 0.65
1050	2.78 ± 0.33
1100	2.50 ± 0.52

The effects of the homogenization temperature and time on the total reaction layer thickness are presented in Figures 9.5 (a) and (b), respectively. The results demonstrate that neither the homogenization temperature nor time has an influence on the reaction layer thickness. These results are similar to the values obtained for the investigation of the first soaking temperature. The similarity between the results suggests that the growth of the reaction layer between the ABA and the silicon nitride ceramic is mostly completed prior to reaching the second soaking temperature.

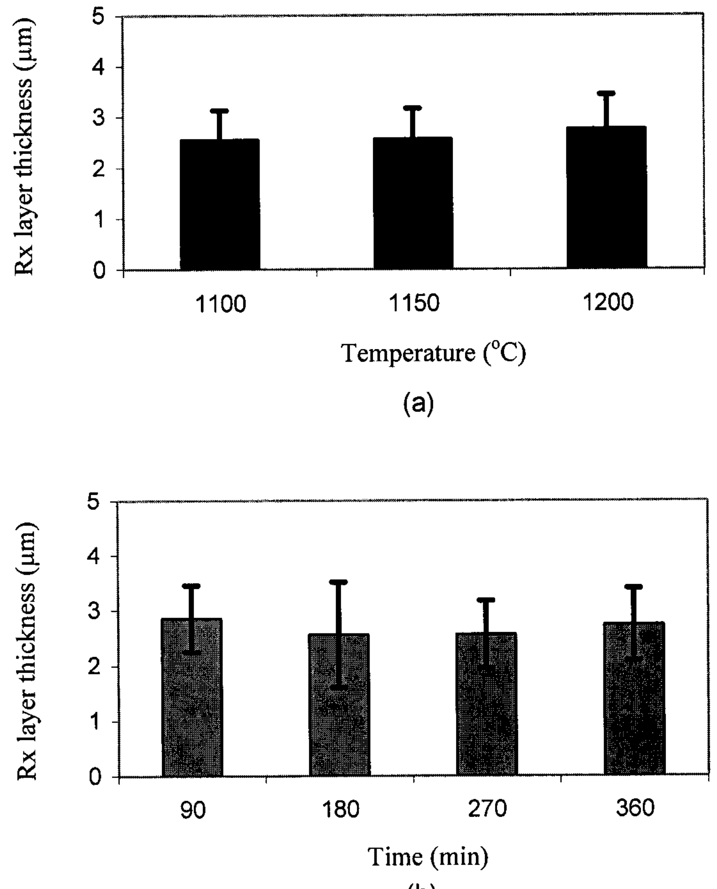

(a)

(b)

Figure 9.5 – Effect of (a) homogenization temperature and (b) time on total reaction layer thickness.

Figure 9.6 presents a representative microprobe line scan of the Si_3N_4/Ni interface. The results correlate with the microstructure, indicating a large concentration of titanium near the interface and diffusion of copper into the nickel interlayer. The titanium concentration near the interface is responsible for the reaction with the ceramic, forming the interface. The highest copper concentration was measured near the interface. For the lower homogenization conditions (in terms of diffusion), the highest copper concentration measured was 60wt%, i.e. for a sample soaked at 1100°C for 270 minutes. From the Cu-Ni phase diagram, the solidus temperature of a 60Cu-40Niwt% alloy is approximately 1240°C [9.2], demonstrating that for this lower extreme condition, enough diffusion was achieved and isothermal solidification had occurred. For any sample being joined for longer times or higher temperatures, the copper concentration near the interface is lower, raising the melting temperature of the copper-rich zone of the core interlayer. The reheating of such a sample even above the joining temperature will not necessarily re-form a liquid at the interface, demonstrating that the conditions for PTLPB were achieved.

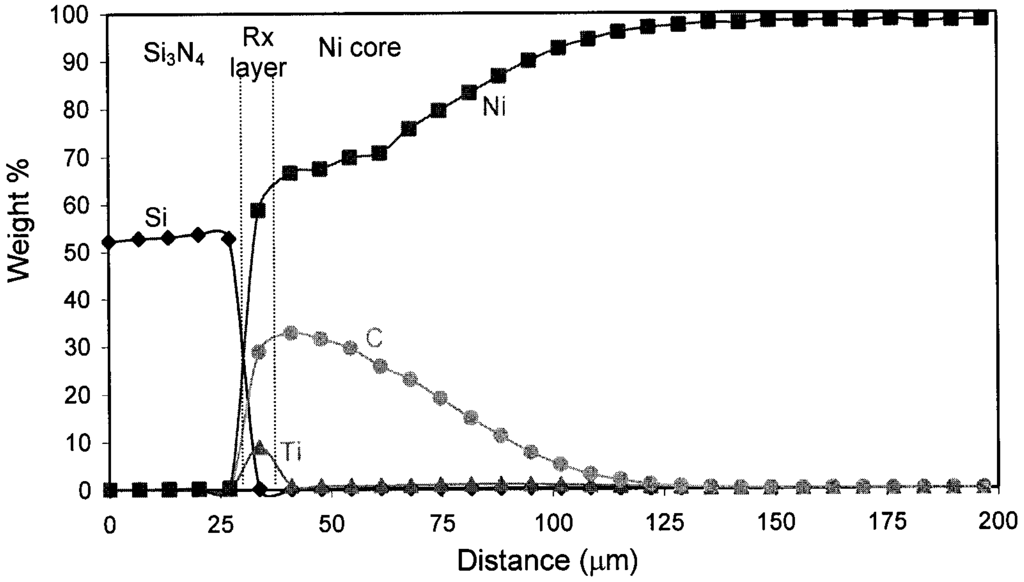

Figure 9.6 - Microprobe line scan across the Si_3N_4/Ni interface of a sample homogenised at 1150°C for 180 minutes.

Figure 9.7 presents the peak copper concentration measured close to the interface as a function of homogenization condition. It can be observed that the copper concentration decreases in a parabolic manner. The same behavior is expected for samples homogenized at higher and lower temperatures but with different diffusion kinetics. The dashed lines represents the variation of yield strength of a Ni-Cu alloy as a function of the composition [9.3].

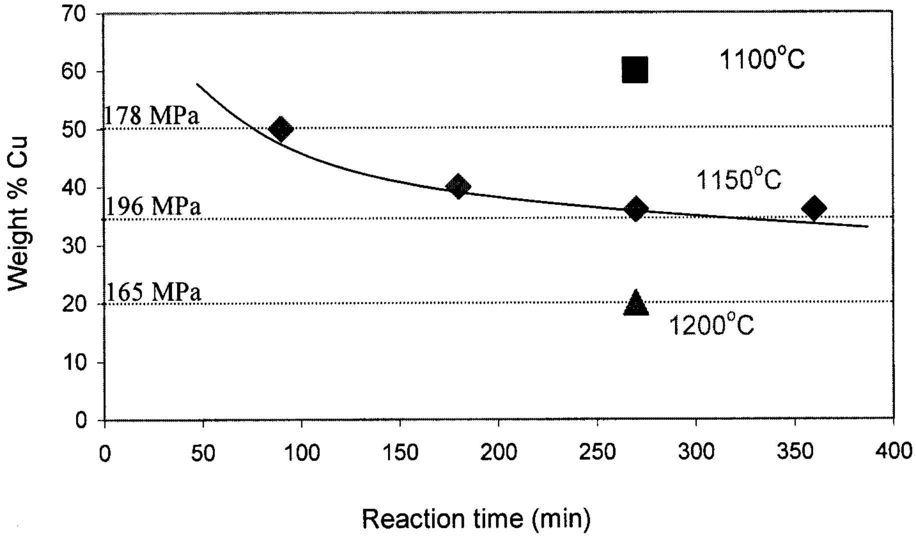

Figure 9.7 – Maximum Cu concentration observed near the interface as a function of reaction time.

9.3.1.2 Ni/FA-129 interface characterisation

Figure 9.8 presents a representative secondary electron micrograph of the interface of the Ni/Fe_3Al alloy formed after diffusion. This interface was obtained after an homogenization at 1100°C for 270 minutes. Three regions are clearly observed; the nickel interlayer, the reaction layer formed through diffusion and the FA-129 intermetallic. A low level of porosity is observed at the interface. It can also be observed that the reaction layer extends into the grain structure of the FA-129. This penetration suggests diffusion at the grain boundary of the intermetallic alloy and the reaction layer. EPMA was used to analyse the composition of the intermediate layer formed in between the Ni core and the FA-129 parent material. A representative microprobe line scan is presented in Figure 9.9. The Ni interlayer and the iron aluminide alloy are on the left and right hand side of the line scan, respectively. The intermediate phase is clearly observed in between and its composition is mainly Ni, Fe and Al. Cr concentration decreases slowly from the FA-129 to the boundary with the reaction product.

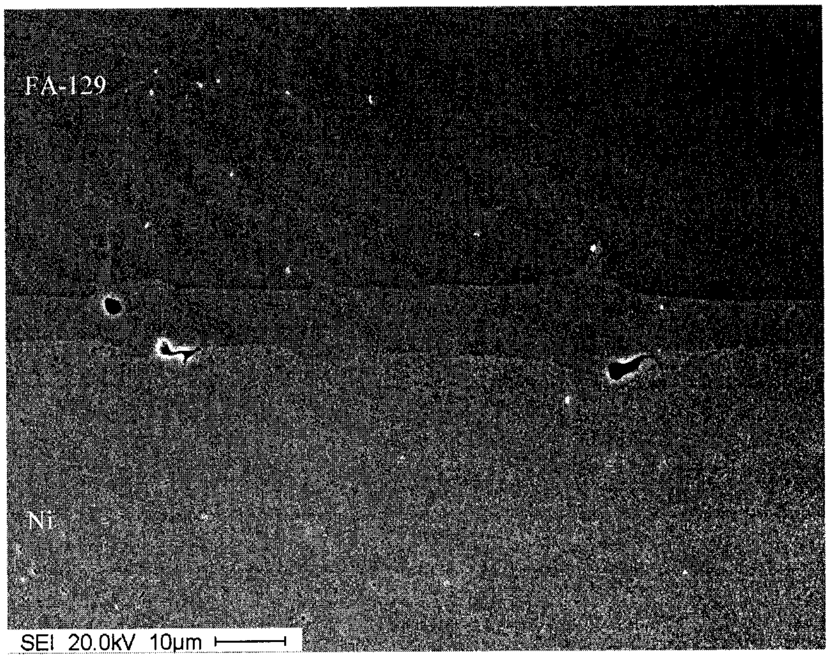

Figure 9.8 – SEM micrograph of the Ni/FA-129 interface.

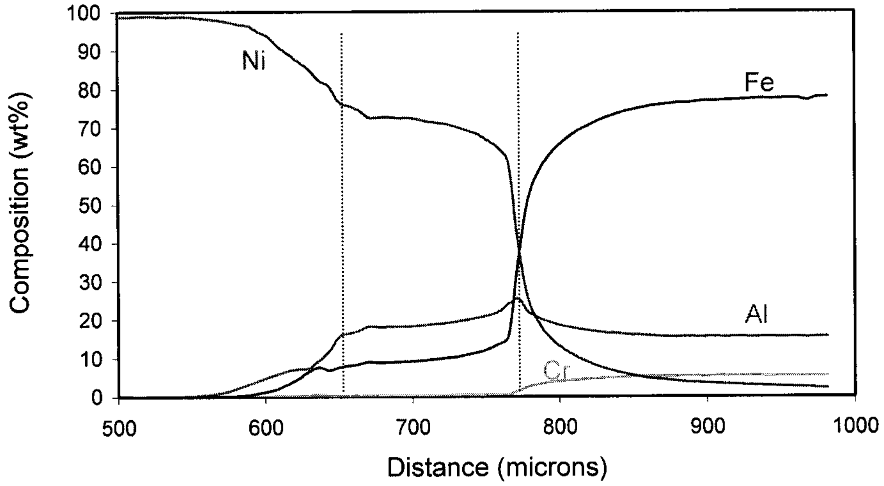

Figure 9.9 – Microprobe line scan across the interface shown in Figure 9.8.

The homogenization condition has an influence on this reaction layer thickness. Table 9.2 presents the effect of homogenization temperature and time on the layer thickness. As expected, the interlayer thickness increases with temperature and time. However, regardless of the heat treatment performed, the chemical composition of the reaction layer, analysed by EPMA, remains similar (71-74wt% Ni, 18-20 wt% Al and 5-9 wt% Fe).

Table 9.2 – Effect of joining parameters on thickness of reaction layer formed.

Effect of time @ 1150°C (minutes)	Reaction layer thickness (μm)	Effect of temperature (°C) @ 270 minutes	Reaction layer thickness (μm)
90	63	1100	56
180	75	1150	108
270	108	1200	130
360	121		

A projection of the chemical composition of the reaction layer on the 600°C isotherm of the Fe, Ni, Al ternary phase diagram [9.4] is presented in Figure 9.10. The intersection falls into the zone $\alpha'+\beta2$. These phases are Ni_3Al and NiAl intermetallics with Fe atoms replacing Ni on some atomic sites. A series of in-depth X-Ray spectra acquired through the layer thickness were performed to verify the presence of these compounds and a sample diffraction pattern is presented in Figure 9.11. The pattern confirms the presence of the Ni_3Al and NiAl phases.

Measurements of the Vickers microhardness of the reaction layer gave results of 374±22 HV. These hardness data are slightly higher than the literature values for both intermetallics tested alone (NiAl = 328 HV [9.5] and Ni_3Al = 311 HV [9.6]). Tan et al. have determined that the hardness of a Ni-Fe-Al ternary β phase is ≈380 HV for an intermetallic with a similar composition to the reaction layer [9.7]. A strengthening effect should occur when both phases are mixed.

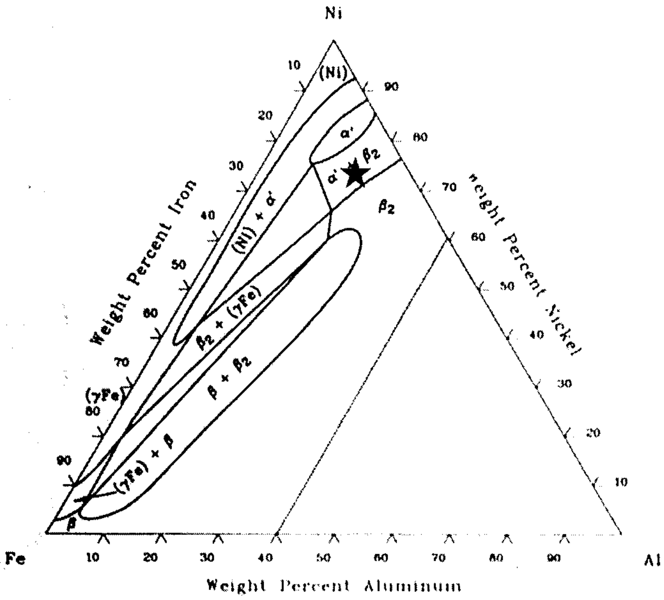

Figure 9.10 – Projection of chemical composition on Fe, Ni and Al ternary phase diagram at 600°C [9.4].

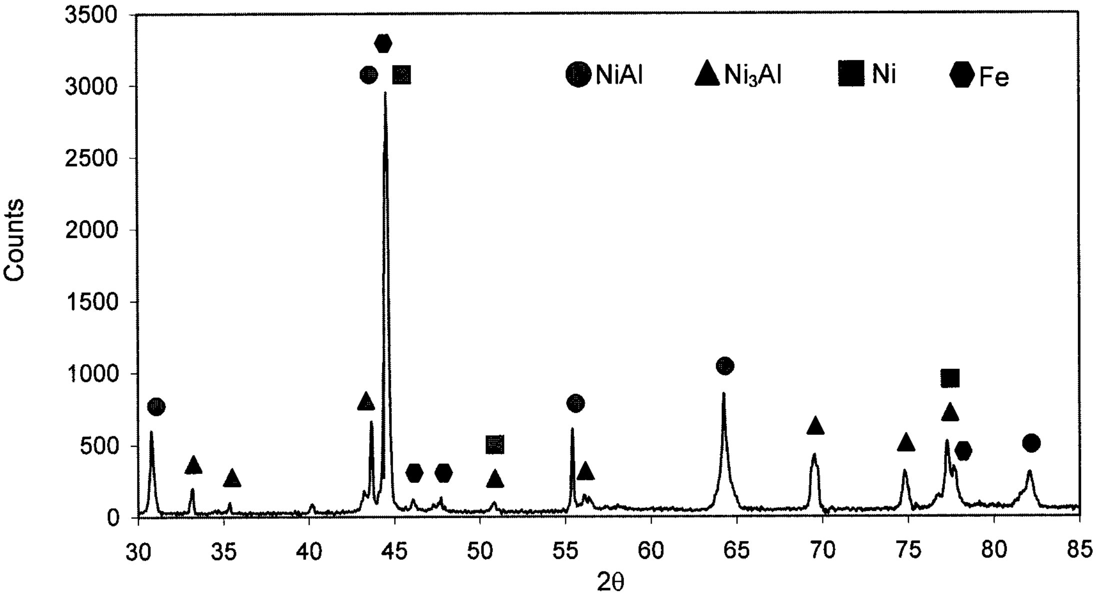

Figure 9.11 – X-ray diffraction pattern of intermediate layer.

9.3.2 Mechanical properties

The bending strength of the joint was evaluated and the results are presented in Figure 9.12. The average strength obtained was 80 MPa, independent of the joining parameters. For all conditions, the failure occurred at the Si_3N_4/Ni interface, suggesting that the interfacial strength between the Ni and FA-129 alloy is higher than this value. Also, the load vs extension curve showed only linear-elastic behavior, without plastic deformation, indicating that the yield strength of the nickel-core interlayer was not reached.

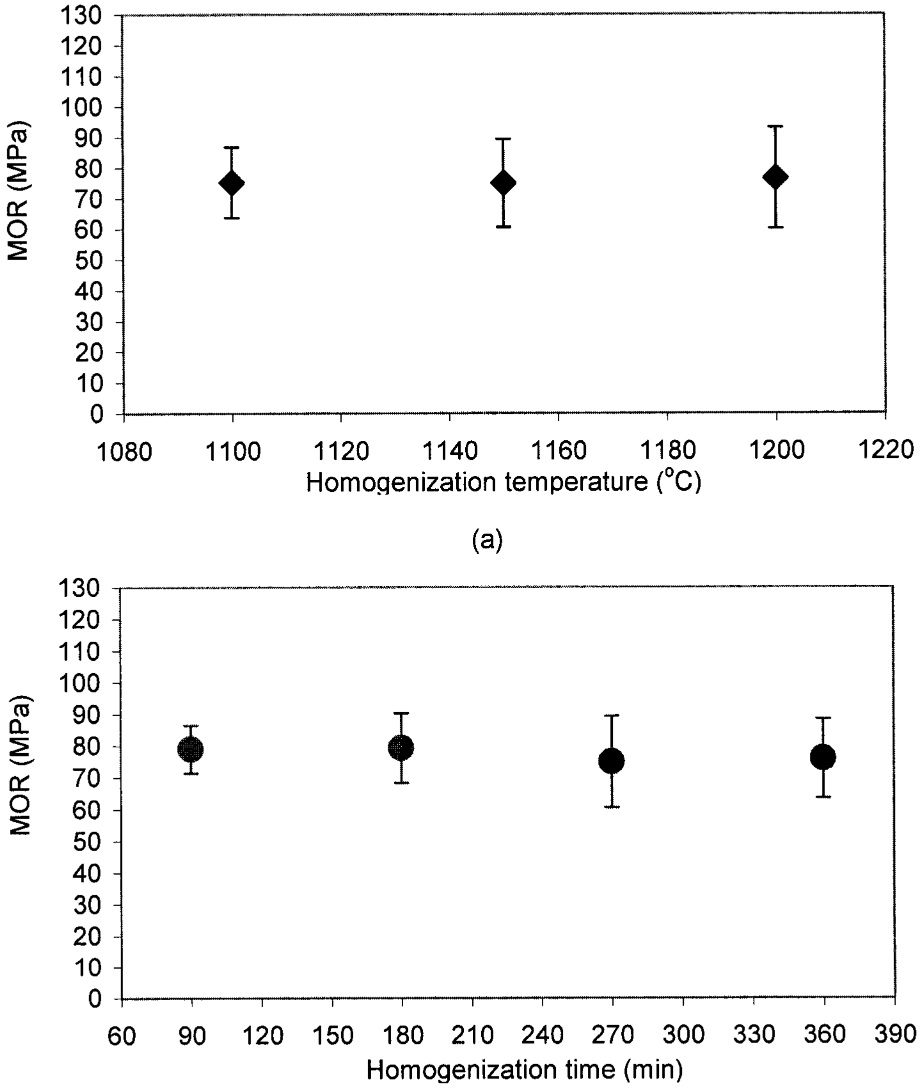

(a)

(b)

Figure 9.12 – Flexural strength as a function of homogenization time and temperature.

9.4 Discussion

The microstructure of the interface is similar to a typical metal-ceramic interface in the sense that TiN is formed through reaction between Ti and silicon nitride. However, the corresponding silicide layer was not observed, even with FESEM for samples that had reached the homogenization temperature. The evolution of a reaction layer formed between Si_3N_4 and Ti from an active filler metal is influenced by many parameters, such as elemental concentration, diffusion coefficient, solubility limits. After the first holding time, the interface is composed of both silicide and nitride layers. Raising the temperature increases the solubility limit of silicon into the copper-nickel and dissociation of the Ti_5Si_3 occurs, releasing free Si for diffusion into the Ni interlayer and Ti for reaction with Si_3N_4, leading to further growth of the TiN layer. Obviously, Ti also diffuses towards the Ni interlayer.

Perpendicular cracking was observed within the reaction layer for every joining condition studied (Fig. 9.3). These cracks are associated with the difference in thermal expansion mismatch between the different layers. The coefficient of thermal expansion of the silicon and titanium nitride are respectively: $3.2X10^{-6}$ $^{o}C^{-1}$ for Si_3N_4 [7.6], $9.35X10^{-6}$ $^{o}C^{-1}$ for TiN [7.6]. The residual stresses produced during cooling are relieved by transverse interfacial cracking. However, the density of transverse cracking will influence the strength of the joints.

Cu diffusion will have an effect on the plasticity of the Ni interlayer near the reaction layer. The yield strength of a Ni-rich Cu alloy increases to a maximum of nearly 200MPa for a composition around 30wt%Cu due to solid solution strengthening [9.3]. The homogenization treatment shows that for all conditions except the low homogenization temperature, the maximum Cu concentration at the junction of the TiN layer is approximately 30wt%Cu. In addition, the reduction in Cu concentration in the Ni core occurs slowly over a distance of up to 150 microns in the highest diffusion case. The residual stresses commonly reach their peak close to the interface. A soft layer with a high level of plasticity is optimum for absorbing residual stresses. However, the presence of this Cu concentration in Ni requires residual stresses of nearly 200 MPa to initiate plastic deformation. The yield strength of Ni-Cu alloys with such composition is 10 times higher than for a pure Cu interlayer [9.3]. With regard to residual stress absorption, the employment of such a thick Cu interlayer in combination with a thick Ni interlayer as diffusion core, should be detrimental as the residual stress induced in the ceramic body will be higher than the residual stresses produce in the case of pure Ni (σ_{ys} of alloy is 80% higher than annealed Ni). However, this Cu interlayer has to be present in order to reduce the diffusion of Ti in Ni, and the subsequent formation of Ni_3Ti intermetallic, which would reduce the quantity of Ti available for reaction.

The formation of the intermetallic phase at the Ni/FA-129 interface occurs through the Al foil with the diffusion of Al from the FA-129. The intermetallic formation occurs due to the high soaking temperature and long time. Previous experiments have shown that only a typical diffusion couple was formed between Ni/Al/FA-129 at 1025°C for a soaking time of 120 minutes. Mehrer et al. have demonstrated that Al diffuses faster than Fe in the ordered state and that the same behavior was found in Ni_3Al intermetallics [9.8]. In addition, the residual thickness of the Ni interlayer measured through EPMA line scan is relatively constant compared to its initial values, suggesting that the dissolution of the iron aluminide alloy combined with the diffusion of Al from the FA-129 to the Ni interlayer is the preferential mechanism for the diffusion layer formation. The presence of intermetallics in the grain boundaries of the iron aluminide suggests that (Fig 9.8) the FA-129 dissolved along the grain boundaries.

The strength of a metal-ceramic interface is a combination of the strength of the interface (adhesive strength of the reaction layer) and the magnitude of the residual stresses produced during cooling. Normally, when large residual tensile stresses are produced along the edge of the ceramic in the butt joint configuration, they promote a concave-convex type of fracture through the ceramic. Observation of this type of fracture suggests that the interfacial strength is higher than the reduced tensile strength of the ceramic. However, in the present work, as all the fractures occurred at the interface, the residual stresses should have been absorbed by localized failure perpendicular to the reaction layer and delamination in some locations. These local defects act as stress concentration zones and ease crack propagation, reducing the strength of the joint. The similarity between all the flexural strengths measured is directly associated with the joint microstructure. The reaction layer, mainly composed of nitrides, has a similar thickness (within experimental error) for all joints. In addition, the same type of defects have been observed in all cases. As a result, similar interfacial strengths and residual stresses would be expected, explaining the flexural behavior of the samples.

9.5 References

[9.1] G. Ceccone, M.G. Nicholas, S.D. Peteves, A.P. Tomsia, B.J. Dalgleish and A.M. Glaeser, An Evaluation of the Partial Transient Liquid Phase Bonding of Si_3N_4 using Au coated Ni-22Cr Foils, Acta Materialia, Vol.44, No.2, 1996, p657-667.

[9.2] ASM Handbook Volume 3, Phase Diagrams, ASM International, 1994 p2•173.

[9.3] W.F. Smith, Structure and Properties of Engineering Alloys, McGraw-Hill, New-York, USA, 1993.

[9.4] ASM Handbook Volume 3, Phase Diagrams, ASM International, 1994 p3•14-15.

[9.5] H.X. Zhu and R. Abbaschain, Microstructure and Properties of *in situ* NiAl-Al_2O_3 Functionnally Gradient Composites, Composites: PartB, Vol.31, 2000, p383-390.

[9.6] S.K. Shee, S.K. Pradhan and M. De, Effect of Alloying on the Microstructure and Mechanical Properties of Ni_3Al, Journal of Alloys and Compounds, Vol.265, 1998, p249-256.

[9.7] Y. Tan, T. Shinoda, Y. Mishima and T. Suzuki, Stoichiometry Splitting in the Ni-Fe-Al Ternary β Phase, Journal Japan Institute of Metals, Vol.57, No.7, 1993, p840-847.

[9.8] H. Mehrer, M. Eggersmann, A. Gude, M. Salamon and B. Sepiol, Diffusion in Intermetallic Phases of the Fe-Al and Fe-Si systems, Materials Science and Engineering, A239-240, 1997, p889-898.

Chapter 10

General Discussion

10.1 Introduction

The production of a metal-ceramic joint is really sensitive to factors such as the components to be joined, the joining process used, the joining parameters, the choice of the filler metal and the joint configuration. In such terms, the process to optimise the performance of this type of interface is tedious. In addition, proper utilisation of characterisation techniques is implied.

The formation of the interface between the ceramic and the metal is mandatory for the establishment of a joint. The mismatch in electronic configuration requires that an intermediate reaction layer has to be created in order to form an interface. This reaction layer can be formed different ways but, it must be present. The main process used to form such reaction layer is the simple addition of an active element in the filler metal to create an active filler metal possessing the thermodynamic potential to destabilise the ceramic atomic bond and form a reaction layer composed of intermetallics [10.1]. In fact, the electronic discontinuity is graded through the different layers formed at the interface. The main elements possessing such driving forces are titanium, zirconium, hafnium, vanadium, niobium and chromium [1.33]. These element are strong carbide, nitride or oxide formers, giving them the potential to be used for joining most ceramics. In addition, they are not only used in metal-ceramic joints but in other metallurgical applications such as steel.

10.2 Characterisation Tools

The interface formation is driven by breakage of the ceramic bond by the active element and the formation of intermetallics at the interface. This interface formation occurs initially at an atomistic level and further thickening occurs with time for a given temperature [10.2]. The strength of the interface is nearly zero for an atomistic reaction layer but rises quite quickly after the initial contact has been made. An interface possessing an acceptable level of strength is obtained for a reaction layer thickness in the order of a micrometer. TEM has been utilised by some researchers to characterise the interface composition but as sample preparation is already tedious, the preparation of metal/ceramic interfaces is even more difficult. Utilisation of focused ion beam (FIB) is an excellent way for producing thin foils, but the cost associated with this technique deters its use. Previous to the appearance of the field emission gun microscope (FE-SEM), researchers used the conventional tungsten filament microscope, in which the applied voltage necessary to obtain sufficient energy to generate a satisfactory beam current for analysis is higher than for the new generation of microscopes. The interaction volume grows exponentially with respect to the applied voltage, thus low accelerating voltage SEM allows the characterisation of smaller interfaces [10.3]. Both phenomenon are illustrated in Figure 10.1. The introduction of new microscopes was also associated with the development of new detectors facilitating the acquisition of more detailed images at higher magnification.

The utilisation of a low energy beam, such as the field emission microscope is able to provide, reduction of the interaction volume but brings another phenomenon, which is the penetration of the beam in the material. Conventionally, the characterisation of an electrical insulator, such as ceramic, implies the application of a thin conductive coating at the surface of the specimen. When a SEM is operated at low voltage, the coating absorbs the majority of the beam energy, leaving traces of X-ray for the specimen characterisation itself. The development of the technique to determine the E_2 energy of a material now becomes mandatory. At this particular energy, the electrical insulation properties are not a factor as the sample is under a charge balance. Working at such accelerating voltage provides the possibility of analysing ceramic material without coating.

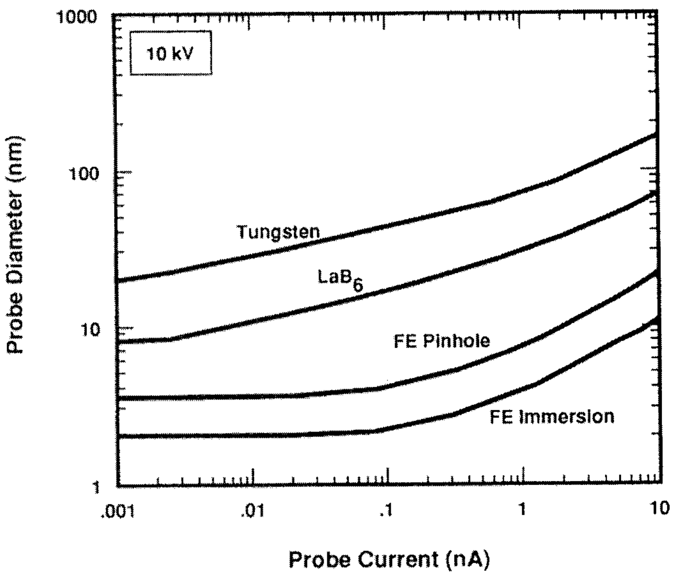

Figure 10.1 – Comparison of probe diameter as a function of different electron sources in SEM [10.3]

The E_2 energy determined for different ceramic is presented in Table 10.1. The E_2 energy of Al_2O_3 was determined by Joy et al. using the colored square method, were AlN was measured using the E_{DHL} method. In the case of Si_3N_4, for an acceleration voltage of 3 keV, the detection of the Si (1,740 keV [10.3]) is detected but not at its maximal concentration. In addition, the typical standarless commercials algorithms of analysis of the chemical composition remain a "black box" type of calculation and are not precise enough for good analysis.

Table 10.1 – E_2 energy of different ceramics

Ceramic	E_2 Energy (keV)	Reference
Si_3N_4	3.02	Chap. 2
AlN	2.68	10.4
Al_2O_3	4.2	10.3

However, this technique has drawbacks. Firstly, as each phase possesses it own appropriate E_2 energy, a material composed of two different insulating phases with different E_2 energies cannot be characterized without coating, as the complementary phase will exhibit charging. Secondly, as the E_2 energy is a material property, the beam energy then becomes fixed and limits the possibility of x-ray generation in the material. The chemical detection now becomes more sensitive to the excitation energy of the respective atoms present in the material to be characterised, as presented in the previous graph.

10.3 Iron Aluminide Alloy Intermetallic

After having demonstrated the importance of the determination of E_2, which justify the acceleration voltage used for M-C interface line scan, we will be turning now to the materials of interest in this project. The family of iron-rich aluminide intermetallics (Fe_3Al) changes their atomic structure with respect to temperature. They possess a DO_3 structure from room temperature up to the transformation temperature $DO_3 \rightarrow A2$, where they adopt this structure. An increase in temperature changes this structure to the Fe-Al solid solution. All studies on brazing this material with different filler metal based-alloy have shown that the wetting behavior is strongly influenced by the diffusion of aluminum from the substrate into the molten drop [3.1, Chap 3-4]. This Al diffusion has a more significant effect on the wettability by copper if Cr is present in the substrate. The aluminum diffusion is known to decreases the melting temperature of Ag, Au, Cu and wetting has been observed at temperatures lower than the nominal reference melting temperature, suggesting alloying [3.10, 10.5, 10.6]. As a general observation, the wettability of the iron aluminide (alloy or not), is associated with significant penetration of the molten metal in the substrate along the grain boundaries. The reduction in Al content in the iron aluminide alloy lattice increases the density of the alloy, which in turn, reduces the volume of the unit cell [3.11]. This reduction of volume is associated with the grain boundary penetration as diffusion of aluminum occurs preferentially down the grain boundaries. In fact, the decohesion of the intermetallic structure is directly associated with this diffusion phenomenon.

In order to obtain wetting of the intermetallic, one method can be related to the reduction of aluminum diffusion gradient. In cases where the gradient in aluminum is avoided (in the situation where the filler metal contains a similar amount of Al than the substrate), Al should not diffuse. This is related to the observation of chemical equilibrium between the Al content detected in the grain structure and in the filler metal. Preliminary experiments on wetting of FA-129 with Cu-16wt%Al have confirmed this statement. On the other hand, the penetration of copper-based alloys was observed to be lower when the melting temperature of the filler metal was decreased by alloying (becoming to an eutectic composition). The system Cu-Ti possesses such Cu-rich eutectic at 78% (875°C) and can be a suitable alloying element for depressing the melting temperature. It has been demonstrated that in the case of high-Ti content alloy (75-25), the diffusion of Al is no longer the main factor responsible for the wettability. The formation of new compounds, such as the Fe_2Ti compounds should have a lower free energy of reaction than the Al diffusion and instead of observing the penetration of the molten liquid along the grain boundaries, a reaction front is now observed. Penetration depth of this reaction front is lower than the penetration at grain boundaries and suggests that a high Ti content will be an appropriate solution to avoid decohesion of the intermetallic structure.

10.4 Fabrication of High Ti-content Active Brazing Alloy

After having demonstrating the needs of using a Ti-rich filler metal to reduce the damage to the microstructure, the fabrication of a Ti-rich Cu alloy was initiated but was more problematic than it appears due to the high reactivity with elements such as C, N and O. This reactivity, which makes them attractive for ceramic brazing, complicates their processing through conventional melting as reactions will occur with the ceramic crucible and changes in chemical composition will ensue. In addition, the transition elements, commonly used as active elements, produce a series of intermetallics across their respective phase diagrams as they have a reduced solid solubility in the base filler metal. The shaping of foil for example, of a brazing alloy containing a high concentration of active element after melting and casting will then be complicated as the intermetallic possesses a lower ductility. Experiments where sintered pellets of Cu-25Ti intermetallics were rolled and shown to introduce numerous cracks and results in rejection of the rolled final product.

Powder mixing, to be applied in the form of paste, was attempted in order to form a homogeneous mixture but the large density difference created major segregation problems. The utilization of a heavier element than titanium would have been easier. In addition to the density, the segregation of the powder is affected by the size of the particulates, and an optimum condition had to be found but does not ensue a segregation-free mix. In the present case, the reduction in Ti particle size is limited as it would lead towards combustibility of the powder [10.7] and manipulation or handling is more complicated. In addition, the powder mixture will be exposed to the brazing atmosphere and absorption of impurities or residues from the binder (if used), may contaminate the brazing alloy. In the present work, the utilization of electroless coating became a key technology in producing such an alloy. This coating procedure allows for the possibility of plating on non-conductive surfaces when the proper pre-treatment is performed prior to plating. Moreover, the formation of a composite powder offers potential advantages such as an increase in diffusion area and formation of a more inert protective shell, (Cu for instance), which surrounds the Ti core. The electroless plating process is based on the chemical reduction of a salt at the surface of a substrate. In order to occur, close control of the bath chemistry must be performed. The results obtained have shown a significant increase of the particle size when the solution pH is increased. In addition, the morphology of the plated deposit changes from 3D clusters to 2D pellets. In addition, the increase in pH was found to create agglomeration problems.

The melting of the composite powder is a function of the degree of diffusion occurring in the powder during the heating stage. The formation of intermetallics should initiate at low temperature and their growth rate will increase with respect to the temperature. The eutectic melting of the powder will initiate in the coating of the powder and subsequent dissolution of the remaining solid component into the liquid will occur. The liquid reaches the surface of the powder prior to completion of the Ti-core dissolution. However, in the highest complete melting temperature observed with DSC was 915°C, which is lower than the lowest joining condition used.

The melting of the diffusion couple was found to be a function of the level of interdiffusion between both components involved. In the Cu-Ti binary system, the lowest melting point present in the phase diagram is the Cu_3Ti_2-Cu_4Ti eutectic (78wt%Cu; 875°C [6.1]). The first liquid to appear will be formed at this interface. The effect of heating rate influences the level of diffusion, which is observed by the thickness of the intermetallics layers compared with different heating rate. The liquid formed initially occurs within the shell of the coated powder. This liquid gains solubility in Cu and Ti and then dissolves the remaining solid to reach the final melting of the composite powder at high temperature. This multi-step melting is observed when the powder was melted in the sessile drop set-up. The powder pill was still in its original configuration at 912°C. The solid pill should contain a certain level of liquid. In addition, powder mixtures with copper as a diluent metal show that the initial melting step of the powder is similar to the powder alone but once liquid reaches the surface, the dilution of the molten ABA, by dissolution of pure Cu, begins.

10.5 Metal-Ceramic Reaction Layer Formation

As mentioned previously, the formation of the reaction layer is the key step in the formation of a reliable interface. In all three joint systems studied in this project, the active element of the filler metal, reacting with the silicon nitride ceramic is titanium. Figure 10.2 presents a schematic representation of all three configurations investigated in Chapter 7, 8 and 9. In all three cases, the layer described as ABA is responsible for forming the reaction layer with the ceramic. However, the component adjacent to the active brazing alloy possesses a different elemental composition and therefore affects the diffusion and reaction behaviour of the composite powder.

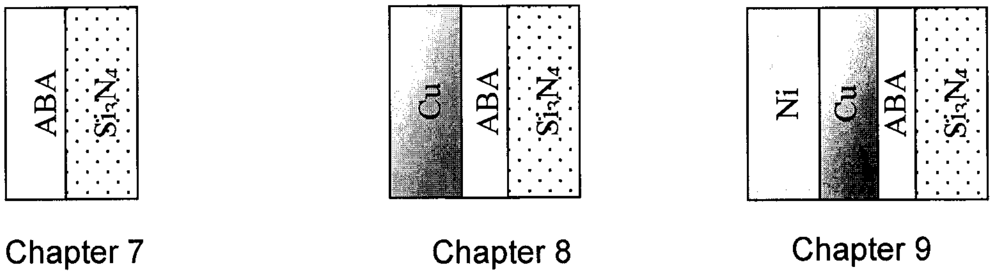

Figure 10.2 Sketch of the three different diffusion couples occuring at the Si_3N_4 interface.

10.5.1 Direct Brazing of Si_3N_4

In the case where only the active filler metal was present (Chapter 7), the concentration of titanium in the filler metal was considered constant. Similar observation was reported by Nakao et al. [7.3] on their study of reaction layer formation in the system Cu-Ti/AlN. The growth of the reaction layer was proven not to be influenced by the concentration of active element as the consumption of Ti becomes negligible compared to the initial concentration present in the filler metal. This is well illustrated by the possibility of using the parabolic growth model, which refers to systems which do not deviate from linear behavior as a function of the square root of time. The modeling of the effective reaction layer growth in this system has shown an activation energy of 64 kJ/mol, which is considered low in the case of metal/ceramic interface growth but is directly related to the availability of Ti close to the growth front. The effective activation energy was determined as a growth competition occurs between the nitride and silicide layer. Researchers have found activation energy values higher in ABA/Si_3N_4 systems (between 200-300 kJ/mol [7.2, 7.4]) but their analysis was carried out on filler metal containing lower amounts of Ti combined with the growth of a nitride layer only, which acts as a diffusion barrier. Other diffusion, reaction and dissolution phenomenons occur at the TiN/Ti_5Si_3 interface.

In this case, the formation of the different layers is influenced by the joining conditions, including the furnace environment. Initially, the reaction layer is composed of the two phases that Ti is able to form when reacting with Si_3N_4, which are TiN and Ti_5Si_3. The composite type of reaction layer transforms slowly to form a bi-layer reaction zone, which in turn, grows with respect to the different diffusion and solubility coefficients. The growth competition between the different reaction promotes shows that in this case, the silicide layer is more stable than the TiN layer during the earlier portion of the diffusion controlled stage. However, further diffusion saturates the silicide layer and development of the TiN layer becomes appreciable.

Kim et al. [7.2] have demonstrated that a change in reaction layer morphology occurs between a Cu-10Ti and a Cu-15Ti alloys and Si_3N_4 ceramic, passing from a composite reaction layer to a bi-layer reaction layer. Under low Ti-concentration, the activation energy is 200-220 kJ/mol and for higher concentration, it rises to approximately 320 kJ/mol. However, in the case of Cu-

15Ti, only the TiN layer was measured, explaining such high activation energy. At 970°C, the reaction layer thickness measured was below 1.5 microns for wetting experiments of 60 minutes, which is a value slightly lower than the TiN reaction layer thickness obtained for lower temperature and shorter time of Cu-25Ti on Si_3N_4. If in their study, both reaction layers were measured, the activation energy would be near the value calculated in this study.

The activation energy calculated by Nakao et al. [7.3] for the system Cu-22Ti/AlN is 96 kJ/mol, slightly higher than the activation energy observed in our case. However, their system is composed of only one reaction layer (TiN) and therefore the lower value observed for the Si_3N_4 system can easily be lower as the reaction competition will tend to decrease the free energy of the system and more significant thickening occurs. In summary, such low activation energy suggests that the thickening of the reaction layer is important even with low joining conditions (temperature and time) and careful selection of the brazing parameters must be carried out to obtain successful brazing of Si_3N_4 to itself using this filler metal.

10.5.2 Brazing of Si_3N_4 using a Cu interlayer

The presence of a copper layer inserted to absorb the residual stresses produced during cooling between the iron aluminide alloy and the silicon nitride has also the effect of diluting the chemical potential of the active filler metal. Once liquid appears at the surface of the composite powder, possessing the Cu-rich eutectic composition, interaction with the solid Cu layer is initiated. Dissolution of the Cu layer will push the composition towards Cu and solidification can occurs. However, as this phenomenon occurs during the heating ramp of heat treatment, a competition between solidification through diffusion and persistance of melting as temperature increases, continue. In fact, with time, the concentration of Ti in the filler metal layer will be reduced as Ti now possesses a chemical gradient difference in the opposite direction to the ceramic, which will finally reduce the quantity available for reaction.

In general terms, the reaction layer formation follows a similar growth pattern steps as in the case of direct brazing but with reduced kinetics. The activation energy for this case, calculated with the Arrhenius method, was at 137 kJ/mol, which is slightly more than twice the energy calculated in Si_3N_4 brazing. In fact, this directly demonstrates the dilution effect produced by the soft interlayer. By comparing the results obtained for both systems, the reaction layer formed with the copper is approximately half the thickness for the same conditions, which again illustrates the dilution effect by the copper interlayer. The brazing parameters used to calculate the activation energy were into a lower operating window. This provides the possibility of using the parabolic law as no deviation was observed [10.8]. However, by using parameters like time and temperature, non-linear behavior might have been observed as the Ti concentration would have decrease and as other modeling approach, such as the Johnson-Mehl equation or Raic model might be used. The justification for using such small brazing time and low temperature maintains the objective of avoiding excessive growth of the reaction layer, which would directly affect the mechanical properties as demonstrated by Nicholas [1.26]. Similarly to direct brazing, the reaction layer starts to from a composite configuration and further changes occur to create the bi-layer type of interface. The similarity in the results demonstrates the reproducibility of the Cu-Ti system reaction layer development and that the growth layer formation in this system should be similar, independent of the Ti concentration, but with different kinetics.

10.5.3 Partial Transient Liquid Phase Bonding of Si_3N_4

The addition of the Ni interlayer changes again the elemental concentration gradient present at the interface. At first, the initial reaction pattern is identical to the case where the ABA is in contact with the ceramic on one side and with the Cu soft interlayer on the other. The dilution of the ABA is observed in the Cu buffer interlayer. The reaction layer growth morphology is very similar in formation to the case presented in Chapter 8. However, in order to fulfill the requirements for PTLPB, a second homogenisation period is necessary to diffuse the low melting point alloy and having at the interface, compounds with higher melting temperature than the joining temperature. After the first soaking period, the residual copper interlayer is still present: with exception of some dilution of the ABA, no diffusion was observed in the Ni interlayer. Interrupted experiments shown that the Si_3N_4 joined to the Cu interlayer was not joined to the Ni interlayer. For this reason, the joining temperature was raised to achieve the homogenisation of the buffer interlayer with the Ni interlayer. During this step of the heat treatment cycle, the diffusion between Cu and Ni is initiated. However, the presence of nickel not only host the Cu atom, forming a higher melting point alloy but also produces a driving force for the Ti_5Si_3 layer to decompose into atomic Ti and Si. Consequently, Ti diffuses through the Ni interlayer resulting only in a TiN layer at the interface.

Moreover, the dissociated silicon also diffuses into the Ni interlayer. This dissociation (absence of silicide layer at the interface) is proven by two different characterisation techniques, low voltage line scan and XRD [10.9]. In addition, Chen et al. [1.38] have not found a silicide layer at the interface of their system Si_3N_4/Ti/Cu/Ni but small precipitates in the Ni interlayer of Cu. This all reinforces the observed dissolution of the Ti_5Si_3 layer.

10.6 Mechanical Properties of the various Interfaces

The mechanical properties of a ceramic-metal joint are mainly dictated by the interfacial strength (work of adhesion of the reaction layer) and the residual stresses created in the joint during cooling. The residual stresses developed in the ceramic body are a function of the coefficient of thermal expansion mismatch between the metal and the ceramic as well as the joint configuration [10.10, 10.11]. Nakahashi et al. [10.12] have demonstrated the effect of the angle of the joint configuration on the creation of the residual stresses for a Si_3N_4/Cu/SS304 system. The results have shown that for an angle ranging between 70-80^{o} between the interface and the normal direction of the interface, the residual stresses are maximised which in turn minimised the mechanical properties. A reduction of the taper angle from 80° to 20° reduces by 50% the stresses formed during cooling. The utilisation of such a taper angle configuration implies machining costs, which are dramatically high in the case of ceramics. In other words, the mechanical properties of the Si_3N_4/FA-129 obtained in this work can be improved by changing the configuration of the joint, if it becomes necessary. In addition, the strength of the ceramic is related to the fracture toughness as higher bending strengths were obtained for a tougher Si_3N_4 ceramic. The utilisation in this work of the needlelock microstructure provides for a Si_3N_4 ceramic possessing the highest fracture toughness commercially obtainable [10.13] and, thus, reducing the potential for easy crack propagation during testing.

The use of an interlayer to reduce cooling stresses has been studied in order to obtain reliable joints. The plasticity level of the interlayer is important to maximise the absorption. Conventionally, nickel and copper are considered as appropriate interlayers as the yield strength of both metals is relatively low [1.31]. A direct proof was the possibility of forming reliable joints between Si_3N_4 and FA-129 with the presence of the Cu interlayer, which was not achieved previously through direct brazing.

In the case of brazing (Chapter 8) or PTLPB (Chapter 9), a certain diffusion of the brazing alloy in the interlayer occurred, modifying the plasticity behavior of the interlayer. In the case of the Cu-based filler metal/Cu interlayer used here, the only modification of the plasticity behavior is through movement of the active element into the copper interlayer, where some intermetallics or solid solutions are formed, depending on the titanium concentration. As the solubility of Ti in copper is relatively low at room temperature ($\approx$1wt%) [6.1], the effect of solid solution strengthening by Ti can be neglected compared to the effect of the presence of intermetallic precipitates near the interface. The presence of these intermetallics will subsequently reduce the CTE of the interlayer with similar mechanism observed in MMCs [10.14]. However, the ductility of this section of the interlayer is also reduced by the presence and the intermetallic reinforcement and the balance of both effects should be controlled to optimize the absorption of residual stresses.

On the other hand, the utilisation of nickel in combination with the active element produced hard phases, such as Ni_3Ti for the system Ni-Ti. To avoid the formation of such intermetallics, filler metals were used between the interlayer and the ceramic. However, in the case of Cu-based filler metal, the interdiffusion of both compounds is fast and the solid solution strengthening effect in this system is well known. The presence of Cu in the Ni raises the yield strength up to a maximum at a concentration of 70wt%Cu-30wt%Ni. In this work the copper concentration was nearly always in the range which produced the maximum yield strength obtainable by solid solution strengthening [9.3]. Results obtained previously have shown the effect of the Cu buffer layer thickness on the diffusion of Ti in the interlayer. The absence of a layer or a thin Cu layer has shown significant diffusion of Ti, which reduces the quantity available for reaction and promotes the formation of a layer mostly composed of Ni_3Ti, brittle intermetallic with high yield strength which limits the absorption of residual stresses [10.15]. The presence of a high concentration of copper in the nickel interlayer is associated with the presence of a thicker brazing alloy layer. This investigation was done to evaluate the possibility of using a thicker interlayer for PTLPB as conventionally used in sputtered layers but which adds to the final cost of the assembly. The main requirements for the PTLPB process is to have a higher melting temperature interface than prior to assembly. This results in a short or relatively long homogenisation time to reach the compositional requirement to optimise the residual stresses absorption by the interlayer. The utilisation of thicker interlayers was found to be detrimental with respect to the mechanical properties when compared to thinner interlayers.

In summary, the mechanical properties obtained in the case of dissimilar joints (FA-129 to Si_3N_4) by brazing with an interlayer (max. 160MPa) will be hardly increased as the only free parameters available to increase the reaction layer is time as increment in temperature has been shown to have a detrimental effect on the FA-129/Cu interlayer [8.3]. In the case of PTLPB, the results have shown that using a thicker interlayer reduced the properties when compared to joints formed with sputtered interlayers (80 MPa compared to 250 MPa [1.38, Chap. 9]).

10.7 References

[10.1] S.D Peteves, M. Paulastro, G. Ceccone and V. Stamos, The Fabrication Route to Ceramic Joining: Fabrication, Interfacial Chemistry and Joint Properties, Acta Materialia, vol 46, no 7, 1998, p2407-2414.

[10.2] M. Nomura, C. Iwamoto and S.-I. Tanaka, Nanostructure of Wetting Triple Line in a Ag-Cu-Ti/Si_3N_4 Reactive System, Acta Materialia, Vol.47, No.2, 1999, p407-413.

[10.3] J.I. Goldstein, D.E. Newbury, P.E. Chlin, D.C. Joy, A.D. Romie, C.E. Lyman, C. Fiori and E. Lifshin, Scanning Electron Microscopy and X-Ray Microanalysis, Second Edition, Plenum, USA, 1992.

[10.4] M. Brochu, H. Demers, R. Gauvin, M.D. Pugh and R.A.L. Drew, Charging Behavior of Nitride Ceramics using FE-SEM Microscope, Submitted to Microscopy and Microanalysis.

[10.5] ASM Handbook Vol 3, Phase Diagrams (ASM International, USA), p 2•30.

[10.6] ASM Handbook Vol 3, Phase Diagrams (ASM International, USA), p 2•31.

[10.7] Material Safety Data Sheet, Ti powder, product #10386, Alfa Aesar, A Johnson Mattey Company.

[10.8] Y. Nakao, K. Nishimoto and K. Saida, Bonding of Si_3N_4 to Metals with Active Filler Metals, Transaction of the Japan Welding Society, Vol.20, No.1, 1989, p66-76.

[10.9] M. Brochu, M.D. Pugh and R.A.L. Drew, Partial Transient Liquid Phase Bonding of Silicon Nitride to Iron Aluminide Alloy, Joining of Advanced and Speciality Materials IV, Proceedings from Materials Solutions 2001 on Joining of Advanced and Specialty Materials, Indianapolis, Nov. 5-8, 2001, p44-50.

[10.10] J.-W. Park, P.F. Mendez and T.W. Eagar, Strain Energy Distribution in Ceramic-to-Metal Joints, Acta Materialia, Vol.50, 2002, p883-899.

[10.11] J.H. Kim and S.B. Lee, Stress Intensity Factor and Crack Initiation Directions for Ceramic/Metal Joint, Theoretical and Applied Fracture Mechanics, Vol.30, 1998, p27-38.

[10.12] M. Nakahashi, Y. Yasuda, T. Ito and N. Okabe, Design of Silicon Nitride/Stainless Steel Joint for Airtight Seal Parts for in-core Detectors, Proceeding of the 2nd International Soldering and Brazing Conference, AWS, San Diego, February 2003, CD-ROM.

[10.13] Supplier's Data, Ceradyne Inc. Costa Mesa, Ca, USA, 2000.

[10.14] J. Lo, Designing Materials Properties with Squeeze Cast Metal Matrix Composites, Proceeding of the Metal/Ceramic Interactions Symposium, COM 2002, CIM, Montreal, Canada, p123-144.

[10.15] M. Brochu, M.D. Pugh and R.A.L. Drew, Effect of Core Interlayer Choice during Partial Transient Liquid Phase Bonding of Si_3N_4 to an Fe_3Al alloy, Proceeding of the 2nd International Soldering and Brazing Conference, AWS, San Diego, February 2003, CD-ROM.

Chapter 11

CONCLUSIONS

This section presents the conclusion on the results obtained in the previous chapters:

1. The displacement of the EDHL can be used to determine the E_2 energy of Si_3N_4 ceramic. The formation of a surface electrical field changes the kinetic energy of the incident e-beam. The neutral state (E_2) is obtained when the kinetic energy of the incident beam has not been modified. The E_2 energy for Si_3N_4 has been determined to be 3.01 keV.

2. The wetting behavior of Cu on an iron aluminide alloy has been demonstrated. The wettability is influenced by the diffusion of Al from the Fe_3Al alloy to the Cu substrate through the surface oxide film. The presence of Cr in the alloy increased this diffusion, increasing the spreading kinetics.

3. The microstructural interaction between the Cu-XTi alloys has shown that the damage in the microstructure is function of the quantity of Ti present in the alloy. For pure Cu, simple Al and Cu diffusion occurred. The reduction of Al content of the intermetallic reduces the unit volume, creating shrinkage of the grains and decohesion at the grain boundaries. The presence of a low content of Ti shows similar behavior, but in addition, the formation of Fe_2Ti in the grains is observed. The reduction of Al in the intermetallic grains is even higher. A high Ti-content changes the mode of microstructural damage as a reaction phenomenon predominants over diffusion. The penetration in the alloy occurs on a front by formation of Fe_2Ti more than through the grain boundaries by unit cell shrinkage.

4. The fabrication of an active brazing alloy was achieved by electroless deposition on the surface of Ti powder. Increasing the pH of the bath solution has been shown to increase the plating rate to the detriment of the purity of the Cu (higher O concentration). The morphology of the coating is also influenced by the pH as 3D growth is observed at low pH whereas 2D growth occurs at higher pH. The equilibrium contact angle of the alloy on Si_3N_4 has been evaluated to be similar to pre-alloyed brazing alloy but with different spreading kinetics.

5. Thermal analysis has been used to determine the multi-step melting behavior of the composite ABA powder. Melting initiates at 875°C in the coating, when the two-phase region (Cu_4Ti-Cu_3Ti_2) of the diffusion couple reaches the eutectic temperature. Complete melting however, is influenced by the heating rate, which influences the rate of diffusion and dissolution. For a heating rate of 10°C/min, complete melting was observed at 900°C whereas for 40°C/min, complete melting was reached at 915°C. Active liquid reaches the surface at 894°C and reaction with the ceramic is initiated.

6. The mechanical properties of the composite powder where evaluated through Si_3N_4/Si_3N_4 joints. The interfacial reaction layer growth step has been demonstrated. Initially, the reaction layer is composed of both TiN and Ti_5Si_3. The growth of the silicide layer is more important initially and subsequent growth of the TiN layer occurs. Cu was detected in the silicide layer by FE-SEM line scan. The activation energy of the reaction layer growth was calculated to be 64kJ/mol. The high titanium content in the filler metal was demonstrated to be responsible for the low reaction energy. The mechanical properties of the assembly varied between 250 and 400 MPa, depending on the joining parameters. Changes in fracture mode were correlated to the MOR of the joint.

7. Brazing of Si_3N_4 to FA-129 was performed using a Cu interlayer to absorb cooling stresses due to the difference in CTE. The interfacial reaction layer growth steps were similar to the case of brazing Si_3N_4 to itself but with a lower growth rate. The effective activation energy for the reaction layer growth was 137 kJ/mol, which is slightly more than double that for the case of brazing Si_3N_4 to itself. The maximum mechanical strength obtained was 160 MPa, in which case the failure always occurred at the interface.

8. Partial Transient Liquid Phase Bonding was applied to bond Si_3N_4 to FA-129 using a Ni interlayer. The first step of the reaction layer growth is similar to that occurring in the cases of brazing Si_3N_4 to itself and to FA-129. However, the high temperature homogenisation treatment dissolves the silicide layer leaving a single TiN layer at the interface. The silicide then forms a solid solution in the Ni core layer. The formation of a mixture of Ni_3Al/NiAl at the interface between Ni and the FA-129 was reponsible for joint adhesion. This intermetallic layer possesses higher mechancial properties than the Si_3N_4/Ni interface as joint integrity was obtained during testing. The joining parameters had no influence on the reaction layer thickness which explains the similarity in bending strength obtained (80 MPa).

Chapter 12

CONTRIBUTIONS TO ORIGINAL KNOWLEDGE

This chapter presents *the most important* contributions to the scientific literature which occurred during the progress of this research work.

1. A technique for determining the E_2 energy for non-conductive ceramic using FE-SEM was developed. The E_2 energy value of Si_3N_4 was measured to be 3.01 keV.

2. Interfacial line scans of non-conductive materials were successfully performed when the E_0 of the microscope was set at the E_2 of the insulating material. This technique has demonstrated the solubility of Cu in the Ti_5Si_3, which is impossible with conventional SEM microscopy as the interaction volume is too large, showing the potential for this analytical procedure.

3. Wettability of Cu on an iron aluminide alloy has been demonstrated. The interaction between Cu and the iron aluminide alloy showed that Al diffusion is responsible for the microstructure decohesion. A high Ti-

content, copper-based filler metal prevented the Al diffusion by reaction between Ti and Fe forming Fe_2Ti.

4. The fabrication process for an active brazing alloy containing a high level of active element by a plating technique was established. This technique can be extended to all metals which can be deposited by a plating process. The behavior of such a composite powder is similar to conventional types of brazing alloy, in terms of reaction layer composition and mechanical properties. However, the kinetics of the reaction layer growth is influenced by the kinetics of diffusion between the elements of the couple.

5. Sound joints between FA-129 alloy and silicon nitride were produced. However, the utilization of a soft interlayer is mandatory as the residual stresses produced during cooling cannot be absorbed by the intermetallic as the high yield strength is maintained even at moderate temperature. Joining techniques such as brazing and partial transient liquid phase bonding were successful.

Appendix A

Activation Energy

The formation of an interface in a metal-ceramic reactive system is based on a chemical reaction occurring between a ceramic and a metal possessing a high enough thermodynamic potential to destabilize the atomic bonds of the ceramic and to form a reaction product. The growth rate of the reaction is based on the diffusion potential of the active element to form new compounds. The ease of diffusion, which dictates the growth rate, is measured in terms of the activation energy of diffusion.

If the assumption is that the reaction layer growth mechanism (mass-transfer limited) is controlled only by the diffusion of an element in the reaction layer, the growth can be treated by the reaction diffusion concept (pure diffusion). A schematic representation of the reaction layer growth is presented in Figure A1.

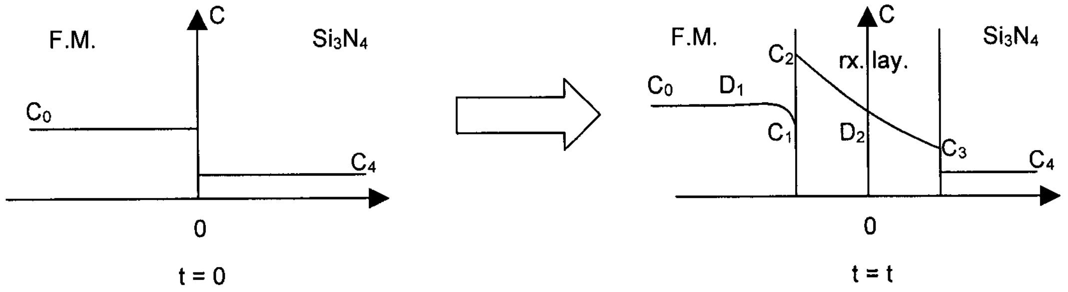

Figure A1 - Schematic representation of the reaction layer growth under the reaction diffusion model.

In the case where the reaction layer grows from the original interface into both sides, some assumptions must be considered:

1. The concentrations of C_1, C_2, C_3 and C_4 remain unchanged,
2. The element is consumed by the reaction with Si_3N_4, and does not diffuse into Si_3N_4,
3. The diffusion coefficients D_1 and D_2 are independent of concentration,
4. The concentration gradient in liquid metal is nearly equal to zero.

These assumptions have to hold in order to correlate the growth to the parabolic law (eq. A1).

$$x = K(Dt)^{1/2} \qquad \text{(eq. A1)}$$

where: x is the thickness of the reaction layer
D is the diffusion coefficient in the reaction layer
K is a constant
t is the time

Finally, the diffusion coefficient is related to the temperature by an Arrhenius-type relationship (eq. A2):

$$D = D_0 \, e^{-Q/RT} \qquad \text{(eq. A2)}$$

where: D is the diffusion coefficient in the reaction layer
D_0 is the frequency factor
Q is the activation energy for diffusion
R is the gas constant
T is the absolute temperature

In addition to the pure diffusion model, other models can be used to calculate the activation energy. Depending on the system and on the time/temperature window studied, the model used should be valid for the data. This appendix will demonstrate that the measurement of the activation energy by the parabolic method for the low content in active element alloys is invalid but it is valid for alloys with high content in active element. Three different systems were chosen: brazing of Si_3N_4 using a Cu-5wt%Cr [7.3, 10.9], brazing of AlN using a Cu-22wt%Ti [7.3] and brazing of Si_3N_4 using a Cu-25wt%Ti alloy [Chap 7].

The total reaction layer thickness increases simultaneously with temperature and /or time. Figure A.2 presents the reaction layer thickness plotted against time for different temperatures for the systems (a) Cu-5Cr, (b) Cu-22Ti and (c) Cu-25Ti, respectively. In the case of the low content alloy (a), the curve possesses a high growth rate initially, which then rapidly plateau. This behavior was not as pronounced in the case of alloy with low content in active element, i.e. (b) and (c).

At higher temperatures and longer times, in some cases, the growth rate of the reaction layer is reduced and the measured reaction layer thickness tends to be constant. The thickness of this reaction layer is commonly called the "equilibrium thickness of the reaction layer, δ_e". Figure A.3 illustrates the parabolic law analysis for the three systems. Two different phenomena are observed, which are functions of the active element content. The low content in active element alloys tends towards the equilibrium thickness of reaction layer, which is not the case for the alloys with high content in active element. Both cases will be described separately.

Low content in active element

In the case of Cu-5Cr filler metal, at the highest temperature and for longer times, the reaction layer gradually deviates from the simple parabolic law because of the consumption, through diffusion, of the active element in the reaction layer. Some of the assumptions for the parabolic model do not hold true anymore. In such a

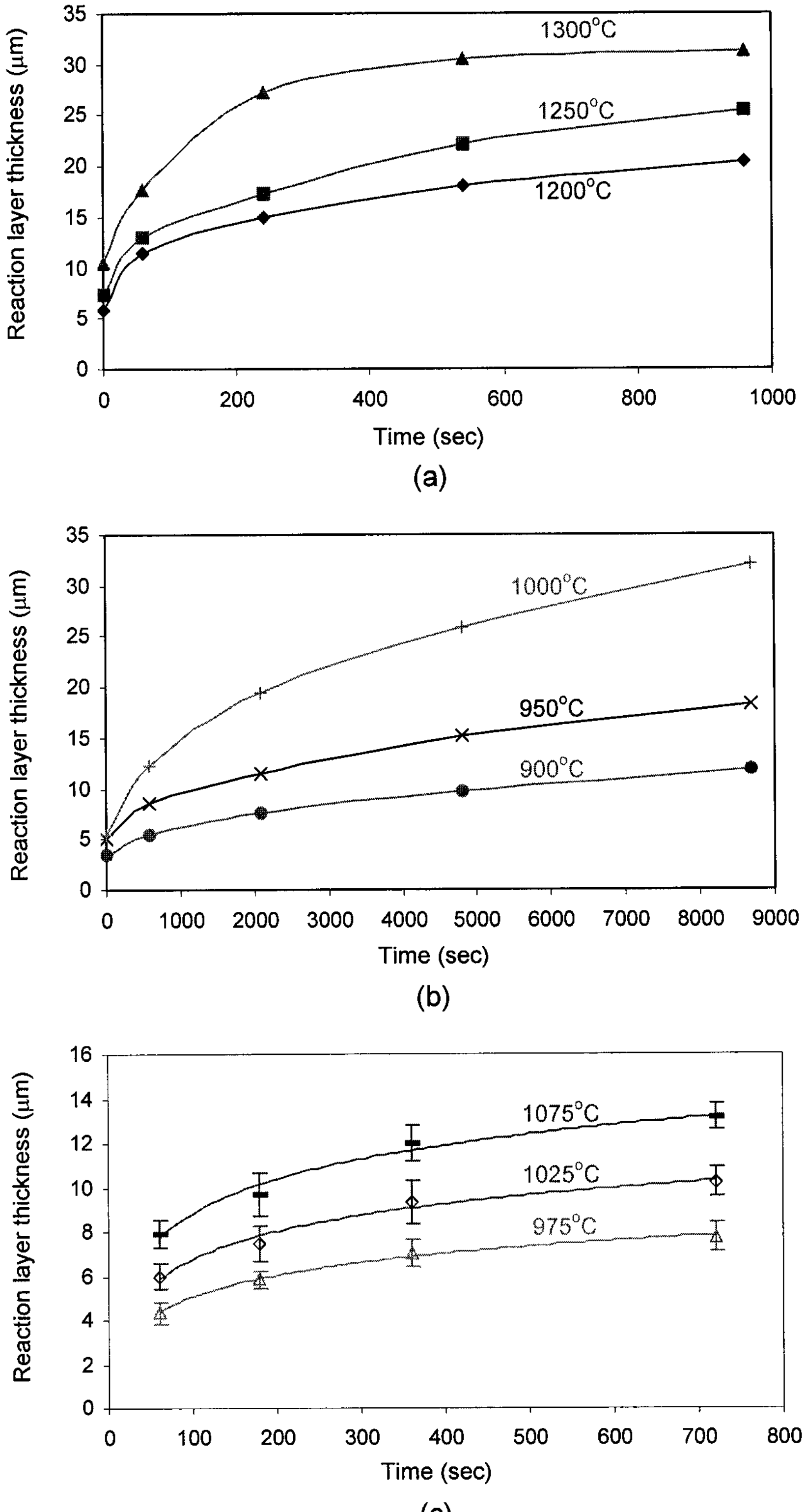

(a)

(b)

(c)

Figure A.2 - Reaction layer thickness measured versus time for the systems (a) Si_3N_4/Cu-5Cr, (b) AlN/Cu-22Ti and (c) Si_3N_4/Cu-25Ti

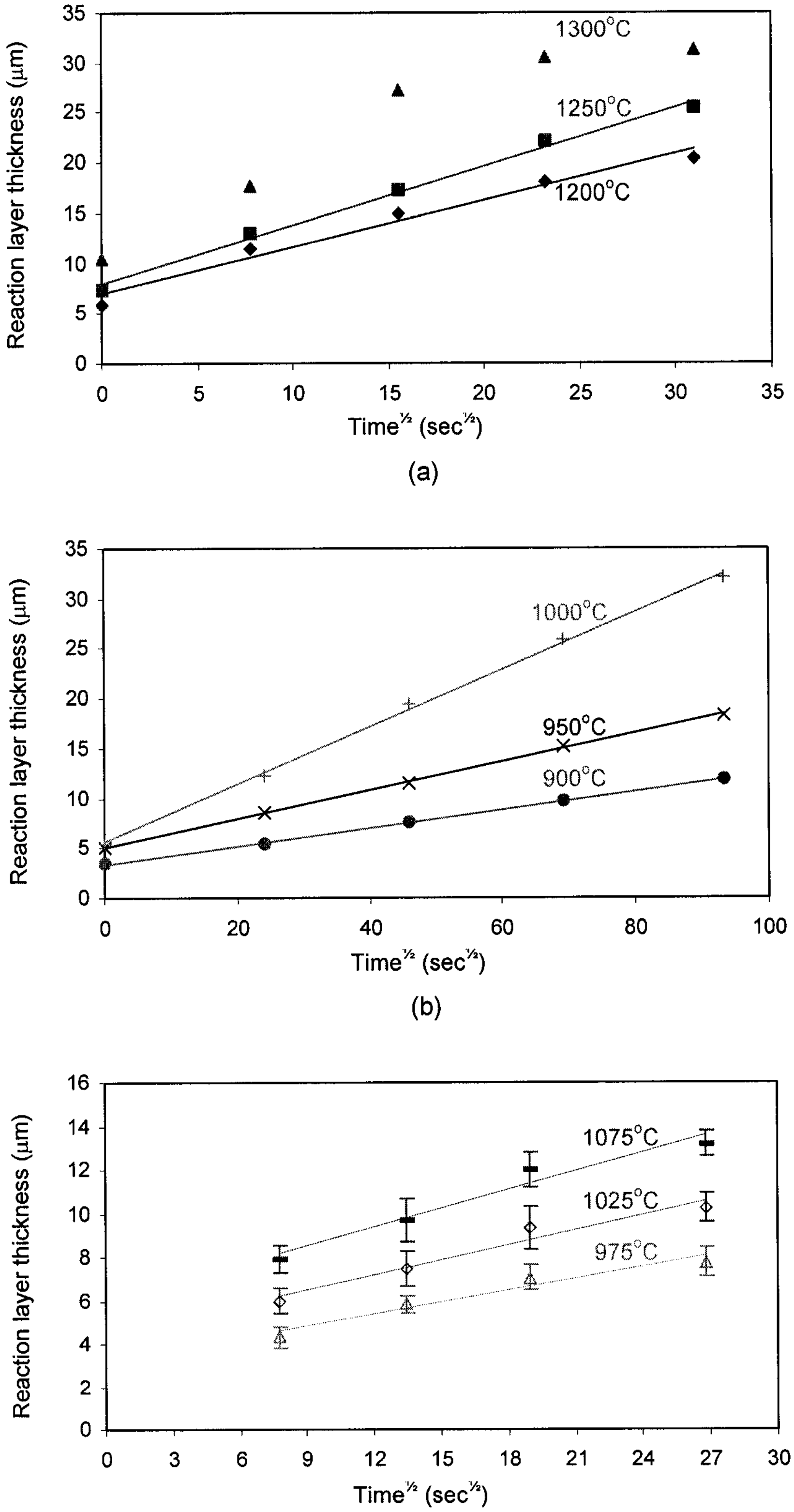

(a)

(b)

(c)

Figure A.3 - Reaction layer thickness measured versus square root of time for the systems (a) Si_3N_4/Cu-5Cr, (b) AlN/Cu-22Ti and (c) Si_3N_4/Cu-25Ti case, the modeling should be divided into two stages as illustrated in Figure A.4. This figure possesses more data points than the curve at 1300°C in Figure A.3, but is the same: only a limited number of points were presented in Fig. A.3 for clarity purposes. In the first stage, the reaction layer growth occurs through pure diffusion of the active element (described by the parabolic model), which then reacts with the Si_3N_4 ceramic. When the reaction layer reaches a certain thickness, named the critical thickness (δ_e), heterogeneity in diffusion is observed which now dictates the diffusion behavior. Raic et al. [A.1] have demonstrated a model based on heterogeneity of the mass transport, which can be applied to the modeling of the reactive system with low active element content. The complete modeling procedure and equation for numerical solving is presented in [A.1].

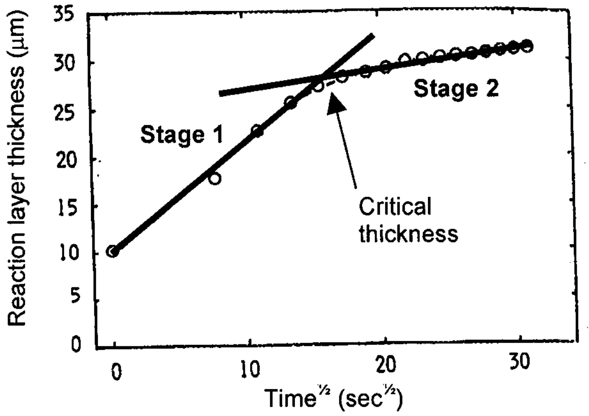

Figure A.4 – Relation between the thickness of the reaction layer and square root of holding time for the two growth stages.

High content in active element

In the case illustrated by examples (b) and (c), the reaction layer growth for the window analyzed, still satisfies the assumptions of the parabolic model. A point that should be made is that for the case of AlN with Cu-22Ti, the curves are still linear after 135 minutes, showing that even after this soaking time, the critical thickness (δ_e) was not reached and that the growth is still under the first stage of the Raic model. Nakao et al. [7.3] attributes the linear behavior to the fact that the concentration of the diffusing element remaining in the molten active alloy near the reaction layer is still sufficiently high, as the initial concentration was high, and the consumption effect (heterogeneity) is not yet significant. In these cases, much higher temperatures and longer times must be used to reach the critical thickness and therefore the Raic model with two stages will be observed. This is observed by a deviation of the experimental points from the linear fit on the graph of reaction layer thickness vs the square root of time, for the longer times and higher temperature, because the critical thickness (δ_e) will be exceeded.

For the two cases, the activation energy can be calculated through eq. A2 and are graphically represented in Figure A.5. The activation energies calculated using the Arrhenius relationship for the system AlN/Cu-22Ti is 137 kJ/mol and for the system Si3N4/Cu-25Ti is 64 kJ/mol. The activation energy for the AlN/Cu-22Ti system is higher than the case of the Si_3N_4 as the reaction layer is composed of only one phase (TiN) as oppose to two phases (TiN and Ti_5Si_3) in the other case and that the atomic bonding energy is higher for AlN than for Si_3N_4 [1.4].

References

[A.1] K.T. Raic, S.P. Nickolajevic, Z.V. Popovic, Modeling of reaction layer growth in Metal-Ceramic Joints Bonded with Filler Metal, Advanced Science and Technology, 1995, p 2231-2238.

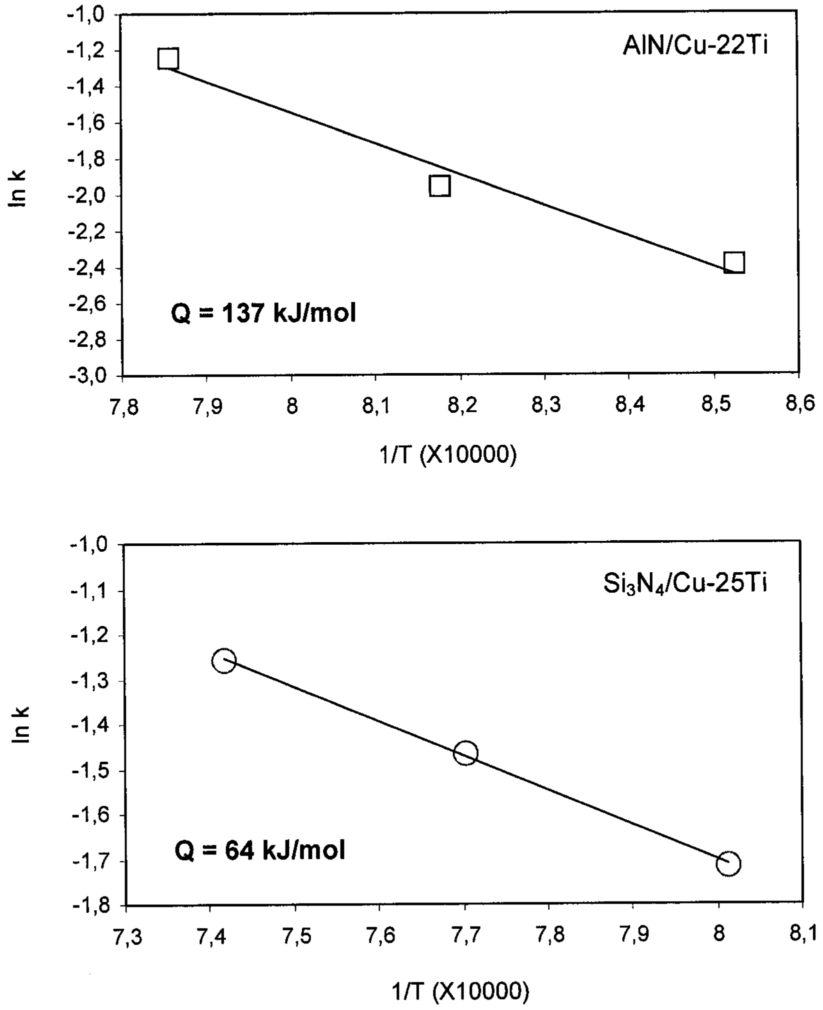

Figure A.5 – Activation energy measurement with Arrhenius equation for the system AlN/Cu-22Ti and Si_3N_4/Cu-25Ti.

Appendix B

Copyright Wavers

This appendix presents all the copyright waver obtained from all co-authors who participated in the redaction of the manuscripts. In addition, the waver from the publisher is also presented. Elsevier publishes all the various journals and therefore, the same agreement relating publication of a manuscript-type of thesis are applied. The following papers were the copyright transfer form were signed before the publication of this thesis:

- M. Brochu, M.D. Pugh and R.A.L. Drew, Wetting Behaviour of Copper on an Iron Aluminide Alloy, Intermetallics, (Chapter 3)
- M. Brochu, M.D. Pugh and R.A.L. Drew, Effect of Titanium Addition during Copper-Iron Aluminide Alloy Interaction, J. of Alloys and Compounds, (Chapter 4)
- M. Brochu, M.D. Pugh, S.F. Corbin and R.A.L. Drew, Assessment of Melting Behavior of Coated Powders, Material Science & Engineering A, (Chapter 6)
- M. Brochu, M.D. Pugh and R.A.L. Drew, Joining Silicon Nitride Ceramic using a Composite Powder as Active Brazing Alloy, Material Science & Engineering A, (Chapter 7)
- M. Brochu, M.D. Pugh and R.A.L. Drew, Brazing of Si_3N_4 Ceramic to an Iron Aluminide Alloy using Cu Interlayer, Ceramics International, (Chapter 8)

The following papers were not finally accepted and therefore, the authors' still retain the copyright. Information regarding the ownership of the copyright for the paper submitted to Microscopy and Microanalysis is also included.

- M. Brochu, H. Demers, M.D. Pugh, R. Gauvin and R.A.L. Drew, Charging Behavior of Nitride Ceramics using FE-SEM Microscope, Microscopy and Microanalysis, (Chapter 2)

- M. Brochu, M.D. Pugh and R.A.L. Drew, Fabrication of a Composite Powder and Utilization as Active Brazing Alloy, Journal of Material Science, (Chapter 5)

- M. Brochu, M.D. Pugh and R.A.L Drew, Partial Transient Liquid Phase Bonding of Si_3N_4 to FA-129 using Nickel as Core Interlayer, Journal of Refractory Metals and Hard Materials, (Chapter 9) authorGATEWAY Getting Published

print page | contact us

ELSEVIER home

Copyright information

Submitting your paper

- Introduction
- Your cover letter to the Editor
- Text file guidelines
- LaTeX file guidelines
- How to send your paper
- Where to send your paper
- Submission checklist

After acceptance

- What happens now?
- Proofreading
- **Copyright information**
- Tracking your paper

- How do I obtain a Copyright Transfer Form?
- Can I post my article on the Internet?
- What rights do I retain as author?
- Why does Elsevier request transfer of copyright?
- Why does Elsevier believe it needs exclusive rights?
- How do I obtain permission to use material from Elsevier publications?
- How do I obtain permission to use material from former Harcourt Health Science publications?
- How do I obtain permission from other publishers?
- Where should I send requests for permission that I receive from other authors?
- Can you provide me with a PDF file of my article?
- What is Elsevier policy on using patient photographs?

How do I obtain a Copyright Transfer Form?

You will receive a form automatically by post once your article is received by Elsevier's Production Department.

Can I post my article on the internet?

Please see the next section: What rights do I retain?

What rights do I retain as author?

As an author, you retain rights for large number of author uses, including use by your employing institute or company. These rights are retained and permitted without the need to obtain specific permission from Elsevier.

- Patent and trademark rights or rights to any process or procedure described in the article.
- The right to photocopy or make single electronic copies of the article for their own personal use, including for their own classroom use, or for the personal use of colleagues, provided those copies are not offered for sale and are not distributed in a systematic way outside of the employing institution.
- The right to post the article on a secure network (not accessible to the public) within the employer's institution.
- The right to retain a preprint version of the article on a public electronic server such as the World Wide Web. Elsevier does not require that authors remove from publicly accessible servers versions of their paper that differ from the version as published by Elsevier. See also

our information on electronic preprints for a more detailed discussion on these points.

- Posting of the article as published on a public server can only be done with Elsevier's specific written permission.
- The right, subsequent to publication, to use this article or any part thereof free of charge in a printed compilation of works of their own, such as collected writings or lecture notes.
- If the article is a "work for hire" made within the scope of the author's employment, the employer may use all or part of the information in this article for intra-company use.
- The right to include the article in a thesis or dissertation provided that this is not to be published commercially.
- The right to present the paper at a meeting or conference and to hand copies of the paper to the delegates attending the meeting.
- The right to publish a different or extended version of the paper so long as it is sufficiently new to be considered a new work.
- The right to expand the article into book-length form for publication.
- The right to re-use parts of the paper in other works, provided that the new work is not to be published commercially.

Other uses by authors should be authorized by Elsevier through the Global Rights Department, and authors are encouraged to let Elsevier know of any particular needs or requirements.

▲……

Why does Elsevier request transfer of copyright?

Elsevier wants to ensure that it has the exclusive distribution right, for all media. Such a right can be obtained through an exclusive license from authors, but there is virtually no difference between transfer and exclusive license. Given that there is virtually no difference, it seems to us that transfer does give an advantage in the elimination of any ambiguity or uncertainty about Elsevier's ability to distribute or sub-license.

▲……

Why does Elsevier believe it needs exclusive rights?

The research community needs certainty with respect to the validity, normally obtained through the peer review process, of scientific papers. The scientific record must be clear and unambiguous. Elsevier believes that by obtaining the exclusive distribution right it will always be clear to researchers that, when they access an Elsevier site to review a paper, they are reading a final version of the paper which has been edited, peer-reviewed, and accepted for publication in an appropriate journal. If Elsevier did not obtain exclusive electronic rights, it is likely that versions of scientific papers would clutter the Internet without clarification of the scientific status of such versions. See also our information on electronic preprints for more detailed discussion on these points.

▲……

How do I obtain permission to use material from Elsevier publications?

Requests for permission to reproduce materials from books and journals published by Elsevier BV, Elsevier Science Ltd, Elsevier Science Inc, Elsevier Science SA, Elsevier Science Ireland Ltd and the Pergamon imprint are handled by the Global Rights Department in Oxford.

▲……

Brochu, Mathieu

From: cbcadmin [cbcadmin@cems.umn.edu]
Sent: Monday, December 01, 2003 4:02 PM
To: Brochu, Mathieu
Cc: Charles Lyman; C.B.Carter
Subject: Re: copyright waver

Mathieu,

I have received a reply from Professor Lyman, the Editor-in-Chief. He suggests that "the way to handle this is to say that we can provide permission to republish through the Cambridge University Press permissions department [Ted Gerney; tgerney@cup.org]. However, the paper must be accepted first; therefore, the revisions that are contemplated must be acceptable to the referees".

As I stated earlier, the Microscopy Society of America (MSA) does not yet own copyright for this article. If your thesis is published first, then the signed copyright form will cover your paper's publication in Microscopy and Microanalysis (see the copyright information inside the Journal). If your thesis is published after the paper is accepted, then permission should be sought from Cambridge University Press.

I hope this answers your question.

On Nov 26, 2003, at 9:53 PM, Brochu, Mathieu wrote:

Dear Microscopy and Microanalysis,

I submitted a paper and it was returned with some modifications to perform on it. However, my university is asking me to get a copyright waver from the editor in order to publish it in my thesis (as I wrote a paper type of thesis). Could you please send me a letter stating that you are lending my the copyright of the paper in order to be included in my thesis.

Thank you very much for your help,

Mathieu Brochu

NRC-AMTC

3385 Griffith street

Ville St-Laurent, Quebec, Canada

H4T 1W5